



Single-Atom Catalysts for the Electroproduction of H_2O_2 in Optimized Acidic Conditions

Haraldsted, Jens-Peter Baernholdt

Publication date:
2022

Document Version
Publisher's PDF, also known as Version of record

[Link back to DTU Orbit](#)

Citation (APA):
Haraldsted, J-P. B. (2022). *Single-Atom Catalysts for the Electroproduction of H_2O_2 in Optimized Acidic Conditions*. DTU Chemistry.

General rights

Copyright and moral rights for the publications made accessible in the public portal are retained by the authors and/or other copyright owners and it is a condition of accessing publications that users recognise and abide by the legal requirements associated with these rights.

- Users may download and print one copy of any publication from the public portal for the purpose of private study or research.
- You may not further distribute the material or use it for any profit-making activity or commercial gain
- You may freely distribute the URL identifying the publication in the public portal

If you believe that this document breaches copyright please contact us providing details, and we will remove access to the work immediately and investigate your claim.

Single-Atom Catalysts for the Electroproduction of H₂O₂ in Optimized Acidic Conditions

A PhD Thesis Project by
Jens-Peter Baernholdt Haraldsted

Supervisor: Associate Professor Jakob Kibsgaard

Co-supervisor: Professor Ib Chorkendorff

Surface Physic and Catalysis (SurfCat)

Department of Physics

Technical University of Denmark



(2022)

Abstract

The planet's transitioning climate necessitates a societal shift towards a sustainable energy infrastructure. This can include the decentralized electroproduction of chemical commodities, such as H_2O_2 from PEM electrolysis reactors. This technology requires the development of electrocatalysts that are active, selective and stable during the operating conditions of scaled-up reactors. Single-atom catalysts anchored on nitrogen-carbon frameworks have promising potential for the selective electroreduction of oxygen to H_2O_2 . The electrochemical testing of such single-atom catalysts is typically conducted with rotating ring disk electrode experiments, which tend to over-perform in comparison to their performances in scaled-up reactors. On the other hand, adapting electrocatalysts to scaled-up reactors is a difficult process that needs to be tailored to each catalyst being tested. Consequently, better methods for electrochemical testing are needed because the research field is limited to rotating ring disk experiments of minimal relevance or resource-intensive scaled-up reactor experiments. The floating electrode technique has shown promise for the oxygen reduction reaction by providing facile access of oxygen gas to the catalyst layer, but this has not yet been utilized for the selective electroreduction of oxygen to H_2O_2 .

The modification of the floating electrode technique to test single-atom catalysts for the electroproduction of H_2O_2 was extensively explored. The results suggest that this floating electrode technique can provide both ideal and relevant conditions: the catalyst is not limited by the lack of oxygen at the higher overpotentials necessary for scaled-up operations, and the electroproduced H_2O_2 has facile escape channels from the abundant electrolyte. This project demonstrates a new application for the floating electrode technique, which has enabled the discovery of the iridium single-atom catalyst with comparable performances to the state-of-the-art cobalt single-atom catalyst in relevant operating conditions. Among the synthesized single-atom catalysts, the highly-active cobalt and iridium catalysts were more stable than the highly-selective platinum and palladium catalysts. In addition, potential degradation mechanisms are discussed, including metal agglomeration of single atom sites due to electrodeposition, and the electroreduction of H_2O_2 to H_2O .

Resume

Det skiftende klima på planeten nødvendiggør et samfundsskifte i retning af en bæredygtig energiinfrastruktur. Dette kan omfatte decentraliseret elektroproduktion af kemiske råvarer, H_2O_2 fra PEM-elektrolysereaktorer for eksempel. Denne teknologi kræver udvikling af elektrokatalysatorer, der er aktive, selektive og stabile under driftsbetingelserne for opskalerede reaktorer. Enkeltatom-katalysatorer forankret på nitrogen-doteret kulstofgitter har potentiale for selektiv elektroreduktion af oxygen til H_2O_2 . Den elektrokemiske testning af sådanne enkeltatom-katalysatorer udføres typisk med elektrodeeksperimenter med rotating ring disk electrode, som har en tendens til at overpræstere i forhold til deres ydeevne i opskalerede reaktorer. På den anden side er tilpasning af elektrokatalysatorer til opskalerede reaktorer en vanskelig proces, der kræver skræddersyes til hver katalysator, der skal testes. Derfor er der behov for bedre metoder til elektrokemisk testning, fordi forskningsfeltet er begrænset til eksperimenter med rotating ring disk electrode af minimal relevans eller ressourcekrævende opskalerede reaktorforsøg. Den floating electrode technique har været lovende for oxygenreduktionsreaktionen ved at give let adgang for oxygengas til katalysatorlaget, men denne er endnu ikke blevet brugt til den selektive elektroreduktion af oxygen til H_2O_2 .

Modifikationen af den floating electrode technique til at teste enkeltatoms-katalysatorer til elektroproduktion af H_2O_2 blev grundigt undersøgt. Resultaterne tyder på, at denne floating electrode technique kan give både ideelle og relevante forhold: katalysatoren er ikke begrænset af iltmanglen ved de højere overpotentialer, der er nødvendige for opskalerede operationer, og det elektroproducerede H_2O_2 har lette flugtkanaler fra den rigelige elektrolyt. Dette projekt demonstrerer en ny anvendelse af den floating electrode technique, som har muliggjort opdagelsen af iridium-enkeltatom-katalysatoren med sammenlignelig ydeevne som den avancerede kobolt-enkeltatom-katalysator under relevante driftsforhold. Blandt de syntetiserede enkeltatom-katalysatorer var de højaktive kobolt- og iridiumkatalysatorer mere stabile end de højselektive platin- og palladiumkatalysatorer. Derudover diskuteres mulige nedbrydningsmekanismer, herunder metalagglomering af enkeltatomsteder på grund af elektroaflejring og elektroreduktion af H_2O_2 til H_2O .

Preface

This thesis is submitted as partial fulfilment of a PhD degree in physics at the Technical University of Denmark (DTU). The work here was conducted from March 2019 to April 2022 with the Surface Physics and Catalysis group (SURFCAT) at DTU's Department of Physics under the supervision of Jakob Kibsgaard and co-supervision of Ib Chorkendorff. The project is funded by Villum Fonden, part of the Villum Center for the Science of Sustainable Fuels and Chemicals (V-SUSTAIN).

I would first like to thank Jakob Kibsgaard and Ib Chorkendorff for giving me this opportunity, which has ended up becoming a very fulfilling experience. Their knowledge and feedback were key assets that guided me through this project. In addition, I must gratefully acknowledge the research environment that Jakob and Ib have helped foster and establish at SURFCAT. Special thanks to Ezra Miller, Sungeun Yang and Johannes Novak Hansen, who were always ready to help me, no matter how busy they were. To both Tim Tichter and Chao Wei, I thank you for your insights and ingenuity. To the unsung heroes of SURFCAT, I humbly thank the floor managers Jacqueline McAnulty, Jakob Ejler Sørensen, and Brian Peter Knudsen for facilitating a safe and effective research environment in ways that I am probably mostly unaware of. I warmly, but cautiously, acknowledge my office mates, our office was fun and full of pranks, which has certainly gotten the best and worst of me: Thomas Smitshuysen, Jakob Bruun Pedersen, Bjarke Valbæk Mygind, Alexander Juul Nielsen and of course Suzanne Andersen, I will remember most of you fondly, for the most part.

Words will never fully encompass the gratitude I have to my family. Their impact has led my life to this singular point. To my parents, for teaching me the values of navigating through life's challenges with courage and integrity. To my siblings, for our purest of friendships and deepest of mutual understandings. Lastly, to my loving wife Emily Beaman, for nurturing me unconditionally with both patience and grace. Who knows where I would be without her.

If I ended up back to three years ago, then I would do this all again without question. There have been too many good memories, and I already miss it.

Jens-Peter Baernholdt Halrøldsted

List of Acronyms

Acac Acetylacetonate

AEM Anion-Exchange Membranes

CA Chronoamperogram

CP-HS-DM Constant-Potential Hybrid-Solvation Dynamic Model

CV Cyclic Voltammogram

DFT Density Functional Theory

ECSA Electrochemical Surface Area

EDS Energy Dispersive X-ray Spectrometry

EXAFS Extended X-ray Absorption Fine Structure

FET Floating Electrode Technique

AuFET Gold-coated Floating Electrode Technique

TiFET Titanium-coated Floating Electrode Technique

GDE Gas Diffusion Electrode

H₂O₂RR Hydrogen Peroxide Reduction Reaction

HAADF-STEM High-Angle Annular Dark-Field Scanning Transmission Electron Microscopy

HER Hydrogen Evolution Reaction

HOR Hydrogen Oxidation Reaction

ICP-MS Inductively Coupled Plasma Mass Spectrometry

MEA Membrane Electrode Assembly

M-N/C Metal-Nitrogen-Carbon Materials/Catalysts

MN_x Single Metal Atom Coordinated with X number of Nitrogen Atoms in a Nitrogen-Carbon Matrix

N-C N-doped hollow carbon sphere

NPMC Non-Precious Metal Catalysts

OER Oxygen Evolution Reaction

ORR Oxygen Reduction Reaction

2e- ORR 2-electron pathway

4e- ORR 4-electron pathway

Pd1/C Pd single-atom catalyst anchored on hollow carbon sphere

Pd1/N-C Pd single-atom catalyst anchored on N-doped hollow carbon sphere

PdNP/C Palladium Nanoparticles anchored on carbon

PEM Proton-Exchange Membrane

PEMEC Proton-Exchange Membrane Electrolysis Cell

PEMFC Proton-Exchange Membrane Fuel Cell

RCP Representative Concentration Pathway

RDE Rotating Disk Electrode

RRDE Rotating Ring Disk Electrode

SAC Single-Atom Catalyst

STEM Scanning Transmission Electron Spectroscopy

TEM Transmission Electron Spectroscopy

UV-Vis Ultraviolet-Visible Spectroscopy

XAS X-ray Absorption Spectroscopy

XPS X-ray Photoelectron Spectroscopy

XRD X-ray Diffraction

zPt₂ Zeise's dimer

Appended Papers

Paper I

The acidic electrolysis of H₂O₂ in high-mass transport conditions on stable Ir and Co single-atom catalysts.

Jens-Peter B. Haraldsted, Sofie Colding-Jørgensen, Thomas Smitshuysen, Christian Damsgaard, Ib Chorkendorff, Jakob Kibsgaard

In preparation

Paper II

Highly Active, selective, and stable Pd single-atom catalyst anchored on N-doped hollow carbon sphere for electrochemical H₂O₂ synthesis under acidic conditions.

Jiangbo Xi, Sungeun Yang, Luca Silvioli, Sufeng Cao, Pei Liu, Qiongyang Chen, Yanyan Zhao, Hongyu Sun, Johannes Novak Hansen, Jens-Peter B. Haraldsted, Jakob Kibsgaard, Jan Rossmeisl, Sara Bals, Shuai Wang, Ib Chorkendorff

Journal of Catalysis, Volume 393, 2021, Pages 313-323

Contents

Introduction.....	2
1.1 Climate Crisis: a Call for Sustainable Energy	2
1.2 Storing Energy: a Hydrogen Economy	5
1.3 Decentralization of H ₂ O ₂ : a Lucrative Opportunity	7
1.4 Thesis Outline	10
Oxygen Reduction Reaction (ORR)	14
2.1 Electrocatalysis	14
2.1.1 Thermodynamics.....	15
2.1.2 Activation Overpotential	16
2.1.3 Mass Transport Overpotential.....	16
2.1.4 Ohmic Overpotential	16
2.2 Oxygen Reduction Reaction	17
2.2.1 ORR: the 4e ⁻ process.....	18
2.2.2 ORR: the 2e ⁻ process.....	20
2.3 The field of 2e ⁻ ORR SAC's	21
2.4 The challenge of up-scaled ORR experiments.....	26
2.5 Conclusion	30
Experimental Methods.....	32
3.1 Catalyst Characterization	32
3.1.1 X-ray diffraction (XRD).....	32
3.1.2 X-ray photoelectron spectroscopy (XPS).....	33
3.1.3 Scanning transmission electron microscopy (STEM) and energy-dispersive x-ray spectroscopy (EDS).....	34
3.1.4 X-ray absorption spectroscopy (XAS).....	35
3.1.5 Inductively coupled plasma mass spectrometry (ICP-MS).....	36
3.2 Electrochemical measurements	36
3.2.1 RRDE.....	37
3.2.2 Floating electrode technique (FET)	38
3.2.3 Membrane electrode assembly (MEA) experiments.....	40
3.3 H ₂ O ₂ Quantification.....	42
3.2.1 Permanganate (KMnO ₄) titration.....	42
3.2.2 Ultraviolet-visible spectroscopy (UV-Vis)	43

Single Atom Palladium on N-doped hollow carbon spheres	46
4.1 Synthesis of the catalysts samples	46
4.2 Characterization	48
4.3 Electrochemical Measurements	49
4.4 DFT-modelling.....	55
4.5 Conclusion	56
Floating Electrode Technique.....	58
5.1 Floating Electrode for 4e ⁻ ORR	58
5.2 Floating Electrode for 2e ⁻ ORR	67
5.3 Post-article investigations of Pd1/N-C.....	70
5.4 Conclusion	72
Single Atom Catalysts of Interest.....	74
6.1 Experimental Strategy	74
6.2 Determining Catalysts of Interest	75
6.3 Catalyst Synthesis.....	78
6.4 Initial Testing and Characterizations	82
6.5 Extensive Testing and Characterizations	90
6.6 Conclusion	98
References	100
Appendices.....	A1
Appendix A	A1
Appendix B	A9
Appendix C	A38
Appendix D.....	A40

Chapter 1

Introduction

This chapter will explain the motivations behind this project. Namely, it will introduce the validity and seriousness of climate change. It will go on to explain the challenges in transforming global energy infrastructures to address this climate change. Particularly, how to store green electricity from sustainable sources in order to be fully utilized. A hydrogen economy is a very promising solution in this respect, and with it comes lucrative opportunities in the electrification of chemical productions.

1.1 Climate Crisis: a Call for Sustainable Energy

Svante Arrhenius published the theory of climate change and the greenhouse effect in 1896.¹ This greenhouse theory arose from Arrhenius's calculations that depicted earth as a black body, and the rising levels of CO₂ might affect the atmosphere's ability to absorb outgoing radiation from the ground rather than let it escape into space, effectively creating a greenhouse effect.² It would not be until almost a century later that scientists were able to find very suggestive evidence through analyzing trapped air bubbles in ice samples from glaciers aging hundreds of thousands of years old.³

By extracting deep ice cores from glaciers in Greenland, Delmas et al. were able estimate the CO₂ concentrations of Earth's atmosphere up to 800,000 years ago.⁴ Extracting ice cores at different depths from the glaciers corresponds to the age of the ice, where these ice cores get older the deeper they are within a glacier (Figure 1.1a, top). Careful and methodical extraction of these ice cores enabled very sensitive quantification of their gas compositions with gas chromatography. In addition to the CO₂ concentrations, the gas chromatograph also provided insights to the corresponding temperature by analyzing the isotopic ratios of oxygen (Figure 1.1a, bottom). This led to a very consistent correlation between the Earth's temperature and its atmospheric CO₂ concentrations across the past 800,000 years (Figure 1.1b), and thus landmarks evidence for the greenhouse effect on a planetary scale.

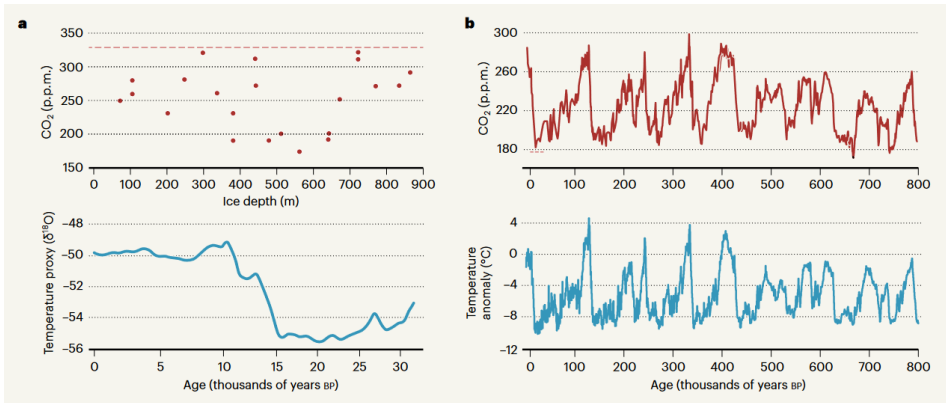


Figure 1.1: Analysis of ice-cores at different depths within a glacier by Delmas et al.⁴ (a, top) CO₂ concentrations of gases extracted from ice cores determined by gas chromatography. Dotted red line corresponds to the CO₂ concentrations during the time of the study in 1980. (a, bottom) Temperature derived from the isotopic ratios of the oxygen content of the extracted gas samples. (b) The resulting CO₂ and temperature records over the past 800,000 years. The consistent trend between CO₂ and temperature landmarks strong evidence for the greenhouse effect on a planetary scale. From ³

Since the industrial revolution, there has been a distinct rise in CO₂ concentrations that has become statistically significant enough to the point where scientists can claim with confidence that this rising trend is the result from human activity, specifically from the combustion of fossil fuels to power our modern civilization and its conveniences.⁵ To put it bluntly, for the past 800,000 years, the CO₂ concentration of the earth's atmosphere has oscillated between 150 to 330 ppm and it has just exceeded 400 ppm in the past decade. Even more alarming is that humanity is emitting more CO₂ every year from the previous year.

Already we are beginning to see changes on Earth's climate that is jeopardizing our planet's ability to sustain life. Glaciers melting will cause the sea level to rise which compromises coastal cities with flooding and tropical storms.⁶ These coastal cities are assets worth trillions of dollars, and are home to 40% of the world's population. A more urgent issue is freshwater scarcity, which is already affecting four billion people.⁷ Fresh water is necessary for crop growth, and wildlife biodiversity for ecosystems vital for food supplies of all life on this planet.⁸ It is difficult to predict how severe the implications of climate change actually are because of the complexity of our planet's ecosystem and the complexity of our modern civilization.⁹ As a result, there are many uncertainties in how both Earth and humanity will respond, making it difficult to determine how to prepare for what may happen in the future. While not able to predict the future, the use of scenarios has been utilized for strategic planning in militaries and private businesses to provide the most robust solutions under a wide range of possible futures.¹⁰ Climate scientists have adopted these

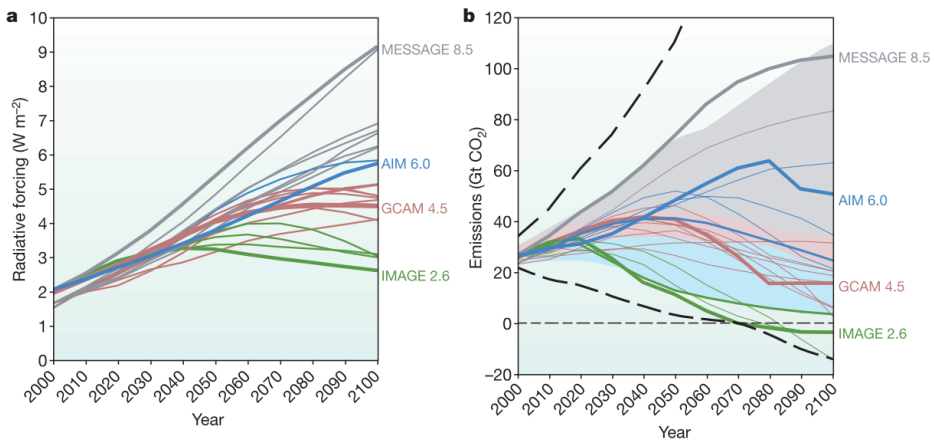


Figure 1.2: Representative concentration pathways projected to 2100. The radiative forcing (a) is the net radiation absorbed ($\text{W}\cdot\text{m}^{-2}$) relative to pre-industrial era and the emissions (b) are a measure of the net CO_2 (Gt) in the atmosphere. Grey shaded areas refer to reference scenarios¹¹, blue areas represent mitigation scenarios, and pink represent a mixture of reference and mitigation scenarios¹². From ⁹

systems and summarized batches of scenarios into what is called representative concentration pathways (RCP's) to systematically determine how to best use our efforts and resources. A parallel approach, rather than a sequential approach, is used to generate RCP's to better account for feedback relationships in these dynamic systems. A radiative forcing scenario is the summary of different combinations of economic, technological, demographic, policy, and institutional futures that lead to the roughly the same result (Figure 1.2a). Radiative forcing is simply the energy flux in the atmosphere caused by natural and/or anthropogenic factors, exactly like Arrhenius's black body experiments. A natural cause affecting radiative forcing could be less reflection of incoming radiation due to less glacial area or increased absorption in the atmosphere due to increased methane concentrations from thawing permafrost. An anthropogenic cause are things like CO_2 emissions and reduced land cover. The results of radiative forcing scenarios will not only affect the climate scenarios but also create feedback loops on the socio-economic scenarios and emissions scenarios (Figure 1.2b) that initially caused them. As of 2021, the world is in a red scenario according to Figure 1.2b but a grey scenario according to Figure 1.2a, confirming the underestimation and severity of these feedback loops.

Continuing to increase CO_2 concentrations (Figure 1.2, grey-colored RCP's) is a precarious experiment for the only planet humanity has to live on, yet we still need an energy infrastructure to maintain our modern civilization. There is therefore a call for sustainable energy to allow our modern civilization to exist in harmony with our planet's ecosystem, and potentially mitigate the damage we have already done (Figure 1.2, red-colored RCP's).

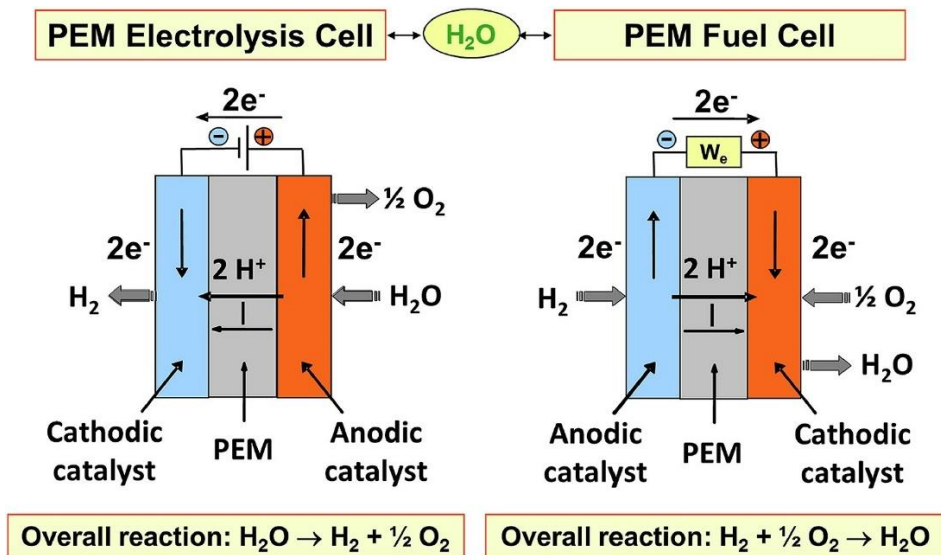


Figure 1.3: Schematic of a PEM electrolysis cell (left) and a PEM Fuel cell (right).¹³

1.2 Storing Energy: a Hydrogen Economy

The good news is that we have technologies that can meet humanity's energy demands 100 times over without emitting greenhouse gases.¹⁴ Rather than combusting fossil fuels, green electricity is derived by wind, solar, and geothermal means, by simply harnessing energy that is already present, and converting it to electricity. The issue with this green electricity is it is derived from energy that is not always present: solar panels cannot generate electricity when the sun has set, and wind turbines cannot generate electricity without wind. The main challenge to achieving a sustainable energy landscape is storing this green electrical energy so that it can be used when it is needed, rather than when it is available.^{15,16}

The two most promising technologies for energy storage are redox-flow batteries and H_2 electrolysis/fuel cells. Redox flow batteries are ideal because they can efficiently charge and discharge energy. However, storing energy solely in redox flow batteries has impracticalities; excess electrical energy is wasted once redox flow batteries are fully charged. In addition, electrical energy is difficult to transport over long distances. An elegant solution is using H_2 electrolysis/fuel cells in tandem with redox-flow batteries because these two technologies accommodate each other's strengths and weaknesses. Excess electrical energy can be converted into chemical energy in the form of H_2 gas as an energy storage of an effectively limitless magnitude. In addition, H_2 is also easier transport through gas tanks and gas pipelines.

fuel cell requires high-energy chemical inputs (H_2 , O_2), and outputs electricity and low-energy chemicals (H_2O).

The electrochemical reactions mentioned occur at certain voltage potentials (V) where catalysts are necessary. Even with the best catalysts, this technology will never be 100% efficient at converting between chemical and electrical energy (Figure 1.4). This is because there are activation over potentials required on both electrodes, as well as concentration over potential due to mass transport, and ohmic drop resistances from the proton-conducting and electron-conducting components of the electrochemical cell. As a result, an electrolysis/fuel cell will never be more than 70% efficient simply due to the fundamental laws of thermodynamics, where a more realistic state-of-the-art energy efficiency of 50-60% is estimated.¹³ This impracticality is inherent in all processes where energy is converted from one form to another, such as a combustion engine that is only 20-30% effective at converting fuel energy into effective power.

Common criticisms are that H_2 economy is too expensive and energy inefficient. While electrolysis/fuel cells will only be about 50-60% efficient at converting this energy, this is still plenty, since we would have excess green electricity anyways, and this inefficiency can be mitigated with redox-flow batteries in tandem, which have an energy efficiency of over 80%. A H_2 economy is criticized as being too expensive, but this criticism simply lacks perspective if we are simply comparing it to a fossil fuel economy that has conveniently ignored the cost of climate change in the past decades.¹⁹ The underestimation of the feedback loops in the RCP's (Figure 1.2) suggests it is unlikely we can accurately calculate the future cost of climate change today. A valid criticism of the H_2 economy is the scarcity of the metals necessary to catalyze these reactions. Platinum and Iridium are the best catalysts to use as electrodes for these PEM technologies, but the scarcity of these metals means that PEM technologies need to find catalysts based on more earth-abundant metals in order to scale up to be a relevant technology for the planet's green energy infrastructure. Catalysts based on iron and cobalt are presently being investigated for these purposes.^{20,21}

1.3 Decentralization of H_2O_2 : a Lucrative Opportunity

The global energy demands were 18 TW in 2013, where electricity and transportation accounts for 2.1 TW and 3.3 TW, respectively.²² A H_2 economy maps out a clear path towards a sustainable future for these energy sectors. A more intriguing area is

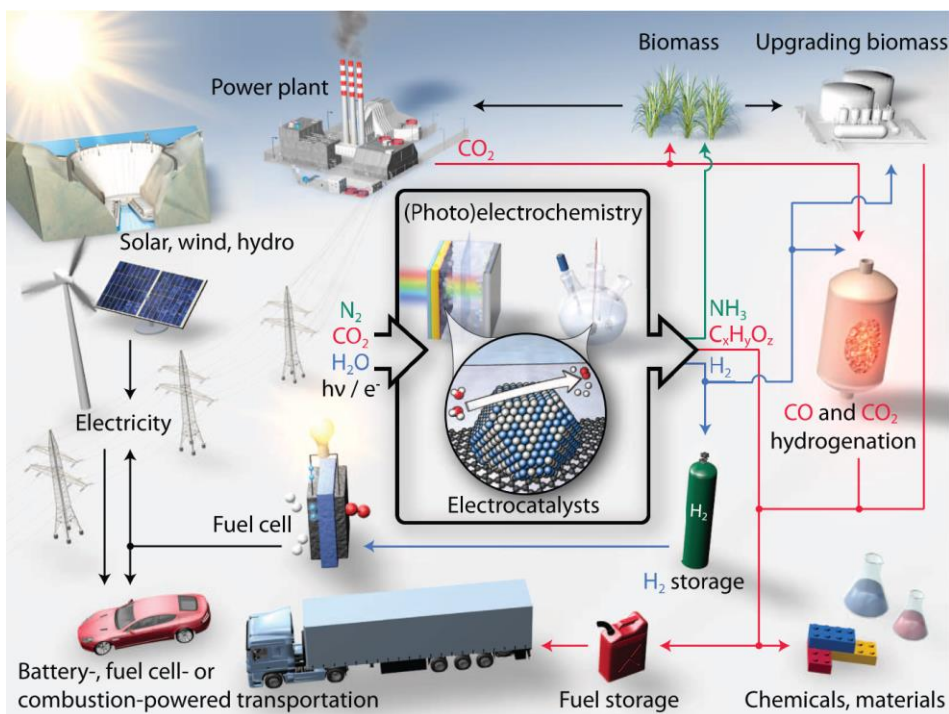


Figure 1.5: Schematic of a sustainable energy landscape based on electrocatalysis. From ²²

the industrial chemical production sector, accounting for 1.5 TW, of which is derived exclusively from fossil fuels. Among the most prevalent chemical precursors include hydrogen (50 Mt year⁻¹), hydrogen peroxide (2.2 Mt year⁻¹), ethylene (115 Mt year⁻¹), propylene (73 Mt year⁻¹), methanol (40 Mt year⁻¹), and ammonia (175 Mt year⁻¹). The electrification of these processes would only require the abundantly available precursors of N₂, CO₂, H₂O, and the appropriate electrocatalysts to optimize the chemical transformations involved (Figure 1.5). Among these chemicals, hydrogen peroxide (H₂O₂) is interesting because it can be produced at a cheaper cost with an electrolysis cell compared to conventional methods. It is economically viable today, even in a fossil fuel economy.

H₂O₂ is a strong oxidant that is mainly used in industrial applications and water treatment processes. One of H₂O₂'s appeals as a green oxidant is its 47% active oxygen content (wt. %) and only H₂O as a waste product. It is only second to O₂ itself (100% active oxygen content).^{23,24} Unlike O₂, H₂O₂ requires a low energy input to be utilized. It is effective under mild reaction conditions with a catalyst, typically utilizing Fenton's Process, where Fe cations generate hydroxyl radicals.²⁵

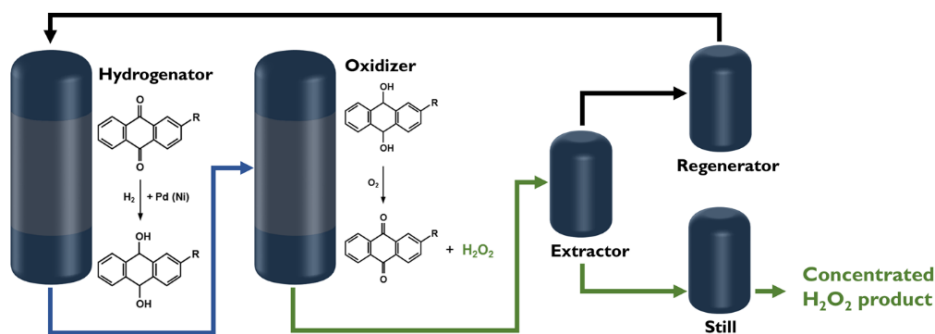


Figure 1.6: Schematic of the anthraquinone process summarized by four major steps: hydrogenation, oxidation, H_2O_2 extraction and treatment of the working solution. From ²⁶

H_2O_2 is presently produced by the anthraquinone process, which is summarized by four major steps: hydrogenation, oxidation, H_2O_2 extraction and treatment of the working solution (Figure 1.6).²⁷ The advantage of this process is that it yields high concentrations of H_2O_2 (~70 wt.%) suitable for most applications. The disadvantages are that it requires large centralized facilities. This means that transporting this highly concentrated oxidant is both costly and dangerous. It also requires high-energy inputs and results in high waste yields including separation steps to remove organic impurities that require high volumes of solvents. Some of these solvent mixtures even necessitate regeneration due to unwanted side reactions occurring during the hydrogenation and oxidation steps.²³ So while H_2O_2 is inherently a green chemical, the means to produce it and transport it to the point-of-use are not green.

To the point, the industrial anthraquinone process for H_2O_2 production has a rough cost of \$1.5 kg- H_2O_2 without accounting for transportation and storage costs. A compact PEM electrolysis cell can be deployed at the point-of-use, circumventing transportation and storage costs, and requires only H_2O , O_2 , and electricity to make H_2O_2 at a cost less than \$1.0 kg- H_2O_2 .²⁸ Taking into account yearly demands (2.2 Mt year⁻¹), this corresponds to redefining a growing industry worth billions of dollars in annual revenue.

The motivation of this research apparent: reduce the planet's yearly carbon emissions, and earn billions of dollars while doing it. The race for innovating this technology has started roughly a decade ago, involving numerous tech start-ups and research groups in pursuit. Research revolves around electrocatalysts to selectively reduce oxygen to hydrogen peroxide on the cathode (ORR) or to selectively oxidize water to hydrogen peroxide on the anode (OER).^{29,30} Figure 1.7 summarizes these

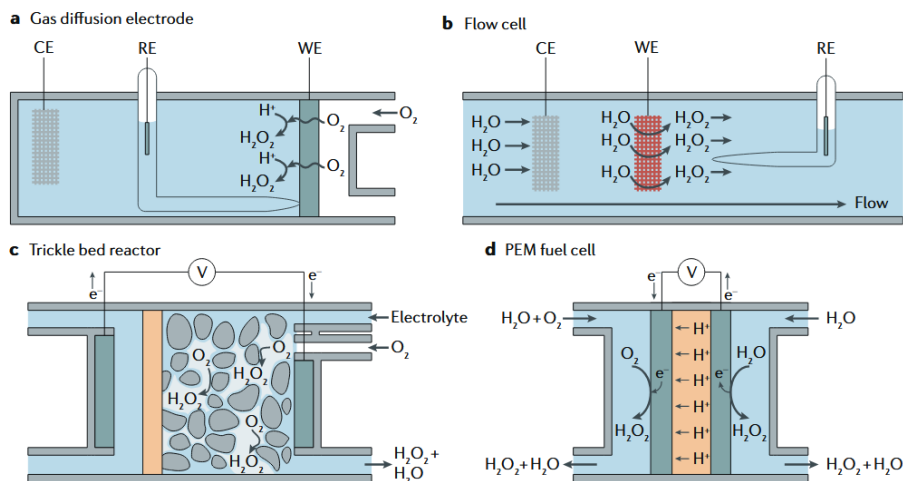


Figure 1.7: Potential reactor configurations for the electroproduction of H₂O₂ including gas diffusion electrodes (a) and trickle bed reactors (c) for the cathodic electroproduction of H₂O₂, and a flow cell for the anodic electroproduction of H₂O₂. Each approach has its advantages and disadvantages, while the PEM reactor (d) presents the potential to harness both processes in tandem from a single reactor design. From ³⁰

reactions as well as the different reactor designs, each with their own various advantages.³⁰ This research includes engineering components of reactors with promising potential for scale-up. These challenges are mainly having a high surface area electrode with many catalyst sites for high H₂O₂ outputs, but also allows the H₂O₂ to desorb away from the catalyst layer to avoid any further reactions. A gas diffusion electrode (Figure 1.7, a) is typically a porous carbon cloth/paper with a hydrophobic treatment on one side to preserve the gas channels (the O₂ source), while a catalyst ink is deposited on the opposite side, in contact with electrolyte (the H⁺ source). This fragile balance between proton channels, oxygen channels, and H₂O₂ channels can also be achieved with a trickle bed reactor (Figure 1.7, c). Interestingly, a flow cell that selectively oxidizes H₂O to H₂O₂ bypasses the need for oxygen channels. Both of these endeavors (ORR and OER selective for H₂O₂) can potentially be utilized in tandem in a PEM reactor (Figure 1.7, d). However, this thesis will focus on catalysts for cathodic electrodes selective for ORR to yield H₂O₂.

1.4 Thesis Outline

The necessity to transition the planet's energy infrastructure to be more sustainable has been introduced. This includes the decentralized electroproduction of chemical commodities, which motivates this project. The focus of this project is to find better catalysts for these decentralized PEM H₂O₂ electrolysis reactors. In order to do this we need faster and better ways to test these catalysts.

My PhD work has revolved around the synthesis of single-atom catalysts (SAC) and the electrochemical testing of these catalysts for the selective electroreduction of oxygen to hydrogen peroxide in acidic conditions. I was responsible for the experimental planning, synthesis, electrochemical testing and the initial characterizations (ICP-MS, XPS, XRD) of these single atom catalysts, while HAADF-STEM, EDS, and EXAFS characterization were performed by colleagues. The metals used for the single atom catalyst samples were cobalt, palladium, platinum, and iridium.

In the field of the oxygen reduction reaction for the 2-electron pathway ($2e^-$ ORR), the electrochemical testing of such single atom catalysts is typically limited to rotating ring disk electrode (RRDE) experiments. These RDDE experiments tend to overperform in comparison to the performances of reactors based on membrane electrode assemblies (MEA). A large portion of this project is the modification of the floating electrode technique (FET) for $2e^-$ ORR to provide these catalysts with ideal but relevant conditions: the catalyst is not limited by the lack of O_2 at the higher overpotentials necessary for scaled-up operations, and the electroproduced H_2O_2 has the facile escape channels from the abundant electrolyte. This FET provides a better performance indicator for catalysts than RRDE, while not being as resource-intensive as scaled up MEA reactors.³¹⁻³⁴ The subsequent chapters of this thesis are outlined as follows:

Chapter 2 is a technical introduction briefly summarizing electrocatalysis and the field of ORR. It will introduce how density functional theory calculations can be used to screen active catalysts that are selective towards either the $4e^-$ or the $2e^-$ ORR pathways that yield either H_2O or H_2O_2 , respectively. It will introduce the promising single atom catalysts, as well as go over the shortcomings of the traditional methodologies used in fields pursuing better more active ORR catalysts.

Chapter 3 goes over the experimental methods, including electrochemical set-ups and characterization techniques.

Chapter 4 revolves around the international collaboration resulting in the article, Highly Active, selective, and stable Pd single-atom catalyst anchored on N-doped hollow carbon sphere for electrochemical H_2O_2 synthesis under acidic conditions published in Journal of Catalysis. Here I was involved in testing a Pd single-atom catalyst (Pd1/N-C) in a GDE set up. This initial experience exposed me to both the successes and shortcomings of benchmarking $2e^-$ ORR performances that sparked the motivations for the rest of my work.

Chapter 5 includes my visit to Kucernak's research group at Imperial to learn the standard Floating Electrode Technique (FET) first hand. It will talk about how similar HOR and $4e^-$ ORR activity benchmarks were reproduced, but also mention some discrepancies that deserve considerations for future $4e^-$ ORR FET experiments. It also presents the journey of extensively trouble-shooting the modification of the FET for the analysis of $2e^-$ ORR performances. This includes

some initial experiments using the Pd1/N-C catalyst (Chapter 4), which yielded results with some interesting implications in the research field.

Chapter 6 talks about how I synthesized various single atom catalysts with different metals (Co, Pd, Pt, Ir) and how I strategically screened this pool of catalysts to utilize the limited time and resources on the best catalysts containing single atom sites, and then characterizing them to actually prove they are single atoms. It demonstrates the utility provided by the modified FET for the analysis of 2e⁻ ORR performances and sums up the project with some concluding remarks.

Chapter 2

Oxygen Reduction Reaction (ORR)

The Oxygen Reduction Reaction (ORR) is the cathodic reaction in PEM Fuel cells and PEM H₂O₂ electrolyzers. This chapter will give a general overview of ORR by giving a brief introduction to electrocatalysis. It will then summarize the different competing reactions on an ORR cathode based on Nørskov's Density Functional Theory (DFT) calculations, and how electrocatalysts can be optimized for the selectivity and activity of the desired reactions. It will then present the potential of single atom catalysts, and lastly how the field of ORR can be improved with electrochemical testing that is more representative of operating conditions.

2.1 Electrocatalysis

Explaining the physical form of a catalyst is tricky, but Chorkendorff and Niemantsverdriet manage to find an elegant answer.³⁵ *'Catalysts come in many shapes and sizes consisting of virtually any material imaginable.^{36–38} They range from atoms up to zeolites, from metals to acids, and from solids to dissolved salts in a solution.'*

An electrocatalyst is typically a metal surface where species can adsorb, react, and desorb, where each of these steps has an activation barrier. A series of these reaction steps results in an electrochemical reaction. The activation barrier of an electrochemical reaction, also known as the activation overpotential (E_{act}), summarizes all of the activation barriers of the reaction steps. A catalyst does one thing during all of this: it improves the kinetics of a reaction by lowering the activation energy barrier (E_{act}) necessary to facilitate it. For an electrochemical reaction, this means more current per overpotential spent. A catalyst does not change the thermodynamics of the reaction (E_{cell}).

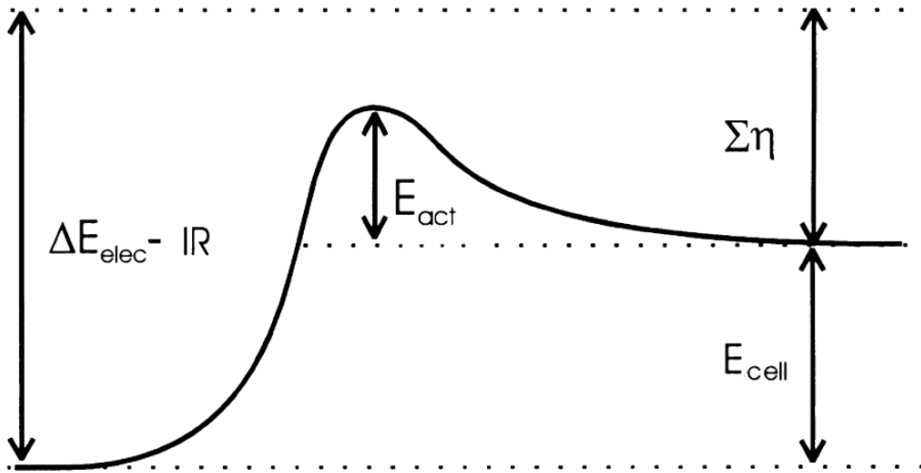


Figure 2.1: Energy losses involved in an electrochemical reaction.³⁹

2.1.1 Thermodynamics

Figure 2.1 is a potential energy diagram of an electrochemical reaction. Since the result is a net gain in energy, we can assume it is a reaction from a PEM electrolysis cell, where the potential energy is shown in terms of voltage. The minimum necessary voltage to start an electrochemical reaction on an electrode, E_{cell}^0 , is defined as:

$$E_{cell}^0 = \frac{\Delta G^0}{nF} \approx \frac{\Delta A}{nF} = E_{cell} \quad (2.1)$$

$$\Delta G^0 \approx \Delta A = \Delta H - TR\Delta n - T\Delta S \quad (2.2)$$

Where ΔG^0 is the change in Gibbs free energy, n is the number of electrons transferred. For the sake of simplicity, we will assume variations in standard conditions to be negligible, and therefore approximate ΔG^0 to be ΔA (enthalpy of formation). As a result, the electrolysis of water can be summarized to $\Delta A = 237$ kJ/mol, and $E_{cell} = 1.23V$, using equations 2.2 and 2.1, respectively. In a theoretical world, where everything is perfect, this would be the voltage required to drive a PEM electrolysis cell. In reality, to drive an electrolysis cell at a certain current (I), the actual voltage (E_{elec}) is defined as:

$$\Delta E_{elec} = E_{cell} + IR + \Sigma\eta \quad (2.3)$$

Where IR is the current-dependent ohmic overpotential from the resistances in the proton-conducting and electron-conducting components of the cell and where $\Sigma\eta$ is the sum of the other overpotentials. $\Sigma\eta$ includes the activation overpotentials (E_{act}) at both the cathode and the anode, as well as the mass transport overpotential (E_{MT})

due to the accumulated concentrations of the gaseous products on the electrode surfaces.

2.1.2 Activation Overpotential

Activation overpotential (E_{act}) can be summarized by the Butler-Volmer equation (2.4) which is commonly simplified to equation (2.5):

$$i = i_0 \cdot \left\{ \exp \left[\frac{\alpha_a n F E_{act,a}}{RT} \right] - \exp \left[\frac{\alpha_c n F E_{act,c}}{RT} \right] \right\} \quad (2.4)$$

$$E_{act} = \frac{RT}{n\alpha F} \ln \frac{i}{i_0} \quad (2.5)$$

Where i is the electrode current density, i_0 is the exchange current density, and n is the number of electrons transferred during the reaction. α_c and α_a are the dimensionless charge transfer coefficients of the cathode and anode respectively.⁴⁰

2.1.3 Mass Transport Overpotential

Mass Transport Overpotential (E_{MT}) occurs where current density becomes large enough to impede the access of reactants to the active sites on a catalyst. This overpopulation of reacting molecules on the active sites slows down the reaction rate. E_{MT} can be estimated using the Nernst equation:

$$E_{MT} = \frac{RT}{nF} \ln \frac{C}{C_0} \quad (2.6)$$

Where C is the product concentration and C_0 is the reactant concentration (assumed to be bulk concentration).⁴⁰

2.1.4 Ohmic Overpotential

Ohmic overpotential, also known as ohmic drop or ohmic losses, is defined by Ohm's Law:

$$E_{Ohm} = IR = \frac{\delta}{\sigma} I \quad (2.7)$$

Where σ is the material conductivity and δ is the material thickness. In a PEM-electrolysis cell, E_{Ohm} will come from the electrical-wiring and the proton – conducting Nafion membrane. The Nafion membrane is typically the main contributor of E_{Ohm} in a PEM device.⁴⁰

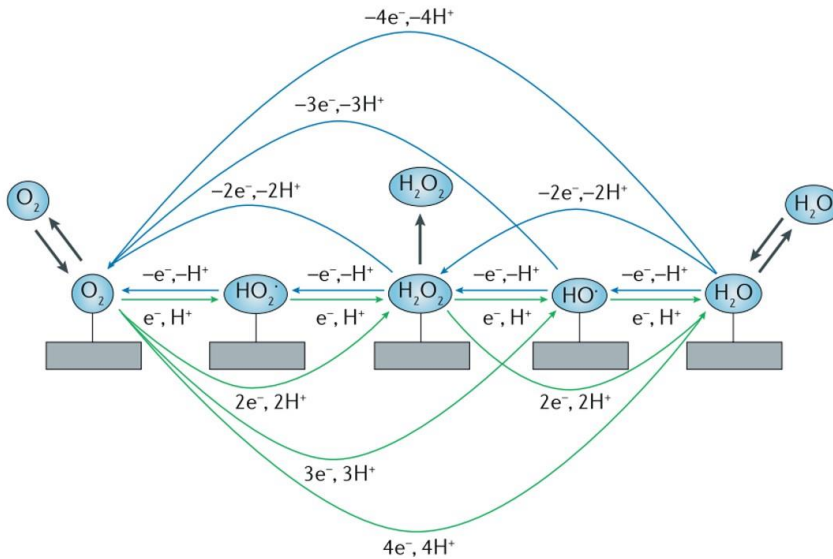
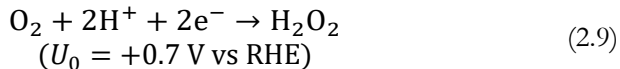
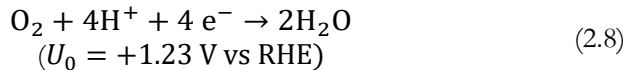


Figure 2.2: The many different reaction pathways during Oxygen Reduction Reaction (green arrows) and Oxygen Evolution Reaction (blue arrows). Intermediates are derived from the associative mechanism. From ³⁰

2.2 Oxygen Reduction Reaction

The oxygen reduction reaction is complex (Figure 2.2). It has numerous reaction steps, which have multiple different pathways. The oxygen reduction reaction (ORR) can electroreduce O_2 to H_2O via the 4-electron pathway ($4e^-$), which is necessary for a PEM fuel cell (Eq 2.8). Alternatively, it can also electroreduce O_2 to H_2O_2 via the 2-electron pathway ($2e^-$), which is necessary for a PEM H_2O_2 -electrolyzer (Eq 2.9).



A good ORR catalyst for both $4e^-$ and $2e^-$ ORR involves not just good activity but also good selectivity towards their intended reactions. This is essential if the catalyst is to perform well in real-world applications. A catalyst designed for $4e^-$ ORR has to be well over 99% efficient towards H_2O because every molecule of H_2O_2 produced can cause problems to various components of the PEM fuel cell over time.^{41–44} And on the other side, a catalyst designed for $2e^-$ ORR has to be efficient towards H_2O_2 , in order to stay economically competitive. In summary, for a good ORR catalyst, the $4e^-$ and $2e^-$ pathways must be as mutually exclusive as possible: it is either a good $4e^-$ or a good $2e^-$ catalyst, but it cannot be both.

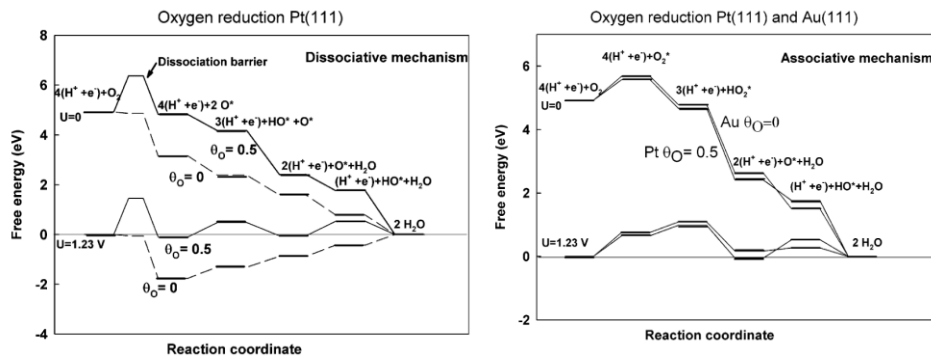
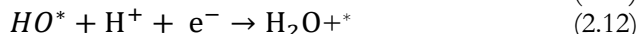
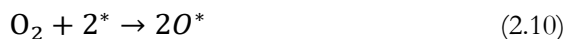


Figure 2.3: Free energy diagrams for the oxygen reduction reaction. (left) the dissociative mechanism on a Pt(111) surface at two different oxygen coverages ($\theta_O = 0$ and 0.5). (right) the associative mechanism on Pt(111) and Au(111) surfaces (Pt $\theta_O = 0.5$ and Au $\theta_O = 0$) From ⁴⁵

2.2.1 ORR: the 4e⁻ process

Density functional theory (DFT) proposes two mechanisms for 4e⁻ ORR: the dissociative mechanism and the associative mechanism. They are defined by what happens to the initially adsorbed oxygen ($*O_2$ where * is denoted for a surface site). In the dissociative mechanism (Figure 2.2, left), O_2 will adsorb to 2 surface sites ($*$) and dissociate into two O^* species:



In the case of the commonly studied Pt(111) surface, Nørskov et al.⁴⁵ showed that the high stability of the O^* and HO^* intermediates (ΔE_O and ΔE_{OH}) means they are the rate-limiting step for the overall reaction. These intermediates are effectively ‘thermodynamic sinks’ and are the main contributors for the activation overpotential (E_{act}) for 4e⁻ ORR on a Pt(111) surface. This can be seen in Figure 2.2 (left), when the electrode potential (U) is set to 1.23 V, with an assumed oxygen coverage (θ_O) of 0. It is thermodynamically unfavorable for O^* to react to HO^* and for HO^* to react to H_2O . It should be noted that these steps get more thermodynamically favorable as the oxygen coverage starts to accumulate ($\theta_O=0.5$), but then the initial dissociation barrier increases. As we move this Pt(111) cathode to more cathodic potentials (reducing potentials), we can see that setting the electrode to 0 V ($U=0$) results in favorable thermodynamic reaction steps, assuming low oxygen coverage ($\theta_O=0$) is maintained to mitigate the initial dissociation barrier.

In contrast to the dissociative mechanism, O_2 adsorbs to 1 surface site ($*$) and does not dissociate in the associative mechanism (Figure 2.2, right). It protonates to form

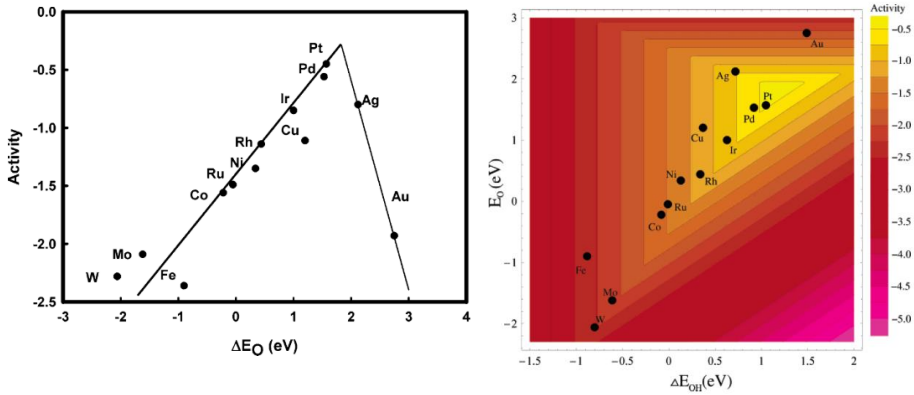
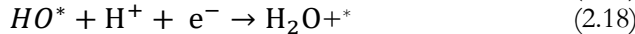
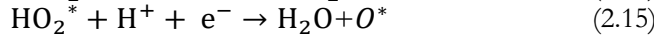
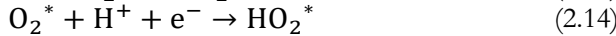


Figure 2.4: Volcano plots of 4e⁻ ORR activity ($\theta_{\text{O}}=0.25$) based on Sabatier's principle. (Right) Activity based on the stability (ΔE_{O}) of the rate-limiting O* species. (Left) Activity based on the stabilities (ΔE_{O} , ΔE_{OH}) of both the rate-limiting O* and HO* species. From ⁴⁵

a peroxy intermediate (HO₂*) which then reacts to H₂O and O*. This remaining O* goes on to react just like the O* species from the dissociative mechanism, with the same free energy values (Figure 2.2, $\theta_{\text{O}}=0.5$) (and therefore the same rate-limiting steps). Equations from the associative mechanism are as follows:



In summary, if the rate-limiting species are too stable (strong-binding = low values of ΔE_{O} and ΔE_{OH}) then the desorption of these species becomes the rate-limiting step. However, if the rate-limiting species are too unstable (weak-binding = high values of ΔE_{O} and ΔE_{OH}) then the adsorption of these species becomes the rate-limiting step. The optimal binding energy interactions being neither too strong nor too weak is a general concept in the heterogeneous catalysis field: it is known as Sabatier's Principle. Sabatier's Principle is presented in volcano plots (Figure 2.4, left) or contour plots (Figure 2.4, right) and is a valuable tool in the search for an electrocatalyst with optimal activity.

The field of ORR, 4e⁻ catalysis is generally dominated by Pt and its various alloys. Nørskov et al. concluded that Pt is the best pure metal catalyst for ORR 4e⁻, and the optimum ORR 4e⁻ catalyst is a metallic alloy that binds slightly weaker to the O* and HO* intermediates than metallic Pt (slightly larger ΔE_{O} and ΔE_{OH} than Pt). Consequently, the most promising catalysts in the field of PEMFC ORR 4e⁻ focuses mostly on modifying Pt to bind slightly weaker by alloying Pt with other metals.

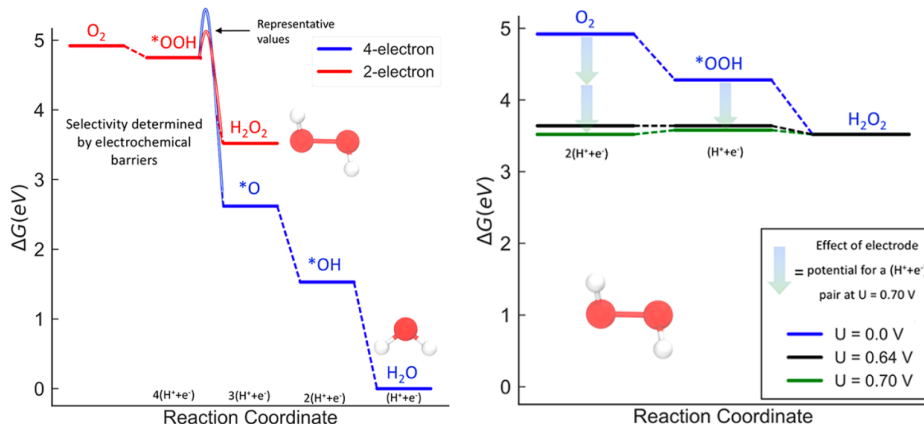


Figure 2.5: (left) Free energy diagram of the 4e⁻ (blue) and 2e⁻ (red) ORR pathways on Au(111). (right) Free energy diagram of the 2e⁻ ORR pathway on PtHg₄ alloy. From ⁴⁶

There are various configurations of PtNi and PtCo alloys that do this while remaining stable.^{47–50} Research in this area mainly focuses on getting the most activity from the smallest amount of platinum, but also searching for alternatives that are not as scarce as platinum typically known as non-precious metal catalysts (NPMC).^{20,21,51–54}

2.2.2 ORR: the 2e⁻ process

There is only one proposed mechanism for the 2e⁻ ORR resulting in H₂O₂. It is a deviation from the 4e⁻ ORR associative mechanism, where the peroxy intermediate (HO₂^{*}) reacts to form H₂O₂ instead. The oxygen atoms of the peroxy intermediate (HO₂^{*}) never split to form 2 separate species:

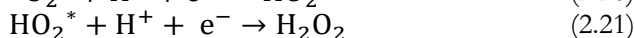
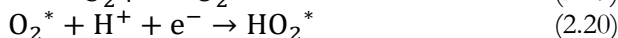


Figure 2.5 (left) presents the Free energy diagram of the associative mechanism for Au(111). Here we can see there are two competing reactions (Eq 2.15 and 2.21). Despite the dissociation of HO₂^{*} to O^{*} is more thermodynamically favorable, experimental results show Au(111) favors H₂O₂. Nørskov et al. conclude must be due to a lower energy barrier for the H₂O₂ pathway.⁴⁶ This principle governing 2e⁻ ORR is known as an electronic effect. Research has been pursued to optimize weak-binding catalysts, like Au and Ag, by making them more active.^{55,56}

Figure 2.5 (right) shows a state-of-the-art PtHg₄ alloy presented by Siarostami et al. that requires very little activation energy (U₀=0.70V, U=0.64V, E_{act}=0.06V).⁵⁷ This is due to a principle known as a geometric effect (Figure 2.6, left). PtHg₄ alloys result

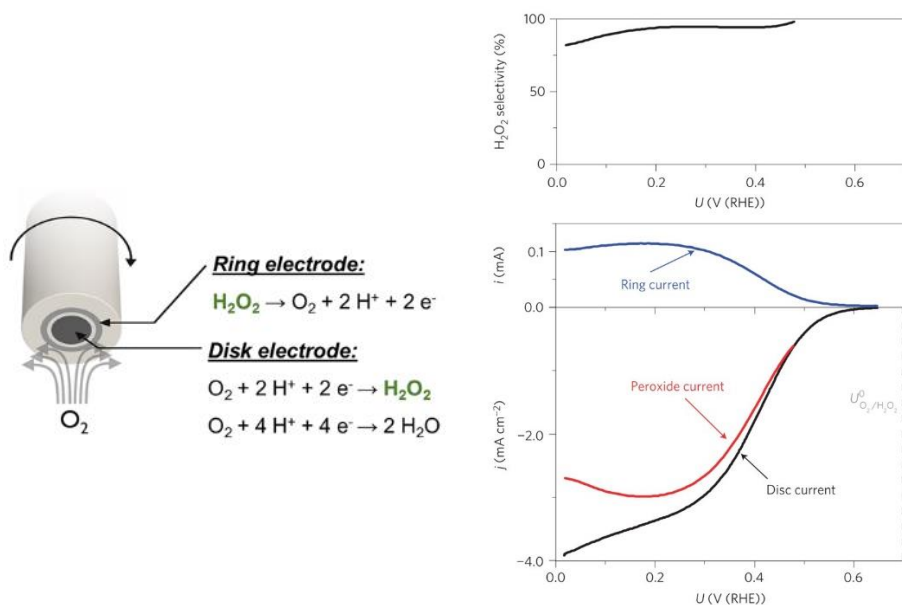


Figure 2.6: (Left) Schematic of a Rotating Ring Disk Electrode (RRDE) O_2 -saturated electrolyte is reduced on the disk where the convection subsequently moves the reduced species outward radially to the Pt ring that oxidizes the electroproduced H_2O_2 . (Right) Cathodic sweep from an RRDE experiment of a PtHg_4 disk. HgClO_4 was electrodeposited onto the $\text{Pt}(111)$ disk to create a PtHg_4 surface. Data taken at 50 mV/s and 1600 rpm at room temperature in O_2 -saturated electrolyte (0.1M HClO_4). H_2O_2 selectivity calculations were oxygen-normalized (λ_{O_2}). From ⁵⁷

in isolated Pt atoms surrounded by weak-binding Hg atoms. This single atom site geometry selectively destabilizes the O^* intermediate compared to the HO_2^* intermediate and as a result facilitates the 2e^- ORR pathway resulting in H_2O_2 . These findings sparked the field of single-atom catalysts (SAC) for 2e^- ORR, given their potential to provide optimal active site structures.

2.3 The field of 2e^- ORR SAC's

The selectivity and activity of the single-atom catalysts for 2e^- ORR are typically benchmarked by a brief cathodic sweep on a Rotating Ring Disk Electrode (RRDE) (Figure 2.6, top left, right). Such RRDE experiments permit quick and easy determinations of catalytic activity as well as selectivity towards H_2O_2 . An RRDE has a disk component with the catalyst of interest dispersed on it that will electroreduce oxygen as it is being cathodically swept from $\sim +0.9V_{\text{RHE}}$ to $0V_{\text{RHE}}$. The activity of the catalyst is simply determined by the cathodic current of the disk electrode during this sweep. In addition, there is a platinum ring around the disk that is set at an oxidizing potential of $+1.20V_{\text{RHE}}$. This Pt ring will consequently oxidize

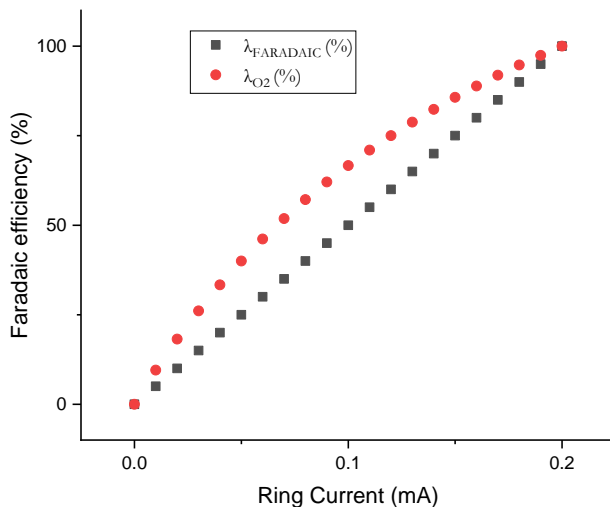


Figure 2.7: Discrepancy of electron-normalized Faradaic Efficiency ($\lambda_{\text{Faradaic}}$), and oxygen-normalized Faradaic Efficiency (λ_{O_2}) as a function of the same ring current (i_R). Assumed $i_D = 1$ mA and $N = 0.2$ for the disk current and collection efficiency.

a calibrated fraction of the H_2O_2 produced from the disk electrode. This oxidizing current in tandem with a disk's cathodic sweep, determines how much H_2O_2 the catalyst of interest is making, where the peroxide activity (selectivity) of the catalyst can be determined. The selectivity of a catalyst, its Faradaic Efficiency, is its peroxide current divided by its disk current (Figure 2.6, bottom right). Literature will generally present Faradaic Efficiency (%) in two different ways: electron-normalized Faradaic Efficiency ($\lambda_{\text{Faradaic}}$), and oxygen-normalized Faradaic Efficiency (λ_{O_2}):

$$\lambda_{\text{Faradaic}} (\%) = \frac{i_R}{i_D} \times 100 \quad (2.22)$$

$$\lambda_{\text{O}_2} (\%) = \frac{2 \times i_R}{i_D + \frac{i_R}{N}} \times 100 \quad (2.23)$$

Where i_R is the measured ring current, i_D is the measured disk current, and N is the calibrated collection efficiency of the ring (see Chapter 3 for more details). Figure 2.7 shows how calculating the O_2 Faradaic Efficiency creates a positive bias if normalizing to O_2 and that this bias increases as the selectivity gets worse. Nevertheless, λ_{O_2} is used as a way to inflate the selectivity results of a catalyst, which is useful for publishing articles. Even though the current we are measuring is likely derived from O_2 , the reality is we are measuring current. Therefore, normalizing to

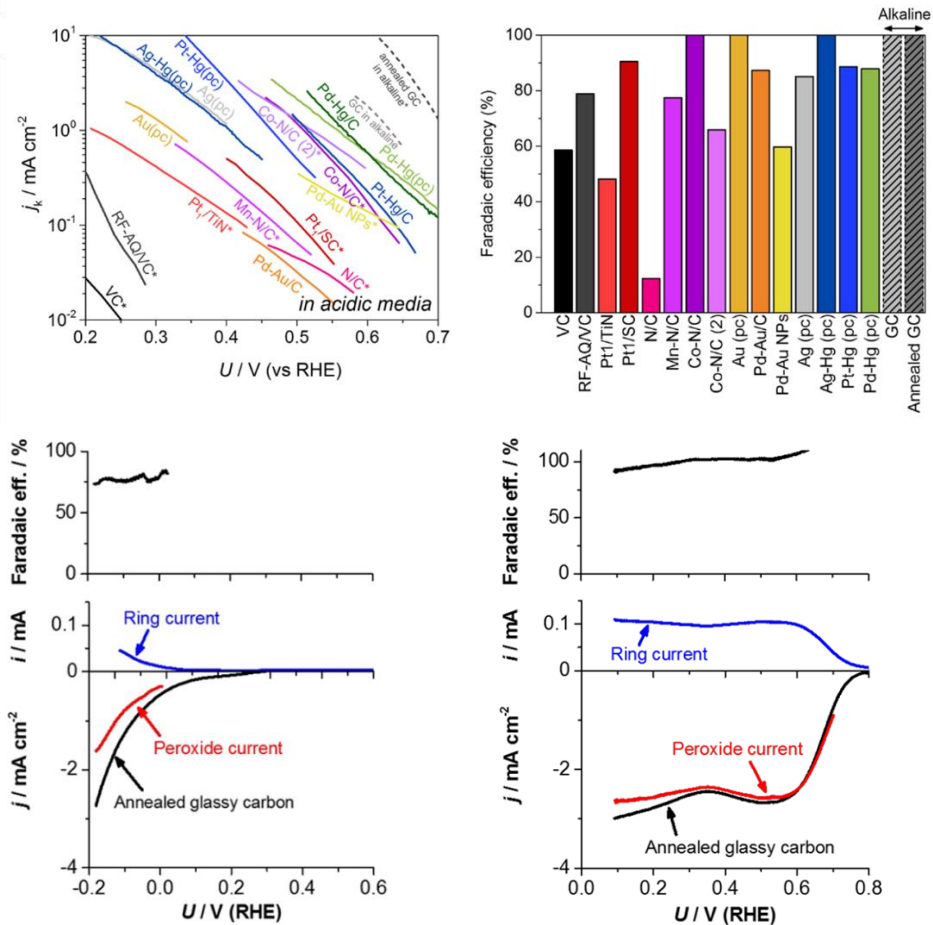


Figure 2.8: Figure adapted from ²⁶. (Top, left) Tafel plot of kinetic current densities for H₂O₂ production in acidic media based on RRDE experiments. (Top, right) corresponding H₂O₂-selectivity data. Oxygen Reduction RRDE experiments of annealed GC in acidic conditions (bottom, left) and alkaline conditions (bottom, right). Data taken at 50 mV/s and 1600 rpm at room temperature in O₂-saturated electrolyte (0.1M HClO₄ or 0.1M KOH). Data adapted from (Pt-Hg(pc), Pt-Hg/C)⁵⁷; (Pd-Hg(pc), Pd-Hg/C)⁵⁸; (Pd-Au/C)⁵⁵; (Au(pc))⁵⁹; (Pd-Au NPs)⁵⁶; (Co-N/C)⁶⁰; (Co-N/C(2))⁶¹; (Mn-N/C)⁶²; (Pt1/TiN)⁶³; (Pt1/SC)⁶⁴; (riboflavin-anthraquinone supported Vulcan XC72 (RF-AQ/VC), Vulcan XC72 (VC))⁶⁵; (N/C, N-doped carbon)⁶⁶. From ²⁶

electrons, $\lambda_{\text{Faradaic}}$, is better because it's a simpler calculation that circumvents unnecessary assumptions.

Pt and Pd alloyed with Hg (PtHg₄ and PdHg₄ respectively) were among the first SAC's tested for 2e⁻ ORR in acidic conditions by Siarostami and Verdaguar et al. While very active, the Hg can potentially corrode into the effluent over time, this means that these catalysts had little, if any, commercial applications. This is due to the health hazards from the exposure to Hg. The Hg-alloys were followed shortly

after by Yang et al., but their Pt₁TiN catalyst was not nearly as active.⁶³ The Tafel plot (Figure 2.8, top, left) summarizes the activity of various SAC's based their RRDE cathodic sweep experiments. A Tafel plot measures activity on the log scale ($j_k / \text{mA cm}^{-2}$) as a function of overpotential ($E_{\text{act}} \approx U - U_0$ where $U_0 = 0.7V_{\text{RHE}}$). It only takes the kinetically-limited section of a cathodic sweep e.g. before the sweep's slope starts to degrade markedly, like before $U < 0.4V_{\text{RHE}}$ in Figure 2.6 (right). Tafel plots give us a general idea of the overpotentials and kinetic activity of these catalysts. From the Tafel plot, we can conclude that the best catalyst for 2e⁻ ORR is annealed glassy carbon (GC) in alkaline conditions, better than any SAC's in acidic conditions.

It is well known that 2e⁻ ORR is more facile in alkaline conditions, with a simple annealed glassy carbon stub having the state-of-the-art performance (Figure 2.8). However, the fundamental reasons for the differences between acidic and alkaline conditions remained elusive, as concluded by Yang et al.²⁶ The activity of an annealed glassy carbon stub is so strikingly good in both activity and selectivity, that one has to wonder why we do not just replace an acidic PEM H₂O₂ electrolyzer to an alkaline AEM H₂O₂ electrolyzer. Yang et al. summarizes a few of the technical hurdles in H₂O₂ electrolyzers based on anion-exchange membranes (AEM).²⁶ H₂O₂ in alkaline conditions is typically unstable, as it takes the deprotonated form of HOO⁻ in solutions with high pH. In addition, AEM's presently lack the conductivity and stability to be commercially viable compared to PEM's.⁶⁷ Even if AEM is improved in these areas, these membranes have a fundamental problem in that they would have to selectively conduct HO⁻ anions without conducting HOO⁻ anions, which is yet another loss of the desired H₂O₂ product. Finally, if AEM H₂O₂ electrolyzers require KOH electrolyte, then this defeats the entire purpose of a decentralized reactor that initially needed only water, air, and electricity, since the transport of KOH salts has the same drawbacks as transporting concentrated H₂O₂ from a centralized anthraquinone facility. There are many single atom catalysts showing impressive results, but they are irrelevant if they are in alkaline conditions. To conclude: AEM H₂O₂ electrolyzers have numerous problems, but none of them are at the catalyst level. This very important detail is why the pursuit of catalysts for the 2e⁻ ORR *in acidic conditions* is a relevant topic, and why the pursuit of catalysts for the 2e⁻ ORR *in alkaline conditions* is irrelevant.

With relevant pursuits in mind, among the most promising SAC's are porphyrin-like carbon-based varieties, where a metal atom is anchored by graphitic nitrogen species on a carbon lattice. These carbon frameworks provide a high surface area substrate to maximize a single metallic atom's interface, where these single atoms are generally considered as the active sites for ORR.⁶⁸⁻⁷² Until recently, these metal-nitrogen-carbon materials (M-N/C) have mainly focused on 4e⁻ ORR.^{51,52,73-75} This was likely inspired by experiments based on model M-N/C compounds such as porphyrins and phthalocyanines for the 4 e⁻ pathway.^{51,53,73-75} Despite this, the challenge behind

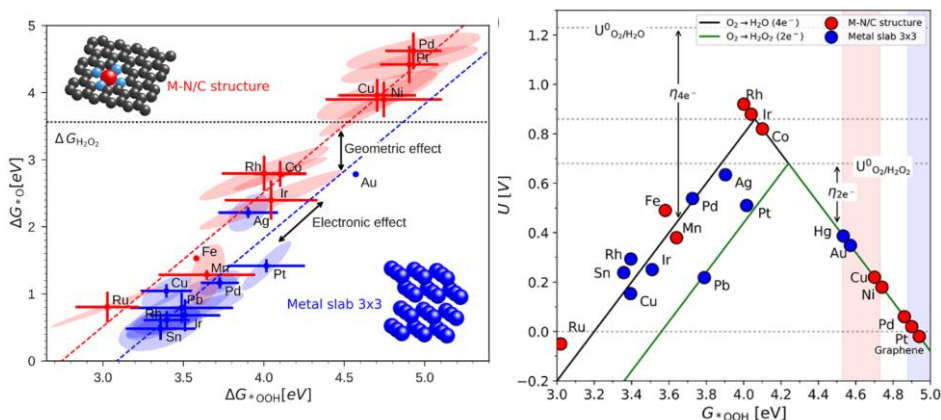


Figure 2.9: Comparison of select metals in the form of 3x3 metal slabs (blue) and M-N₄/C sites (red). (left) Adsorption trends as function of the free energies of ΔG_{*O} and ΔG_{*OOH} . (right) Sabatier Volcano Plot for ORR, where the limiting potential is assumed and therefore plotted as a function of ΔG_{*OOH} (left green line = 2e⁻ ORR, left black line = 4e⁻ ORR). M-N/C catalysts to the right of the vertical red band have weak enough *O binding to thermodynamically favor H₂O₂ production. Metallic slab catalysts (representing pure metal alloy catalysts) to the right of the vertical blue band have weak enough *O binding to thermodynamically favor H₂O₂ production. From ²⁶

what governs a M-N/C's selectivity between the 2e⁻ and 4e⁻ pathway has still not been elucidated, particularly in acidic conditions.^{41,76} Figure 2.8 shows the preliminary DFT calculations of various metals in the form of M-N/C catalysts compared to their metallic form. However, there are numerous M-N/C's with selectivity for 2e⁻ ORR, including Cobalt, and Palladium from experimental results.^{77,78} There are a number of structural factors that are thought to affect an M-N/C's activity and selectivity. There is evidence suggesting that the surrounding moiety of the single atom site will affect its ORR selectivity.^{79,80} Jung et al. partially pyrolyzed a CoN₄ catalyst, resulting in a higher prevalence oxygen functional groups in the surrounding carbon lattice of the atomic CoN₄ site. It's thought that the electron withdrawing groups, such as C-OH, C-O-C, and C=O, will alter the charge state of the CoN₄ site and facilitate 2e⁻ ORR by making the *OOH intermediate less stable.⁸⁰ Zhang et al. came to similar conclusions regarding atomic Co from their experiments with partially oxidized carbon nanotubes as supports.⁷⁹ Choi et al. had similar observations where partially oxidized Fe-N/C had lower activity but higher selectivity towards 2e⁻ ORR.⁴¹ Yet there are still CoN_x findings supporting selectivity towards 4e⁻ ORR.⁸¹ Geometric configuration of the carbon surrounding this CoN_x site may also play a significant role, as seen with FeN₄.⁸²

The coordination of the atomic site is also thought to affect an M-N/C's activity and selectivity.⁶⁹ The number of N atoms the central metal atom is anchored with is known typically known as its coordination number. Typically, M-N/C's have a porphyrin-like coordination number of 4 and focus on optimizing the 4e⁻ ORR.⁸³⁻⁸⁵ In contrast, a coordination number of 6 is thought to be optimal for 2e⁻ ORR, at

least for the weak-binding Pd single atoms, which likely extends to Pt atoms as well.⁷⁸ The types of nitrogen atoms coordinated with the metal center also have an effect, where they are categorized as either pyridinic, pyrrolic or graphitic, in this context.^{81,86} A graphitic edge-site FeN₄ catalyst is a notable work in this regard (for 4e⁻ ORR).^{74,87,88} Similarly, a FeN₄ catalyst with a pyrrolic-N coordination have shown to be more active than a FeN₄ catalyst with a pyridinic-N coordination.⁸⁹ Gao et al. utilized this weaker-binding shift from pyrrolic-N coordinations to make CoN_x sites optimal 2e⁻ ORR.⁷⁷

Zhao et al. have recently proposed a constant-potential hybrid-solvation dynamic model (CP-HS-DM) to thermodynamically explain selectivity trends of ORR across different pH values, where they use the ubiquitous, yet mysterious, Co-N/C catalyst as an example.⁹⁰ As we have established, a CoN_x site thermodynamically prefers to break the O-OH bond to facilitate 4e⁻ ORR in spite of conflicting experimental results. The CP-HS-DM is able to assess the kinetic information on the electrochemical steps at the solid-water interface, which are not assessed using conventional models. These findings confirm that the activation energy of O-OH bond breaking can be higher than that of *-O bond breaking, thereby confirming Nørskov et al.'s speculations (Figure 2.5, left).⁴⁶ Zhao et al. explains that the initial stretching of the O-OH bond can induce an energy barrier higher than the breaking of *-O, thus preferring the H₂O₂ formation. Particularly, they discovered that the proton affinity plays a critical role in the selectivity. For a CoN_x site, decreasing potential promotes proton adsorption to the former O in *-O-OH, thereby increasing the H₂O₂ selectivity. Finally, Zhao et al. are able to explain the lower H₂O₂ selectivity in acidic conditions for the carbon catalysts, like the annealed GC in Figure 2.8 (bottom, left). According to the CP-HS-DM, the proton prefers the latter O in *-O-OH resulting in a lower H₂O₂ selectivity for carbon catalysts in acidic conditions.

2.4 The challenge of up-scaled ORR experiments

One recurrent challenge for many ORR catalysts remains the discrepancy in both performance in RRDE experiments compared to scaled-up PEM reactors.⁹¹ The discrepancies between RRDE conditions and MEA conditions are summarized in Figure 2.10. For 4e⁻ ORR (Figure 2.10, top), Stephens et al. compared the mass activity (A/mg_{Pt}) at +0.9 V_{RHE} of the 'state-of-the-art' Pt catalysts between RRDE measurements (e.g. Liquid half-cell) and MEA measurements (e.g. Fuel Cell). There are obvious differences between the conditions between PEM reactors and RRDE experiments. RRDE currents from the cathodic sweeps are measured on a disk (0.2 cm²) typically rotating at 1600 rpm in O₂-saturated 0.1M HClO₄ electrolyte. The catalysts being tested in these conditions quickly become mass transport limited at high potentials due to inefficient O₂ availability. In PEM reactor conditions, the

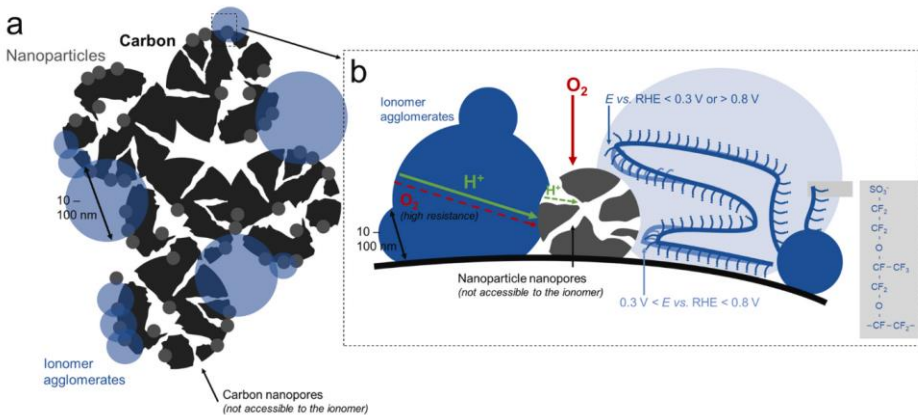
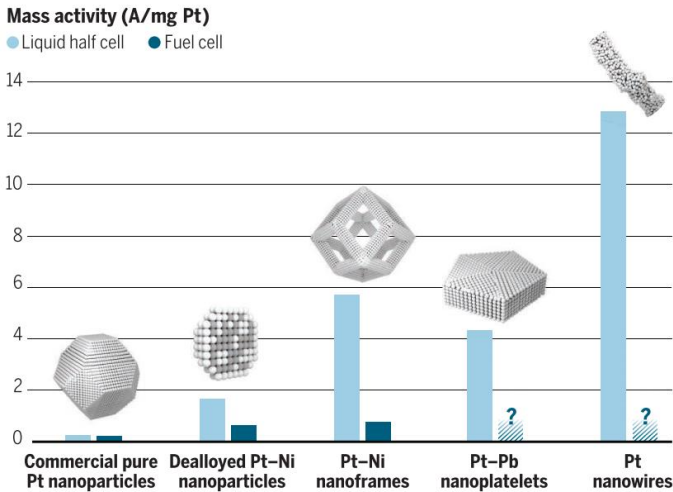


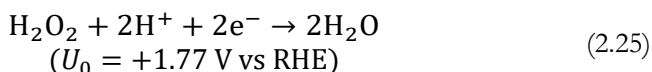
Figure 2.10: (top) Stephens et al. compare the $4e^-$ ORR mass activity ($\text{A}/\text{mg}_{\text{Pt}}$) at $+0.9 \text{ V}_{\text{RHE}}$ of the ‘state-of-the-art’ Pt catalysts between RRDE measurements (e.g. Liquid half-cell) and MEA measurements (e.g. Fuel Cell).⁹² Data adapted from (Commercial pure Pt nanoparticles and Pt-Ni nanoframes)^{93,94}; (De-alloyed Pt-Ni nanoparticles)^{95,96} (Pt-Pb nanoplatelets)⁹⁷; (Pt nanowires)^{98,99}. (bottom, a) A schematic illustration of the heterogeneous Nafion coverage with a Pt/C catalyst. Ly et al. attributes this to Nafion (ionomer) agglomerates ($d = 10\text{-}100 \text{ nm}$) that naturally occur during catalyst ink preparation. (bottom, b) Inset emphasizes the electrostatic interactions between the Nafion and nanoparticles during open-circuit and operation potentials.¹⁰⁰

ORR catalyst is deposited onto a gas diffusion layer that is compressed into a membrane electrode assembly (MEA). These PEM reactor conditions are not comparable to RRDE conditions, because RRDE uses an electrolyte that is highly proton conductive (HClO_4), and a gas that is saturated in this electrolyte, circumventing triple-phase boundary complications. Ly et al. emphasize the critiques of Stephens et al. regarding the relevance of ORR catalyst performances in RRDE conditions. Ly et al. categorize these $4e^-$ ORR Pt catalysts as ‘disorder catalysts’

because they increase the surface area of their Pt metal to improve their mass activity, but this trick only works in RRDE conditions.^{97–99,101–104} This disorder is typically implemented on the nanoscale, where O₂-saturated liquid electrolytes (HClO₄) can easily penetrate small porosities of carbon supports and facily provide O₂ and H⁺. By optimizing catalyst structures around these luxuries, the limitations become strikingly evident when implemented in fuel cells with drastically different conditions from liquid electrolytes. In conclusion, testing catalysts only for RRDE conditions provides too narrow of a scope where this optimization essentially perpetuates a scientific field of empty promises, unless MEA configurations can be improved.

The shortcomings of MEA configurations is generally assumed to be at the nanoscale, where a delicate triple phase boundary takes place.^{105,106} This is because without HClO₄ electrolyte, the Nafion becomes the sole source of H⁺ for a catalyst.¹⁰⁰ It has been found that Nafion coverage of a deposited catalyst is heterogeneous, where some portions of the catalyst will lack adequate H⁺ contact (too little Nafion contact) while other portions of the catalyst will lack adequate O₂ contact (too much Nafion contact).^{107,108} Ly et al. effectively illustrates this phenomena in Figure 2.10 (bottom) where it has been evidenced that Nafion forms agglomerates of 10-100 nm in diameter during typical catalyst ink preparations.^{109,110} This renders the catalytic sites inside the nanopores inactive because the larger Nafion agglomerates cannot reach them.^{111,112} Ly et al. concludes that poor Nafion/catalyst contact leads to numerous problems such as increased resistances from compromised O₂/H⁺ transport due to preferential flooding of nanopores, electrostatic interactions, and catalyst poisoning.^{113–118}

Yang et al. found similar scale-up challenges for 2e⁻ ORR (Figure 2.11) when comparing the Faradaic Efficiency of the ‘state-of-the-art’ catalysts across RRDE, GDE, and MEA measurements.²⁶ Just like 4e⁻ ORR, RRDE performances are much better than the MEA performances. Furthermore, in this context, the gas diffusion electrode (GDE) is fully submerged in O₂-saturated HClO₄, where the hydrophobic carbon cloth captures extra O₂ for the catalyst layer. Despite circumventing proton-transport issues with HClO₄, the Faradaic Efficiency is also notably worse for Pt-Hg/C and Au/C in these GDE experiments. With increased catalyst loadings, the transport of H₂O₂ away from the electrode becomes important so that it doesn’t further react.¹¹⁹ This is because H₂O₂ can readsorb/dissociate or simply electroreduce further to H₂O (H₂O₂RR) as seen in equations 2.24 and 2.25 respectively:



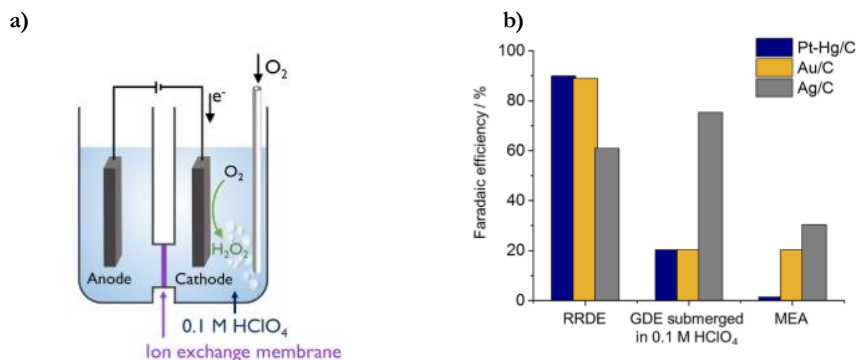


Figure 2.11: (a) schematic of a GDE submerged in O₂-saturated electrolyte (0.1M HClO₄) (b) Yang et al. compared the 2e⁻ ORR Faradaic Efficiency of the ‘state-of-the-art’ catalysts across RRDE, GDE and MEA measurements. From ²⁶

In a MEA setup, the electroproduced H₂O₂ has to diffuse through the catalyst layer in order to be utilized, but the local concentrations of H₂O₂ can be large enough to facilitate this H₂O₂RR as well as other chemical reactions. This is why H₂O₂RR performance is another variable to consider when contemplating suitable catalysts for scaled-up conditions.^{120–122}

In the case of M-N/C’s, local concentrations of H₂O₂ can be particularly problematic for the stability of such ORR catalysts.^{41,123} Choi et al. suggests H₂O₂ will preferentially oxidize carbons close to the FeN_x site, increasing hydrophilicity and therefore the rate that subsequent H₂O₂ will attack the catalyst structure.⁴¹ One suggestion that is possibly appropriate for scaled up 2e⁻ ORR operations is mentioned by Ly et al. where the carbon supports are doped with nitrogen to improve ionic contact without smothering the catalyst in Nafion agglomerates.

There has been progress in bridging RRDE and MEA experiments. Ehelebe et al. suggest a non-submerged GDE to benchmark 4e⁻ ORR (briefly mentioned in Chapter 1, Figure 1.7, a).¹²⁴ This GDE setup gains some benefits of RRDE experiments: cheap, fast, and can use a reference electrode to better control the potential (V). This GDE setup also gains some benefits of MEA experiments: higher currents, more realistic mass transport, and, despite using HClO₄ electrolyte, comparable triple phase boundaries (assuming this electrolyte is not O₂-saturated). In addition, Kucernak’s Floating Electrode Technique (FET) achieves similar benefits (see Chapter 5 for more details).¹²⁵ However, there is limited literature on scaling up M-N/C catalysts for 2e⁻ ORR, where a notable example is Yang et al. providing a thorough investigation of the Pd1/N-C, but only in submerged GDE tests (see Chapter 4 for more details).⁷⁸

2.5 Conclusion

This chapter has given a brief overview over the very established field of the Oxygen Reduction Reaction. The underlying thermodynamics provides the foundations for DFT calculations that elucidate the stability of the various intermediates that occur on the catalyst surface of a cathode for ORR. In turn, catalysts can be rationally designed to optimize ORR activity through systematic minimization of activation overpotentials (E_{act}) and tuned for selectivity towards either the 4e⁻ or the 2e⁻ pathways governed by electronic and geometric effects. The carbon-based SAC's anchored in nitrogen functionalities known as M-N/C's, show particular promise for 2e⁻ ORR in acidic conditions. However, the literature on M-N/C performance in relevant MEA conditions is severely lacking. While this is starting to be addressed in the field of 4e⁻ ORR, there are still opportunities for interesting investigations regarding benchmarking M-N/C catalysts for 2e⁻ ORR, particularly because this field faces different challenges.

Chapter 3

Experimental Methods

This chapter will summarize the experimental methods that were used to assess the catalysts of interest in this project. The catalyst characterization section will go over the analytical tools used to gain insights of the catalyst's structure and elemental composition. The electrochemical measurements section will go over the procedures used for the various experimental setups to measure a catalysts activity and stability. Lastly, the H₂O₂ quantification section will elaborate how the 2e⁻ ORR's main product of interest, H₂O₂, was quantified.

3.1 Catalyst Characterization

A prominent claim in the field of M-N/C electrocatalysts is the resourceful use of low amounts of metal to achieve high electrochemical mass activity ($\text{mA} \cdot \text{g}_{\text{metal}}^{-1}$). In the case of M-N/C electrocatalysts, these metal single atoms coordinated to nitrogen species result in optimized MN_x sites. Such claims require extensive characterizations in order to suggest that the electrochemical performance of an M-N/C catalyst sample can be attributed to these MN_x sites. The characterization techniques that will be discussed in this section are x-ray diffraction (XRD), x-ray photoelectron spectroscopy (XPS), Scanning Transmission Electron Microscopy (STEM), energy dispersive x-ray spectroscopy (EDS), extended x-ray absorption fine structure (EXAFS), x-ray absorption near edge structure (XANES), and inductively coupled plasma mass spectrometry (ICP-MS).

3.1.1 X-ray diffraction (XRD)

XRD is typically used to detect the various crystal structures of a material via the elastic scattering X-rays described by Bragg's Law.¹²⁶ An incoming x-ray beam will cause the material (known as the scatterer) to emit spherical waves that will mostly cancel each other out via destructive interference. If the scatterer has symmetrical atomic arrangements (e.g. a crystal lattice) then these spherical waves will synchronize via constructive interference to form signals in discrete angles (θ) relative to the incoming x-ray beam and the scatterer's plane. These angles are defined by the atomic spacing (d) of the symmetrical atomic arrangements. The various signals that are formed from this constructive interference results in spots (e.g. reflections) on a diffraction pattern. In principle, any form of radiation could

be used to form a diffraction pattern. However, the best diffraction patterns come from x-rays because they have wavelengths (λ) in the same orders of magnitude as the atomic spacing (d) of crystal lattices (1-100 Å). Bragg's Law (equation 3.1) provides the discrete angle (θ) of diffraction that results from the constructive interference of a scattering.

$$n\lambda = 2d \sin \theta \quad (3.1)$$

XRD doesn't provide any direct insights of MN_x sites in an M-N/C catalyst. Rather, XRD is a useful sanity check because XRD should not detect any metal lattices in a properly synthesized M-N/C catalyst (no news is good news). If it detects a metal lattice, then it is likely that the single atom catalysts synthesis has failed where significant portions of the metal precursor have agglomerated (e.g. nanoparticles).

3.1.2 X-ray photoelectron spectroscopy (XPS)

XPS is a surface-sensitive technique that can be used to quantify the elemental composition of a material. In addition, XPS can provide insights to the chemical and electronic states of these detected elements. XPS measurements are dictated by the photoelectric effect, where core electrons are emitted from a sample after the adsorption of photons from an incident x-ray beam.¹²⁷ The kinetic energy of these emitted core electrons is measured and permits the identification of elemental species on the basis that each element has a characteristic set of binding energies. By the conservation of energy, different binding energies of core electrons will result in different kinetic energies measured of emitted core electrons. This measurement results in an XPS spectrum, which is a frequency distribution of photoelectrons detected per binding energy level (E_B), derived from the measured kinetic energy. Emission peaks will occur at certain binding energies that depend on the element that emitted the photoelectrons. Since the number of photoelectrons detected is proportional to the concentration of the element, these emission peaks can be integrated (after background correction) to quantify the elemental composition of a material's surface. This technique can even determine the chemical state of the element, since the characteristic set of binding energies of an element will shift based on its chemical state. This can be used to determine the oxidation state of metal surface, or even differentiate nitrogen species in a carbon lattice.⁷⁸

It should be stressed that this is a surface-sensitive technique. The emitted photoelectrons that escape the material without energy losses are exclusively close to the surface.¹²⁷ Electrons deeper in the bulk of a sample will scatter due to inelastic processes. As a result, this technique cannot quantify the elemental bulk of a material; XPS only provides insights at the surface and near-surface levels of a material. The detection of XPS is roughly around 0.1-1.0 (at. %), but can be improved to 0.01 (at. %) if it is a heavy element is in a matrix of predominantly light elements (e.g. Ir or Au in a carbon-nitrogen matrix).¹²⁸

A typical XPS sample was prepared by drop casting a catalyst-ethanol dispersion onto a silica wafer. In a typical XPS measurement, a Theta Probe (Thermo Scientific, USA) instrument with a monochromatized Al K α (1486.6 eV) source was used for the recordings of spectra, which were obtained with a pass energy of 100 eV. The spectra were recorded with a step/resolution of 0.1 eV and dwell time of 50 ms. The beam size was 50 μm for all measurements.

3.1.3 Scanning transmission electron microscopy (STEM) and energy-dispersive x-ray spectroscopy (EDS)

Transmission electron microscopy (TEM) enables resolution of images at the Ångström scale, transcending the diffraction limits of preceding microscopes using visible light. TEM utilizes a beam of electrons transmitting through an adequately thin sample (100 nm) to form an image based on the interaction of the electrons with the sample.¹²⁹ An electron gun generates this electron beam by applying very high voltages (100-300 kV) to a cathode, which will generate a current to an anodic extraction plate (via thermionic or field electron emission). The electron beam that exits past the anodic extraction plate is divergent, and can be manipulated via magnetic lenses and electrostatic fields both before and after reaching the sample. The electron beam that passes through is collected by a detector and creates an image. Depending on the operation mode, the contrasts that form this image can be based on the density, atomic number, or crystal structure.

Scanning Transmission Electron Microscopy (STEM) will focus this electron beam to a small spot size (0.05-0.2 nm) and scan over the sample to raster an image. High-angle annular dark-field scanning transmission electron microscopy (HAADF-STEM) uses an annular dark-field detector to exclusively detect the high-angle scattered electrons ($>5^\circ$) that pass through the sample.¹³⁰ This results in a high-resolution atomic-scale image with contrasts based on atomic number (Z-contrast). HAADF-STEM is particularly useful to render images of MN_x sites in M-N/C catalysts, where the single metal atoms are notably heavier than their carbon-nitrogen matrix.

Energy dispersive x-ray spectroscopy (EDS) is an analysis that can be used in parallel with other techniques, including HAADF-STEM.¹³¹ EDS can be thought of as the opposite of XPS: rather than applying an x-ray beam on a sample to measure the emitted electrons, EDS applies an electron beam on a sample to measure the emitted x-rays. When an electron beam ejects an inner shell electron of an atom, an outer shell electron will fill in the resulting electron hole in the inner shell. An outer shell electron is in a higher energy state, so when it moves down to a lower energy state in the inner shell, it emits the excess energy in the form of x-rays. The x-rays emitted have a characteristic set of energies unique to the element that the electron was ejected from. Similar to XPS, the resulting emission peaks on an EDS spectrum will be uniquely dependent on the elements that emitted them. Since each element has a characteristic set of peaks, a sample's elemental composition can be derived from an EDS spectrum since it is a frequency distribution, where the magnitude of the

characteristic peaks of an element is proportional to the element's concentration (similar to an XPS spectrum).

Unlike XPS, EDS has the potential to analyze elemental concentrations of the bulk, where the interaction volume of a sample emitting x-rays can be in the micro scale, since emitted x-rays are better at escaping the sample compared to emitted electrons. However, when EDS is coupled with STEM the interaction volume is quite limited since the spot size is roughly 0.2 nm and the sample is roughly 100 nm thick.

3.1.4 X-ray absorption spectroscopy (XAS)

X-ray absorption spectroscopy (XAS) is a technique that identifies the local coordination and moieties of elemental species of a sample at the bulk level.¹³² XAS analysis requires a synchrotron to achieve high intensity x-ray beams with a narrow energy ranges. This allows analysis of elements in a sample in the ppm range. An incident x-ray beam of a certain energy will eject a core electron of an element (e.g. the photoelectric effect just like XPS). Like EDS, a high-energy outer-shell electron can relax into the low-energy inner-shell electron hole to emit x-rays (fluorescence). Since sample absorbs energy from the incident x-ray beam, XAS is simply a transmission technique where the energy loss of the x-ray beam is measured. XAS determines the absorption coefficient of the element by measuring its energy absorption as the incident x-ray beam increases incrementally. An alternative way to determine this absorption coefficient is by measuring the fluorescence intensity, since the fluorescence intensity will be proportional to the absorption coefficient.

XAS can be distinguished into two distinct techniques: x-ray absorption near-edge structure (XANES) and extended x-ray absorption fine structure (EXAFS). XANES analysis occurs in the low energy region (~5-150 eV), while EXAFS analysis occurs in the higher energy regions (~150-2000 eV). XANES provides the chemical and electronic state of the absorbing element in the bulk of a sample.¹³² An element has distinct core electron energies, which are also dependent on the element's coordination and oxidation state. Because of this, only x-rays of distinct energies will interact with the core electrons of an entire sample. Therefore, XANES circumvents the high backgrounds from other elements in a sample, making it a very powerful tool to analyze MN_x sites in M-N/C catalysts. EXAFS provides the local moieties of an element in a sample.¹³² The emitted photoelectrons can interact with the surrounding non-excited atoms, which can cause the photoelectrons to backscatter and create an interference signal. The nature of these backscattered photoelectrons are dependent on the atomic element causing the backscatter and its distance from the initial excited atom emitting the photoelectron. This can be useful for characterizing M-N/C catalysts since it is suggested that the local moieties can affect an MN_x site's electrochemical performance.

3.1.5 Inductively coupled plasma mass spectrometry (ICP-MS)

Inductively coupled plasma mass spectrometry (ICP-MS) is a type of mass spectrometry that is typically used to measure metals at very low concentrations (ppt) in a liquid sample. Through meticulous acid digestions, bulk metal contents of catalyst powders can be determined via ICP-MS. Argon inductively coupled plasma is roughly 6000 K, which allows the continuous ionization of metal species introduced through a flow.¹³³ The resulting singly-charged ions have a mass-to-charge ratio dependent on their atomic mass. The mass of these singly-charged ions are detected with a mass filter, typically a quadrupole. This scanning mass filter allows only ions with a specific mass-to-charge ratio to pass at a time, which will hit a detector, typically a dynode electron multiplier.¹³⁴

In a typical acid digestion, 20 μl of catalyst ink was added to 2 ml of aqua regia (3:1 HCl:HNO₃) for 48 hours. The instrument typically used for the inductively coupled plasma-mass spectrometry (ICP-MS) measurements was the Thermo Fischer, model iCAP-QC ICP-MS at the Department of Physics at the Technical University of Denmark. Kinetic energy discrimination (KED) mode was used to remove polyatomic interferences. For each set of measurements, external iridium, titanium, platinum, palladium and niobium standards were prepared and used to calibrate the instrument (PlasmaCAL, Iridium $1003 \pm 5 \mu\text{g/ml}$, 10% HCl), (PlasmaCAL, Titanium $1000 \pm 5 \mu\text{g/ml}$, H₂O / 0.24% F⁻), (TraceCERT, Niobium $1000 \pm 5 \mu\text{g/ml}$, H₂O / 2% HNO₃ / trace HF).

3.2 Electrochemical measurements

All electrochemical measurements were conducted in a three electrode electrochemical glass H-cell with a potentiostat (RDE, FET, MEA) or a bi-potentiostat (RRDE) (VMP2, Bio-Logic). Iridium oxide (IrOx) nanoparticles dispersed titanium felt was used as a counter electrode, which was isolated in its own compartment by a Nafion membrane in the H-cell. A mercury-mercurous sulfate reference electrode (SI Analytics) was used as the reference electrode, which was isolated in its own compartment by a ceramic frit. The ohmic drop was measured by electrochemical impedance spectroscopy at different potentials (typically +0.60, +0.40 +0.20, and 0.00 V_{VRHE}) and compensated manually after the measurements.

All glassware used was cleaned in three steps. First, the glassware was cleaned with piranha acid digestion (24h) and rinsed 3-4 times with milli-Q water. This removes any organic contaminants. Second, the glassware was cleaned with aqua regia acid digestion (24h) and rinsed 3-4 times with milli-Q water. This removes any metal contaminants. Finally, the glassware is boiled in milli-Q water 5-6 times to remove any sulfides.

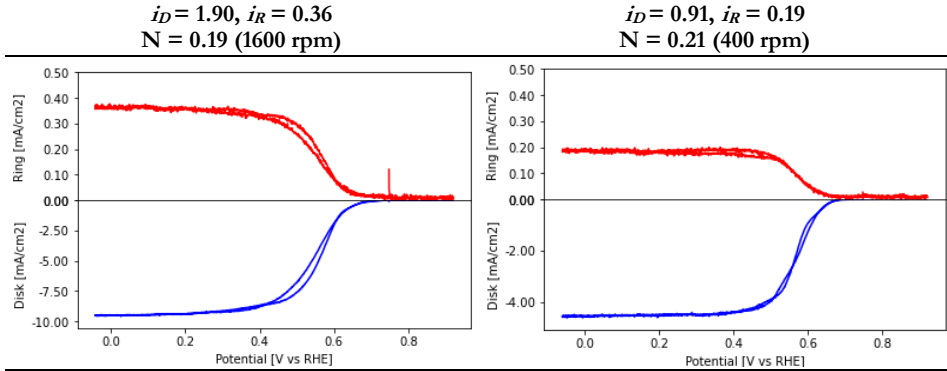


Figure 3.1: Calibration of the collection efficiency ($N \approx 0.20$) of the Pt ring. A glassy carbon disk was used for the ferrocyanide/ferricyanide redox couple in Ar-saturated 1 M KCl with 10 mM $K_3[Fe(CN)_6]$ at room temperature. CV measurements with a scan rate of $50 \text{ mV}\cdot\text{s}^{-1}$ and with variable a rotating rate of 1600 and 400 rpm (left, right, respectively).

3.2.1 RRDE

The Pt-ring collection efficiency ($N \approx 0.20$) was calibrated from CV experiments of the ferrocyanide/ferricyanide redox coupling using a glassy carbon disk (Figure 3.1).¹³⁵ Since this redox coupling is highly facile and there are no competing reactions, we can assume a selectivity ($\lambda_{Faradaic}$) of 100% (Equation 3.2). This means that the collection efficiency can be determined from ratio between the ring current (i_R) and disk current (i_D), as presented in Equation 3.3:

$$\lambda_{Faradaic} (\%) = 100 = \frac{i_R}{N} \times 100 \quad (3.2)$$

$$N = \frac{i_R}{i_D} \quad (3.3)$$

A catalyst ink is prepared with 1 mg of catalyst per 1 ml of 3:1 ethanol:milli-Q and sonicated for 30 minutes. Then, $1 \mu\text{l}$ of 5% Nafion solution (per mg of catalyst) was added to the ink and sonicated for an additional 3 hours, making sure to keep the temperature below $40 \text{ }^\circ\text{C}$ during this sonication. Typically, $15 \mu\text{l}$ of catalyst ink is drop casted onto a glassy carbon electrode, resulting in a catalyst loading of $75 \mu\text{g}\cdot\text{cm}^{-2}$ for the measurement.



Figure 3.2: (left) Soxhlet extractor with Au-coated PCTE membranes. (right) vacuum deposition setup for the catalyst deposition on the metal-coated PCTE membrane.

Before performing RRDE measurements, platinum ring electrode was activated by cycling between 0.05 V and 1.6 V for 100 cycles with a scan rate of $500 \text{ mV}\cdot\text{s}^{-1}$ in an N_2 -saturated 0.1 M HClO_4 . RRDE measurements were in O_2 -saturated 0.1 M HClO_4 with a scan speed of $20 \text{ mV}\cdot\text{s}^{-1}$ and a rotating rate of 1600 rpm at room temperature. Initial cycles in N_2 -saturated 0.1 M HClO_4 were avoided in the catalyst samples synthesized in chapter 6, as it was suspected to contribute to lower performances.

3.2.2 Floating electrode technique (FET)

First, the floating electrode is prepared. Metal (Au or Ti) is sputtered onto a PCTE membrane $\sim 100 \text{ nm}$ thickness to be the current collector for the deposited catalyst. The metal-coated PCTE membranes are then placed in a Soxhlet extractor for 8 hours with milli-Q water and stored in clean glass petri dishes (Figure 3.2, left).

A catalyst stock ink is prepared with 1 mg of catalyst per 1 ml of 3:1 ethanol:milli-Q and sonicated for 30 minutes. Then, 20 μl of 5% Nafion solution (per mg of catalyst) was added to the stock ink and sonicated for an additional 3 hours, making sure to keep the temperature below $40 \text{ }^\circ\text{C}$ during this sonication. The FET catalyst ink is then prepared by diluting 10 μl of stock ink into 10 ml of 3:1 ethanol:milli-Q and sonicated for 1 hour (yielding an ink with a catalyst concentration of 1 μg catalyst per ml). A piece of metal-coated PCTE membrane is placed between the Teflon mask and a new piece of filter in the vacuum deposition setup (Figure 3.2, right).

The Teflon mask has a diameter of 0.2 cm to control the geometric area of the catalyst spot, with an ink holder of about 2 ml. Typically, 800 μl of the FET catalyst ink is added, and vacuum is applied for 20-25 minutes. This yields a loading of roughly $\sim 10 \mu\text{g}\cdot\text{cm}^{-2}$, which has been verified by ICP-MS, and confirms the deposition efficiency equation presented in Zalitis et al.¹²⁵ After catalyst deposition, Teflon AF (1% in FC-40) is applied on to the back of the catalyst spot (0.1 μl). The floating electrode is then placed back in the clean glass petri dish and stored in vacuum chamber for 24 h at room temperature. Afterwards, excess membrane around the catalyst spot is trimmed. The day before testing, the electrode is placed into the Soxhlet extractor for 3-4 hours with milli-Q water and then left to dry overnight.

For an FET measurement, the electrode is attached to the Teflon holder with Teflon tape where the holder is then secured to the glass lid of the H-cell (Figure 3.3). Ensure the metal-coating of the floating electrode is adequately in contact with both Au-wires (1 for working electrode, and 1 for working sense).

In the case of benchmarking $4e^-$ ORR and HER/HOR on commercial Pt/C, an Au-coated floating electrode is used. FET experiments use 1 M HClO_4 that is initially purged with N_2 gas for 10 minutes and an RHE is prepared. An initial CV is run for 20 cycles at $100 \text{ mV}\cdot\text{s}^{-1}$ and 3 cycles at $20 \text{ mV}\cdot\text{s}^{-1}$ between $+0.06$ and $+1.00 V_{\text{VRHE}}$ under N_2 headspace. Impedance is then conducted to account for the ohmic drop $+0.4 V_{\text{VRHE}}$ with an amplitude of 0.01V, 30 points from 10^5 Hz to 0.1 Hz (log scale) under N_2 headspace. The $4e^-$ ORR and HER/HOR activities are measured intermittently in rounds where the headspace is first purged with N_2 gas for 1 min when switching between H_2/O_2 gases. Each round consists of 2 CV cycles from -0.10 to $+1.00 V_{\text{VRHE}}$, where the first cycle is conducted at $20 \text{ mV}\cdot\text{s}^{-1}$ and the second cycle is $10 \text{ mV}\cdot\text{s}^{-1}$. The rounds continue between $4e^-$ ORR and HER/HOR measurement while monitoring the maximum HOR current (at roughly $+0.25 V_{\text{VRHE}}$) and ORR current at $+0.60 V_{\text{VRHE}}$. When the ORR $10 \text{ mV}\cdot\text{s}^{-1}$ cycle results in less than a 5% increase from the previous round, one final round is performed and then an impedance measurement is taken again. The initial cycles run under N_2 headspace is repeated (20 cycles at $100 \text{ mV}\cdot\text{s}^{-1}$ and 3 cycles at $20 \text{ mV}\cdot\text{s}^{-1}$ between $+0.06$ and $+1.00 V_{\text{VRHE}}$) followed by a CO-strip. After disassembly, catalyst spot on the floating electrode is cut off and acid digested in aqua-regia for ICP-MS analysis to determine the absolute metal loading (Pt) of the experiment.

In the case of benchmarking $2e^-$ ORR on a M-N/C catalyst, a Ti-coated floating electrode is used. The FET experiments use 1 M HClO_4 where the volume of this electrolyte in the cathode chamber is carefully accounted for (usually 80-85 ml). The electrode is cycled in an O_2 gas headspace for 5-10 cycles at $20 \text{ mV}\cdot\text{s}^{-1}$ between $+0.06$ and $+1.00 V_{\text{VRHE}}$ and then impedance is conducted to account for the ohmic drop $+0.4 V_{\text{VRHE}}$ with an amplitude of 0.01V, 30 points from 10^5 Hz to 0.1 Hz (log scale). The electrode is then cycled for an additional 3 cycles where the last cycle

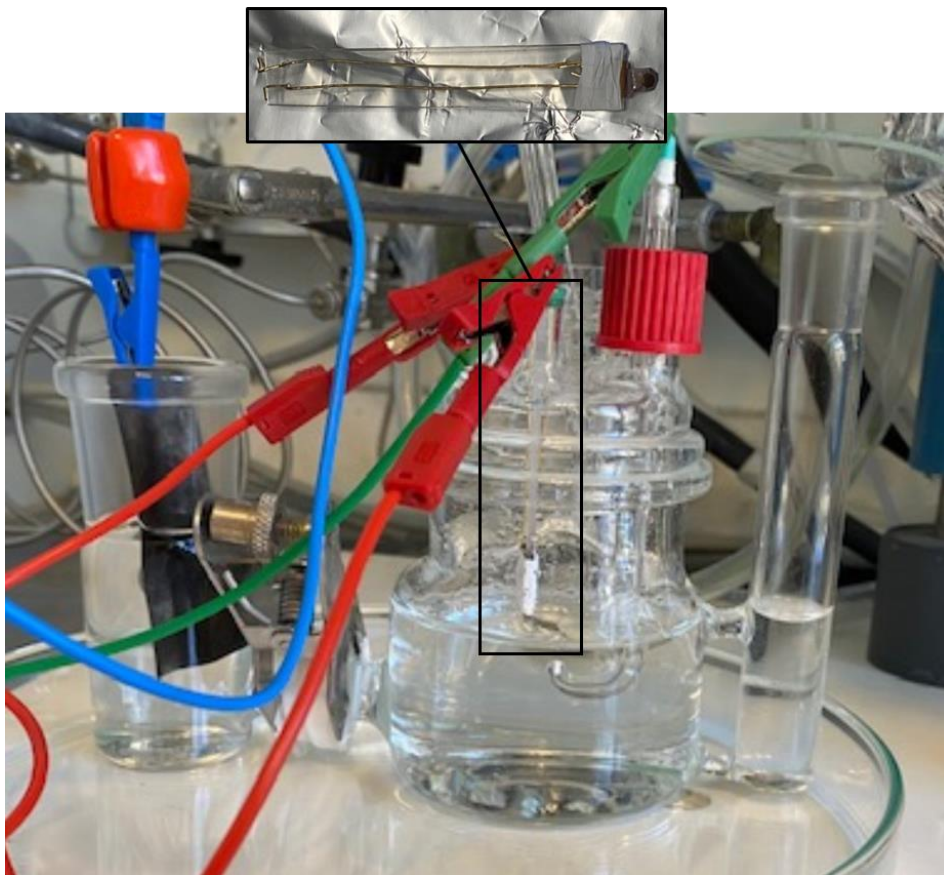


Figure 3.3: Experimental setup used for the floating electrode. A glass H-cell with a Nafion membrane separates the anode and cathode, while the reference electrode chamber is separated by a ceramic frit. Reference electrodes used were (RHE) for $4e^-$ ORR and HER/HOR and (Hg:HgSO₄) for $2e^-$ ORR. Typically, an iridium oxide (IrOx) nanoparticles dispersed titanium felt was used as a counter electrode.

sweeps directly at to the potential used for the CA experiment (typically ~ 0.00 V_{VRHE}). H₂O₂ is quantified in batches using UV-VIS-assisted KMnO₄ titration. Carefully accounting for the electrolyte volume that is removed and replaced.

3.2.3 Membrane electrode assembly (MEA) experiments

The half-MEA electrode was prepared by drop-casting the FET catalyst stock ink onto the carbon cloth GDE (~ 1.0 cm_{geo}²), where it is subsequently heat-pressed to a Nafion membrane, and installed into a glass H-cell (Figure 3.4). The separate anode (from the MEA) allows the facile application of a reference electrode from the anode chamber. The bubbler was gently pressed against the back of the half-MEA electrode while delivering O₂ gas to the 0.1 M HClO₄ electrolyte.



Figure 3.4: Experimental setup used for the half-MEA experiments. A glass H-cell with the half-MEA separates the anode and cathode, while the reference electrode chamber is separated by a ceramic frit. The iridium oxide (IrOx) nanoparticles dispersed titanium felt was used as a counter electrode, which remained separate to allow the use of a reference electrode (Hg:HgSO₄).

An MEA experiment followed the same experimental protocol as an FET experiment for $2e^-$ ORR. The electrode is cycled in an O₂ gas headspace for 5-10 cycles at $20 \text{ mV}\cdot\text{s}^{-1}$ between $+0.06$ and $+1.00 \text{ V}_{\text{VRHE}}$ and then impedance is conducted to account for the ohmic drop $+0.4 \text{ V}_{\text{VRHE}}$ with an amplitude of 0.01 V , 30 points from 10^5 Hz to 0.1 Hz (log scale). The electrode is then cycled for an additional 3 cycles where the last cycle sweeps directly at to the potential used for the CA experiment (typically $\sim 0.00 \text{ V}_{\text{VRHE}}$). H₂O₂ is quantified in batches using UV-VIS-assisted KMnO₄ titration. Carefully accounting for the electrolyte volume that is removed and replaced.

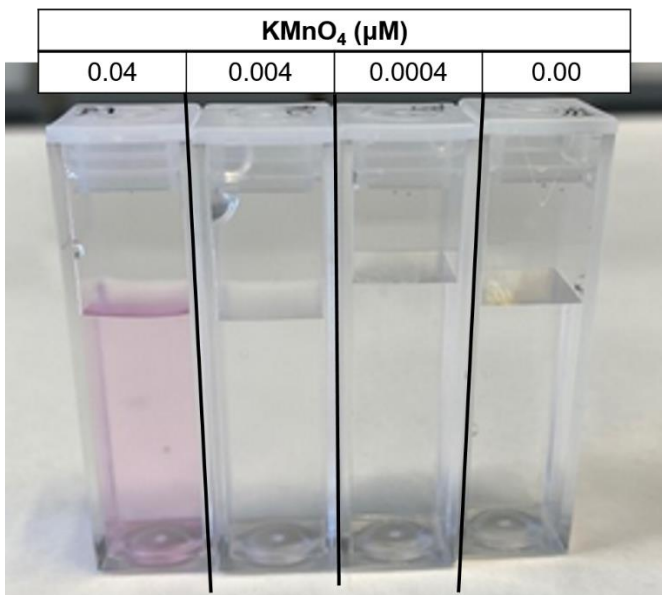


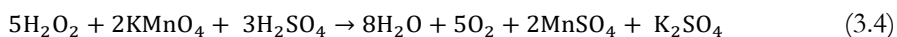
Figure 3.5: Solutions with various KMnO₄ concentrations (0-0.04 μM). Typical KMnO₄ titrations do not need to account for the excess 0.004-0.04 μM KMnO₄ when quantifying H₂O₂ concentrations >10ppm.

3.3 H₂O₂ Quantification

Appropriately accurate and precise H₂O₂ quantifications are essential for determining the selectivity of a 2e⁻ ORR catalyst during an experiment. KMnO₄ titration is adequate when quantifying H₂O₂ concentrations >10ppm, where the color change apparent to the naked eye is sufficient (Figure 3.5). However, the FET experiments have an inherently low absolute catalyst loading on a small catalyst spot, resulting in H₂O₂ concentrations <10 ppm. This necessitated the assistance of UV-VIS to account for the excess KMnO₄ in order to avoid over estimating the H₂O₂ being made during a CA experiment.

3.2.1 Permanganate (KMnO₄) titration

A permanganate (KMnO₄) titration can be used to quantify H₂O₂.¹³⁶ KMnO₄ solutions have a strong purple color at even low concentrations. It can therefore be used as a titrant for H₂O₂, which will react with MnO₄⁻ to form a colorless Mn²⁺ species:



The chemical reaction depicted in Equation 3.4 is generally facilitated in the presence of H_2SO_4 (excess H^+). When the incrementally added MnO_4^- species have exhausted the H_2O_2 in solution, the excess MnO_4^- will quickly turn the solution purple (Figure 3.5). Using the stoichiometric molar ratios from Equation 3.4, one can determine the H_2O_2 concentration with the amount of KMnO_4 added being known.

With known electrolyte volume and known H_2O_2 concentration, the moles of H_2O_2 can be determined. Since the electroreduction of O_2 to H_2O_2 is a $2e^-$ process (Chapter 2, Equation 2.9), 1 mol of H_2O_2 is the equivalent of 2 mol of e^- ($n = 2$). Therefore, the amount of charge (coulombs, C) used to make H_2O_2 ($C_{\text{H}_2\text{O}_2}$) can be determined with Faraday's constant ($F = 96500 \text{ C}\cdot\text{mol}^{-1}$) as shown in Equation 3.5. The ratio of $C_{\text{H}_2\text{O}_2}$ and C_{total} (from the initial CV's and subsequent CA) results in the selectivity ($\lambda_{\text{Faradaic}}$) of the CA experiment (Equation 3.6).

$$C_{\text{H}_2\text{O}_2} = (\text{mol}_{\text{H}_2\text{O}_2}) \times nF \quad (3.5)$$

$$\lambda_{\text{Faradaic}} (\%) = \frac{C_{\text{H}_2\text{O}_2}}{C_{\text{total}}} \times 100 \quad (3.6)$$

3.2.2 Ultraviolet-visible spectroscopy (UV-Vis)

Ultraviolet-visible spectroscopy is used to quantify concentrations of transition metal ions and certain organic compounds in a liquid sample. Transition metal ions have d electrons that can absorb visible light resulting in the intensely colored solutions. The wavelengths of light absorbed are dependent on the energy gap of the resting state and the excited state.¹³⁷ Like XAS, UV-Vis is a transmission technique where the energy loss of the incident UV-Vis light (I_0) is measured (I) across incrementally discrete energy values (800 to 400 nm when quantifying KMnO_4 concentrations). These measured transmittance values (%T, Equation 3.7) are converted to absorbance (A) which is defined by Beer-Lambert's law (Equation 3.8).

$$\%T = \frac{I_0}{I} \times 100 \quad (3.7)$$

$$A = \log_{10} \left(\frac{I_0}{I} \right) = \epsilon cL \quad (3.8)$$

Where L is the path length through the sample (typically 1 cm), c is the concentration of the absorbing species (M) and ϵ is the molar absorptivity ($\text{M}^{-1}\cdot\text{cm}^{-1}$). As mentioned, UV-VIS is used to account for the excess KMnO_4 in order to avoid over estimating the H_2O_2 being made during a CA experiment.

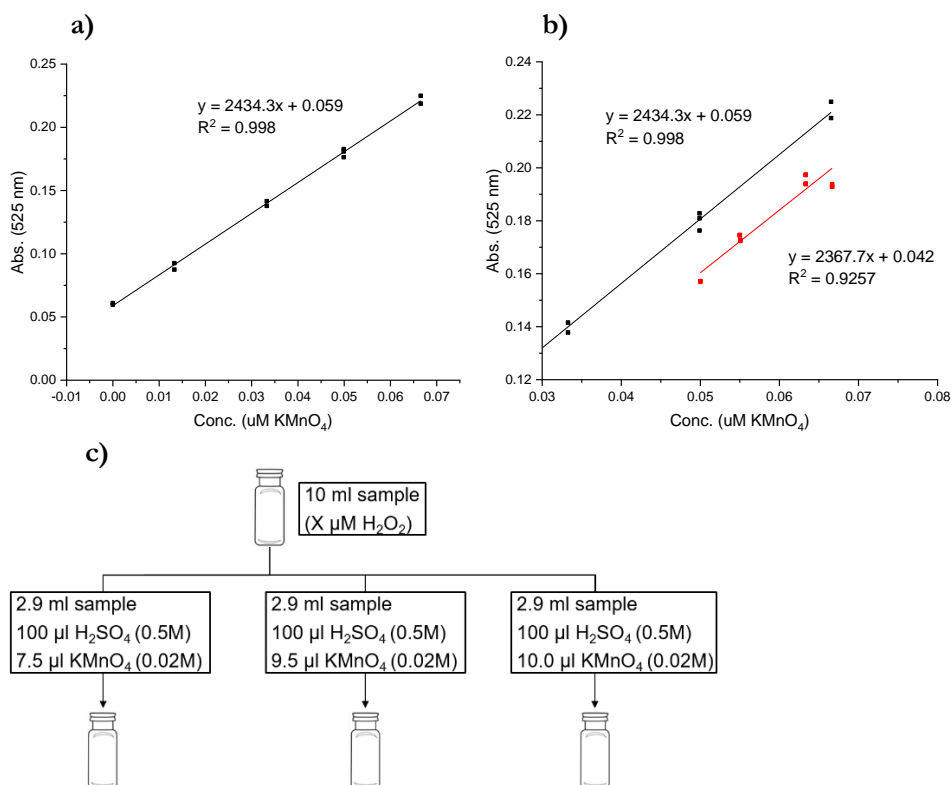


Figure 3.6: UV-Vis assisted KMnO₄ titration. (a) a typical calibration curve from external standards showing the absorbance (525 nm) as a function of KMnO₄ concentrations. (b) typical measurement where internal standards of variable concentrations of KMnO₄ are added to the H₂O₂-containing sample (schematic presented in c). The difference in absorbance between the sample (red), and the external calibration curve (black) translates to the KMnO₄ consumed by H₂O₂. In (b) this translates to a measurement of $1.7 \pm 0.26 \mu\text{mol}_{\text{H}_2\text{O}_2}$.

Before a selectivity measurement, a calibration curve for UV-VIS using external standards is prepared about 2-3 times a week (Figure 3.6, a). A typical selectivity measurement will collect 10 ml of electrolyte from a CA experiment (replacing the 10 ml if continuing the CA experiment). This 10 ml sample is split into three 2.9 ml samples with 100 uL of H₂SO₄ added. The samples are titrated until they turn purple, at which point variable concentrations of KMnO₄ are added to each sample (Figure 3.6, c). The excess KMnO₄ concentrations are measured in the UV-VIS and compared to an external calibration curve (Figure 3.6, b). The difference in absorbance between the sample, and the external calibration curve translates to the KMnO₄ consumed by H₂O₂. In Figure 3.6 (b), this translates to a measurement of $1.7 \pm 0.26 \mu\text{mol}_{\text{H}_2\text{O}_2}$.

Chapter 4

Single Atom Palladium on N-doped hollow carbon spheres

This chapter will go over the article, Highly Active, selective, and stable Pd single-atom catalyst anchored on N-doped hollow carbon sphere for electrochemical H_2O_2 synthesis under acidic conditions published in *Journal of Catalysis*. This was an international collaboration, where I worked closely with Johannes Novak Hansen and Sungeun Yang on the electrochemical experiments. I was mainly responsible for the experiments representing ‘scaled-up’ conditions of an electrochemical reactor. This was achieved by submerging a gas-diffusion electrode (GDE) in O_2 -saturated HClO_4 . The successes of these experiments also came with shortcomings that sparked my future investigations to better test catalysts in better ‘scaled-up’ conditions.

This work presents atomically dispersed Pd single atoms anchored on doped nitrogen species on hollow carbon nanospheres (Pd1/N-C). The Pd1/N-C has mass activities that are comparable to the state-of-the art benchmarks, but more importantly brings forth stability benchmarks and scaled-up performances, both of which are severely lacking in the field of porphyrin catalysts for acidic $2e^-$ ORR. The Pd1/N-C also has a systematic set of control experiments to elucidate the effects of individual parameters that might contribute to the $2e^-$ ORR activity.

4.1 Synthesis of the catalysts samples

Four catalyst samples were prepared: Pd1/N-C, Pd1/C, PdNP/C, and N-C (Figure 4.1). In addition, three distinct steps can distinguish the synthesis of the Pd1/N-C. The first step is the synthesis of the GO-wrapped SiO_2 spheres ($\text{SiO}_2@\text{GO}$). The second step is transforming $\text{SiO}_2@\text{GO}$ to N-doped hollow carbon nanospheres (N-C). Lastly, Pd species were applied to N-C by wet impregnation to form Pd1/N-C. This is summarized in Figure 4.1 (a).

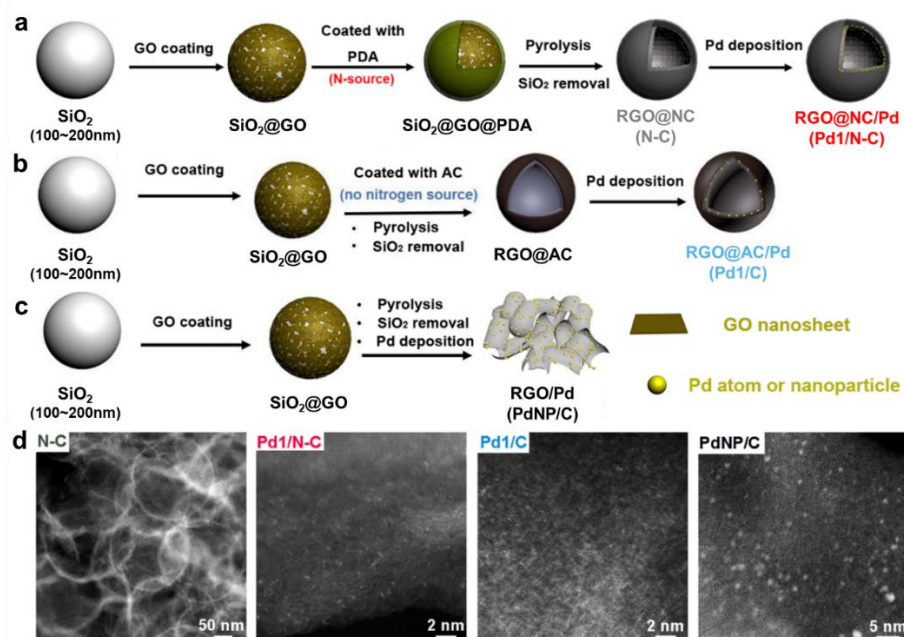


Figure 4.1: Schematic of the synthesis of (a) N-doped hollow carbon nanospheres without Pd (N-C) and Pd single-atom anchored at N-doped hollow carbon nanospheres (Pd1/N-C), (b) Pd single-atom at non-doped hollow AC nanospheres (Pd1/C), (c) Pd nanoparticles deposited on RGO (PdNP/C), and representative HAADF-STEM images of the catalysts. From⁷⁸

The synthesis of SiO₂@GO can be summarized as follows: SiO₂ spheres (100–200 nm) were synthesized by the Stöber method.¹³⁸ These SiO₂ spheres act as scaffolding for the carbon precursors to form the hollow nanosphere structures during the first pyrolysis step. The preparation of the graphitic oxide precursor (GO) was based on the Hummers method.¹³⁹ 0.2g of SiO₂ spheres were dispersed in 100ml ethanol for 20 minutes, and then 1 ml of 3-aminopropyltrimethoxysilane (APTMS) was added and the solution was refluxed for 5 hours to obtain amine-functionalized SiO₂ nanospheres. They were then centrifuged and redispersed in 100 ml of DI water, and 30 ml of 0.2 mg/ml GO aqueous solution and stirred for 1h. The final product was collected with centrifugation, washed with D.I. several times, and dried at 60 °C overnight.

It should be noted that the amino groups from the amine-functionalized SiO₂ nanospheres form very stable hydrogen bonds with oxygen functional groups from the GO. In addition to hydrophobic electrostatic interactions, this leads to a very stable structure between the SiO₂ scaffolding and the initial GO precursor.^{140,141} The presence of 3-aminopropyltrimethoxysilane (APTMS) is also interesting in the context of an ORR catalyst. APTMS is used to modify surfaces, where they self-assemble into monolayers in anhydrous conditions.¹⁴² APTMS typically makes

surfaces more hydrophobic in addition to providing functional groups for chemical reactions.¹⁴³

To transform SiO₂@GO into N-doped hollow carbon spheres (N-C), they first had to be coated by polydopamine (PDA), an N-containing precursor.¹⁴⁴ 200 mg of as-prepared SiO₂@GO spheres were dispersed in 100 mL of 2 mg*mL⁻¹ dopamine Tris solution (pH 8.5, 10 mM Tris buffer) and allowed to react for 36 h under stirring at room temperature. This resulted in polydopamine-coated SiO₂@GO (SiO₂@GO@PDA). After several washing steps and freeze drying, the powder was pyrolyzed at 900 °C for 3 h under an inert atmosphere (N₂ or Argon), where the GO and PDA carbon precursors graphitized together to form N-doped carbon nanospheres (SiO₂@N-C). Finally, SiO₂@N-C was ‘hollowed out’ by etching away the SiO₂ cores with (2%) HF solution to form N-C.

The final step is to anchor Pd atoms into the N-C interface. A suspension of 50/50/0.5 mg (of H₂O/N-C/K₂PdCl₄ respectively) was stirred in an ice bath for 2h, then the powder was rinsed several times with H₂O, and finally freeze-dried to form Pd1/N-C. While catechols from the PDA are great for binding metals, such functional groups typically burn away in 900 °C.^{145,146} It is therefore likely that these Pd atoms are anchored in porphyrin-like configurations within the N-C interface, as evidenced later.

Pd1/C (Figure 4.1, b) was prepared exactly like the Pd1/N-C with one key difference: the SiO₂@GO was coated by amorphous carbon precursor (AC) without any N-content instead of PDA. This AC was the result of pyrolyzing glucose precursors. PdNP/C (Figure 4.1, c) were prepared exactly like the Pd1/N-C and Pd1/C samples except that it did not have a second coating of carbon precursors at all. This resulted in amorphous nanosheet structures that affected the wet impregnation of the Pd to form nanoparticles, as evidenced later.

The resulting four samples, Pd1/N-C, Pd1/C, PdNP/C, and N-C, allow us to investigate the effects of different parameters on the electrochemical performance of the main catalyst of interest, Pd1/N-C. Lacking single atom sites, the PdNP/C was prepared as a control sample for the single atom parameter. Lacking N-doped species, the Pd1/C was prepared as a control sample for the effect of the N-doped species. Lastly, lacking any Pd at all, the N-C was prepared as control sample for the effects of the carbon support around the Pd species of the other samples.

4.2 Characterization

Scanning electron microscopy (SEM) confirmed the hollow-sphere morphology of the samples (or lack thereof in the case of PdNP/C). The Brunauer-Emmett-Teller (BET) method was used to determine the specific surface areas to be 635.7 m²g⁻¹ and 460.9 m²g⁻¹ for the N-C and RGO carbon supports, respectively. High-angle annular dark-field scanning transmission electron microscopy (HAADF-STEM) evidenced atomically dispersed Pd species on the Pd1/N-C, and Pd1/C samples and Pd clusters (0.4-3 nm) for the PdNP/C sample (Figure 4.1, d). XPS analysis

quantified the nitrogen content (3.82 at. %) of Pd1/N-C with the species distribution of graphitic-N (54.2%), pyridinic-N (21.0%) and pyrrolic-N (20.7%). XPS and ICP-MS confirmed a metal weight of (0.3 wt. %) for the Pd-containing samples.

The most important characterizations for these samples are X-ray absorption near edge structure (XANES) and extended X-ray absorption fine structure (EXAFS). XANES and EXAFS provide the chemical state and coordination environment of the dispersed Pd atoms, respectively. The chemical valence of the Pd1/N-C sample was higher than that of a Pd foil, confirming that the Pd atoms had not agglomerated into metallic configurations. The coordination environment of the Pd species suggested electron-rich N atoms (with lone-pairs), further confirming that Pd species existed as isolated atoms and anchored by N doped carbon support. Quantitative least-squares EXAFS curve-fitting analysis determined that there were roughly 6 N atoms coordinated with a Pd, with an average N-Pd bond length of 2.13 Å. This was determined to be a much stronger fit than other possibilities, such as a coordination of four N atoms.

4.3 Electrochemical Measurements

Initial electrochemical performance of Pd1/N-C was assessed with the commonly utilized RRDE, to compare to the literature. The Tafel Plot presented in Figure 4.2 (a) shows the specific activities ($\text{mA}_{\text{H}_2\text{O}_2} \cdot \text{cm}^{-2}$) of the different polycrystalline catalysts to compare intrinsic activities of catalyst surfaces. The Pd1/N-C measurements had a metal concentration of $2.15 \text{ nmol}_{\text{Pd}} \text{ cm}_{\text{geo}}^{-2}$, within the range of low index surfaces of precious metals ($2.00\text{-}2.53 \text{ nmol}_{\text{M}} \text{ cm}_{\text{geo}}^{-2}$, M = Pt, Pd, Au, Ag). It can be seen that Pd1/N-C has a higher specific activity than Ag(pc) and Ag-Hg(pc) and lower than Pt-Hg(pc) and Pd-Hg(pc).

It has been mentioned in Chapter 2 (2.3) that SAC's, particularly based on metal-nitrogen-carbon frameworks (M-N/C's), have promising potential in maximizing a single metallic atom's site's interface. The main merits of M-N/C catalysts such as Pd1/N-C are their high utilizations per mass of these precious metals. The Tafel Plot presented in Figure 4.2 (b) shows the mass activities ($\text{mA}_{\text{H}_2\text{O}_2} \cdot \text{g}_{\text{metal}}^{-1}$) among comparable SAC's, particularly the Co-based M-N/C's (Co-N/C(1,2,3,4)).^{60,61,77,80} In this comparison, Pd1/N-C exceeds Pt-Hg/C and Co-N/C(1) but still has less mass activity than Pd-Hg/C and Co-N/C(2,3,4). However, since palladium is a heavier atom than cobalt ($\text{Pd}=106.42 \text{ g} \cdot \text{mol}^{-1}$, $\text{Co}=58.93 \text{ g} \cdot \text{mol}^{-1}$), normalizing activity to mass means that Co-based catalysts have ~ 2 times the active metal sites available compare to a Pd-based catalyst. The Tafel Plot presented in Figure 4.2 (d) shows the molar activities ($\text{mA}_{\text{H}_2\text{O}_2} \cdot \text{mol}_{\text{metal}}^{-1}$) to better compare the activities of the metal sites where Pd1/N-C is only exceeded by Pd-Hg/C and Co-N/C(4). Since Hg-containing catalysts have limited applications, this means that Pd1/N-C and Co-N/C(4) are the most promising for commercial applications among the state-of-the-art catalysts for $2e^-$ ORR in acidic conditions.

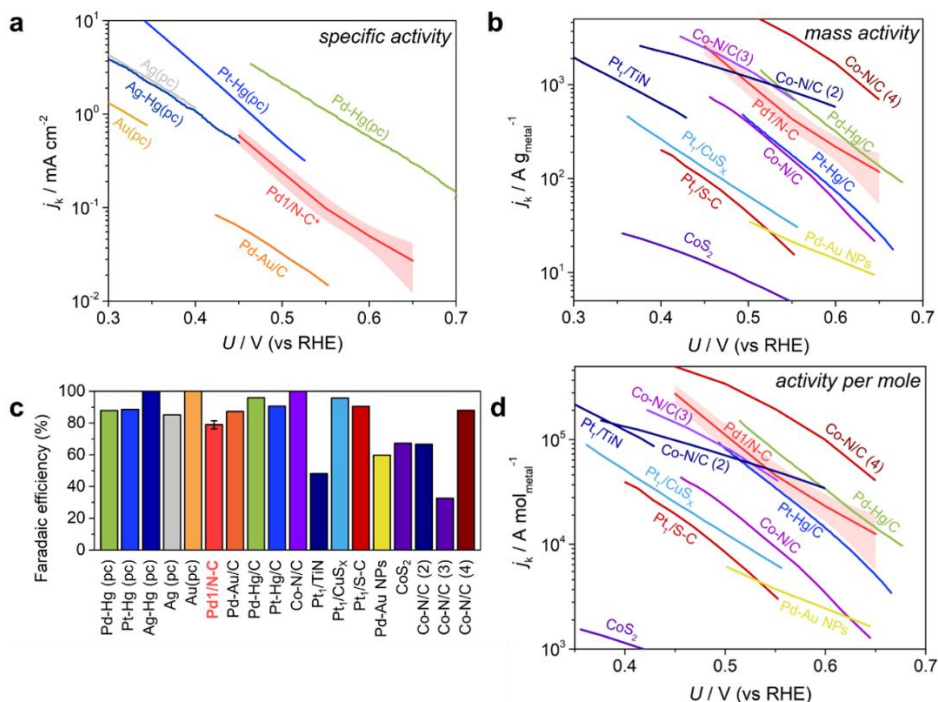


Figure 4.2: Tafel plot comparison (a,b,d) of state-of-the-art catalysts and present work for electrochemical production of H₂O₂ as well as (c) Peak faradaic efficiency. Tafel plots of mass-transport corrected kinetic current densities for electrochemical H₂O₂ production in acidic media based on RRDE measurements for (a) specific activity, (b) mass activity and (d) molar activity. Red line and pale red bands of Pd1/N-C indicate mean and standard deviation of three independent measurements. Data adapted from (Pd1/N-C)⁷⁸; (Pt-Hg(pc), Pt-Hg/C)⁵⁷; (Pd-Hg/C)⁵⁸; (Pd-Au/C)⁵⁵; (Au(pc))⁵⁹; (Pd-Au NPs)⁵⁶; (Co-N/C)⁶⁰; (Co-N/C(2))⁶¹; (Co-N/C(3))⁸⁰; (Co-N/C(4))⁷⁷; (Pt₁/TiN)⁶³; (Pt₁/S-C)⁶⁴; From ⁷⁸

Additional RRDE experiments were done with Pd1/N-C to compare it with the three control samples (Pd1/C, PdNP/C, and N-C) elucidate the effects of individual parameters (Figure 4.3, a). Pd1/N-C was the most active and selective catalyst, with the highest H₂O₂ specific current ($j_{\text{H}_2\text{O}_2} = 2.7 \text{ mA}_{\text{H}_2\text{O}_2} \text{ cm}^{-2}$) and the highest faradaic efficiency of 85 ($\pm 2.5\%$) at +0.25V_{RHE}. Pd1/C had lower specific current ($j_{\text{H}_2\text{O}_2} = 1.9 \text{ mA}_{\text{H}_2\text{O}_2} \text{ cm}^{-2}$) and slightly lower faradaic efficiency of 75 ($\pm 2.5\%$). PdNP/C had a H₂O₂ specific current ($j_{\text{H}_2\text{O}_2} = 1.6 \text{ mA}_{\text{H}_2\text{O}_2} \text{ cm}^{-2}$) and a faradaic efficiency of 65 ($\pm 2.5\%$) at +0.25V_{RHE}. Lastly, the N-C support had a H₂O₂ specific current ($j_{\text{H}_2\text{O}_2} = 1.0 \text{ mA}_{\text{H}_2\text{O}_2} \text{ cm}^{-2}$) and a faradaic efficiency of 63 ($\pm 2.5\%$) at +0.25V_{RHE}.

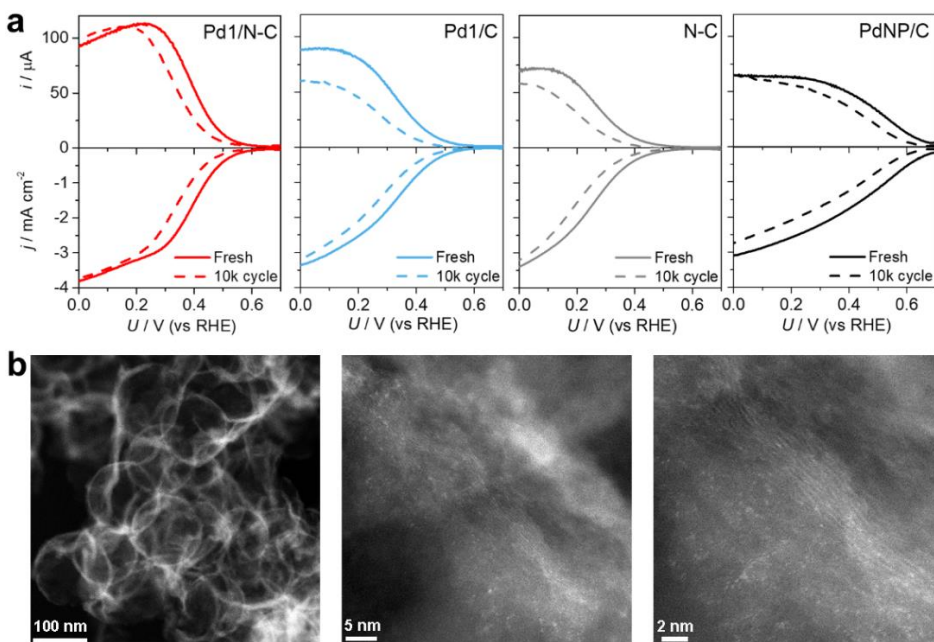


Figure 4.3: Electrochemical durability assessment by 10,000 cycle “on-off” test. (a) Oxygen reduction reaction on different catalysts using a rotating ring-disk electrode before and after 10,000 cycle “on-off” durability test. Measurements in O_2 -saturated 0.1 M HClO_4 with a rotating rate of 1600 rpm at room temperature. “On-off” durability test was performed by potential cycling between 0.05 V to 0.7 V with a scan rate of 500 mV s^{-1} in O_2 -saturated 0.1 M HClO_4 with a rotating rate of 400 rpm at room temperature. (b) Aberration-corrected HAADF-STEM image of Pd1/N-C SAC and enlarged HAADF-STEM image after 10,000 cycle “on-off” test. From⁷⁸

The low performance of N-C suggests insignificant effects from the carbon support. The lower H_2O_2 selectivity of PdNP/C is consistent with the literature, where nanoparticles facilitate $4e^-$ ORR activity, in contrast to single atom sites facilitating $2e^-$ ORR activity. The lower activity and lower H_2O_2 selectivity of Pd1/C suggests that the N-dopant coordination with the Pd single-atom is a key variable for the high activities and selectivities of the Pd1/N-C.

In addition, efforts were also made to assess stability (Figure 4.3, a). RRDE cathodic sweeps were performed after 10,000 cycles ($+0.05$ to $+0.7 \text{ V}_{\text{VRHE}}$ with a scan rate of $500 \text{ mV} \cdot \text{s}^{-1}$) in O_2 -saturated 0.1 M HClO_4 to simulate ‘on-off tests’, which is a common accelerated stress test used for PEMFC reactors. The ring currents of all samples onset at larger over potentials after the on-off test, suggesting catalyst corrosion. The Pd1/N-C retained the most of its initial H_2O_2 specific current ($j_{\text{H}_2\text{O}_2} = 2.3 \text{ mA}_{\text{H}_2\text{O}_2} \text{ cm}^{-2}$, 80% retention), suggesting it is the most stable. This is followed by PdNP/C ($j_{\text{H}_2\text{O}_2} = 1.2 \text{ mA}_{\text{H}_2\text{O}_2} \text{ cm}^{-2}$, 76% retention), then Pd1/C ($j_{\text{H}_2\text{O}_2} = 0.8 \text{ mA}_{\text{H}_2\text{O}_2} \text{ cm}^{-2}$, 42% retention), and finally N-C ($j_{\text{H}_2\text{O}_2} = 0.4 \text{ mA}_{\text{H}_2\text{O}_2} \text{ cm}^{-2}$, 40% retention). The relatively decent stability of the PdNP sample is expected,

given the notorious instability of SAC's. The notable performance loss of N-C suggests that the H_2O_2 is reacting with the catalyst, confirming corrosion of the carbon support, where modifications to the functional groups of the remaining carbon graphene lattice is likely. With this in mind, the performance loss in Pd1/C makes some sense. As the anchoring carbons corrode away as CO_2 from H_2O_2 oxidation, the Pd atomic sites will likely start to agglomerate together to form agglomerates and eventually nanoparticles. This is loosely supported by the RRDE cathodic sweeps, where perhaps the initial performance of Pd1/C is looks similar to Pd1/N-C but the degraded performance of Pd1/C looks more like PdNP/C. The most surprising finding is how stable the Pd1/N-C is compared to all three of the control samples. Figure 4.3 (b) shows HAADF-STEM images of Pd1/N-C to suggest that the atomic sites were maintained.

Yang et al. used half-wave potentials (potentials where current density reaches -1.5 mA cm^{-2}) to compare before and after stability tests to come to different conclusions: Pd1/N-C:(0.40 to 0.35 V), Pd1/C(0.33 to 0.27 V), N-C:(0.26 to 0.21 V), and PdNP/C (0.45 to 0.35 V). This would suggest that the PdNP/C is in fact the least stable catalyst. I have concluded that this type of analysis is more sensible in measuring $4e^-$ ORR onsets before and after stress tests, where the cathodic slopes are significantly steeper and therefore half-wave potentials are easier to visualize and compare. While it is assumed that half-wave potentials are showing kinetic limitations, this will have some inherent bias against the PdNP/C sample with a shallow enough slope to question if it was ever really kinetically limited. In addition, half-wave potential comparisons do not highlight how the 'relevant selectivity' is affected, so comparing the specific activity ($\text{mA}_{\text{H}_2\text{O}_2} \text{ cm}^{-2}$) at a substantial enough overpotential to justify reactor conditions ($+0.25V_{\text{RHE}}$) provides an analysis that is more meaningful.

In lieu of reactor conditions, the catalysts were also tested on a gas diffusion electrode (GDE) submerged into the O_2 -purged 0.1 M HClO_4 electrolyte with the working electrode potential held at ($+0.20V_{\text{RHE}}$) for 1-3 hours (Figure 4.4, a). This better represents reactor conditions, where there is minimal convection and bulk H_2O_2 concentrations reached above 100 ppm. H_2O_2 concentrations were quantified by KMnO_4 titrations (see Chapter 3). Since the catalysts had different currents, H_2O_2 concentrations were quantified in accordance to how much charge ($C = A*s$) had passed (rather than time), to better compare between the catalysts. All samples were tested 3 times each (refer to appendix C) in the GDE set-up, and H_2O_2 concentrations were quantified at 5 C, 10 C, and 15 C.

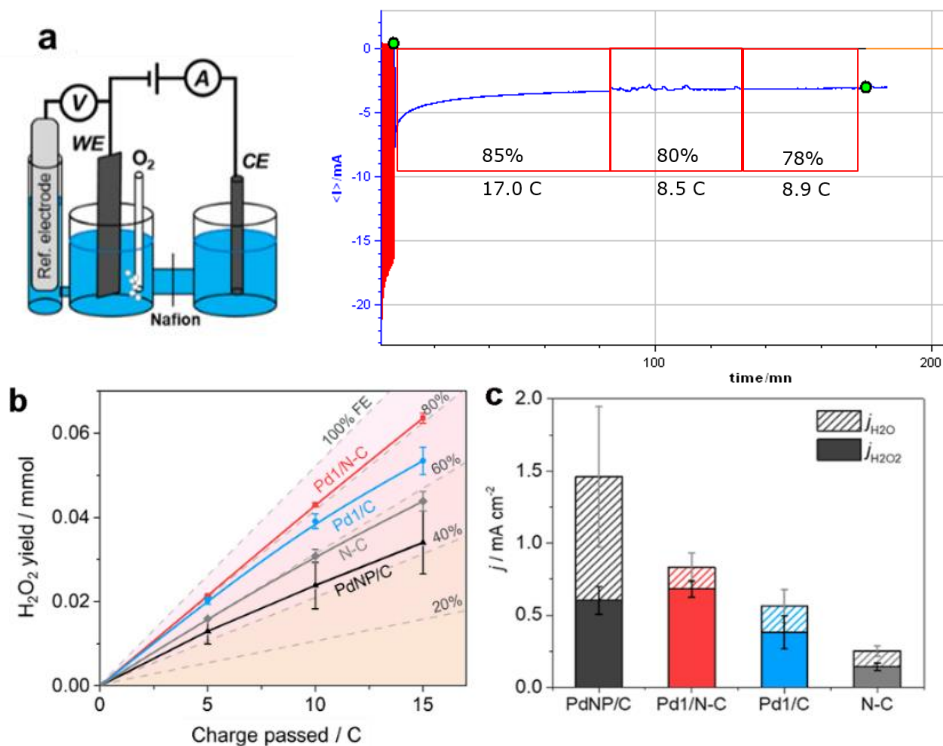


Figure 4.4: Electrochemical production of H₂O₂ using three compartments set-up with a GDE submerged in O₂-saturated electrolyte (0.1M HClO₄). (a) Schematic of three-compartment set-up and a CA of Pd1/N-C exhibiting an irreproducible performance anomaly up to 34C of charge (2 cm² geometric electrode). (b) H₂O₂ yield over charge accumulated up to 15 C. Potential of working electrode was held at +0.2 V_{VRHE}. Dashed lines indicate corresponding lines for given faradaic efficiencies. (c) Partial current densities (H₂O₂ and H₂O current at +0.2 V_{VRHE}) of the GDE measurements from (b). H₂O₂ concentrations quantified by KMnO₄ titrations. From⁷⁸

The N-C sample maintained an average H₂O₂ current of ~0.30 mA_{H₂O₂} cm⁻² (55-60% F.E.) across 15C. The PdNP/C maintained an average H₂O₂ current of ~0.60 mA_{H₂O₂} cm⁻² (30-40% F.E.) across 15C. The Pd1/C maintained an average H₂O₂ current of ~0.40 mA_{H₂O₂} cm⁻² (65-75% F.E.) across 15C. Pd1/N-C maintained an average H₂O₂ current of ~0.75 mA_{H₂O₂} cm⁻² (80-82% F.E.) across 15 C. The net faradaic efficiencies and average H₂O₂ currents are summarized in Figure 4.4 (b and c, respectively). In contrast to RRDE results, PdNP/C had better performances than Pd1/C and N-C. This finding is less surprising when analyzing the data strictly on H₂O₂ output, where the conclusions remain similar. In addition, conclusions remain consistent regarding the N-C being the poorest catalyst in both activity, stability and H₂O₂ output. One final note is that the initial performances of Pd1/N-C and Pd1/C were very similar in terms of H₂O₂ output (after 5C), however the Pd1/C's selectivity drops significantly while also increasing in current.

This increase in current and drop in selectivity further suggests that the Pd species in Pd1/C start to agglomerate into nanoparticles, since the performances transform to something similar PdNP/C. HAADF-STEM analysis would have been interesting for the degraded Pd1/C catalyst, but was unfortunately not available.

The Pd1/N-C catalyst maintained consistent currents and selectivity demonstrating benchmark stability for 2e⁻ ORR performance. One of the challenges with testing this catalyst was how hydrophobic that catalyst layer was initially. Initial measurements cycles in both the RRDE and GDE measurements demonstrate very poor activity, due to the catalyst layer not being properly ‘wetted’. This is highlighted because the Pd1/N-C catalyst was the hardest catalyst to ‘wet’ among multitudes of different catalysts I have tested in the past 3 years. In fact, this catalyst was so hydrophobic that spray depositing the ink on the carbon paper to create a more homogenous catalyst layer was actually detrimental to the performance. It took me two months to discover that drop casting the catalyst was a key detail to reproduce Sungeun’s GDE experiments. One GDE experiment of Pd1/N-C (Figure 4.4, a) proved exceptional compared to the other Pd1/N-C experiments. It maintained an average H₂O₂ current of ~1.40 mA_{H₂O₂} cm⁻² (82% F.E.) across more than 34C of charge. The only difference is that this catalyst ‘aged’ in trace amounts of HClO₄ and H₂O₂ for a few weeks, when the initial testing had complications early on, and the electrode was not properly rinsed before being stored. These results came by accident and were unable to be reproduced. However, it must be mentioned because this is an exceptional benchmark, to effectively maintain doubled the 2e⁻ ORR performance for doubled the amount of charge, during which the localized H₂O₂ concentrations would be at least double as well. It is my speculation that HClO₄ and H₂O₂ oxidized the carbon support ‘just right’ to give the perfect balance of hydrophilicity/hydrophobicity that resulted in such a unique performance. Similar phenomena have been shown with Co-based M-N/C’s.^{79,80} Despite not being able to reproduce this exceptional anomaly, the Pd1/N-C catalyst remains an exceptional benchmark in performance and activity.

The stability of Pd1/N-C could be due to its uniquely substantial hydrophobicity. I attribute this to the APTMS precursor that was utilized to functionalize the SiO₂ nanospheres in the initial stages of the Pd1/N-C synthesis. Pyrolyzed precursors similar to APTMS have been shown to stay mostly intact and have suitable applications in metal sorption from soil.¹⁴⁷ However this precursor wasn’t treated with HF (HF will potentially remove the Si functionality) and pyrolysis was only conducted at 600 °C compared to our 900 °C. Given the disparity in stability between the Pd1/N-C and the Pd1/C, it is likely that this APTMS precursor provided stability in two-fold: its polar functionalities created stable anchoring bonds for the Pd²⁺ atom, while its non-polar functionalities were immediately available at an atomic scale minimize the interaction of the polar H₂O₂ molecule with the catalyst interface. However, the speculation of APTMS’s potential role is partially

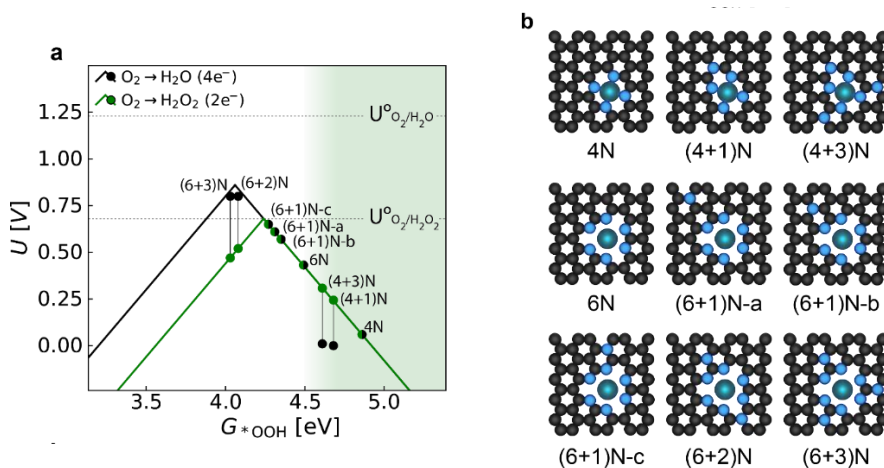


Figure 4.5: DFT calculations of the optimal coordination of a Pd single atom. (a) Sabatier Volcano Plot where the limiting potential is assumed and therefore plotted as a function of ΔG^{*OOH} (left green line = 2e⁻ ORR, left black line = 4e⁻ ORR). Each structure has an onset potential for 2e⁻ ORR (green dots) and 4e⁻ ORR (black dots), connected by a black vertical line for readability. If these potentials coincide, the dot is half-green, half-black. The green area represents the theoretical 100% H₂O₂ selectivity threshold. (b) Unit cell rendering for the Pd-SAC structures modelled. Black, teal and light blue spheres represent C, Pd and N atoms, respectively. From⁷⁸

confounded with the polydopamine precursors that were also used. Perhaps a safer speculative conclusion is that these doped N atoms probably donate electron density to Pd²⁺ resulting in enhanced activity and stability.

4.4 DFT-modelling

The conclusion of how the doped N atoms affect a Pd-N_x site's ORR performance leads us sharply into the proposed DFT calculations. It is immediately apparent that the Sabatier Volcano plot introduced in Chapter 2 (Figure 2.9) does not explain the activity of a Pd-based M-N/C catalyst. This plot assumes the Pd atom is coordinated with 4 nitrogen atoms (4N), where Pd-N₄ site is predicted to be a very weak binder for *OOH, e.g. a highly selective but inactive catalyst well within the shaded green area (where $\lambda_{\text{Faradaic}} \approx 100\%$) in Figure 4.5 (a). However, a 6N coordination results in stronger interactions between the active Pd-N₆ site and the reaction intermediates, resulting in increased activity (Figure 4.5, a). A 6N coordination suggests larger graphene vacancy (Figure 4.5, b) resulting in a decreasing electronic effect due to greater distances between the N ligands and the Pd center.

It has also been mentioned that the surrounding moiety of a M-N/C site can affect its activity. For example, a Co-N_x site surrounded by electron withdrawing functional groups (oxygen-based) results in improved 2e⁻ ORR activity.¹⁴⁸ The N ligands interacting with the Pd center are assumed to be pyridinic, but there could be N

atoms in the surrounding moiety, most likely graphitic N, that can also engage in the electron density of the PdN_x site. The number of these electron-withdrawing graphitic-N moieties ('X') is denoted as (4+X)N for the 4N models and (6+X)N for the 6N models. In addition, the position of the extra graphitic nitrogen in the (6+1)N coordination was also investigated, denoted (6+1)N-a, (6+1)N-b, (6+1)N-c (Figure 4.5, a,b). The (6+3)N and (6+2)N coordinations favor the 4e⁻ ORR volcano, while the (6+1)N coordinations were calculated to be optimal, as they approached the peak of the 2e⁻ ORR volcano. Specifically the (6+1)N-c, where this graphitic nitrogen moiety has resonance stabilization with the Pd-N₆ site. The (4+3)N and (4+1)N coordinations are have a higher overpotential (2e⁻ ORR onsets at +0.25V), as well as a possible decrease in selectivity at even higher overpotentials (4e⁻ ORR onsets at +0.25V). It is therefore likely that the Pd1/N-C is has a 6N coordination, given the onset potentials of Pd1/N-C presented in the RRDE experiments (Figure 4.3, a), as well as the quantitative least-squares EXAFS curve-fitting analysis (average N-Pd bond length of 2.13 Å suggests a 6N coordination). While it's likely that the majority of the Pd sites are 6N coordinated, it is also realistic to assume that the synthesized catalyst is likely a mixture of many different kinds of sites. The heterogeneous nature of Pd-N_x sites has many implications. Perhaps there is a minority of (6+1)N-c sites responsible for a majority of the 2e⁻ ORR activity. These musings remain speculations because while we have an improved ORR activity model accounting for coordination and moieties, these difference have not been validated with experimental results.

4.5 Conclusion

This work introduced me to the field of single atom catalysts for 2e⁻ ORR conditions, and I must humbly thank Johannes Novak Hansen and Sungeun Yang for including me to help finish this project. The Pd1/N-C would become the first of many different kinds of M-N/C catalysts that I would end up testing throughout my PhD. As I learned more in this 2e⁻ ORR field, it would repeatedly become clear to me how thorough this work actually was. Simply cycling the catalyst 10,000 times in O₂-saturated electrolyte already puts this work a step above average, where it has become common to simply cycle the catalyst N₂-saturated electrolyte claiming that this is actually relevant according to the US department of energy. This is a bit of sneaky practice, because cycling in N₂-saturated electrolyte is the 1st of many stability tests, where there is even a disclaimer mentioning this is designed for commercial Pt/C and may not be suitable or relevant for other catalysts.

However, this work went beyond the 'on-off' accelerated stress test in RRDE conditions. The GDE tests provided key insights to the stability of the catalysts, especially with the systematic set of control samples (Pd1/C, PdNP/C, and N-C). Lastly, improved DFT models accounting for coordination and surrounding moiety of the PdN_x sites were brought forth, providing a plausible explanation for the improved activity of the Pd-based M-N/C. However, we were not able to fully confirm this model because our catalyst samples were not systematically controlled for coordination or moieties. Perhaps if we had another Pd1/N-C sample that had

a different coordination confirmed by EXAF's that also conformed with the DFT model then there would have been a much stronger story. In addition, the GDE tests did not really simulate scaled-up operations, because the electrodes were submerged in O₂-saturated electrolyte, which circumvents the triple phase boundary. O₂-saturated electrolyte is a key reason why RRDE experiments perform better than scaled up operations. Nevertheless, the GDE's were stagnant and likely had to rely on the gas that accumulated in the gas diffusion layer. As a result, the GDE experiments do provide some validity but it could be better, especially since I could not reproduce my best GDE results of Pd1/N-C (Figure 4.4, a). This is what sparked my interest in to testing ORR catalysts in better and more relevant conditions.

Chapter 5

Floating Electrode Technique

As already mentioned, an alternative approach to RDDE is needed that enables high transport measurements. The submerged GDE experiments (Chapter 4) fall short in this regard, with similar geometric currents ($\text{mA}\cdot\text{cm}_{\text{geo}}^{-2}$) to RRDE. Kucernak founded the floating electrode technique (FET) as an approach that can facilitate high-mass transport conditions with its facile access to gas inputs. My interests are to take this FET and apply it to state-of-the-art M-N/C's for $2e^-$ ORR.

This chapter will go over my visit to Kucernak's electrochemistry group at Imperial, where I learned the FET first-hand from the exceptionally generous help of Xiaoqian Lin and Colleen Jackson. An extra special thanks must go to Professor Kucernak for allowing me to visit and humbly learn. I will briefly go over how I took this knowledge and replicated it at DTU. I will also mention some discrepancies that I believe deserve considerations for future $4e^-$ ORR FET experiments. Lastly, I will go over how I successfully modified this system to better look at $2e^-$ ORR performances, with interesting initial experiments using the Pd1/N-C catalyst from Chapter 4.

5.1 Floating Electrode for $4e^-$ ORR

Among the first demonstrations of the floating electrode technique (FET) was presented by Zalitis et al., published in *Journal of Physical Chemistry and Chemical Physics*, 2013 (summarized in Figure 5.1). The goal of the FET is to have something as facile as RRDE experiments while avoiding mass transport limitations at higher over potentials reminiscent of scaled-up reactor conditions. A porous gas diffusion electrode floating on aqueous electrolyte allows the supply of reactant gas to the surface sites of a catalyst from behind the catalyst layer while still having facile access to protons (Figure 5.1, a). This FET is also compatible with a 3-electrode set-up, enabling good control and awareness over the potentials applied to the working electrode (Figure 5.1, b) which is something scaled-up reactors struggle with because it is not trivial to incorporate a reference electrode in such systems. Briefly, a floating electrode is a gold-coated porous membrane (PCTE), where the catalyst ink is

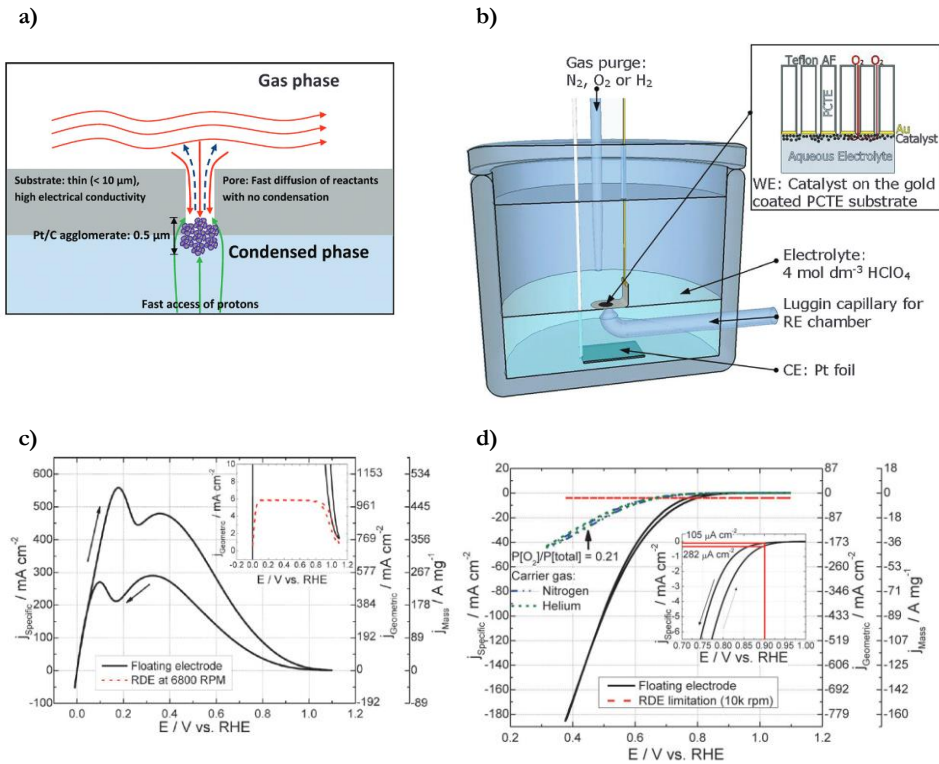


Figure 5.1: Zalitis et al. demonstrates the floating electrode technique (FET). (a) A diagram of a catalyst nanoparticle with high mass transport due to being in equilibrium on a porous floating electrode and (b) a diagram of a floating electrode set-up. HOR CV (c) of a floating electrode ($2.2 \mu\text{g}_{\text{Pt}} \cdot \text{cm}^{-2}$) with commercial 60% Pt/C. The inset (c) shows the HOR activity of Pt on RDE in comparison (6.8K rpm). ORR CV (d) of a floating electrode ($4.9 \mu\text{g}_{\text{Pt}} \cdot \text{cm}^{-2}$) with commercial 60% Pt/C. The dashed line refers to the RDE limiting current density of $14 \text{ (mA} \cdot \text{cm}^{-2}\text{)}$ (10k rpm). Partial pressure measurements using nitrogen (blue dash-dot line) or helium (green short-dash line) as the carrier gas are shown for $\text{P}[\text{O}_2]/\text{P}[\text{total}] = 0.21$, synthetic air. The inset (d) shows the curve between 0.7 and 1 V vs. RHE, with the activity at 0.9 V vs. RHE highlighted. The ordinate axis corresponds to the specific current density (left), geometric current density (first right) and mass activity (second right). FET measurements run in 4M (HClO_4) at $10 \text{ (mV} \cdot \text{s}^{-1}\text{)}$ at 298 K, Pt counter electrode, and RHE reference electrode. RDE measurements run in 0.5M (HClO_4) at $10 \text{ (mV} \cdot \text{s}^{-1}\text{)}$. From ¹²⁵

deposited via vacuum filtration, and a hydrophobic treatment of Teflon AF is applied to the back of the electrode to protect the gas channels from flooding due to capillary forces (details in Chapter 3).

Zalitis et al. demonstrates the effectiveness of the FET technique through the HOR and $4e^-$ ORR performances it was able to achieve from a commercial Pt/C catalyst (HOR and ORR summarized in Figure 5.1, c and d, respectively).¹²⁵ For HOR, this translates to a peak mass activity of $497 \text{ (A} \cdot \text{mg}_{\text{Pt}}^{-1}\text{)}$ at $+0.18 \text{ V}_{\text{VRHE}}$. For ORR, this

translates to a peak mass activity of 165 ($\text{A} \cdot \text{mg}_{\text{Pt}}^{-1}$) at $+0.38 \text{ V}_{\text{RHE}}$. Both demonstrating activities of at least two orders of magnitude in improvement compared to RDE, which is limited by low concentrations of saturated O_2 in the aqueous electrolyte. While the y-scale can be manipulated accordingly, the ORR scan is arguably curved between $+0.60$ and $+0.80 \text{ V}_{\text{RHE}}$, suggesting kinetically-limited activities at relevant potentials ($+0.65 \text{ V}_{\text{RHE}}$) for fuel cell operations.

Zalitis et al. explains that significant improvements in ORR activity were not evident when using O_2 -saturated electrolytes, suggesting that the ORR activity can be exclusively attributed to the fast gas phase diffusion through the pores enabled by the hydrophobic Teflon AF treatment on the back of the porous electrode. To further verify that the floating electrode was free from gaseous mass transport effects, ORR activity was measured in a partial pressure of O_2 (0.21) but with two different carrier gasses (N_2 or He). Since He is a lighter gas, oxygen can diffuse faster through this carrier gas matrix it compared to the heavier N_2 gas. Gaseous mass transport effects would be evident if there was more ORR activity when using the He carrier gas compared to the N_2 carrier gas.³⁴ However, there was no significant difference in ORR activity between these partial pressure measurements using He (green short-dash line) or N_2 (blue dash-dot line), as presented in Figure 5.1 (d). Zalitis et al. concludes this notable ORR activity with some interesting remarks. At the time of publication, it was the best ORR mass activity of Pt ever measured, even better than the state-of-the-art fuel cell performances: Zalitis et al. compares their benchmark mass activity of $4.2 (\text{A} \cdot \text{mg}_{\text{Pt}}^{-1})$ at $+0.8 \text{ V}_{\text{RHE}}$ (using FET) to Gasteiger et al.'s mass activity of $0.2 (\text{A} \cdot \text{mg}_{\text{Pt}}^{-1})$ at $+0.8 \text{ V}_{\text{RHE}}$ (using PEMFC).¹⁴⁹ However, the FET experiment had higher partial pressure of O_2 (101 kPa) meaning we can translate Gasteiger et al.'s mass activities to roughly $4.2 (\text{A} \cdot \text{mg}_{\text{Pt}}^{-1})$. Zalitis et al. also mention that even after adjustments to factor the O_2 partial pressures, the FET experiment still has better mass activities since the FET achieved this mass activity at only $25 \text{ }^\circ\text{C}$, while Gasteiger's PEMFC achieved this mass activity at $80 \text{ }^\circ\text{C}$.

After failing to reproduce these results at DTU, I was fortunate enough to be able to learn the FET first-hand at Imperial in November 2019 (the good graces provided by Professor Kucernak cannot be thanked enough). The PhD. student, Xiaoqian Lin, and Post Doc., Collen Jackson taught me that there was much more involved to the FET protocol than what the published literature states because Zalitis et al. didn't fully understand how the FET worked at the time (which is completely understandable). After years of optimization and carefully detailed protocols, it became very apparent how necessary this visit was, since this very necessary information was published the following year (by Lin in 2020).¹⁵⁰ Lin et al.'s optimization of the FET is summarized in Figure 5.2, where the most notable and necessary missing detail is the 'break-in' procedure. The 'break-in' procedure

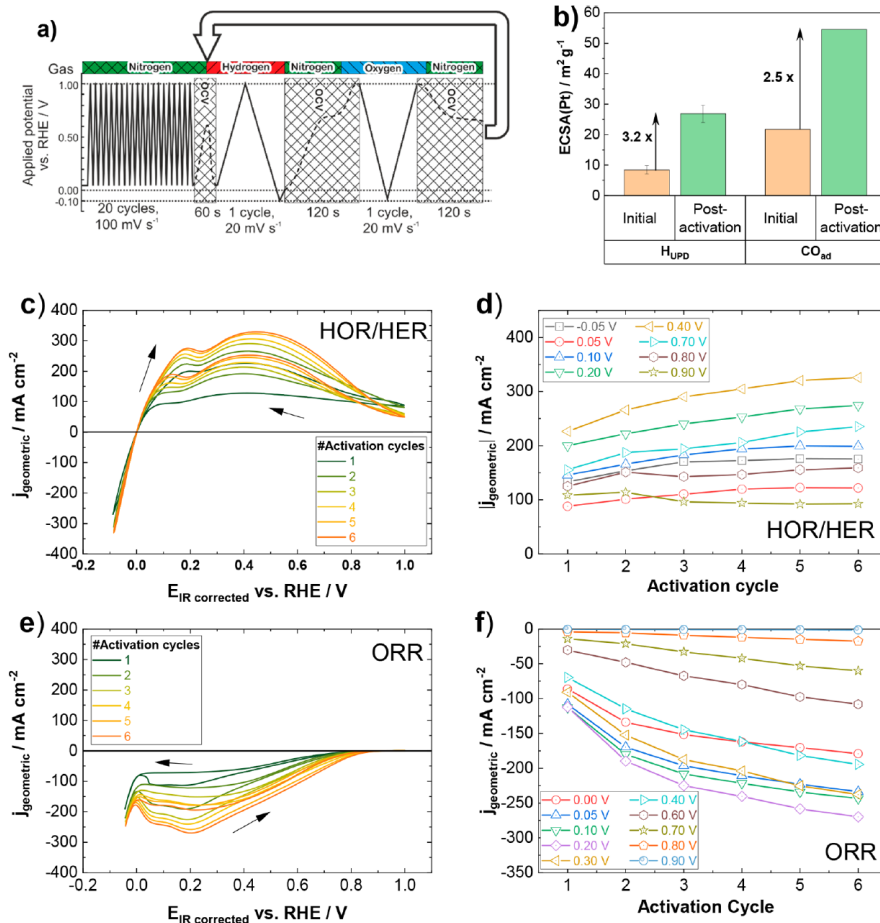


Figure 5.2: Summary of the break-in procedure used for floating electrodes (FE's), and the evolution of performances during this break-in procedure. (a) Schematic of the cleaning and break-in procedure. (b) Comparison of the ECSA measured before and after the break-in procedure using HUPD and CO-stripping. Examples of cyclic voltammograms as a function of the break-in cycle with a (c) H_2 gas headspace and (e) O_2 gas headspace. Evolution of performance depicted by the extracted values from the anodic scans at specific potentials for the (d) HOR/HER and (f) ORR results in (c) and (e), respectively. All potentials are vs RHE. The loading of the electrode is $8.0 \mu\text{g}_{\text{Pt}} \cdot \text{cm}_{\text{geo}}^{-2}$ (JM 50% Pt/C). CV's were run under the conditions of 101 kPa, 298 K, 1 M HClO_4 , and 20 mV s^{-1} . From ¹⁵⁰

involves alternating between ORR and HOR/HER scans, where N_2 is intermittently purged to avoid the direct mixing of H_2/O_2 gases from transitions (Figure 5.2, a). It functions similarly to PEMFC procedures used to properly 'wet' the catalyst layers for better access to protons. Lin et al. suggest that this alternation of the FE between oxidizing and reducing conditions can better equilibrate the triple phase boundary because the generated H_2O_2 (from the ORR sweeping below $+0.7 \text{ V}_{\text{RHE}}$) can attack

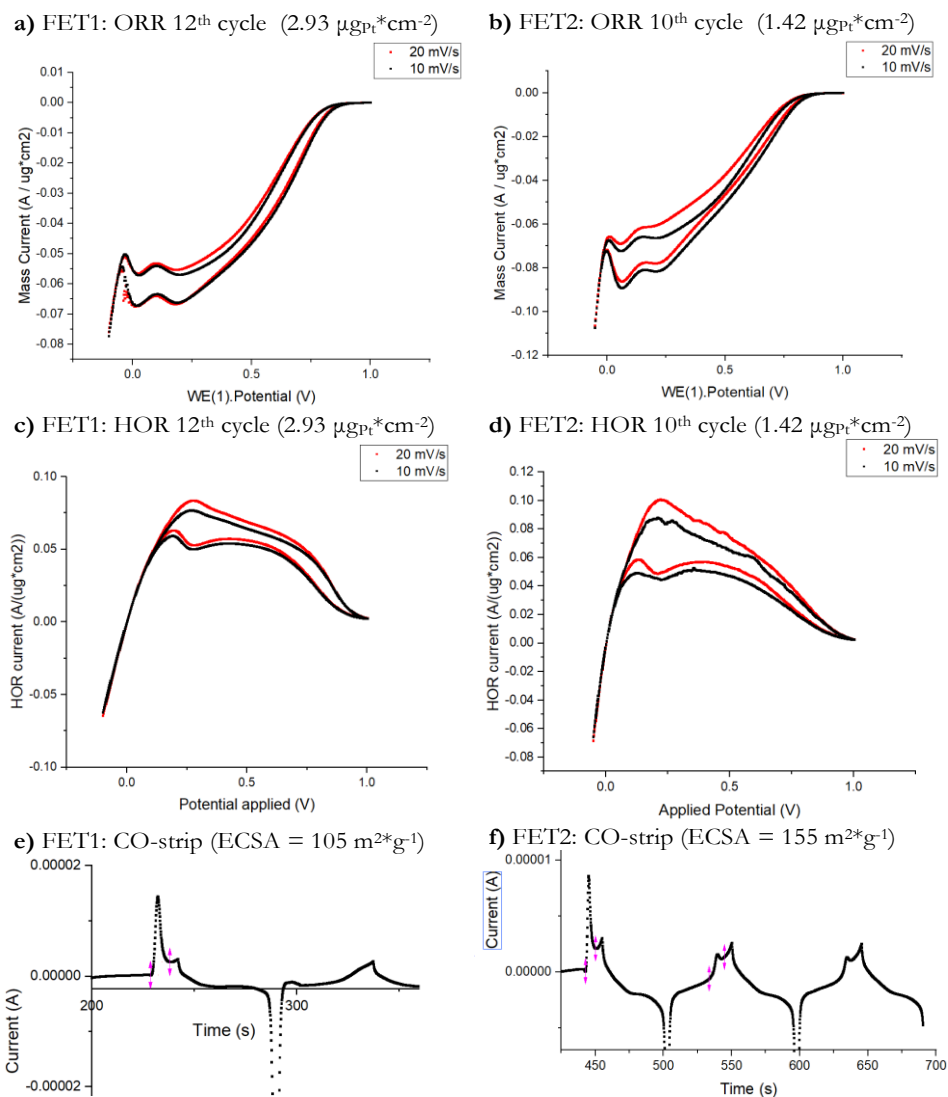


Figure 5.3: Two separate FET experiments, FET1 ($2.93 \mu\text{g}_{\text{Pt}} \text{ cm}^{-2}_{\text{geo}} \pm 3.30 \% \text{RSD}$) and FET2 ($1.42 \mu\text{g}_{\text{Pt}} \text{ cm}^{-2}_{\text{geo}} \pm 5.37 \% \text{RSD}$), performed at Imperial. Mass activities ($\text{A} \cdot \mu\text{g}_{\text{Pt}}^{-1}$) of ORR (a+b) and HOR (c+d) were alternately measured each cycle. Each cycle consists of a $20 \text{ mV} \cdot \text{s}^{-1}$ and $10 \text{ mV} \cdot \text{s}^{-1}$ for each reaction. After the cycles are finished, a CO-strip is performed (20 minutes 1000 ppm CO headspace, then purge with N_2 for 10 minutes, while holding the potential at $+0.1 \text{ V}_{\text{VRHE}}$. Finally scanned 3 cycles between $+0.06 \text{ V}$ and $+1.00 \text{ V}$ (start and stop at 0.1 V) at a scan rate of $20 \text{ mV} \cdot \text{s}^{-1}$. CV's were run under the conditions of 101 kPa , 298 K , 1 M HClO_4 , and 20 mV s^{-1} .

Table 5.1: ORR mass activities ($\text{mA}\cdot\mu\text{g}^{-1}$) of commercial 60% Pt/C at various operation potentials: $+0.65 V_{\text{VRHE}}$, $+0.60 V_{\text{VRHE}}$, and $+0.55 V_{\text{VRHE}}$. Roughly calculated slopes are included to give an intuition of how much the performances are compromised by various losses to resistance.

Experiment	($\text{mA}\cdot\mu\text{g}^{-1}$) @0.65V	($\text{mA}\cdot\mu\text{g}^{-1}$) @0.60V	($\text{mA}\cdot\mu\text{g}^{-1}$) @0.55V	slope (0.65V-0.60V) ($\text{mA}\cdot\mu\text{g}^{-1}$)/(V)	slope (0.60V-0.55V) ($\text{mA}\cdot\mu\text{g}^{-1}$)/(V)
Zalitis, Imperial ¹²⁵ 2013	27	42	62	300	400
Zhang, Imperial ¹⁵¹ 2020	35	48	63	260	300
Haraldsted, Imperial 18-11-2019 (FET2)	30	38	44	160	120
Haraldsted, DTU 11-08-2020 (x2Au-HiNaf)	15	27	41	240	280
Haraldsted, DTU 17-09-2020 (x1Au-LoNaf)	9	14	19	96	104
Haraldsted, DTU 23-09-2020 (x1Au-HiNaf)	35	45	54	200	180

overly-dry areas. The effects of these ‘activation cycles’ are effectively illustrated with increasing HOR and ORR activities presented in Figure 5.2 (c+d and e+f, respectively), as well as the notable increase in electrochemically active surface area (ECSA) determined by CO-stripping. It will be briefly mentioned that the ECSA is derived from the total charge (C) of the stripped CO, which is determined by integrating the CO peak typically between $+0.65 V_{\text{VRHE}}$ and $+0.85 V_{\text{VRHE}}$. A CO peak is depicted (current vs time) in Figure 5.3 (e+f), where the subsequent scan (where all CO should be removed) is used for background subtraction. The ECSA ($\text{m}^2\cdot\text{g}^{-1}$) is then calculated by taking this CO charge and dividing it by the standard charge of one monolayer CO surface coverage (roughly $420\cdot 10^{-2} \text{C}\cdot\text{m}^{-2}$) and the actual value of loaded Pt (g) on the electrode (determined by ICP-MS).

Figure 5.3 shows how I successfully reproduced the FET under the careful supervision of Xiaoqin Lin at Imperial and Table 5.1 shows that I was able to take it back with me to DTU. At DTU, I experimented with a few variables to see if I could get even better results, such as varying Nafion content, different kinds of gold-coated membranes and also better ways to apply the hydrophobic Teflon layer. These endeavors yielded results of little interest, but most notably: I was never able to fully reproduce Zalitis et al.’s benchmark ORR activities. While similar activities were eventually achieved, it always seemed like my FET experiments were mass-transport limited in comparison because my slopes were never nearly as steep as Zalitis et al.’s work (summarized in Table 5.1).

A concerning detail became the realization that chronoamperometry (CA) experiments for Pt/C loaded floating electrodes never worked for ORR, since I would always lose my current over time (within minutes). It seems the Imperial group had similar issues where ORR CA experiments would sharply degrade within hours, as evidenced by Zhang et al. (Appendix A, Figure A.2).¹⁵¹ Interestingly, they had consistent HOR currents in CA experiments, which likely rules out that the flooding of the catalyst layer as the issue. Zhang et al. provide a convoluted speculation of stable Pt-oxide formations that inhibit the ORR activity, (specifically O^* from Equation 2.11, Chapter 2). Consequently, there are some discrepancies around the FET that I don't fully understand because:

1. The FET performances are solely based on this 'break-in' procedure, where it is simply repeated until performances stop increasing. Interestingly, this 'break-in' procedure improves ORR activities more than the HOR activities (Figure 5.2).
2. Despite these ORR-activity improvements, the FET cannot maintain an ORR current at $+0.6 V_{\text{VRHE}}$ for CA experiments, where CA experiments are a notable focus for research on scaled-up systems. This is notably bizarre because the FET can maintain an HOR current.
3. The very low absolute Pt loadings (nanograms but on a small 0.031 cm^2 catalyst spot) would suggest later electrochemical reaction onsets. This has been reported in previous literature.¹⁵² Yet new literature benchmarks FET against the RDE in the kinetic onset regions, where the RDE will have higher absolute loadings of Pt.¹⁵³
4. The absolute necessity of a gold current collector. Au is roughly x20 more conductive than Ti (Au: $44.2 \times 10^6 \text{ S} \cdot \text{m}^{-1}$, Ti: $2.4 \times 10^6 \text{ S} \cdot \text{m}^{-1}$), but my Au-coated FET's have an ohmic drop of $\sim 0.3 \Omega$, while my Ti-coated FET's have an ohmic drop of $\sim 500 \Omega$ (more on this later in the chapter). This is a difference of roughly x2000 fold instead of the x20 fold difference suggested by the material conductivities.

At this point, I had some suspicions about the validity of the benchmark $4e^-$ ORR activities provided by the FET and it stems mainly from the highly conductive Au-coating used as a current collector. It is fair to assume that Au will be mostly inactive for ORR in the regions between $+1.00$ and $+0.60 V_{\text{VRHE}}$, especially relative to Pt. However, the Au-loading is much larger (100 nm coating) compared to the absolute Pt loading (in the nanogram magnitudes), and the Au will be active for $2e^-$ ORR below $+0.60 V_{\text{VRHE}}$. My hypothesis is that this porous electrode is partially a sponge to electrolyte, and that electrolyte accumulates significant local concentrations of H_2O_2 generated from the Au due to the repeated cathodic sweeps from the break-in procedures. These local concentrations of H_2O_2 can then be reduced by the Pt around $+0.95 V_{\text{VRHE}}$, as supported by literature.¹⁵⁴ This H_2O_2 RR activity would therefore be confounded with the benchmark $4e^-$ ORR activities exhibited by the

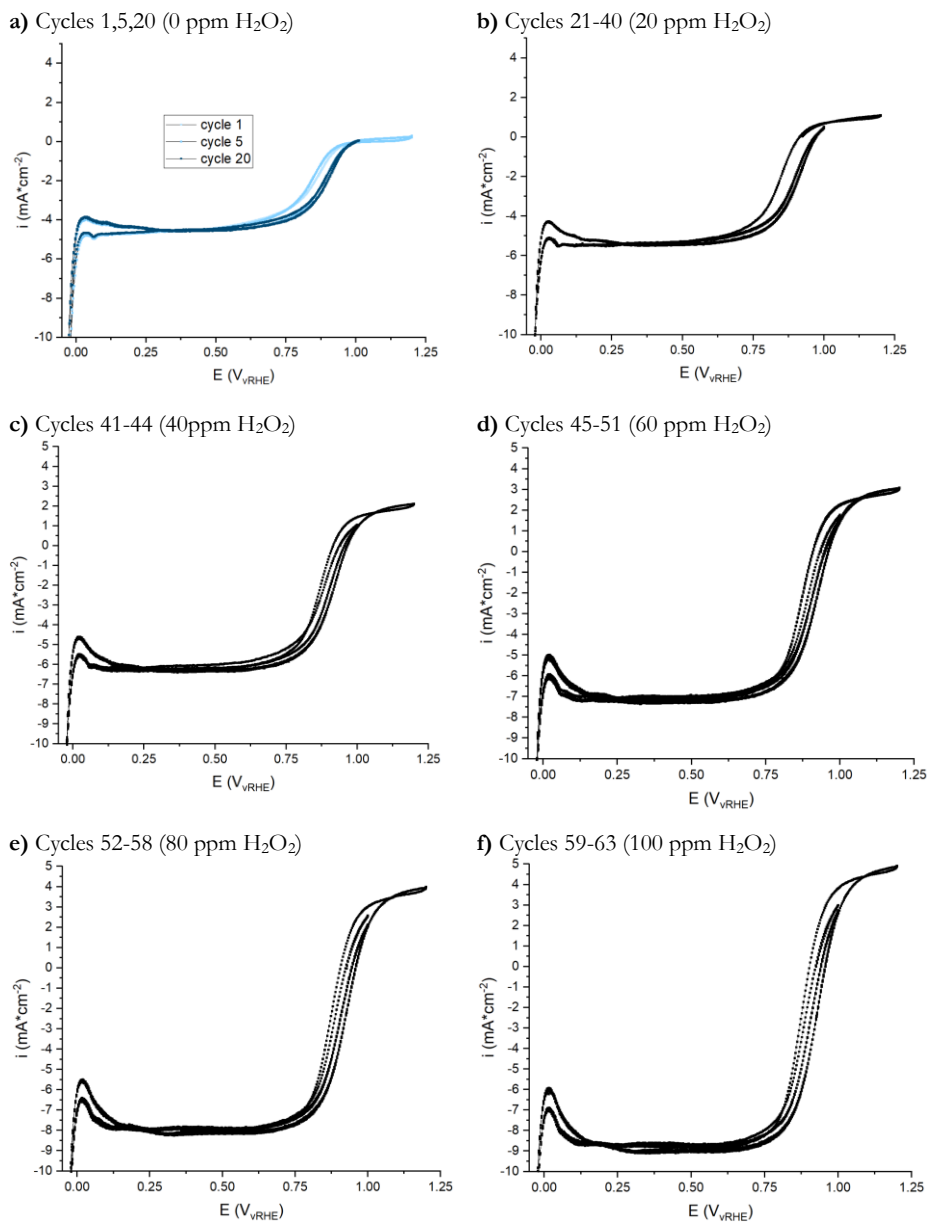


Figure 5.4: A non-optimized RDE measurement of commercial %60 Pt/C ($30 \mu\text{g}_{\text{Pt}}\cdot\text{cm}^{-2}$) deposited on an Au disk where the H₂O₂ concentrations are intermittently increased in the electrolyte: (a) cycles 1-20 (0 ppm H₂O₂), (b) cycles 21-40 (20 ppm H₂O₂), (c) cycles 41-44 (40 ppm H₂O₂), (d) cycles 45-51 (60 ppm H₂O₂), (e) cycles 52-58 (80 ppm H₂O₂), and (f) cycles 59-63 (100 ppm H₂O₂). Measurements in O₂-saturated 0.1 M HClO₄ with a scan speed of 20 mV*s⁻¹ and a rotating rate of 1600 rpm at room temperature.

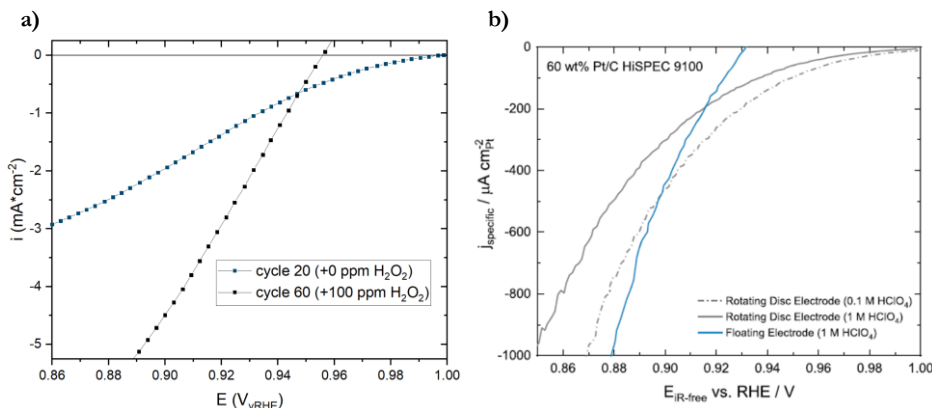


Figure 5.5: Anodic scans of Pt-based catalysts. (a) A non-optimized RDE measurement of commercial %60 Pt/C ($30 \mu\text{g}_{\text{Pt}}\cdot\text{cm}^{-2}$) deposited on an Au disk (cycle 20, blue). Adding 100 ppm H_2O_2 (cycle 60, black) suggests state-of-the-art mass activities ($\sim 0.18 \text{ A}\cdot\text{mg}_{\text{Pt}}^{-1}$, at $+0.90 \text{ V}_{\text{VRHE}}$). (b) Jackson et al.'s FET measurement reaching a mass activities of ($\sim 0.28 \text{ A}\cdot\text{mg}_{\text{Pt}}^{-1}$, $\pm 10\%$, at $+0.90 \text{ V}_{\text{VRHE}}$). Measurements in O_2 -saturated 0.1 M HClO_4 with a scan speed of $20 \text{ mv}\cdot\text{s}^{-1}$ and a rotating rate of 1600 rpm at room temperature. (b) is from ¹⁵³

FET. The oxidation of H_2O_2 to O_2 ($\text{H}_2\text{O}_2\text{OR}$) is fairly straightforward: it's the reverse of $2e^-$ ORR at $+0.7\text{V}_{\text{VRHE}}$ (Chapter 2, Equation 2.21). H_2O_2 reduction ($\text{H}_2\text{O}_2\text{RR}$) occurs at the much more oxidizing potential of $+1.77\text{V}_{\text{VRHE}}$ (Chapter 2, Equation 2.25). This means that there is a point between $+0.7\text{V}_{\text{VRHE}}$ and $+1.77\text{V}_{\text{VRHE}}$ where the oxidizing and reducing overpotentials from each reaction would 'cancel out'. In other words, there would be a potential of zero current. For Pt, this is around $+0.95 \text{ V}_{\text{VRHE}}$.¹⁵⁴ For Au, it is a little bit more complicated since the $\text{H}_2\text{O}_2\text{OR}$ is confounded with an oxide coverage that starts to form around $+0.90 \text{ V}_{\text{VRHE}}$.^{153,155} In fact, Jackson et al. claim that the presence of H_2O_2 is actually making their Pt ORR performance worse, (since Au would be oxidizing). A quick experiment was therefore conducted to challenge this claim and hopefully provide a strong notion of how H_2O_2 affects ORR experiments. To test my $\text{H}_2\text{O}_2\text{RR}$ hypothesis: 60% Pt/C was deposited onto an Au-disk ($30 \mu\text{g}_{\text{Pt}}\cdot\text{cm}^{-2}$) and the ORR current was measured while intermittently increasing H_2O_2 concentrations of the electrolyte (Figure 5.4). The cathodic sweep would start at $+1.20 \text{ V}_{\text{VRHE}}$ and then sweep down to and cycle between $+1.00 \text{ V}_{\text{VRHE}}$ and $-0.1 \text{ V}_{\text{VRHE}}$. The initial cycles were performed in $0 \text{ ppm H}_2\text{O}_2$, and provides a testament to how this RDE measurement is non-optimized (Figure 5.4, a). The intermittently increasing the H_2O_2 concentrations (20-100 ppm H_2O_2 , Figure 5.4, b-f) also increases the mass-transport current since the H_2O_2 supplements the O_2 -saturation as an additional species to be reduced in the electrolyte. Interestingly, this increase in cathodic current ($\sim +0.65 \text{ V}_{\text{VRHE}}$) is almost exactly mirrored by an increase in the oxidative current ($\sim +1.20 \text{ V}_{\text{VRHE}}$).

The similarities between my Pt/C measurements with 100 ppm H₂O₂ (zero current at +0.955 V_{VRHE}) and Jackson et al.'s published FET data (zero current at +0.93 V_{VRHE}) is quite uncanny (Figure 5.5). It should be stressed that my initial measurements at 0 ppm H₂O₂ are quite poor, and that some H₂O₂ contamination can make this data look drastically better. Even the initial 20 cycles with 0 ppm H₂O₂ (Figure 5.4, a), we can see improving catalyst performance, which can be a combination of catalyst wetting and H₂O₂ build-up from the Au-disk. Since the FET is a porous interface floating on top of a static electrolyte, the diffusion of H₂O₂ will be very slow. Therefore, the effect of H₂O₂ build-up in the Pt/C catalyst layer of a floating electrode is likely to be more significant, especially when considering how much more Au is present compared to Pt in the FET.

This H₂O₂RR theory would explain why the break-in procedure is essential for these FET experiments and also why the CA's ORR activity degrades so rapidly: it is simply consuming local H₂O₂ concentrations that are not being replenished by the Au from the further cycling below +0.6 V_{VRHE}. In addition, it has been demonstrated that the presence of H₂O₂ can create the illusion of improved ORR onset and kinetic performances (Figure 5.5, a). Lastly, the discrepancy between the known electrical conductivities and impedance spectra of the Au-FET and Ti-FET experiments suggests that the Au is electrochemically active across the entire potential window being tested. It should be noted that this H₂O₂RR hypothesis is a little presumptuous and requires more evidence. However, I believe that attributing the O₂-activity exclusively to the ORR in FET experiments to be much more presumptuous at this point.

On the other hand, HOR/HER are facile in comparison to H₂O₂RR, particularly since adsorbed hydrogens species (*H) will begin to inhibit ORR and H₂O₂RR.¹⁵⁴ Therefore, floating electrodes will remain a great tool to benchmark these reactions. It might even be acceptable to assess ORR activity at higher overpotentials (+0.65 V_{VRHE}), assuming it is corrected with oxidative currents observed at (+1.2 V_{VRHE}). However this is probably too generous: we still need to see a floating electrode that can maintain ORR currents during a CA experiment, as well as replicating benchmark ORR activities using a different metal for the current collector (Ti for example), where it should be possible to compensate this increased resistance with conventional impedance methods.

5.2 Floating Electrode for 2e⁻ ORR

In principle, the FET for 2e⁻ ORR holds promise.²⁶ Floating on the electrolyte would provide an electrode with fast access to protons, and fast escape channels for H₂O₂ (assuming there is convection present in the electrolyte), while still accessing gas inputs directly from the facile gas phase. A fortunate surprise was that the FET was able to hold a 2e⁻ ORR current in CA experiments and that introducing a stir bar to

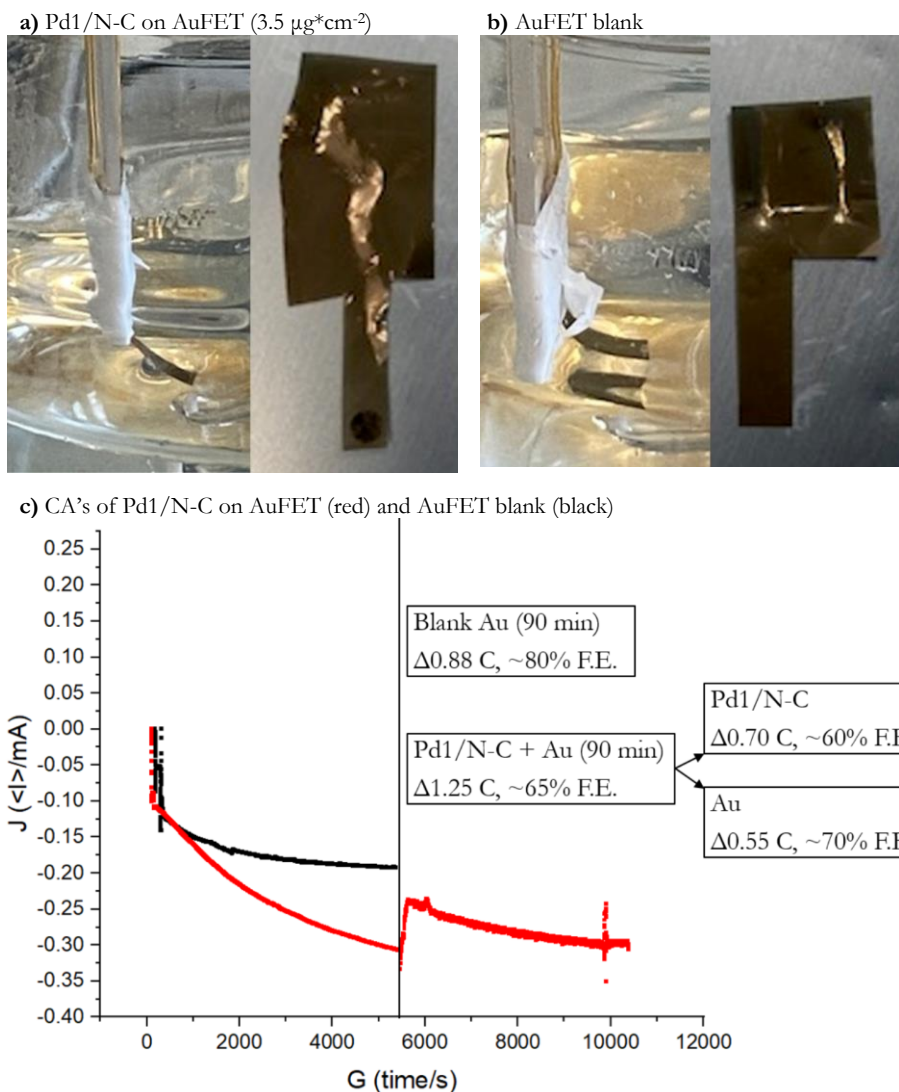


Figure 5.6: One of the initial experiments of the floating electrode technique for $2e^-$ ORR, where the Au-background is accounted for. Pd1/N-C ($3.5 \mu\text{g}\cdot\text{cm}^{-2}$) deposited on an AuFET (a), as well as a blank AuFET for background. CA's of these samples were conducted for 90 minutes at $+0.25 \text{ V}_{\text{RHE}}$ in 1 M HClO_4 at room temperature, where H_2O_2 was quantified with KMnO_4 titration. Actual measured current is depicted from the catalyst spot of roughly 0.031 cm^2 . In addition to the area of gold in contact with the electrolyte which was also roughly estimated based on the pictures (a+b). Deconvolution of ORR charge and H_2O_2 generated was attempted but subject to substantial error.

provide gentle convection in the electrolyte was enough to allow the H_2O_2 to escape the catalyst layer. One challenge became the Au background, since it is also active for $2e^-$ ORR. Initially, the Au background was estimated to be around $1.1 \text{ mA}\cdot\text{cm}^{-2}$

at $+0.2 V_{\text{VRHE}}$.¹⁵⁶ By roughly estimating the geometric area of Au in contact with the electrolyte, it could be assumed that Au was contributing to roughly $0.15 \text{ mA}\cdot\text{cm}^{-2}$. This was confirmed with a blank Au FE compared to an Au FE loaded with Pd1/N-C ($3.5 \mu\text{g}\cdot\text{cm}^{-2}$) summarized in Figure 5.6 (Pd1/N-C is from Chapter 4). Despite the abundance of Au relative to the catalyst spot (absolute loading of $0.11 \mu\text{g}$) the Au was only contributing to half the current. This made some sense, and with enough experiments (5-10 blanks, and 5-10 loaded with various amounts of Pd1/N-C), the data could be good enough to deconvolute the ORR activities provided by the Au and the catalyst spot. It was even observed that increasing contact to Au would increase the ORR current by the predictable amounts similar to $1.1 \text{ mA}\cdot\text{cm}^{-2}$ (Appendix A, Figure A.3). Unfortunately, repeated measures resulted in high variability, which could be expected to some degree. It became clear that the Au increases its contact with the electrolyte over time. It was eventually discovered that a drop of electrolyte ‘condensing’ above ‘sea level’ where the electrolyte was in contact with the electrode (Appendix A, Figure A.4). This suggests that the control to account for the Au background activity was futile because it was growing overtime during CA experiments. This discovery rendered the deconvolution of the O_2 -activity of the actual catalyst spot to be a completely hopeless endeavor.

This was validated by doing ‘true blank’ measurements where the Au-coated electrode was loaded with an inactive catalyst, a Vulcan carbon support ($3.5 \mu\text{g}\cdot\text{cm}^{-2}$), to ensure similar access to O_2 and H^+ to an actual floating electrode sample loaded with a catalyst of interest. In addition, I included TiFET samples, where the membrane is coated with titanium instead of gold, since titanium is inactive for ORR. The 2 weeks of work was supposed give me a strong understanding of my background (summarized in Appendix A, Figure A.5). Instead, it proved that the Au was more active than anticipated: up to $\sim 9.0 \text{ mA}\cdot\text{cm}^{-2}$ instead of $\sim 1.1 \text{ mA}\cdot\text{cm}^{-2}$ and that this activity was increasing at variable rates over time. The porous network within the PCTE membrane results in a high surface area interface.¹⁵⁷ Coating this interface with gold and in combination with increased contact to the electrolyte from capillary forces means that is very difficult to estimate the O_2 -activity attributed to the Au background. These pores are not like a fiber optic cable, they crisscross so that it is effectively a sponge, which explains why condensing drops form above electrolyte contact (Appendix A, Figure A.4).¹⁵⁷

These findings meant that titanium-coated floating electrodes were exclusively used for future experiments. The later onsets are attributed to the high-ohmic drops as well as the very low absolute loadings on catalysts with rather low activities (at least

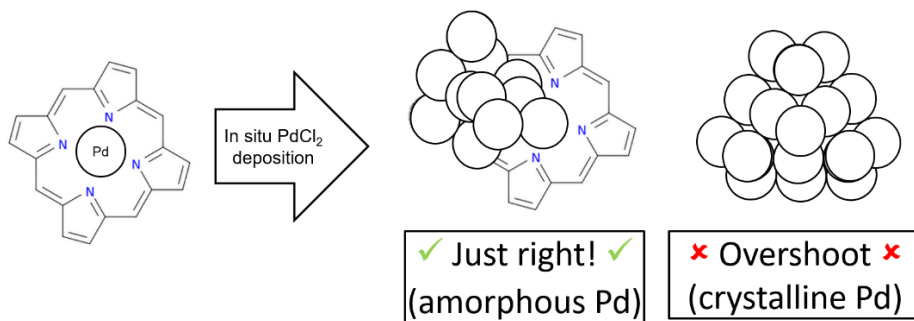


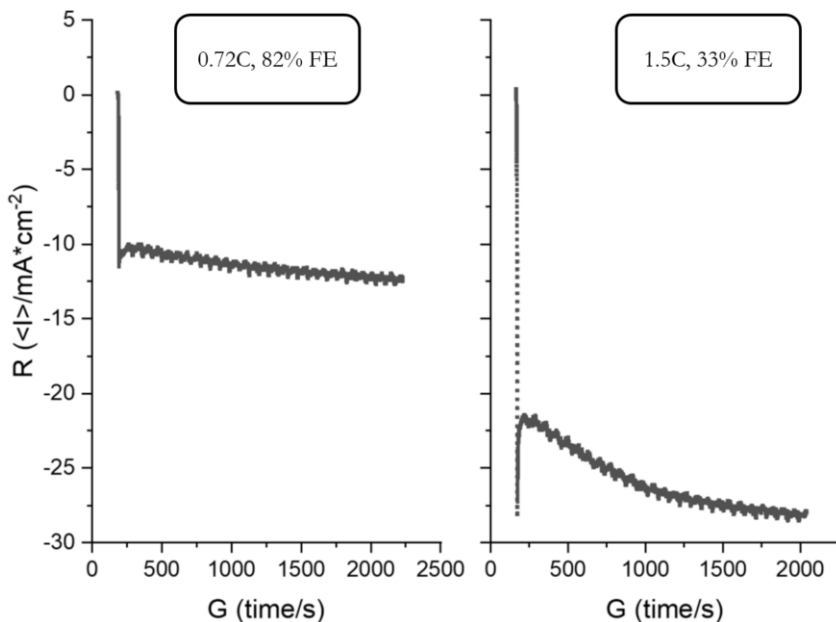
Figure 5.7: Schematic of the in situ electrodeposition of Pd^{2+} species onto potential PdN_x sites

compared to Pt performing $4e^-$ ORR and $\text{H}_2\text{O}_2\text{RR}$). Yet this sponge-effect also proved able to give electrolyte contact to the Au-wires, contributing Au-background activities on titanium-coated floating electrodes (TiFET). This was observed during a sanity check after cutting off the catalyst spot of an experiment, where there should be no electrochemical activity (Appendix A, Figure A.5). This resulted in moving the Au-wires much further up and using a piece of titanium metal as the current collector in direct contact with the floating electrode. These experiments will be discussed in Chapter 6, Section 6.5.

5.3 Post-article investigations of Pd1/N-C

Wang et al. conducted an interesting investigation of in-situ electrodeposited Pd for $2e^-$ ORR in acidic conditions.¹⁵⁸ The electrodeposition of Pd on Vulcan in O_2 -saturated electrolyte allowed better control of smaller amorphous Pd^{2+} species that are selective for $2e^-$ ORR, where it is generally known that electrodeposition of Pd on carbon in N_2 -saturated electrolyte will quickly result in larger crystalline nanoparticles active for $4e^-$ ORR. One method for this electrodeposition was holding a potential (+0.1, +0.45, or +0.70 V_{VRHE}) in low amounts of PdCl_2 concentration (5.0 μM) for 10 minutes in the O_2 -saturated electrolyte. However, the downside to this amorphous Pd on Vulcan was its poor stability. Given the stability of the Pd1/N-C catalyst (Chapter 4), the in situ electrodeposition of amorphous Pd anchored on stable PdN_x sites could possibly solve these stability issues (Figure 5.7). In addition, amorphous Pd could be electrodeposited on the blank N-C hollow spheres (N-C) as a control, since this exceptionally hydrophobic carbon support is also speculated to attribute to Pd1/N-C's stability. After some trouble shooting, the electrodeposition method was adjusted for an FET electrode: the electrodeposition was held at +0.45 V_{VRHE} , for 20 seconds in 1.0 μM PdCl_2 . The lower duration and concentration are justified by the lower absolute catalyst loadings inherent on the FET. Before the PdCl_2 was added, the electrolyte was also first saturated with O_2 .

a) Pd1/N-C(AuFET) pre-deposition (left) and post-deposition (right)



b) N-C(AuFET) pre-deposition (left) and post-deposition (right)

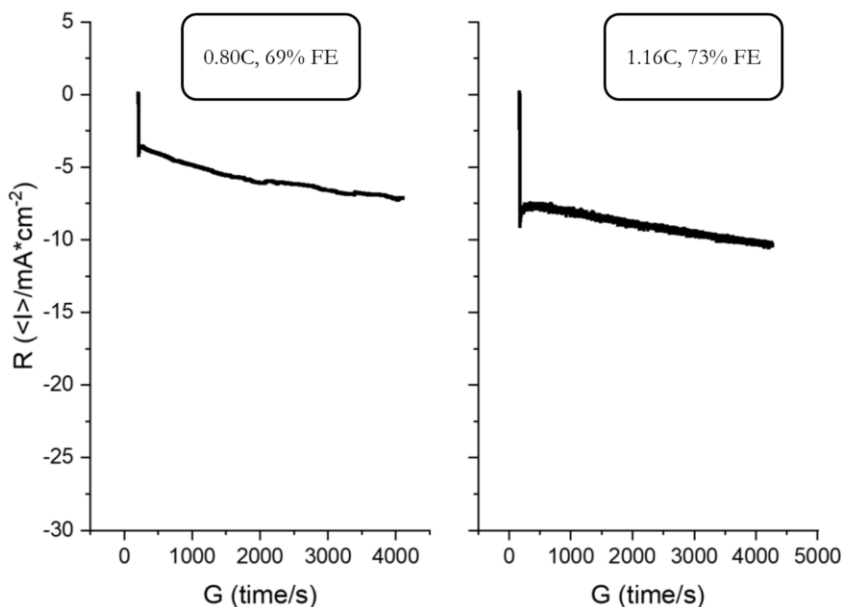


Figure 5.8: CA AuFET experiments (catalyst loadings = $\sim 3.5 \mu\text{g}^* \text{cm}^{-2}$, $+0.25 V_{\text{VRHE}}$) of Pd1/N-C (a) and N-C (b) catalysts before and after the in situ electrodeposition of Pd²⁺ species. In-situ electrodeposition was performed at $+0.45 V_{\text{VRHE}}$ in O₂-saturated electrolyte with $1.0 \mu\text{M}$ PdCl₂ for 20 seconds. The $\lambda_{\text{faradaic}}$ values are from quantified H₂O₂ concentrations determined by KMnO₄ titration and corrected by a factor of 0.8 to roughly counteract overestimation.

The in situ electrodeposition of Pd²⁺ species onto the Pd1/N-C resulted in an increase in total current (from 11 to 27 mA*cm⁻²) and a decrease in selectivity (82% to 33% $\lambda_{\text{faradaic}}$) (Figure 5.8, a). For N-C, the catalyst improved in both total current (from 6 to 9 mA*cm⁻²) and selectivity (69% to 73% $\lambda_{\text{faradaic}}$) (Figure 5.8, b). Interestingly, the post-electrodeposition N-C performance is similar to the pre-electrodeposition Pd1/N-C performance, suggesting that the N-C actually gained PdN_x sites during this in situ electrodeposition. Since the Pd1/N-C likely gained crystalline Pd agglomerates, the Pd1/N-C experiment was also attempted with even less concentration (0.1 μM PdCl₂), but yielded the similar results. This is interesting because this suggests that the first electrodeposited Pd²⁺ atom onto carbon is significantly less facile than the subsequent electrodeposited Pd²⁺ atoms, since the trends extrapolated from Wang et al.'s data would predict selectivities over 90% (Appendix A, Figure A.7). Lastly, the Pd1/N-C experiment was also attempted with a concentration 1.0 μM (dichloro(ethylenediamine)palladium(II)), to simulate concentrations of partially fragmented PdN_x site in solution. This had no noticeable effect on the Pd1/N-C performance, suggesting the ethylenediamine ligands inhibit the electrodeposition and agglomeration of Pd²⁺ atoms.

These findings have significant implications for the feasibility of utilizing SAC's for scaled up systems. Given how 20 ppt of Pd²⁺ atoms can ruin a Pd1/N-C catalysts performance in just 20 seconds, the likelihood of running such a catalyst for days seems unlikely. This is emphasized the fact that scaled up systems have issues with current collector corrosion, as well as anodic migration that results in transition metal concentrations in the ppt range.¹⁵⁹ It should be noted that these results are unreliable because they were performed on AuFET. Nevertheless, there were notable differences between how the Pd1/N-C and N-C catalysts responded to this in situ Pd²⁺ electrodeposition. It is therefore mentioned, especially since it has interesting implications.

5.4 Conclusion

The floating electrode technique (FET) remains a useful tool to provide catalyst layers with facile access to protons and gas inputs directly from the gas phase. This circumvents the mass transport limitations of RDE experiments, as well as the resource-intensive limitations of the intricate MEA experiments.³¹⁻³⁴ While the FET was successfully reproduced at DTU, the ORR activities never quite reached the benchmark performances published by Kucernak. However, a theory has been brought forth that suggests increasing H₂O₂ concentrations results in the overestimation of 4e⁻ ORR activity due to the likely emergence of H₂O₂RR activity during 'break in' procedures. This H₂O₂RR activity is demonstrated with RDE experiments that look very similar to some published FET experiments. In addition, it is possible that this H₂O₂RR is affecting other benchmark RDE experiments as well. It is generally understood that PtNi alloys result in the leaching of Ni^{x+} species. What is not commonly understood is that these leached Ni^{x+} species can subsequently electrodeposit onto the carbon support, where it could result in a

catalyst site that generates H_2O_2 , which would in turn contribute to $\text{H}_2\text{O}_2\text{RR}$ activity of the Pt catalyst, particularly affecting onset performances.

Despite not being able to hold a $4e^-$ ORR current at $+0.6 \text{ V}_{\text{VRHE}}$ for CA experiments, it was a very fortunate surprise to discover that the FET could hold a $2e^-$ ORR current at $+0.25 \text{ V}_{\text{VRHE}}$ even with Ti-coated floating electrodes. This chapter teaches a valuable lesson on how important it is to not underestimate your background contributions in electrochemical measurements because they can be very hard to account for. I personally will try to avoid measurements with possible background activities as often as I can in the future: the complications it provides will likely not exceed the benefits compared to alternative methods.

The in situ Pd^{2+} electrodeposition experiments on Pd1/N-C and N-C catalysts have some interesting implications on the stability of M-N/C catalysts for $2e^-$ ORR. Before these experiments, I would probably have speculated that the electrodeposition of metals only occurs in inert N_2 -saturated electrolytes, and would not be able to compete with ORR. However, it has become clear that the PdN_x sites are very sensitive to Pd^{2+} electrodeposition, which effectively destroy the catalyst's selectivity for $2e^-$ ORR, in just 20 seconds of exposure to trace concentrations (~ 20 ppt Pd^{2+}), and this is during ORR operations. This provides further insights of degradation mechanisms, particularly of agglomeration of Pd1/N-C during extended durations of $2e^-$ ORR operations. In addition, the improved performance of the blank N-C catalysts after the Pd^{2+} electrodeposition treatment also has significant implications. There are scaled up systems using metal-free carbon catalysts, which can possibly be accumulating MN_x sites active for $2e^-$ ORR during extended operations.^{28,160,161}

Chapter 6

Single Atom Catalysts of Interest

This chapter will go over the majority of my work and results during the latter half of my PhD. Throughout this project, I had some ideas about some interesting M-N/C's worth testing, and wanted to test them in the novel FET method I had spent so long developing. As we have already discussed, FET provides the catalyst with the 'ideal conditions' particularly because the catalyst is not limited by the lack of O₂ at higher overpotentials necessary for scaled-up operations. As also discussed, the escape channels for the electroproduced H₂O₂ are also important. Sparked by this idea, I led this project where I was responsible for the experimental planning, synthesis, electrochemical testing and the initial characterization. The help of Thomas Smitshuysen and Sofie Colding-Jørgensen was essential for extensive characterizations. Thomas facilitated the EXAFS measurements at Lund as well as provided the data analysis. Sofie provided HAADF-STEM and EDS measurements of catalyst samples as well.

6.1 Experimental Strategy

As we have seen in Chapter 4, properly testing single atom catalysts requires a lot of time and resources. At the same time however, we want to test as many catalysts as possible. I therefore adopted a systematic process to better utilize my time and resources. This involved screening and testing a wide range of catalysts and their variations, and then focusing time and resources on the best ones. Figure 6.1 illustrates the overall experimental strategy of how I investigated various single atom catalysts. It is organized in 4 phases: (1) determining catalysts of interest; (2) catalyst synthesis, (3) initial testing and characterization; (4) extensive testing and characterization.

Determining the catalysts of interest includes the relevant metals and ease of synthesis. Experimental and DFT calculations from the literature narrows the scope of promising catalysts. In addition, the catalysts of interest need to have a relatively simple synthesis method, otherwise a systematic investigation would be limited.

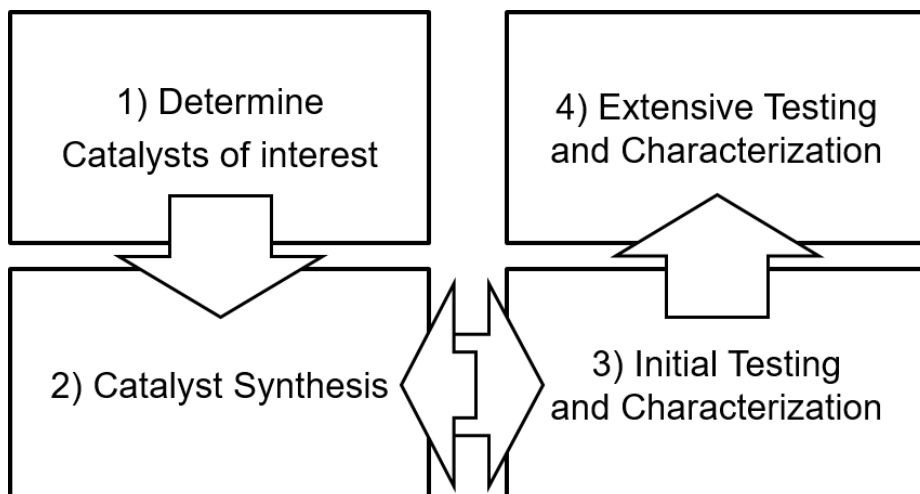


Figure 6.1: Schematic of the overall experimental strategy, where the pool of potential catalysts gets smaller after each phase in order to most optimally utilize time and resources.

These catalysts of interest are then synthesized. This involves tuning many different parameters including precursor ratios, ramp up time, and different metal precursors. The synthesized catalysts go through an initial screening. They are electrochemically tested on the RRDE to get a general notion of their activity and selectivity. Relatively quick and cheap characterizations are then performed to get a general idea of the metal content and if there are any nanoparticle agglomerates, where XPS provides a quick assessment of the elemental composition of the surface, while XRD will detect metals that have agglomerated into nanoparticles. This also enables quick feedback to guide the adjustments of the next synthesis procedures (Figure 6.1, steps 2+3).

The best catalysts will then be thoroughly analyzed. They will be electrochemically tested on both a MEA and FET set-ups to benchmark their performance representative of operating conditions. As well as extensively characterized with EXAFS, HAADF-STEM, EDS, and ICP-MS. EXAFS will provide the coordination environments of the metal species of the entire sample. HAADF-STEM will evidence atomically dispersed sites. ICP-MS will provide the total metal content of the catalyst. These tests and characterizations are both time and resource consuming and therefore are preserved for the best performing catalysts from the initial testing.

6.2 Determining Catalysts of Interest

Determining the catalysts of interest, specifically carbon-based single atom catalysts, was based on two main criteria: ease of synthesis and catalysts with decent performances from the literature. High temperature pyrolysis ($>800\text{ }^{\circ}\text{C}$) is the most

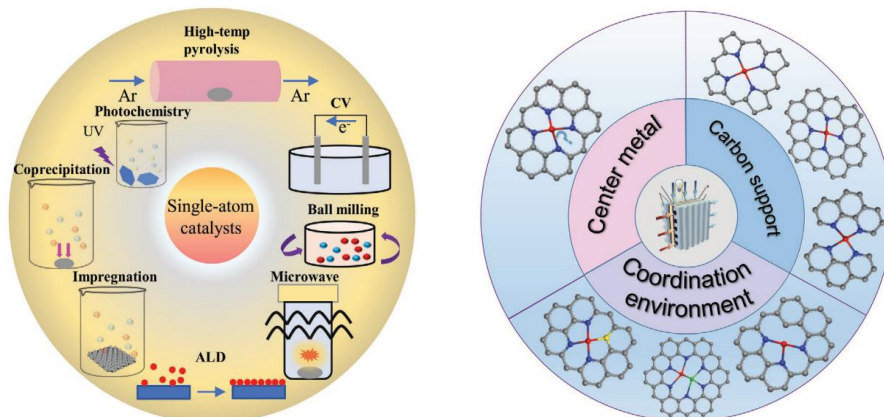


Figure 6.2: (left) Schematic of various synthesis strategies that can be mixed and matched for M-N/C synthesis. (right) Illustration summarizing the different strategies used to adjust an M-N/C's activity and selectivity through electronic effects. From ⁶⁹

common synthetic strategy, but it becomes difficult to control the structure of the MN_x sites because complex reactions start to occur. Therefore, lower-temperature strategies are more appealing. Wet-impregnation methods on already pyrolyzed carbon supports that can even be assisted with UV energy (photochemistry) or coprecipitates (metal-chelating organic ligands). The initial synthesis strategies I pursued included wet-impregnation of species on to various carbon supports including commercial carbon blacks, pyrolyzed citrate precursors, GO solutions, and C_3N_4 . These failed to be active for reasons unknown. The most notable is summarized in Figure B.1 (Appendix B), where Mg-catalyzed pyrolysis formed a triazine- C_3N_4 , that was then wet impregnated by allyl-Pd dimer precursors, followed by an additional mild pyrolysis step (300 °C). It became clear that despite some literature's claims, C_3N_4 does not adequately conduct electricity to be used as a carbon support for electrochemistry. Figure 6.2 (left) summarizes various strategies of which single atom catalysts can be synthesized. Given the facilities available at DTU, methods based on ball milling and high temperature pyrolysis became the decidedly most appropriate for my purposes. This is because the first single atom catalyst I successfully synthesized, that actually had good $2e^-$ ORR activity came from the article 'Enabling Direct H_2O_2 Production in Acidic Media through Rational Design of Transition Metal Single Atom Catalyst' published by Gao et al.

Figure 6.3 (a, b) presents Gao et al.'s various featured M-N/C's synthesized from transition metal acetates. Among these, the cobalt sample (Co-NC) had the best performance that was even validated in scaled-up conditions. This catalyst also had a quite simple synthesis: it involved three precursors (12g melamine, 2g L-alanine, 50mg transition metal acetate), two dry mixing steps in an agate ball mill, one wet milling step, two pyrolysis steps, and one acid washing step.

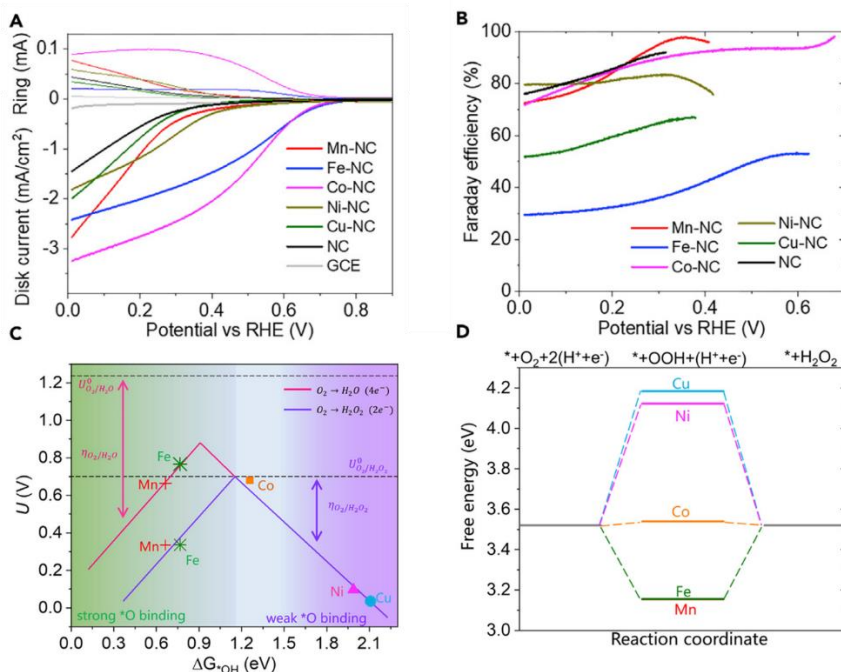


Figure 6.3: Results from Gao et al. (a) RRDE cathodic sweeps of M-N/C catalysts in O₂-saturated electrolyte (0.1M HClO₄) and (b) corresponding oxygen-normalized H₂O₂ selectivity (λ_{O_2}). (c) Activity-volcano plots for 4e⁻ and 2e⁻ ORR of MN₄ sites with N-pyrrolic coordinations. (d) Free energy diagram for 2e⁻ ORR of MN₄ sites (U = +0.7 V_{VRHE}). From 77

From this synthesis, Figure 6.3 (c) shows us a very different volcano plot from the one introduced in Chapter 2 (Figure 2.9, right). A CoN_x site was originally understood to be strong-binding (e.g. low values of ΔE_{OH}), and therefore optimal for 4e⁻ ORR activity. However, Gao et al. propose that the anchoring nitrogens in the CoN_x site are pyrrolic instead of pyridinic (Appendix B, Figure B.2). This coordination environment (Figure 6.2, right) causes an electronic shift in the CoN_x site to be weaker-binding (e.g. higher values of ΔE_{OH}), and therefore optimal for 2e⁻ ORR activity (Figure 6.3, d). In essence, it takes the opposite strategy of the Pd-1/N-C catalyst presented in Chapter 4. Rather than making an inactive but selective catalyst more active (making PdN_x sites stronger binding), Gao et al. makes an active catalyst less active and more selective (making CoN_x sites weaker binding).

However, it is unclear whether Gao et al.'s DFT calculations account for electron withdrawing moieties (e.g. graphitic nitrogen) which are hypothesized to make MN_x sites stronger binding. Taking into account the volcano plots presented in Figure 2.9, Figure 4.5, and Figure 6.3, I thought it would be interesting to extend this synthesis method to Iridium, Platinum and Palladium. Iridium was selected because IrN_x sites are theorized to be strong-binding like Cobalt (CoN_x sites). In addition, despite being weak binding, Platinum and Palladium are included due to their previous successes albeit in with different strategies. At a minimum, Pt and Pd could possibly validate a

hypothesis. Assuming the nitrogen peaks look the same in the XPS results, we can potentially be testing variable metal centers while the carbon support and coordination environment variables (Figure 6.2, right) are decently controlled for, since coordination environments are typically governed by pyrolysis temperature.^{162,163} However, M-N bond energies are likely to deviate depending on the metal center. This means that assuming similar carbon supports and coordination environments between different metal precursors is a large enough assumption to warrant some form of evidenced confirmation at some point.

6.3 Catalyst Synthesis

Chorkendorff and Niemantsverdriet describe the complexities of catalysis synthesis as a mixture of science, art and wisdom.^{35,164,165} Science because some of the underlying chemistries involved are known. Art because some of the underlying chemistries involved are not known. Wisdom because inexplicable failures from many trials will guide the next. This has also been my experience. While the synthesis method is fairly straightforward, there were little details that proved to be essential for a successful M-N/C product. This section will go over some of those details, and later be confirmed in the subsequent section (6.4 Initial Testing and Characterization).

The synthesis procedure was adopted from Gao et al. with a some modifications.⁷⁷ First, 0.4 g L-alanine, and 15 mg metal precursor were milled in an agate mortar. Then, 2.5 g melamine added and the powder was dry-mixed in an agate ball mill (precursors presented in Figure 6.4). Then 15ml of ethanol and 3 ml of HCl were added and milled in an agate mortar and pestle until mostly dry, and left to dry overnight. The mixture was dry-mixed again in the ball mill before being pyrolyzed in N₂ atmosphere. The pyrolysis ramp-up procedure was from room temperature to 600 °C at a ramping rate of 2.5 °C /min, then hold at 600 °C for 120 min, then ramp to 900 °C at 5 °C /min and hold for 90 min, where then the furnace was naturally cooled down to room temperature. The obtained black solid materials were milled in an agate mortar and pestle and then washed by 2M HCl aqueous solution at 80 °C for 24 h under stirring to remove metal particles. The acid-washed materials were dried and then annealed again in N₂ at 800°C for 1 h at a heating rate of 10 °C/min to recover the crystallinity. Figure 6.4 summarizes this synthesis process where metal precursors were not limited to transition metal acetates, particularly since these precious metal acetates were not available and some not necessarily monoatomic metal species. Acetylacetonates were available (PdAcac, PtAcac, IrAcac), in addition various chloro-Pt precursors (PtCl₂, PtCl₄, H₂PtCl₆,) were investigated, as well as Zeise's dimer (zPt₂).

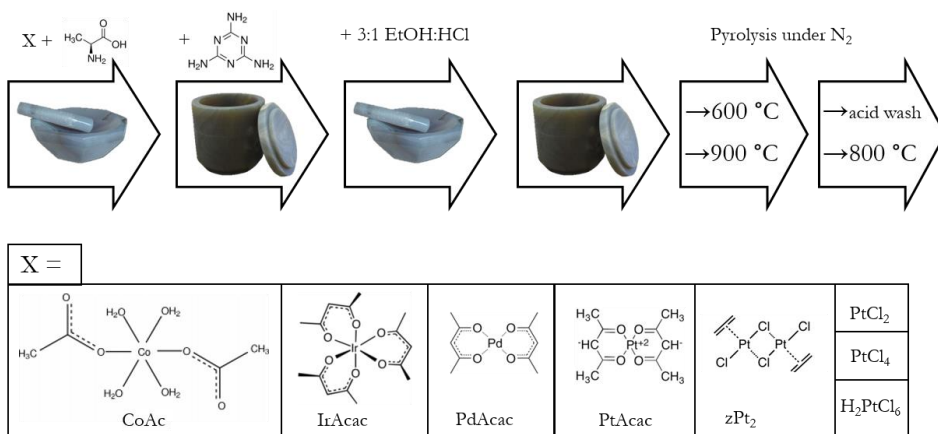


Figure 6.4: precursors (12g melamine, 2g L-alanine, 50mg transition metal acetate), 2 dry mixing steps in an agate ball mill, 1 wet milling step, 2 pyrolysis steps, and 1 acid washing step.

The melamine is the most abundant precursor in the dry mixing step. Reproducibility of this synthesis improved when the initial milling step was added to ensure that sufficient metal precursor was in local contact with the chelating L-alanine. This likely formed a cobalt-alanine in the brief wet-chemistry step (where 3:1ml EtOH:HCl is added, milled, and left to dry overnight). Cobalt-alanine has been known to catalyze polymerization between functionalized benzene rings, with a 96% yield for 1h in EtOH.¹⁶⁶ I speculate some of this chemistry was relevant during this time. In addition, cobalt-alanine has two 5-membered ring-ligands that are reminiscent of a pyrrole-coordinated CoN_x site (Appendix B, Figure B.3).

It is well understood how melamine polymerizes during pyrolyzation in inert atmospheres (N₂ or Ar).^{167–169} In the first stage of heating to 600 °C, the primary amine groups of the melamine and alanine will begin nucleophilic attacks on electrophilic localities to form C₃N₄. However, such nucleophilic attacks can also target other electrophilic species if introduced into the mixture, such as carbocations from partially decomposed precursors or metallic cations. Gao et al. support this in their previous works, specifically with XPS analysis of Ni and S co-doped C₃N₄ after heating at 600 °C.¹⁷⁰ The synthetic pathways involved during this pyrolysis ramp-up are summarized in Figure 6.5. The second stage of heating to 900 °C causes the graphitization of the melon/C₃N₄ polymers, where a substantial amount of decomposition occurs and cyano-carbonaceous products are released. A great deal of mass is lost during this process, where the final product is roughly 1% of the total mass of the initial precursors. During this pyrolysis, it is important to keep the N₂ gas flow very low to avoid sublimation of the precursors.

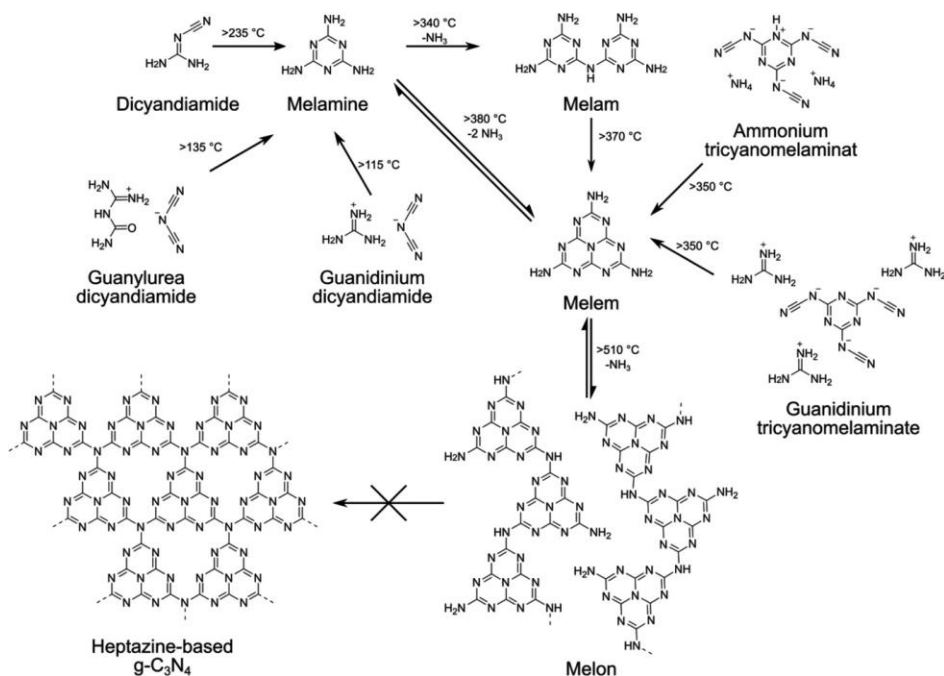


Figure 6.5: Synthetic pathways to the carbon nitride family of materials, where approximate reaction onset temperatures were based on variable-temperature XRD. From¹⁶⁸

Selecting suitable metal precursors that catered to the various processes involved in this procedure required an attention to details. Two of those details were namely the metals solubility in 3:1 EtOH:HCl (wet chemistry step) and the metal precursors stability during the pyrolysis ramp up to $600\text{ }^\circ\text{C}$. Poor solubility means the wet chemistry has little efficacy, the next section will discuss how important this step potentially is. Poor stability during pyrolysis ramp up suggests that the metals can start to agglomerate before the primary amines can perform nucleophilic attacks ($>500\text{ }^\circ\text{C}$) on the single metallic cations. This would result in nanoparticles rather than MN_x sites on the final powder. The different Pt-containing precursors that were explored (PtAcac, PtCl_2 , PtCl_4 , H_2PtCl_6 , zPt_2 , PtS_2 , PtAn) can potentially provide information in this regard. In regards to M-N/C for acidic 2e- ORR, there is evidence that higher metal loadings (specifically Co) can lead to agglomeration and compromised selectivity.⁸⁰ Therefore, molar ratios between the metal precursors and the other precursors (L-alanine and melamine) was somewhat explored: metal:alanine ranged from 1:75-250 and metal:melamine ranged from 1:300-1200. However exploring between different precursor samples is likely futile, given the solubility and stability parameters would confound this analysis. The most notable synthesized catalyst powders worthy of discussion are summarized in Table 6.1.

Table 6.1: Various synthesized carbon powders based on cobalt, iridium, platinum and palladium with precursors used as listed. In addition, specific activity ($\text{mA}_{\text{H}_2\text{O}_2} \cdot \text{cm}^{-2}$) and selectivity (%) at operation potentials (+0.25V_{VRHE}).

Sample	Metal precursor		L-alanine	Melamine	EtOH	HCl	RRDE (+0.25V _{VRHE})		
	Name	mg	g	g	ml	ml	$\text{mA}_{\text{H}_2\text{O}_2}^*$ cm^{-2}	$\lambda_{\text{Faradaic}}$ c (%)	λ_{O_2} (%)
CoSAC2	CoAc	14.1	0.58	3.28	4.2	0.8	1.9	61	76
CoSAC2.2							1.35	44	61
IrSAC1	IrAcac	7.3	0.314	2.26	2.2	0.4	2.05	79	88
IrSAC1.2							1.25	63	77
IrSAC3	IrAcac	13	0.392	2.34	3.9	0.8	1.65	64	78
PtCl2	PtCl2	7.5	0.2	1.16	2.3	0.5	1.00	53	69
PtCl4(1)	PtCl4	18.5	0.388	2.42	5.6	1.1	1.94	67	80
PtCl6	PtCl6	28	0.47	2.86	8.4	1.7	0.58	32	48
PtAcac1	PtAcac	18.9	0.98	4.75	5.7	1.1	0.88	58	74
PtAcac1.2							0.75	40	57
PtCl4(2.1)	PtCl4	24.6	1.01	6.04	7.4	1.5	0.48	38	55
PtCl4(2.2)	PtCl4						0.3	17	30
PtCl4(4.1)	PtCl4	12	0.5	3	3.6	0.7	0.4	44	62
PtCl4(4.2)							0.45	35	51
PtCl4(5)	PtCl4	16	0.4	2.4	4.8	1.0	0.43	19	32
PtCl4(6)	PtCl4	17.4	0.44	2.48	5.2	1.1	2.3	92	96
zPt2	zPt2	25.7	0.67	3.97	7.7	1.5	1.04	65	79
PtAlan	PtAlan	24	1	6	7.2	1.4	0.78	36	53
IrSAC4	IrAcac	16.7	0.765	3.96	5.0	1.0	1.28	75	86
IrSAC4.2							0.57	67	80
IrSAC5	IrAcac	11.3	0.395	2.56	3.4	0.7	0.85	54	70
IrSAC6	IrAcac	7.3	0.350	1.87	2.2	0.4	1.3	74	85
PdAcac1	PdAcac	8	0.283	1.54	2.4	0.5	1.68	80	89
PdAcac2	PdAcac	6.6	0.243	1.38	2.0	0.4	1.23	75	85
PdAcac3	PdAcac	4	0.165	0.825	1.2	0.2	1.01	53	69
CoSAC1	CoAc	11	0.25	1.3	3.3	0.7	2.0	65	78
CoSAC3	CoAc	10.7	0.399	2.38	3.2	0.6	2.1	62	76

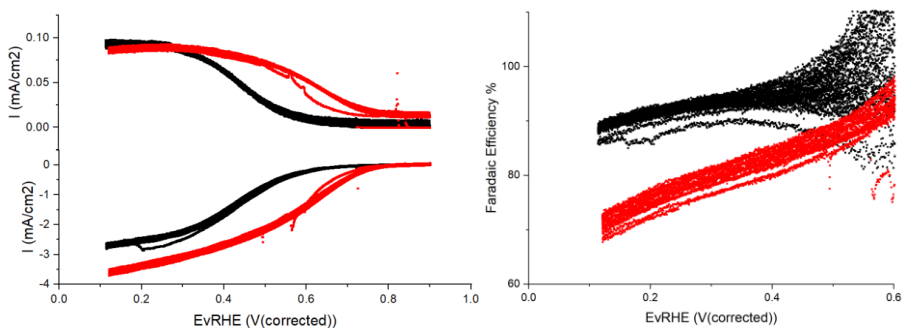


Figure 6.6: ORR performance of CoSAC1 (red) and IrSAC1 (black). (left) RRDE cathodic sweeps and resulting selectivity. H_2O_2 selectivity calculations were oxygen-normalized (λ_{O_2}). Measurements in O_2 -saturated 0.1 M $HClO_4$ with a rotating rate of 1600 rpm at room temperature.

6.4 Initial Testing and Characterizations

Among the twenty-seven catalyst samples (Table 6.1), four were cobalt-based, seven were iridium-based, thirteen were platinum-based, and three were palladium-based. The RRDE performances were assessed based on specific activity ($mA_{H_2O_2} \cdot cm^{-2}$) and selectivity ($\lambda_{Faradaic}$ and λ_{O_2}) at operation potentials ($+0.25V_{VRHE}$). While assessing performance at $+0.25V_{VRHE}$ might not necessarily be fair to all catalysts, it is also important to see how catalysts perform at higher overpotentials and industrially-relevant currents. I concluded that $+0.25V_{VRHE}$ as a fair compromise, similarly to how the Pd1/N-C catalyst was assessed in Chapter 4. In addition, the mass loading of these RDE measurements is $75 (\mu g \cdot cm^{-2})$ unless otherwise noted.

The state-of-the-art single atom cobalt catalyst (CoSAC) was successfully reproduced from the literature (Table 6.1, CoSAC 1, 2.1, 2.2, 3).⁷⁷ CoSAC1 had an activity of $\sim 2.0 (mA_{H_2O_2} \cdot cm^{-2})$ and a faradaic efficiency of 65% ($\lambda_{Faradaic} = 58\%$, $\lambda_{O_2} = 78\%$), (presented in Figure 6.6, red). Similarly, Gao et al. reports a performance of $\sim 2.1 (mA_{H_2O_2} \cdot cm^{-2})$ and a faradaic efficiency of 75% ($\lambda_{Faradaic} = 75\%$, $\lambda_{O_2} = 85\%$). CoSAC2 and CoSAC2.2 came from the same dry-mixed precursor batch with one distinction: some powder was left aside where the wet chemistry step (milling in 3:1 EtOH:HCl) was skipped and went directly to pyrolysis, and resulted in the CoSAC2.2 sample. As can be seen, CoSAC2 has similar performances to CoSAC1, with $\sim 1.9 (mA_{H_2O_2} \cdot cm^{-2})$ and a faradaic efficiency of 61% ($\lambda_{Faradaic} = 61\%$, $\lambda_{O_2} = 76\%$). In contrast, CoSAC2.2 had significantly worse performances in comparison: $\sim 1.35 (mA_{H_2O_2} \cdot cm^{-2})$ and a faradaic efficiency of 44% ($\lambda_{Faradaic} = 44\%$, $\lambda_{O_2} = 61\%$). This stresses the importance of the wet chemistry step, where cobalt alanine is likely formed and the precursors likely polymerize to some extent (Appendix B, Figure B.3).¹⁶⁶ CoSAC3 was among one of the final samples prepared and further

demonstrates the reproducibility of the method ($\sim 2.1 \text{ mA}_{\text{H}_2\text{O}_2} \cdot \text{cm}^{-2}$, $\lambda_{\text{Faradaic}} = 62\%$, $\lambda_{\text{O}_2} = 76\%$). The CV's of CoSAC2.2 and CoSAC3 can be found in Appendix B (Figure B.4). In addition, it is noted that the XPS revealed a 3.8 wt.% of cobalt in CoSAC1, while Gao et al. reported 1.8 wt.% of cobalt. The precursor molar ratios of the precursors in CoSAC1 was 1:45:165 ($\text{mol}_{\text{metal}}:\text{mol}_{\text{L-alanine}}:\text{mol}_{\text{melamine}}$). As a result, the L-alanine, and melamine precursors were doubled in the subsequent batches: CoSAC2-2.2 and CoSAC3 had molar ratios of 1:80:325 and 1:75:310 ($\text{mol}_{\text{metal}}:\text{mol}_{\text{L-alanine}}:\text{mol}_{\text{melamine}}$), respectively. The XPS consequently measured lower amounts of cobalt: CoSAC2 had a 3.2 wt.%, CoSAC3 had a 2.7 wt.% and CoSAC2.2 had a 1.7 wt.%. Interestingly, the CoSAC2.2 had lower amounts of cobalt detected, which further emphasizes the wet chemistry step. The lower amounts of cobalt detected in CoSAC2.2 can be plausibly explained with the following theory: the cobalt is more likely to agglomerate during pyrolysis, where these agglomerates are leached out in the subsequent acid washing step. However, such agglomerations would have to be quite small and amorphous since the XRD analysis of CoSAC1+2.2+3 show little to no signs of cobalt nanoparticles (Appendix B, Figure B.31).

The iridium single atom catalysts (IrSAC) used iridium acetylacetonate (IrAcac) as a precursor (Table 6.1, IrSAC 1, 1.2, 3, 4, 4.2, 5, 6). The IrSAC's performed well, just like the CoSAC's, which starts to validate the strong-binding theory around the IrN_x and CoN_x sites. Figure 6.6 (black) presents the RRDE performance IrSAC1: $\sim 2.05 \text{ mA}_{\text{H}_2\text{O}_2} \cdot \text{cm}^{-2}$, $\lambda_{\text{Faradaic}} = 79\%$, $\lambda_{\text{O}_2} = 88\%$. IrSAC1 skipped the final steps of the synthesis (acid wash and second 800°C), while IrSAC1.2 is the IrSAC1 sample after the final steps of the synthesis, resulting in a notably lower performance: $\sim 1.25 \text{ mA}_{\text{H}_2\text{O}_2} \cdot \text{cm}^{-2}$, $\lambda_{\text{Faradaic}} = 63\%$, $\lambda_{\text{O}_2} = 77\%$. It is assumed that the acid washing step is used to leech out any potential nanoparticles that may have formed, but metallic iridium cannot be leached out with HCl like metallic cobalt can. As a result, the final steps were omitted from the remaining IrSAC samples (IrSAC 3, 4, 4.2, 5, 6). In addition, XPS detected Pt in the IrSAC1 sample (0.9 wt.% Ir and 2.8 wt.% Pt) which was interestingly not detected in the IrSAC1.2 sample (2.5 wt.% Ir). Hence more iridium samples were prepared. IrSAC3 yielded similar results ($\sim 1.65 \text{ mA}_{\text{H}_2\text{O}_2} \cdot \text{cm}^{-2}$, $\lambda_{\text{Faradaic}} = 63\%$, $\lambda_{\text{O}_2} = 78\%$) without any Pt detected (XPS: 0.5 wt.% Ir). Both IrSAC4 and IrSAC4.2 resulted in lower performance, however IrSAC4.2 was notably worse: (IrSAC4: $\sim 1.28 \text{ mA}_{\text{H}_2\text{O}_2} \cdot \text{cm}^{-2}$, $\lambda_{\text{Faradaic}} = 75\%$, $\lambda_{\text{O}_2} = 86\%$) (IrSAC4.2: $\sim 0.57 \text{ mA}_{\text{H}_2\text{O}_2} \cdot \text{cm}^{-2}$, $\lambda_{\text{Faradaic}} = 67\%$, $\lambda_{\text{O}_2} = 80\%$). It is unclear why these performances were notably different. My speculation is the sample in 4.2 was not properly milled during the wet-chemistry step. Another speculation is the sample was not dry enough before pyrolysis. This could perhaps explain their lower Ir content detected in XPS: (IrSAC4: 0.2 wt.% Ir) (IrSAC4.2: 0.2 wt.% Ir). Nevertheless, lower Ir content validates the IrSAC4 sample. The CV's of IrSAC4 and IrSAC4.2 can be found in Appendix B (Figure B.5).

IrSAC3 had a molar ratio of 1:165:700 ($\text{mol}_{\text{metal}}:\text{mol}_{\text{L-alanine}}:\text{mol}_{\text{melamine}}$), while IrSAC4 only had a molar ratio of 1:250:925 ($\text{mol}_{\text{metal}}:\text{mol}_{\text{L-alanine}}:\text{mol}_{\text{melamine}}$). Yet, manipulating the molar ratios of the precursors in order to achieve a higher Ir loading also proved

to be ineffective. IrSAC5 had a molar ratio of 1:190:881 ($\text{mol}_{\text{metal}}:\text{mol}_{\text{L-alanine}}:\text{mol}_{\text{melamine}}$) with a poor performance similar to IrSAC4.2: (IrSAC5: $\sim 0.85 \text{ mA}_{\text{H}_2\text{O}_2} \cdot \text{cm}^{-2}$, $\lambda_{\text{Faradaic}} = 54\%$, $\lambda_{\text{O}_2} = 70\%$). IrSAC6 successfully reproduced the average performance of IrSAC4: (IrSAC6: $\sim 1.30 \text{ mA}_{\text{H}_2\text{O}_2} \cdot \text{cm}^{-2}$, $\lambda_{\text{Faradaic}} = 74\%$, $\lambda_{\text{O}_2} = 85\%$, XPS: 0.7 wt.% Ir). The only explanation I have for IrSAC6's performance is one that validates my previous speculations: I was extra thorough and attentive during this synthesis. The CV's of IrSAC5 and IrSAC6 can be found in Appendix B (Figure B.5). Unfortunately, I also speculated that the notable performance of IrSAC1 was attributed to the presence of Pt, which could be potentially PtN_x sites. As we will see next, I spent a lot of time exploring possible PtSAC samples.

The initial platinum single atom catalysts (PtSAC) that were investigated used platinum acetylacetonate (PtAcac) as a precursor. PtAcac1 had an activity of $\sim 0.88 \text{ (mA}_{\text{H}_2\text{O}_2} \cdot \text{cm}^{-2})$ and a faradaic efficiency of 58% ($\lambda_{\text{Faradaic}} = 58\%$, $\lambda_{\text{O}_2} = 74\%$) where it skipped the final steps of the synthesis (acid wash and second 800 °C). PtAcac1.2 is the PtAcac1 sample after the final steps of the synthesis, resulting in lower performance: $\sim 0.75 \text{ (mA}_{\text{H}_2\text{O}_2} \cdot \text{cm}^{-2})$ and a faradaic efficiency of 40% ($\lambda_{\text{Faradaic}} = 40\%$, $\lambda_{\text{O}_2} = 57\%$). The CV's of PtAcac1 and PtAcac1.2 can be found in Appendix B (Figure B.6). PtAcac1 and PtAcac1.2 were synthesized around the same time as IrSAC1 and IrSAC1.2, where I came to the same conclusions in regards to omitting the final steps of acid washing and the second pyrolysis step.

The PtAcac samples had notably lower activity, which is to be expected from a catalyst potential PtN_x sites, but the low selectivity is not be expected (refer back to Chapter 2, Figure 2.9). This poor selectivity is likely due to the fact that the precursors are not stable and the metal species agglomerate before the amines can start to properly react at $\sim 500\text{-}600^\circ\text{C}$. This is supported by Sahu et al.'s thermal gravimetric analysis, where they measured the mass loss of various Pt precursors as they are heated up to 600°C ($10^\circ\text{C} \cdot \text{min}^{-1}$) in an inert N₂ atmosphere.¹⁷¹ The precursors that were tested were PtAcac, PtCl₂, PtCl₄, and H₂PtCl₆ (summarized by Figure B.7, Appendix B). PtAcac (originally 30-40 wt.% Pt) will start to degrade at $\sim 200\text{-}250^\circ\text{C}$ with only 30 %wt. remaining by 250°C , suggesting the acetylacetonate groups have decomposed, leaving behind metallic platinum that has likely agglomerated. Similarly, PtCl₂ (73 wt.% Pt) starts to degrade at $\sim 400\text{-}500^\circ\text{C}$ with only ~ 75 wt.% remaining by 500°C , while PtCl₄, and H₂PtCl₆ degrade nearly immediately but maintain some Cl ligands up until $\sim 450\text{-}525^\circ\text{C}$.

In addition, among the chloroplatinum precursors, there are differences in solubility. PtCl₂ is not soluble in H₂O or EtOH, and requires some HCl to dissolve in solution. In contrast, H₂PtCl₆ is readily soluble in H₂O or EtOH without HCl, while PtCl₄, is somewhere between PtCl₂ and H₂PtCl₆ (but closer to H₂PtCl₆). With variable pyrolysis stability and solubility during the wet chemistry step (3:1 EtOH:HCl), investigating these various chloroplatinum precursors (PtCl₂, PtCl₄, H₂PtCl₆) could provide further insights to what could potentially be occurring during the synthesis. In addition, Pt-alanine (PtAlan) was prepared, to potentially provide additional insights to what could be occurring during the wet chemistry step (special thanks to

Rokas Sažinas for his knowledge in chemical synthesis and the Russian language that made the preparation of Pt-alanine possible).^{172,173} Taken from Dunlop's Thesis (which is directly translated from Volshtein's Russian article), Pt-alanine was prepared as follows: 'One mole of potassium tetrachloroplatinate (II) K₂ [PtCl₄], was treated with 4 moles of alanine and KOH and heated one hour on a steam bath. This was followed by the addition of 2 moles of M HCl. Upon heating 2 to 3 hours this gave, upon cooling, a colorless precipitate of [PtA₂] in 30% yield (where A=alanine residue).' However, it should be noted that my Pt-alanine precipitate was not verified with NMR analysis. The key point to all of this is stressing the fact that the formation of PtAlan is not nearly as facile compared to the formation of CoAlan (Appendix B, Figure B.3). Therefore, synthesizing PtAlan as a precursor could provide insights along with the varying solubility of the chloroplatinum precursors.

PtAlan, PtCl₂ and H₂PtCl₆ exhibited poor performances similar to that of the PtAcac samples (CV's summarized by Figure B.8, Appendix B). PtAlan had an activity of ~0.78 (mA_{H₂O₂}*cm⁻²) and a faradaic efficiency of 36% ($\lambda_{\text{Faradaic}} = 36\%$, $\lambda_{\text{O}_2} = 69\%$). Given how essential the wet chemistry step was for the CoSAC samples, this came as a surprise. It is possible that PtAlan is not particularly soluble, since the Pt-N bonds can be quite stable in organometallic chemistry, this would result in agglomeration in later phases of the pyrolysis. Another possibility is that the Pt just facilitates de-ammonification (loss of -NH₂ functionalities into ammonia) of the organic precursors.^{174,175} This could also explain why the relatively exceptionally-soluble H₂PtCl₆ also yielded poor results: (~0.58 mA_{H₂O₂}*cm⁻², $\lambda_{\text{Faradaic}} = 32\%$, $\lambda_{\text{O}_2} = 48\%$). Perhaps unexpectedly, the least soluble species PtCl₂ had better activity: (~1.00 mA_{H₂O₂}*cm⁻², $\lambda_{\text{Faradaic}} = 53\%$, $\lambda_{\text{O}_2} = 69\%$). In contrast to cobalt, these results suggest that the Pt species should not be too involved during the wet chemistry step. However, PtCl₄ has yet to be mentioned because it seemed to be the most promising.

The first batch of PtCl₄ (known as PtCl₄(1) had a very good specific activity of ~1.95 mA_{H₂O₂}*cm⁻² with decent selectivity ($\lambda_{\text{Faradaic}} = 67\%$, $\lambda_{\text{O}_2} = 80\%$) which is comparable to the state-of-the-art CoSAC samples. This resulted in 5 more batches that were synthesized: PtCl₄(2.1), PtCl₄(2.2), PtCl₄(4), PtCl₄(5), PtCl₄(6). One detail was that the high-performing PtCl₄(1) had a ramp-up rate of 10 °C/min, instead of 2.5 °C/min during the first pyrolysis step. Therefore, I speculated that this faster ramp-up rate to 600°C could possibly have an effect. PtCl₄(2.1) had a ramp-up rate of 2.5 °C/min but resulted in poor performance: (~0.48 mA_{H₂O₂}*cm⁻², $\lambda_{\text{Faradaic}} = 38\%$, $\lambda_{\text{O}_2} = 55\%$). PtCl₄(2.2) came from the same precursor batch with an increased ramp-up rate of 10 °C/min but resulted in even worse performance: (~0.3 mA_{H₂O₂}*cm⁻², $\lambda_{\text{Faradaic}} = 17\%$, $\lambda_{\text{O}_2} = 30\%$). The hypothesis then was that the total mass of the PtCl₄(2.1+2.2) precursor batch was too large for proper dry-mixing in the agate ball mill. As a result, the total mass was halved for PtCl₄(4.1+4.2) and the ramp up experiment was again repeated. PtCl₄(4.1) had a ramp-up rate of rate of 10 °C/min: (~0.40 mA_{H₂O₂}*cm⁻², $\lambda_{\text{Faradaic}} = 44\%$, $\lambda_{\text{O}_2} = 62\%$), and PtCl₄(4.2) had a ramp-up rate of rate of 2.5 °C/min: (~0.45 mA_{H₂O₂}*cm⁻², $\lambda_{\text{Faradaic}} = 35\%$, $\lambda_{\text{O}_2} = 51\%$). Interestingly, both performances improved when using the smaller precursor batch, and the ramp-up rate even seemed to have a smaller effect. Notably, the slower ramp-up rate was

better in both experiments (PtCl₄(2.1+2.2) and PtCl₄(4.1+4.2)), which led me to believe that it was involved with drying the sample out, so that residual O₂ containing solutions couldn't react with Pt at higher temperatures to create oxides and agglomerates. However, given PtCl₄'s thermal stability, I thought it was best to try to slowly ramp-up to 150°C (2.5 °C/min) to properly dry out the sample then ramp up quickly to 600°C (10 °C/min). PtCl₄(5) was prepared this way resulting in similarly poor activities but even worse selectivity: (~0.43 mA_{H₂O₂}*cm⁻², λ_{Faradaic} =19%, λ_{O₂}=32%). The CV's of these samples can be found in Appendix B (Figure B.9 and Figure B.10).

At this point I was confused as to why PtCl₄(1) had such a great performance compared to its subsequent five batches: PtCl₄(2.1+2.2) PtCl₄(4.1+4.2) and PtCl₄(5). I then recalled another small but important detail: the initial catalyst samples that were synthesized, (including PtCl₄(1), CoSAC1, IrSAC(1+1.2+3)) were not milled in an agate mortar during the wet chemistry step. They were briefly milled in the agate ball mill, and then the ball mill was closed and wet-mixed for 3 hours to keep the sample in darkness during the wet chemistry step. The PtCl₄(6) followed this procedure and successfully reproduced the performance of PtCl₄(1): (~2.30 mA_{H₂O₂}*cm⁻², λ_{Faradaic} =92%, λ_{O₂}=96%). It is likely that the presence of UV light during wet chemistry step leads to agglomeration of nanoparticles.¹⁷⁶ This can be controlled if working in low temperatures or darkness. This is supported by XRD results, where metallic Pt facets have been detected, where the PtCl₆ sample has a much stronger signal compared to the PtCl₄ sample (Appendix B, Figure B.32). This could also possibly explain the differences in performance of the IrSAC4 and IrSAC4.2 batch: IrSAC4 had a dark wet chemistry step, while IrSAC4.2 did not. However, IrSAC5 also had a dark wet chemistry step but likely had poor performances due to too large of a precursor batch (nearly 3g) resulting in poor ball mill mixing. This dark wet chemistry step had a minor but noticeable effect on the CoSAC samples as well (CoSAC1+3 were dark, and CoSAC2.1+2.2 were normal).

Despite having great initial performances, the PtCl₄(1+6) samples had stability issues. As shown in Appendix B, Figure B.11, PtCl₄(6) performance degrades substantially after just 30 cycles in the quite forgiving RRDE conditions: (~1.85 mA_{H₂O₂}*cm⁻², λ_{Faradaic} =55%, λ_{O₂}=71%). This degrading performance was similarly shared by the poorer performing PtCl₂ sample. This led me to prepare a PtSAC sample using the Zeise's dimer (zPt₂), with the thought that it was less prone to agglomeration during the wet chemistry step based on the Pd²⁺ electrodeposition results from Chapter 5, (ethylenediamine ligands on Pd²⁺ inhibit electrodeposition and agglomeration). This zPt₂ precursor splits to become monomeric in even slightly polar solutions, especially in the HCl-containing solutions during the dark wet chemistry step. The zPt₂ sample resulted in modest performance (~1.04 mA_{H₂O₂}*cm⁻², λ_{Faradaic} =65%, λ_{O₂}=79%), but more importantly maintained this activity after 50 cycles. Unfortunately, I never had a chance to try the PtAcac precursor again, which also had poor-modest performances but at least maintained them. Lastly, the XPS scans of PtCl₄(1+2.1), zPt₂ samples are provided in Appendix B (Figure B.25-27).

The final metal that was investigated for this synthesis was palladium, where all of the Pd samples underwent dark wet chemistry steps during the synthesis procedure. The performance of PdAcac1 was ($\sim 1.68 \text{ mA}_{\text{H}_2\text{O}_2} \cdot \text{cm}^{-2}$, $\lambda_{\text{Faradaic}} = 80\%$, $\lambda_{\text{O}_2} = 89\%$), and of PdAcac2 was ($\sim 1.23 \text{ mA}_{\text{H}_2\text{O}_2} \cdot \text{cm}^{-2}$, $\lambda_{\text{Faradaic}} = 75\%$, $\lambda_{\text{O}_2} = 85\%$). However PdAcac3 had a lower efficiency of ($\sim 1.01 \text{ mA}_{\text{H}_2\text{O}_2} \cdot \text{cm}^{-2}$, $\lambda_{\text{Faradaic}} = 53\%$, $\lambda_{\text{O}_2} = 69\%$). While not to the same extent as the Pt samples, the PdAcac samples also exhibited performance degradation after cycling over time, likely due to agglomeration.

To elucidate the effects of a possible agglomeration mechanism, PdAcac1 ($\sim 4 \text{ wt.}\%$ Pd) was mixed with 60%Pd on Vulcan in a 19:1 ratio ([PdAcac1]:[60%Pd/Vulcan]) to yield a 7 wt.% Pd sample (Appendix B, Figure B.13). It was hypothesized that this sample would have roughly the same specific activity from the PdN_x sites, but overall a lower selectivity due to the metallic Pd favoring 4e⁻ ORR. Surprisingly, the specific activity of this 19:1 mixture was significantly lower than that of PdAcac1: ($\sim 1.00 \text{ mA}_{\text{H}_2\text{O}_2} \cdot \text{cm}^{-2}$, $\lambda_{\text{Faradaic}} = 21\%$, $\lambda_{\text{O}_2} = 35\%$). This strongly suggests that potential agglomerates not only favor 4e⁻ ORR, but also greatly facilitates H₂O₂RR. The agglomeration is arguably worse than expected because we do not just lose sites, those sites lost to agglomeration also actively go against our purposes with active H₂O₂RR. This phenomenon lends itself to how important it is to avoid even the smallest amount of agglomeration during the synthesis process.

Since the metals being tested have different atomic masses, I determined that it was important to analyze molar activity ($\text{mA}_{\text{H}_2\text{O}_2} \cdot \mu\text{mol}_{\text{metal}}^{-1}$) rather than mass activity, to better visualize the activity per potential MN_x site, by using the metal content determined by XPS (Appendix B, Figure B.19-29). Figure 6.7 (top left) summarizes this, and suggests that an IrN_x site is orders of magnitude more active than any of the other sites. However, one needs to be very careful when normalizing this way, since this kind of analysis will typically favor catalysts with less metal content. Despite having the same catalyst loadings ($75 \mu\text{g}_{\text{catalyst}} \cdot \text{cm}^{-2}$), this analysis does not have the same molar metal loadings ($\mu\text{mol}_{\text{metal}}^{-1}$). Figure 6.7 (top right) takes the data points from all catalyst samples and presents this inherent bias. This bias can also be seen when extrapolating data from Gao et al.'s catalyst loading experiments of his Co-NC catalyst (Appendix B, Figure 14.B, a,b). As can be seen, catalyst loading and total current do not share a linear relationship (Figure 14.B, c) and by converting this data into molar metal loadings ($\mu\text{mol}_{\text{metal}}^{-1}$), we can see the same bias favoring low loadings (Figure 14.B, d). Interestingly, according to Gao et al.'s data, increased catalysts loadings of the Co-NC catalyst doesn't actually increase the specific activity at all: catalyst loadings across 3 orders of magnitude are around $\sim 2.0 \text{ mA}_{\text{H}_2\text{O}_2} \cdot \text{cm}^{-2}$ (Figure 14.B, e). This must be because the CoN_x sites are mass transport limited at +0.25V_{VRHE}, and the increase in total current from higher mass loadings must be predominantly H₂O₂RR (refer to Chapter 2, Section 2.4, Equations 2.24+2.25).

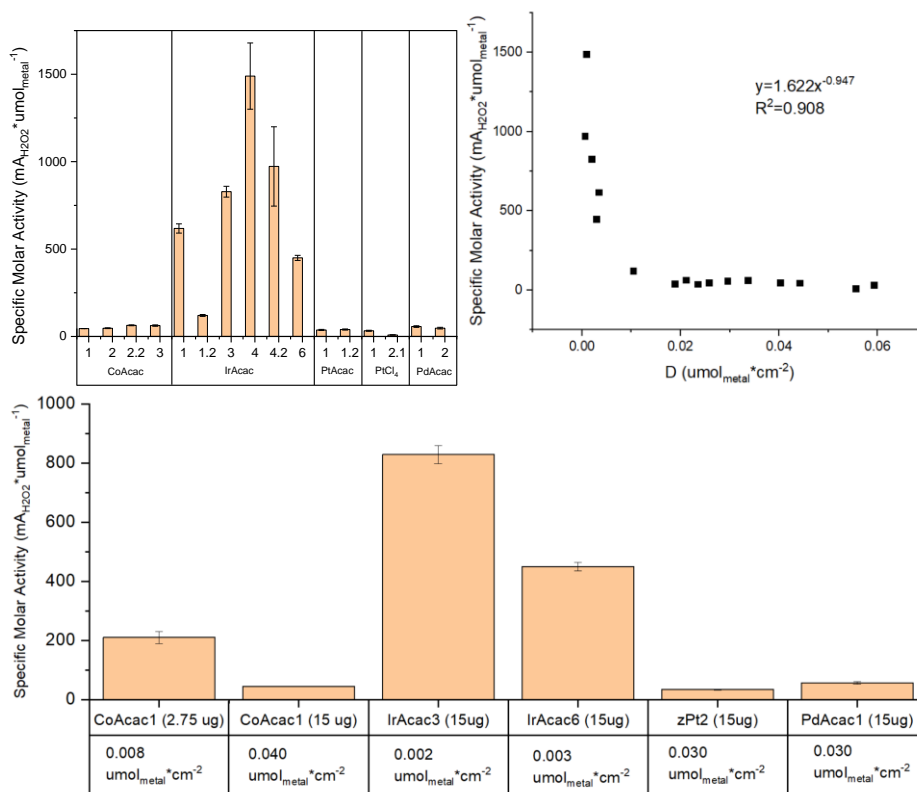


Figure 6.7: (top left) Specific activity ($\text{mA}_{\text{H}_2\text{O}_2}$) normalized to molar metal content ($\mu\text{mol}_{\text{metal}}^{-1}$) to compare the activities of potential MN_x sites in M-N/C catalysts of various metals (Co, Ir, Pt, Pd) and site densities (ranging from 0.001 to 0.06 $\mu\text{mol}_{\text{metal}}^{-1}$). Molar metal content is derived from XPS analysis. (top right) Specific Molar Activity ($\text{mA}_{\text{H}_2\text{O}_2} \cdot \mu\text{mol}_{\text{metal}}^{-1}$ at $+0.25V_{\text{RHE}}$) as a function of molar metal content ($\mu\text{mol}_{\text{metal}}$), revealing a bias in the data towards samples with low molar content (mostly Ir-containing). (bottom) adjusting catalyst loadings to better compare specific molar activities ($\text{mA}_{\text{H}_2\text{O}_2} \cdot \mu\text{mol}_{\text{metal}}^{-1}$) between M-N/C catalysts of different metals.

However, total mass currents still follow the same trends at $+0.6V_{\text{RHE}}$ in Gao et al.'s data (Figure B.14, c) where one would usually assume kinetic limitations are taking precedent from the O_2 -saturated electrolyte. Unfortunately, my data cannot truly be corrected with trend presented in Figure 6.7 (top, right), because we have confounding variables between site density (e.g. molar metal content) and metal type. Iridium has a high atomic weight, and poor solubility, which has resulted in samples with exclusively lower molar metal content (e.g. low site density) that is benefitting from this bias. Figure 6.7 (bottom) depicts samples with various catalyst loadings (e.g. ink dropcasted onto the RRDE disk) to compensate for the variable molar metal

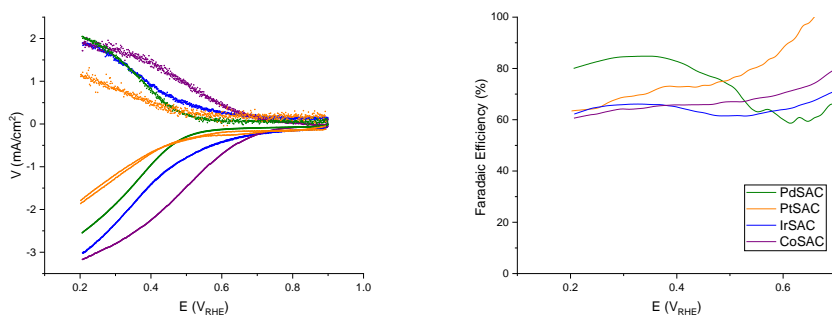


Figure 6.8: RRDE measurement of IrSAC (IrAcac3), CoSAC (CoAcac2), PtSAC (zPt₂), and PdSAC (PdAcac1) samples for 2e⁻ ORR in acidic conditions. Catalyst loadings are 75 μg*cm⁻². Measurements in O₂-saturated 0.1 M HClO₄ with a scan speed of 20 mV*s⁻¹ and a rotating rate of 1600 rpm at room temperature.

contents of the catalysts. The CoAcac1 reproduces the bias presented by Gao et al: CoAcac1 (2.75 μg = 13.75 μg*cm⁻² = 0.008 μmol_{metal}*cm⁻²) and CoAcac1 (15 μg = 75 μg*cm⁻² = 0.040 μmol_{metal}*cm⁻²) have specific molar activities of 210 and 45 (mA_{H2O2}*μmol_{metal}⁻¹), respectively. IrAcac3 (15 μg = 75 μg*cm⁻² = 0.002 μmol_{metal}*cm⁻²) and IrAcac6 (15 μg = 75 μg*cm⁻² = 0.003 μmol_{metal}*cm⁻²) have specific molar activities of 830 and 450 (mA_{H2O2}*μmol_{metal}⁻¹), respectively. Lastly there is zPt₂ (15 μg = 75 μg*cm⁻² = 0.030 μmol_{metal}*cm⁻²) and PdAcac1 (15 μg = 75 μg*cm⁻² = 0.030 μmol_{metal}*cm⁻²) having specific molar activities of 34 and 57 (mA_{H2O2}*μmol_{metal}⁻¹), respectively. Roughly correcting for site density bias, we could extrapolate the IrAcac3 sample's total current to be hypothetically 525 (mA_{total}*μmol_{metal}⁻¹) at a loading of (0.008 μmol_{metal}*cm⁻²), where the selectivity would likely be worse. This would suggest that an IrN_x site is more active and less selective than a CoN_x site, which would confirm our initial hypothesis derived from Figure 2.9. However, such conclusions remain unclear until experiments with better control of molar metal loadings (e.g. MN_x site density) are conducted.

A safer conclusion is that the strong-binding IrN_x sites and CoN_x sites are more active than the weak-binding PdN_x sites and PtN_x sites. However, these weak-binding PdN_x sites and PtN_x sites are more selective, assuming we look at a less mass-transported potential (such as +0.4V_{VRHE} in Figure 6.8). This still supports the initial hypothesis extrapolated from the volcano plots in Figure 2.9 (right) and Figure 6.3 (c). The best performing samples of each metal were used for the subsequent extensive testing and characterization phase, and are presented in Figure 6.8. These the samples will be renamed for simplicity from here on: IrAcac3=IrSAC, CoAcac2=CoSAC, zPt₂=PtSAC, and PdAcac1=PdSAC. A Tafel plot comparing these catalysts will not be shown for one simple reason: without a systematic study where variables such as catalyst supports, catalyst loadings, and actual catalyst site loadings are properly controlled for, Tafel plots can quickly become meaningless. This is partially illustrated by the specific molar activities in Figure 6.7, but can also be seen with later onset potentials on lower catalyst loadings (Figure B14). In

addition, the N1s peaks from the XPS survey scans on some of the catalysts samples were analyzed (samples CoAcac2.2+3, IrAcac4+4.2+6, and zPt₂ in Figures B.17-18, B.22-23, and B.27, respectively). The relatively broad N1s peaks on these samples suggests a wide array of nitrogen types in the sample (pyridinic, pyrrolic, graphitic, pyridinic-O). It was intended to do focused scans but they were not prioritized because the deconvolution of four different peaks of varying widths in a rather narrow range results in very ambiguous peak fittings with multiple possibilities. In addition, this data doesn't characterize the most essential role of nitrogen: determining which kinds of nitrogen species are actually coordinated to our single atom metal sites.

6.5 Extensive Testing and Characterizations

It has already been stressed that RRDE cathodic sweeps do not necessarily translate to a useful 2e⁻ ORR catalyst. This next section will go over the catalysts sample's stability over time in chronoamperometry (CA) experiments in various testing setups, including RRDE, TiFET, and MEA. Initial RRDE CA experiments were assessed at +0.2V_{VRHE} with loadings of 75 μg*cm⁻², which made them comparable to the RRDE CV experiments. Some notable conclusions from these CA experiments include the superior stability of the PtSAC using the zPt₂ precursor (Appendix B, Figure B.33), as well as the impressive stability of the IrSAC catalyst (IrAcac3, Appendix B, Figure B.34). However, the low absolute catalyst loadings (~300 ng_{catalyst} on a catalyst spot of 0.031 cm_{geo}²) inherent in the TiFET experiments results in later reaction onsets. As a result, the RRDE CA experiments had to be assessed at 0.00V_{VRHE} (±0.05V) with lower catalyst loadings of 10 μg*cm⁻² in order to better compare to the TiFET and MEA results. In addition, the Pt ring would not be used to assess H₂O₂ activity, where KMnO₄ titrations are used exclusively to assess H₂O₂ concentrations instead (e.g. RDE CA's).

The RDE results show poor selectivities, which is expected at higher overpotentials 0.00V_{VRHE} (±0.05V) (Figure 6.9). This is likely due H₂O₂RR activity supplementing the O₂-transport limited 2e⁻ ORR activity at higher over potentials, similar to the phenomena presented by Gao et al.'s increased CoSAC catalyst loading data (Appendix B, Figure B.14). However, the IrSAC maintains a selective activity of ~1.10 mA_{H2O2}*cm⁻², at 0.00V_{VRHE} (λ_{Faradaic} =52%), which is still yields a higher H₂O₂ throughput than at +0.20V_{VRHE} (~0.64 mA_{H2O2}*cm⁻², λ_{Faradaic} =72%) (Figure B.34, a). This is likely to due the low catalyst site loading of the IrSAC catalyst. It should be noted that the inconsistent currents from a trapped gas bubble on IrSAC's RDE experiments had no effect on selectivity (Figure 6.9 and B.34). Interestingly, even CoSAC had respectable H₂O₂ throughputs despite higher catalyst loadings and overpotentials: ~1.30 mA_{H2O2}*cm⁻², at 0.00V_{VRHE} (λ_{Faradaic} =54%) which is higher than Gao et al.'s CA experiments at +0.4V_{VRHE} (~0.80 mA_{H2O2}*cm⁻²) and +0.5V_{VRHE} (~0.50 mA_{H2O2}*cm⁻²) (Appendix B, Figure B.35). While Gao et al. use higher catalyst loadings (100 μg*cm⁻²), they use very low overpotentials (+0.4V_{VRHE} and +0.5V_{VRHE}) resulting in low operating currents in their CA experiments.

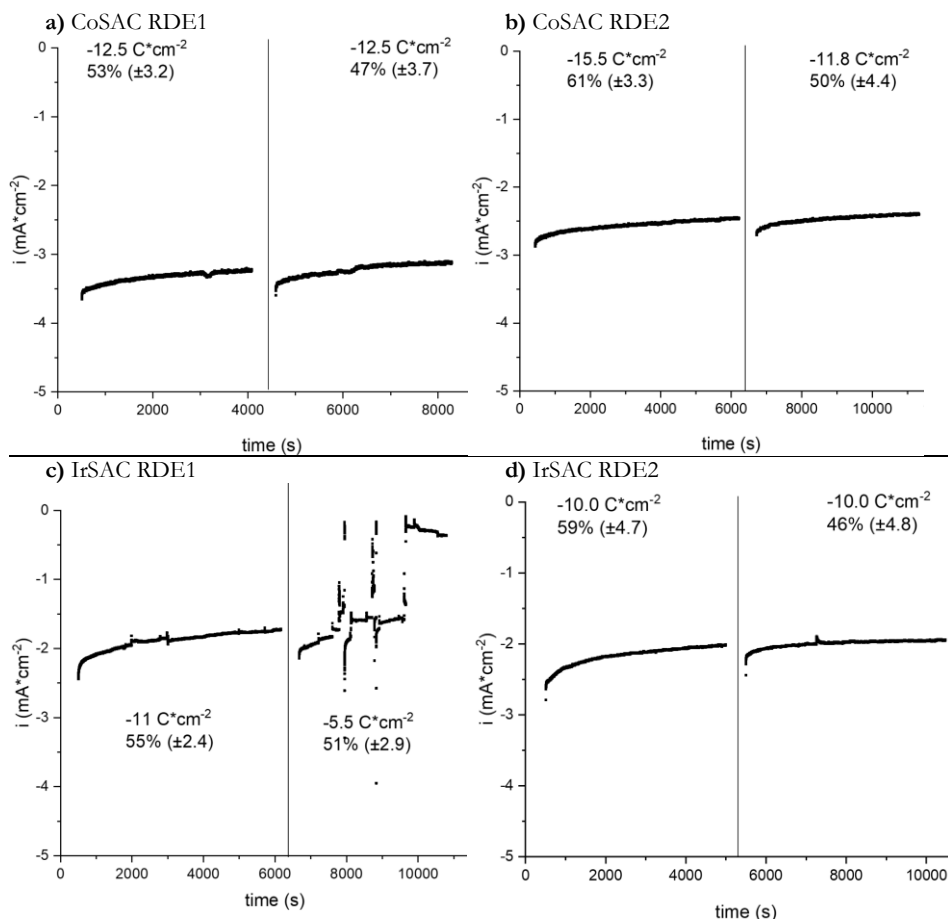


Figure 6.9: RDE CA experiments ($+0.0V_{\text{VRHE}}$) of (a+b) CoSAC ($10 \mu\text{g}\cdot\text{cm}^{-2}$) and (c+d) IrSAC ($10 \mu\text{g}\cdot\text{cm}^{-2}$). Measurements in O_2 -saturated 0.1 M HClO_4 and a rotating rate of 1600 rpm at room temperature. The quantification of H_2O_2 concentration was determined by KMnO_4 titration, yielding the presented faradaic efficiency ($\lambda_{\text{Faradaic}}$) values.

When benchmarking the stability of a catalyst at operating currents, it is arguably more sensible to do so at lower loadings and higher overpotentials, which is contrary to Gao et al.'s approach. By doing so, the delicate engineering of the catalyst layer is better circumvented while the catalyst is experiencing higher mass currents at larger overpotentials. This essentially provides an accelerated stress test at the catalyst level, rather than discovering the side-reactions that can occur when the ORR activity becomes O_2 -transport limited, such as electrodeposition/agglomeration of metal species or $\text{H}_2\text{O}_2\text{RR}$ (Chapter 5). The goal is to see how long a catalyst can last while it is doing what it is supposed to be doing: H_2O_2 throughput per gram of catalyst

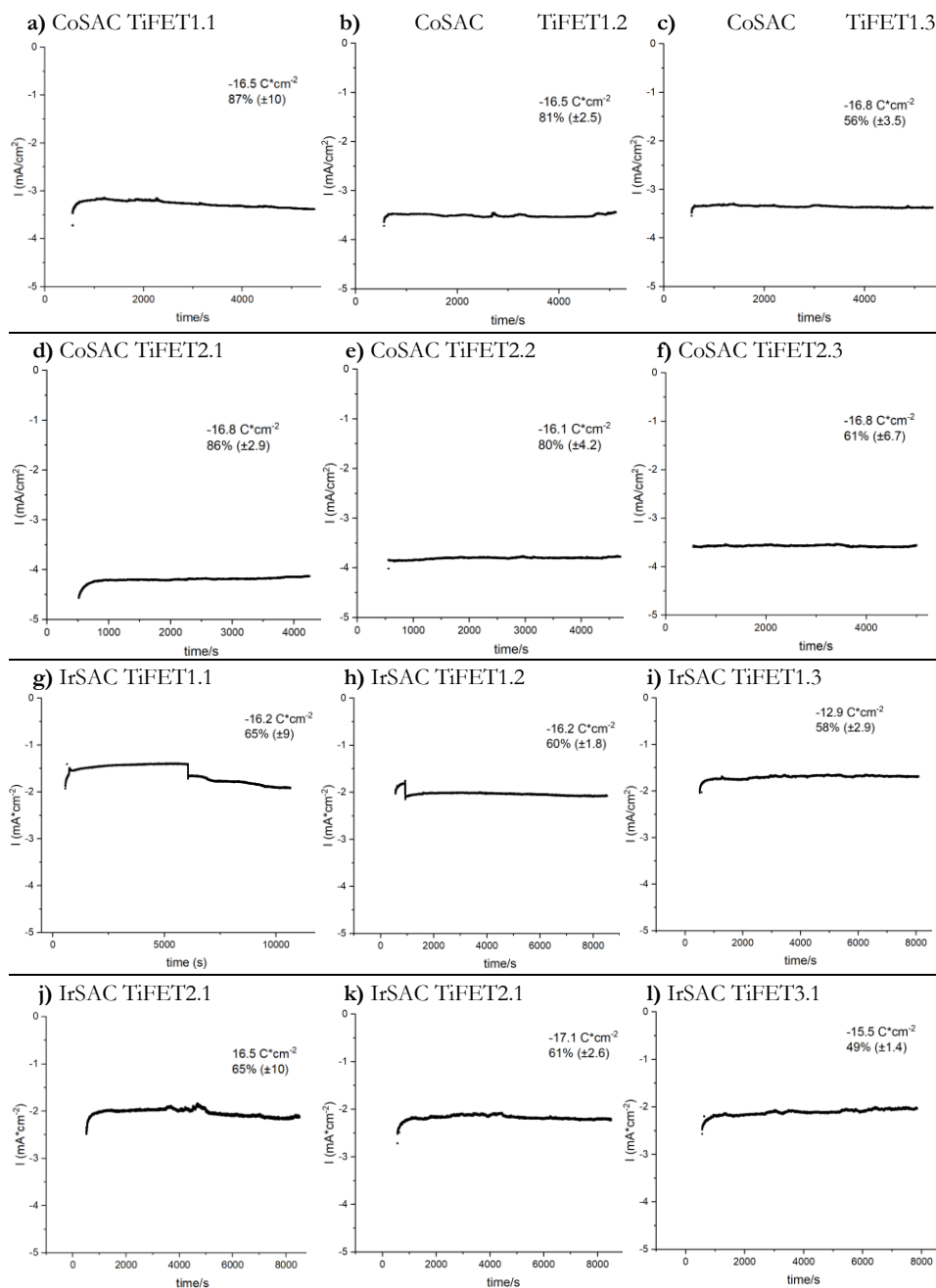


Figure 6.10: CA TiFET experiments (catalyst loadings = $\sim 10 \mu\text{g}\cdot\text{cm}^{-2}$, $0.00V_{\text{VRHE}} (\pm 0.05V)$) of (a-f) CoSAC and (g-l) IrSAC catalysts. Measurements in 1.0 M HClO₄ electrolyte at room temperature. The $\lambda_{\text{faradaic}}$ values are from quantified H₂O₂ concentrations determined by KMnO₄ titration and UV-Vis spectrometry.

($\text{mA}_{\text{H}_2\text{O}_2} \cdot \text{g}_{\text{catalyst}}^{-1}$). Accelerated operations are selected to enable faster conclusions in shorter amounts of time allowing experiments to be better controlled from unforeseen long-term drifts. Assuming a catalyst is provided with conditions that are adequately optimal, then these accelerated operations should be representative of operations at milder conditions that may be more practical. This is the goal of using the floating electrode technique (FET) for benchmarking $2e^-$ ORR performances. By using a titanium coating (TiFET) the floating electrodes have roughly an ohmic drop of 500Ω , but the measured currents of the TiFET experiment are $<0.2 \text{ mA}$ on a catalyst spot of $0.031 \text{ cm}_{\text{geo}}^2$. This means that the ohmic drop doesn't exceed 100 mV , suggesting adequate control of the potential.

Figure 6.10 summarizes these TiFET experiments ($10 \mu\text{g} \cdot \text{cm}^{-2}$ catalyst loading) for CoSAC and IrSAC. Compared to the RDE experiments (totaling $\sim 25 \text{ C} \cdot \text{cm}^{-2}$), CoSAC shows striking H_2O_2 throughputs and selectivity in the TiFET experiments: an average of $\sim 3.1 \text{ mA}_{\text{H}_2\text{O}_2} \cdot \text{cm}^{-2}$, at $0.00 \text{ V}_{\text{VRHE}}$ ($\lambda_{\text{Faradaic}} = 83\%$) in the first $33 \text{ C} \cdot \text{cm}^{-2}$ of operation in two experiments (CoSAC TiFET1 and CoSAC TiFET2) as presented Figure 6.10 (a, b and d, e). These benchmark performances of CoSAC begin to degrade in the subsequent $17 \text{ C} \cdot \text{cm}^{-2}$ of operation: an average of $\sim 2.0 \text{ mA}_{\text{H}_2\text{O}_2} \cdot \text{cm}^{-2}$, at $0.00 \text{ V}_{\text{VRHE}}$ ($\lambda_{\text{Faradaic}} = 58\%$) as presented Figure 6.10 (c and f). Yet despite being degraded, these TiFET batch performances (from 33 to $50 \text{ C} \cdot \text{cm}^{-2}$) still exceed the initial RDE batch performances (from 0 to 12.5 - $15.5 \text{ C} \cdot \text{cm}^{-2}$). The TiFET experiments for IrSAC also resulted in improved H_2O_2 throughputs and selectivity but the improvements were not as striking: $\sim 1.25 \text{ mA}_{\text{H}_2\text{O}_2} \cdot \text{cm}^{-2}$, at $0.00 \text{ V}_{\text{VRHE}}$ ($\lambda_{\text{Faradaic}} = 62\%$) in the first $33 \text{ C} \cdot \text{cm}^{-2}$ of operation in two experiments (IrSAC TiFET1 and IrSAC TiFET2) as presented Figure 6.10 (g, h and j, k). However, the final performances of IrSAC (from 33 to 45 - $50 \text{ C} \cdot \text{cm}^{-2}$) were also less degraded: $\sim 1.1 \text{ mA}_{\text{H}_2\text{O}_2} \cdot \text{cm}^{-2}$, at $0.00 \text{ V}_{\text{VRHE}}$ ($\lambda_{\text{Faradaic}} = 55\%$) as presented Figure 6.10 (i and l).

It is likely that the CoSAC catalyst was notably more O_2 -transport limited in comparison to the IrSAC catalyst in the RDE experiments because it has roughly $\times 30$ times more potential MN_x sites. This would explain the larger improvement the CoSAC catalyst experiences in the TiFET experiments from the RDE experiments. One criticism is simply the TiFET uses lower absolute catalyst loadings, and the resulting bias of low molar metal loading ($\mu\text{mol}_{\text{metal}}$) presented in Figure 6.7 is the reason for the TiFET's improved performances. Nevertheless, it cannot be stressed enough that the selectivity maintained in a CA experiment ($\lambda_{\text{Faradaic}} = 86\%$, $\lambda_{\text{O}_2} = 92\%$) for the CoSAC catalyst (TiFET 1.1+2.1 presented in Figure 6.10, a+d) vastly exceeds any results presented by Gao et al., including CV experiments. The fact that these selectivities are achieved at higher overpotential and H_2O_2 throughputs makes it even more impressive. In addition, the TiFET utilizes O_2 inputs exclusively from the gas phase, demonstrating an optimized triple-phase boundary comparable to scaled-up PEM reactors, where the only difference is the HClO_4 electrolyte supplementing the Nafion for proton transport. This has a very useful application in catalyst ink optimizations, since the point at which Nafion compromises the gas channels can be determined quickly and efficiently.

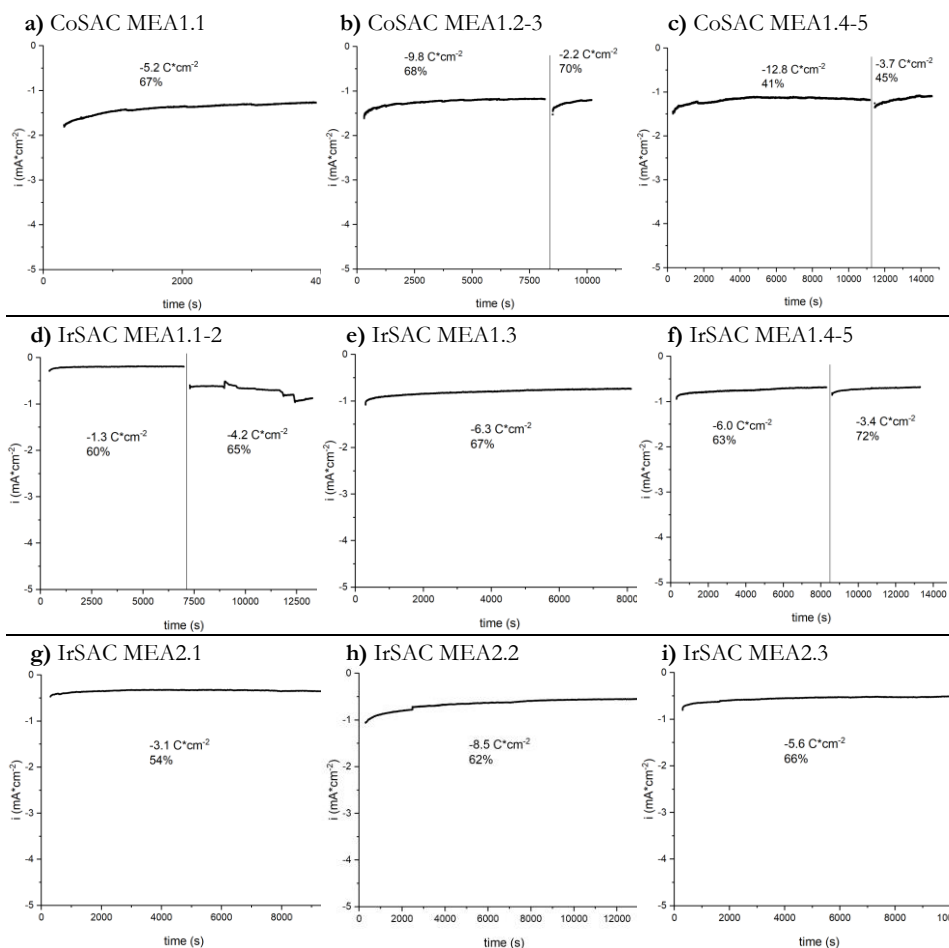


Figure 6.11: CA MEA experiments (catalyst loadings = $\sim 10 \mu\text{g}^*\text{cm}^{-2}$, $0.00V_{\text{VRHE}} (\pm 0.05V)$) of (a-c) CoSAC and (d-i) IrSAC catalysts. Measurements in 0.1 M HClO_4 electrolyte at room temperature. The $\lambda_{\text{faradaic}}$ values are from quantified H_2O_2 concentrations determined by KMnO_4 titration and UV-Vis spectrometry.

While the comparisons between RDE and TIFET experiments do suggest an interesting story, an additional experimental setup that is representative of MEA conditions would make the story significantly more compelling. A CoSAC and IrSAC were tested in a ‘half MEA’ configuration where the anode is separate to allow the analysis of the cathode in MEA conditions. This allows access to a reference electrode to account for the potentials applied. The MEA electrode was prepared by drop-casting the catalyst ink onto the carbon cloth GDE ($\sim 1.0 \text{ cm}_{\text{geo}}^2$), where it is subsequently heat-pressed to a Nafion membrane, and installed into a glass H-cell (Chapter 3).

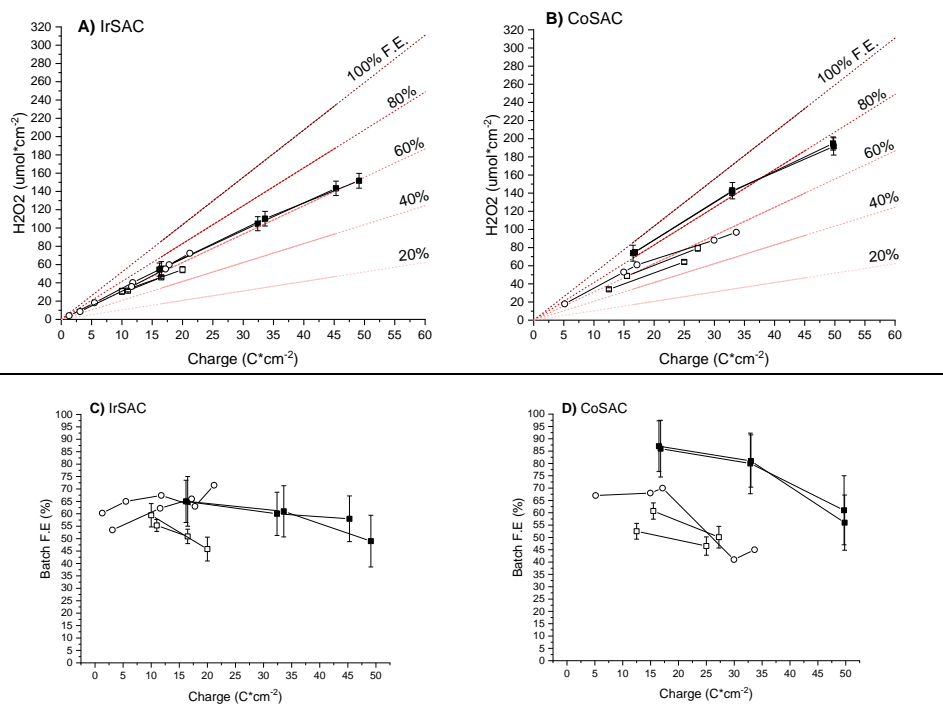


Figure 6.12: H_2O_2 yield over charge accumulated up to $50 \text{ C}\cdot\text{cm}^{-2}$ (■ = FET, □ = RDE, ○ = MEA). All experiments were conducted within the range of -0.05 to $+0.05 \text{ V}_{\text{rhe}}$, with approximate catalyst loadings of $10 \mu\text{g}\cdot\text{cm}^{-2}$. FET experiments were conducted in 1M HClO_4 with an O_2 -saturated headspace. RDE and MEA experiments were conducted in O_2 -saturated 0.1M HClO_4 .

Figure 6.11 summarizes these MEA experiments ($10 \mu\text{g}\cdot\text{cm}^{-2}$ catalyst loading) for CoSAC and IrSAC. The CoSAC MEA experiment shows similar H_2O_2 throughputs and selectivity as the RDE experiments: an initial average of $\sim 1.0 \text{ mA}_{\text{H}_2\text{O}_2}\cdot\text{cm}^{-2}$, at $0.00\text{V}_{\text{rHE}}$ ($\lambda_{\text{Faradaic}} = 67\%$) from 0 to $17 \text{ C}\cdot\text{cm}^{-2}$ (Figure 6.11, a+b) that degrades to $\sim 0.5 \text{ mA}_{\text{H}_2\text{O}_2}\cdot\text{cm}^{-2}$, at $0.00\text{V}_{\text{rHE}}$ ($\lambda_{\text{Faradaic}} = 42\%$) from 17 to $33 \text{ C}\cdot\text{cm}^{-2}$. Like the RDE, the MEA experiments show poorer performance and faster degradation of the CoSAC catalyst compared to the TiFET experiments. The IrSAC MEA experiments show high variability in the H_2O_2 throughputs ranging from 0.1 - $0.6 \text{ mA}_{\text{H}_2\text{O}_2}\cdot\text{cm}^{-2}$, at $0.00\text{V}_{\text{rHE}}$, however the selectivities remained consistent ($\lambda_{\text{Faradaic}} = 55$ - 70%). Despite overall poor performances, the IrSAC catalyst showed no signs of performance degradation across the $>17 \text{ C}\cdot\text{cm}^{-2}$ of operation in the MEA experiments. MEA experiments with increased loadings ($100 \mu\text{g}\cdot\text{cm}^{-2}$ catalyst loading), were also conducted but resulted in very low selectivities for both CoSAC and IrSAC ($\lambda_{\text{Faradaic}} = 41\%$, $\lambda_{\text{Faradaic}} = 28\%$ respectively, from 0 to $\sim 30 \text{ C}\cdot\text{cm}^{-2}$).

It is important to note that all of these experiments used HClO_4 electrolyte to supplement the non-optimized catalyst inks with proton transport. In spite of this,

the MEA experiments had notably poor performances, which highlights the difficulties of scaling up electrochemical processes, particularly the optimization of triple phase boundary to minimize O_2 -transport losses, and facile escape channels for H_2O_2 to avoid H_2O_2RR . It is very difficult to determine whether an experimental configuration provides the ideal conditions for a catalyst. However, the CA performances evidenced by the TiFET experiments are nevertheless impressive for $2e^-$ ORR catalysts in acidic conditions. Figure 6.12 summarizes the performance between the RDE, FET, and MEA configurations, presenting the net selectivities and H_2O_2 throughputs (a, b and Figure B.38) and batch selectivities (c, d).

The later onset potentials of the electrochemical O_2 -based reactions from the TiFET experiments can be explained by the low absolute catalyst loadings (Appendix B, Figure B.37). Increasing absolute catalyst loadings of the FET was attempted with no success. It became difficult to manufacture larger masks to enable larger catalyst spots for the vacuum-filtration deposition, since the slightest tilt in the mask would completely compromise the controlled catalyst deposition. As result, the low loadings and late later onset potentials became a necessary compromise. Later onset potentials increases the risk of O_2 -transport limited activities, which in turn increases the risk of H_2O_2RR as well as the electrodeposition/agglomeration of metal species. In fact, it has already been evidenced by Wang et al. that Pd^{2+} electrodeposition is greatly facilitated at higher over potentials during ORR operations (Chapter 5).¹⁵⁸ The PtSAC and PdSAC samples were also tested but had notably worse stability. The PtSAC had lower H_2O_2 throughputs, selectivity and degraded faster compared

to IrSAC and CoSAC (not shown). The PdSAC failed to maintain consistent currents during CA experiments, where a TiFET experiment is presented as an example in Appendix B (Figure B.36). This suggests a very peculiar phenomena where the inherently active catalyst sites (CoN_x , IrN_x) are actually also inherently more stable since they have higher affinities to $*O_2$. Weak-binding sites (PtN_x , PdN_x) with less affinity to $*O_2$ will inherently be more susceptible to the electrodeposition of metal species. This is exacerbated by the fact that these weak-binding sites will require higher overpotentials that also increases the risk of this electrodeposition. With this in mind, having a highly active MN_x site with low selectivity is favored due to its inherent protections against this electrodeposition phenomenon. In fact, even a MN_x site with affinities towards the undesirable H_2O_2RR can be beneficial for stability by preventing H_2O_2 induced catalyst corrosion. To a certain extent, it can be better that a MN_x site is reducing H_2O_2 rather than H_2O_2 oxidizing a MN_x site resulting in catalyst corrosion.

Lastly, the CoSAC and IrSAC samples were extensively characterized. In the field of M-N/C electrocatalysts, extensive characterizations are necessary conventions in order to suggest that the electrochemical performance of a sample can be attributed to its MN_x sites. The HAADF-STEM images of the CoSAC and IrSAC samples are provided by Sofie Colding-Jørgensen (Figure 6.13). These engaging images of the catalyst samples evidence atomically-dispersed metal sites in a nitrogen-doped carbon framework. In addition, EDS was supplemented in this analysis to determine

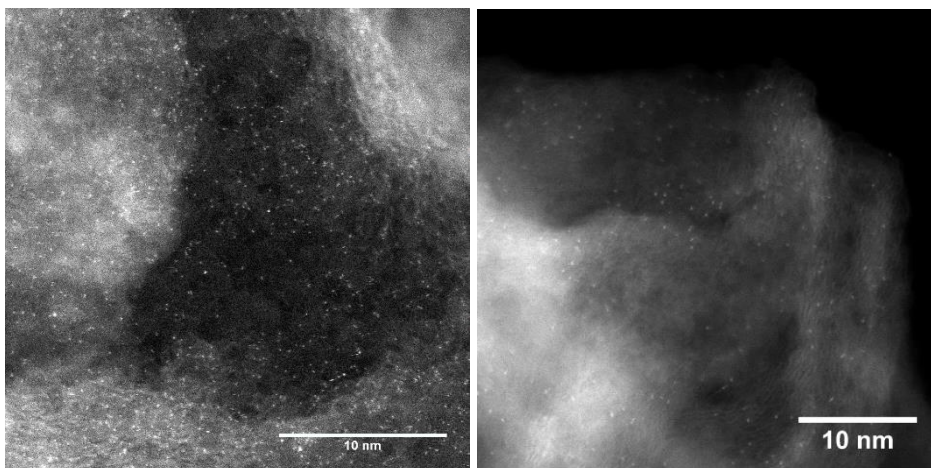


Figure 6.13: HAADF-STEM images of (left) CoSAC and (right) IrSAC catalyst samples. Analysis performed by Sofie Colding-Jørgensen

the elemental compositions of CoSAC and IrSAC (Appendix B, Figure B.39-42, and Figure B.43-47, respectively). The CoSAC sample (CoAcac2) had a cobalt loading of 2.65 ± 0.26 (wt. %) which agrees with the values from XPS analysis (~ 3.0 - 3.3 % wt.). The IrSAC sample (IrAcac3) had an iridium loading of 0.85 ± 0.49 , which also agrees with the values from XPS analysis (~ 0.5 - 0.6 %wt.). Ag and Pt contaminants were detected in the EDS analysis of IrSAC (Appendix B, Figure B.45, and B.47, respectively), where the scan was limited due to sample's carbon matrix burning. ICP-MS analysis estimate that this Ag contamination is an order of magnitude less prevalent than the Ir content (% wt.) (Appendix B. Table B.1). Polycrystalline Ag would therefore have negligible contributions to the $2e^-$ ORR activity as suggested in Chapter 4 (Figure 4.2, a). The Pt contamination is potentially more prevalent and concerning. However, in the worst case, this would manifest as PtN_x sites with similar activities to the zPt_2 sample and be contributing a minor fraction of the $2e^-$ ORR activity, since the Pt content is roughly $\sim 1/10^{\text{th}}$ of the zPt_2 sample. It is more likely that the Pt contamination is in the form of nanoparticles (HAADF-STEM image of PtSb nanoparticle not shown) which would likely be active for H_2O_2RR .

The final analysis that is missing is XANES/EXAFS (in progress). This would provide information of the metal species in the catalyst at a bulk level, particularly the coordination of the atomically-isolated metal species. Metal-nitrogen bond lengths could provide strong indications of the coordinated N-species (e.g. pyrrolic, pyridinic). In addition, the ICP-MS data was also inconclusive for the IrSAC catalyst, due to the difficulties of leaching Ir species from acid digestion. Thermal Gravimetric analysis (TGA) was considered, but not available due to technical difficulties (example of TGA in Appendix B. Figure B.7).¹⁷¹ Future experiments should consider implementing nitrate-reduction stripping to account for electrochemically active MN_x sites.¹⁷⁷

6.6 Conclusion

At the start of this entire project, I was testing the Pd1/N-C catalyst sample in a submerged GDE setup (Chapter 4). The high loadings ($100 \mu\text{g}\cdot\text{cm}^{-2}$) of a catalyst with weak-binding PdN_x sites, in an experimental setup that was likely O₂-transport limited meant that it was very difficult to reproduce the CA experiments. Simply spray-coating the catalyst ink onto the carbon cloth GDE gave incomparably worse results compared to drop-casting. Since then, I have grown and now have strong notions to the complications that were unforeseeable at the time.

The journey to making a better experimental setup was far from smooth (Chapter 5). Becoming adept at the FET and subsequently modifying the FET for 2e⁻ ORR presented many challenges. With these challenges came some key insights that ended up being essential to benchmarking 2e⁻ ORR activities. This includes the possibility of H₂O₂RR and the electrodeposition of metal species during ORR operations, where these unwanted phenomena are more prevalent at higher overpotentials and during O₂-transport limited activities.

The TiFET experiments proved successful, demonstrating improved performances from the CoSAC and IrSAC samples enabled by ‘closer to ideal’ operation conditions. Higher activities were achieved at higher overpotentials without significant O₂-transport limitations. Compared to the RDE and MEA setups, the FET had fewer complications, which highlights the utility of the FET for 2e⁻ ORR, especially for M-N/C catalysts. Notably, the FET provides consistent uniform catalyst depositions onto the GDE, which is a typical complication in PEM devices that is illustrated in the GDE experiments in Chapter 4, as well as the MEA experiments in Chapter 6.

Overall, the results from Chapter 6 suggest some validity in the trends presented in the volcano plots (Figures 2.9 and 6.3) where the activity trend of an MN_x site is roughly Ir>Co>Pd>Pt and the selectivity trend is the opposite Ir<Co<Pd<Pt. These trends seem to be roughly represented in the CV data presented (Table 6.1 and Figure 6.8) but the different amounts of MN_x site loadings in the measurements suggest some catalysts samples were more limited by O₂-transport than others at +0.25V_{VRHE} (Figure 6.7).

Based on these TiFET experiments, it is clear that CoN_x are indeed more selective than IrN_x sites. Compared to IrSAC, the CoSAC experiments had higher selectivities despite having roughly x30 more MN_x sites. While not definitively conclusive, it is likely that IrN_x sites are much more active than CoN_x sites if we assume that the site density bias (Figure 6.7) is adequately addressed by the more ideal conditions provided by the FET setup. The facile access of gas-phase O₂ to the catalyst layer enables accelerated conditions for the catalyst samples to benchmark 2e⁻ ORR stability with much faster experiments (hours instead of days).

The results from Chapter 6 also highlight the possibility of an unexpected trend where the more active and less selective MN_x sites (Ir, Co) are more stable than the less active and more selective sites (Pd, Pt). This is speculated to be because the electrodeposition of metal species will have a harder time competing with the more active strong-binding catalysts during ORR operations. In addition, the undesirable H_2O_2 RR could provide protection from H_2O_2 oxidation and subsequent corrosion of MN_x sites. This provides a robustness of the catalyst when H_2O_2 transport might be compromised during other unexpected component failures of a scaled up system.

This work is significant because it sheds some light on ‘the black box’ of $2e^-$ ORR catalyst performances, where there has been discrepancies between research experiments and scaled-up systems. Assuming the academic field of $2e^-$ ORR wants to remain relevant in the actual applications of this technology, then it will have to make improvements in how it benchmarks $2e^-$ ORR performance and expand from RRDE experiments. This work demonstrates just how important better experimental setups are, while also revealing unexpected results with interesting implications.

Throughout my PhD, I became steadily more unconvinced by applicability of M-N/C's in scaled up systems. By the end of my PhD, I am more convinced that our understandings of catalyst ink formulation, and catalyst deposition on scaled up GDE's is likely quite primitive, especially for $2e^-$ ORR. The FET experiments demonstrate some of an M-N/C's potential, suggesting further improvements in catalyst depositions and optimized three-phase boundaries are needed in the field. I therefore believe this project, and projects similar to it, are only the beginning to something bigger. Our planet's climate is in a transition process that will likely not improve the freshwater scarcity presently affecting four billion people.⁷ H_2O_2 PEMEC is a green technology that provides a promising solution to decentralized areas in need of water treatment, where this decentralized technology can provide a vital function by responding quickly to sudden changes such as incrementally dryer climates in under-developed at-risk areas.

References

1. Arrhenius, S. XXXI. On the influence of carbonic acid in the air upon the temperature of the ground. *London, Edinburgh, Dublin Philos. Mag. J. Sci.* **41**, 237–276 (1896).
2. Rodhe, H., Charlson, R. & Crawford, E. Svante Arrhenius and the greenhouse effect. *Ambio* **26**, 2–5 (1997).
3. Petit, J. R. & Raynaud, D. Forty years of ice-core records of CO₂. *Nature* **579**, 505–506 (2020).
4. Delmas, R. J., Ascencio, J. & Legrand, M. Polar ice evidence that atmospheric CO₂ 20,000yr BP was 50% of present. *Nature* **284**, 155–157 (1980).
5. Hansen, J., Sato, M. & Ruedy, R. Public Perception of Climate Change and the New Climate Dice. 1–19 (2012). doi:10.1073/pnas.1205276109
6. McGranahan, G., Balk, D. & Anderson, B. The rising tide: Assessing the risks of climate change and human settlements in low elevation coastal zones. *Environ. Urban.* **19**, 17–37 (2007).
7. Mekonnen, M. M. & Hoekstra, A. Y. Sustainability: Four billion people facing severe water scarcity. *Sci. Adv.* **2**, 1–7 (2016).
8. Lu, S., Bai, X., Li, W. & Wang, N. Impacts of climate change on water resources and grain production. *Technol. Forecast. Soc. Change* **143**, 76–84 (2019).
9. Moss, R. H. *et al.* The next generation of scenarios for climate change research and assessment. *Nature* **463**, 747–756 (2010).
10. Bradfield, R., Wright, G., Burt, G., Cairns, G. & Van Der Heijden, K. The origins and evolution of scenario techniques in long range business planning. *Futures* **37**, 795–812 (2005).
11. Huntingford, C. & Cox, P. M. An analogue model to derive additional climate change scenarios from existing GCM simulations. *Clim. Dyn.* **16**, 575–586 (2000).
12. Barrie Pittock, A., Jones, R. N. & Mitchell, C. D. Probabilities will help us plan for climate change [1]. *Nature* **413**, 249 (2001).
13. Lamy, C. From hydrogen production by water electrolysis to its utilization in a PEM fuel cell or in a SO fuel cell: Some considerations on the energy efficiencies. *Int. J. Hydrogen Energy* **41**, 15415–15425 (2016).
14. Jacobson, M. Z. *100% Clean, Renewable Energy and Storage for Everything.* (2020).

15. Chu, S. & Majumdar, A. Opportunities and challenges for a sustainable energy future. *Nature* **488**, 294–303 (2012).
16. Nocera, D. G. & Nash, M. P. For the “In This Issue” summary. **104**, (2007).
17. Casadevall, A. V. Active Site Engineering in Electrocatalysis. (2015).
18. Wilberforce, T. *et al.* Modelling and simulation of Proton Exchange Membrane fuel cell with serpentine bipolar plate using MATLAB. *Int. J. Hydrogen Energy* **42**, 25639–25662 (2017).
19. Ricke, K., Drouet, L., Caldeira, K. & Tavoni, M. Country-level social cost of carbon. *Nat. Clim. Chang.* **8**, 895–900 (2018).
20. Bezerra, C. W. B. *et al.* A review of Fe-N/C and Co-N/C catalysts for the oxygen reduction reaction. *Electrochim. Acta* **53**, 4937–4951 (2008).
21. He, H. *et al.* Molecular and electronic structures of transition-metal macrocyclic complexes as related to catalyzing oxygen reduction reactions: A density functional theory study. *J. Phys. Chem. C* **116**, 16038–16046 (2012).
22. She, Z. W. *et al.* Combining theory and experiment in electrocatalysis: Insights into materials design. *Science (80-.)*. **355**, (2017).
23. Campos-Martin, J. M., Blanco-Brieva, G. & Fierro, J. L. G. Hydrogen peroxide synthesis: An outlook beyond the anthraquinone process. *Angew. Chemie - Int. Ed.* **45**, 6962–6984 (2006).
24. Goti, A. & Cardona, F. Hydrogen Peroxide in Green Oxidation Reactions: Recent Catalytic Processes. *Green Chem. React.* **53**, (2013).
25. Fenton, H. J. H. Oxidation of tartaric acid in presence of iron. *J. Chem. Soc. Trans.* **65**, 899–910 (1894).
26. Yang, S. *et al.* Toward the Decentralized Electrochemical Production of H₂ O₂ : A Focus on the Catalysis. *ACS Catal.* **8**, 4064–4081 (2018).
27. Ciriminna, R., Albanese, L., Meneguzzo, F. & Pagliaro, M. Hydrogen Peroxide: A Key Chemical for Today’s Sustainable Development. *ChemSusChem* **9**, 3374–3381 (2016).
28. Xia, Y. *et al.* Highly active and selective oxygen reduction to H₂O₂ on boron-doped carbon for high production rates. *Nat. Commun.* **12**, (2021).
29. Shi, X., Back, S., Gill, T. M., Siahrostami, S. & Zheng, X. Electrochemical Synthesis of H₂O₂ by Two-Electron Water Oxidation Reaction. *Chem* **7**, 38–63 (2021).
30. Perry, S. C. *et al.* Electrochemical synthesis of hydrogen peroxide from water and oxygen. *Nat. Rev. Chem.* **3**, 442–458 (2019).

31. Ticianelli, E. A., Derouin, C. R., Redondo, A. & Srinivasan, S. Methods to Advance Technology of Proton Exchange Membrane Fuel Cells. *J. Electrochem. Soc.* **135**, 2209–2214 (1988).
32. Mukerjee, S. & Srinivasan, S. Enhanced electrocatalysis of oxygen reduction on platinum alloys in proton exchange membrane fuel cells. *J. Electroanal. Chem.* **357**, 201–224 (1993).
33. Neyerlin, K. C., Gu, W., Jorne, J. & Gasteiger, H. A. Determination of Catalyst Unique Parameters for the Oxygen Reduction Reaction in a PEMFC. *J. Electrochem. Soc.* **153**, A1955 (2006).
34. Baker, D. R., Caulk, D. A., Neyerlin, K. C. & Murphy, M. W. Measurement of Oxygen Transport Resistance in PEM Fuel Cells by Limiting Current Methods. *J. Electrochem. Soc.* **156**, B991 (2009).
35. Chorkendorff, I. & Niemantsverdriet, S. W. *Concepts of Modern Catalysis and Kinetics*. (Wiley-VCH, 2013).
36. Busca, G. *Heterogeneous Catalytic Materials, Solids State Chemistry*. (1994).
37. Ertl, G., Knozinger, H., Schuth, F. & Weikamp, J. *Handbook of Heterogeneous Catalysis*. (Wiley-VCH Verlag GmbH, 2008).
38. Lloyd, L. *Handbook of Industrial Catalysts*. (Plenum, 2011).
39. Neagu, C., Jansen, H., Gardeniers, H. & Elwenspoek, M. Electrolysis of water: An actuation principle for MEMS with a big opportunity. *Mechatronics* **10**, 571–581 (2000).
40. Falcão, D. S. & Pinto, A. M. F. R. A review on PEM electrolyzer modelling: Guidelines for beginners. *J. Clean. Prod.* **261**, (2020).
41. Choi, C. H. *et al.* The Achilles' heel of iron-based catalysts during oxygen reduction in an acidic medium. *Energy Environ. Sci.* **11**, 3176–3182 (2018).
42. Feng, Q. *et al.* A review of proton exchange membrane water electrolysis on degradation mechanisms and mitigation strategies. *J. Power Sources* **366**, 33–55 (2017).
43. Dubau, L. *et al.* A review of PEM fuel cell durability: Materials degradation, local heterogeneities of aging and possible mitigation strategies. *Wiley Interdiscip. Rev. Energy Environ.* **3**, 540–560 (2014).
44. De Bruijn, F. A., Dam, V. A. T. & Janssen, G. J. M. Review: Durability and degradation issues of PEM fuel cell components. *Fuel Cells* **8**, 3–22 (2008).
45. Nørskov, J. K. *et al.* Origin of the overpotential for oxygen reduction at a fuel-cell cathode. *J. Phys. Chem. B* **108**, 17886–17892 (2004).

46. Kulkarni, A., Siahrostami, S., Patel, A. & Nørskov, J. K. Understanding Catalytic Activity Trends in the Oxygen Reduction Reaction. *Chem. Rev.* **118**, 2302–2312 (2018).
47. Kitchin, J. R., Nørskov, J. K., Barteau, M. A. & Chen, J. G. Modification of the surface electronic and chemical properties of Pt(111) by subsurface 3d transition metals. *J. Chem. Phys.* **120**, 10240–10246 (2004).
48. Xu, Y., Ruban, A. V. & Mavrikakis, M. Adsorption and dissociation of O₂ on Pt-Co and Pt-Fe Alloys. *J. Am. Chem. Soc.* **126**, 4717–4725 (2004).
49. Ruban, A. V., Skriver, H. L. & Nørskov, J. K. Surface segregation energies in transition-metal alloys. *Phys. Rev. B - Condens. Matter Mater. Phys.* **59**, 15990–16000 (1999).
50. Escudero-Escribano, M., Jensen, K. D. & Jensen, A. W. Recent advances in bimetallic electrocatalysts for oxygen reduction: design principles, structure-function relations and active phase elucidation. *Curr. Opin. Electrochem.* **8**, 135–146 (2018).
51. Zitolo, A. *et al.* Identification of catalytic sites in cobalt-nitrogen-carbon materials for the oxygen reduction reaction. *Nat. Commun.* **8**, 1–10 (2017).
52. Zitolo, A. *et al.* Identification of catalytic sites for oxygen reduction in iron- and nitrogen-doped graphene materials. *Nat. Mater.* **14**, 937–942 (2015).
53. Fei, H. *et al.* General synthesis and definitive structural identification of MN₄C₄ single-atom catalysts with tunable electrocatalytic activities. *Nat. Catal.* **1**, 63–72 (2018).
54. Greeley, J. *et al.* Alloys of platinum and early transition metals as oxygen reduction electrocatalysts. *Nat. Chem.* **1**, 552–556 (2009).
55. Jirkovský, J. S. *et al.* Single atom hot-spots at Au-Pd nanoalloys for electrocatalytic H₂O₂ production. *J. Am. Chem. Soc.* **133**, 19432–19441 (2011).
56. Pizzutilo, E. *et al.* Electrocatalytic synthesis of hydrogen peroxide on Au-Pd nanoparticles: From fundamentals to continuous production. *Chem. Phys. Lett.* **683**, 436–442 (2017).
57. Siahrostami, S. *et al.* Enabling direct H₂O₂ production through rational electrocatalyst design. *Nat. Mater.* **12**, 1137–1143 (2013).
58. Verdager-Casadevall, A. *et al.* Trends in the electrochemical synthesis of H₂O₂: Enhancing activity and selectivity by electrocatalytic site engineering. *Nano Lett.* **14**, 1603–1608 (2014).
59. Jirkovský, J. S., Halasa, M. & Schiffrin, D. J. Kinetics of electrocatalytic reduction of oxygen and hydrogen peroxide on dispersed gold nanoparticles.

- Phys. Chem. Chem. Phys.* **12**, 8042–8052 (2010).
60. Yamanaka, I. *et al.* Electrocatalysis of heat-treated cobalt-porphyrin/carbon for hydrogen peroxide formation. *Electrochim. Acta* **108**, 321–329 (2013).
 61. Campos, M., Siriwatcharapiboon, W., Potter, R. J. & Horswell, S. L. Selectivity of cobalt-based catalysts towards hydrogen peroxide formation during the reduction of oxygen. *Catal. Today* **202**, 135–143 (2013).
 62. Yamanaka, I. *et al.* Study of direct synthesis of hydrogen peroxide acid solutions at a heat-treated MnCl-porphyrin/activated carbon cathode from H₂ and O₂. *J. Phys. Chem. C* **116**, 4572–4583 (2012).
 63. Yang, S., Kim, J., Tak, Y. J., Soon, A. & Lee, H. Single-atom catalyst of platinum supported on titanium nitride for selective electrochemical reactions. *Angew. Chemie - Int. Ed.* **55**, 2058–2062 (2016).
 64. Choi, C. H. *et al.* Tuning selectivity of electrochemical reactions by atomically dispersed platinum catalyst. *Nat. Commun.* **7**, 1–9 (2016).
 65. Wang, A., Bonakdarpour, A., Wilkinson, D. P. & Gyenge, E. Novel organic redox catalyst for the electroreduction of oxygen to hydrogen peroxide. *Electrochim. Acta* **66**, 222–229 (2012).
 66. Hasché, F., Oezaslan, M., Strasser, P. & Feliinger, T. P. Electrocatalytic hydrogen peroxide formation on mesoporous non-metal nitrogen-doped carbon catalyst. *J. Energy Chem.* **25**, 251–257 (2016).
 67. Merle, G., Wessling, M. & Nijmeijer, K. Anion exchange membranes for alkaline fuel cells: A review. *J. Memb. Sci.* **377**, 1–35 (2011).
 68. Liu, H., Song, C., Tang, Y., Zhang, J. & Zhang, J. High-surface-area CoTMPP/C synthesized by ultrasonic spray pyrolysis for PEM fuel cell electrocatalysts. *Electrochim. Acta* **52**, 4532–4538 (2007).
 69. Zhang, J., Yang, H. & Liu, B. Coordination Engineering of Single-Atom Catalysts for the Oxygen Reduction Reaction: A Review. *Adv. Energy Mater.* **11**, 1–20 (2021).
 70. Chen, Z. *et al.* Coordination-controlled single-atom tungsten as a non-3d-metal oxygen reduction reaction electrocatalyst with ultrahigh mass activity. *Nano Energy* **60**, 394–403 (2019).
 71. Xiao, M. *et al.* Identification of binuclear Co₂N₅ active sites for oxygen reduction reaction with more than one magnitude higher activity than single atom CoN₄ site. *Nano Energy* **46**, 396–403 (2018).
 72. Zhu, C. *et al.* Self-Assembled Fe–N-Doped Carbon Nanotube Aerogels with Single-Atom Catalyst Feature as High-Efficiency Oxygen Reduction Electrocatalysts. *Small* **13**, 1–7 (2017).

73. Zagal, J. H. & Koper, M. T. M. Reactivity Descriptors for the Activity of Molecular MN₄ Catalysts for the Oxygen Reduction Reaction. *Angew. Chemie - Int. Ed.* **55**, 14510–14521 (2016).
74. Chung, H. T. *et al.* Direct atomic-level insight into the active sites of a high-performance PGM-free ORR catalyst. *Science (80-.)*. **357**, 479–484 (2017).
75. Yin, P. *et al.* Single Cobalt Atoms with Precise N-Coordination as Superior Oxygen Reduction Reaction Catalysts. *Angew. Chemie - Int. Ed.* **55**, 10800–10805 (2016).
76. Wang, G. *et al.* Highly active atomically dispersed CoN₄ fuel cell cathode catalysts derived from surfactant-assisted MOFs: Carbon-shell confinement strategy. *Energy Environ. Sci.* **12**, 250–260 (2019).
77. Gao, J. *et al.* Enabling Direct H₂O₂ Production in Acidic Media through Rational Design of Transition Metal Single Atom Catalyst. *Chem* **6**, 658–674 (2020).
78. Xi, J. *et al.* Highly active, selective, and stable Pd single-atom catalyst anchored on N-doped hollow carbon sphere for electrochemical H₂O₂ synthesis under acidic conditions. *J. Catal.* **393**, 313–323 (2021).
79. Zhang, Q. *et al.* Direct insights into the role of epoxy groups on cobalt sites for acidic H₂O₂ production. *Nat. Commun.* **11**, (2020).
80. Jung, E. *et al.* Atomic-level tuning of Co – N – C catalyst for production. *Nat. Mater.* **19**, 436–442 (2020).
81. Sun, T., Xu, L., Wang, D. & Li, Y. Metal organic frameworks derived single atom catalysts for electrocatalytic energy conversion. *Nano Res.* **12**, 2067–2080 (2019).
82. Liu, K., Wu, G. & Wang, G. Role of Local Carbon Structure Surrounding FeN₄ Sites in Boosting the Catalytic Activity for Oxygen Reduction. *J. Phys. Chem. C* **121**, 11319–11324 (2017).
83. Xiao, M. *et al.* Microporous Framework Induced Synthesis of Single-Atom Dispersed Fe-N-C Acidic ORR Catalyst and Its in Situ Reduced Fe-N₄ Active Site Identification Revealed by X-ray Absorption Spectroscopy. *ACS Catal.* **8**, 2824–2832 (2018).
84. Zeng, X. *et al.* Single-Atom to Single-Atom Grafting of Pt₁ onto Fe-N₄ Center: Pt₁@Fe-N-C Multifunctional Electrocatalyst with Significantly Enhanced Properties. *Adv. Energy Mater.* **8**, 1–8 (2018).
85. Liu, W. *et al.* A Durable Nickel Single-Atom Catalyst for Hydrogenation Reactions and Cellulose Valorization under Harsh Conditions. *Angew. Chemie - Int. Ed.* **57**, 7071–7075 (2018).

86. Sun, X. *et al.* High-performance single atom bifunctional oxygen catalysts derived from ZIF-67 superstructures. *Nano Energy* **61**, 245–250 (2019).
87. Jiang, R. *et al.* Edge-Site Engineering of Atomically Dispersed Fe-N₄ by Selective C-N Bond Cleavage for Enhanced Oxygen Reduction Reaction Activities. *J. Am. Chem. Soc.* **140**, 11594–11598 (2018).
88. Zheng, F. *et al.* Edge Effect Promotes Graphene-Confining Single-Atom Co-N₄ and Rh-N₄ for Bifunctional Oxygen Electrocatalysis. *J. Phys. Chem. C* **126**, 30–39 (2022).
89. Zhang, N. *et al.* High-purity pyrrole-type FeN₄ sites as a superior oxygen reduction electrocatalyst. *Energy Environ. Sci.* **13**, 111–118 (2020).
90. Zhao, X. & Liu, Y. Origin of Selective Production of Hydrogen Peroxide by Electrochemical Oxygen Reduction. *J. Am. Chem. Soc.* **143**, 9423–9428 (2021).
91. Ball, S. Core-Shell Catalysts in PEMFC Cathode Environments. in *Electrocatalysis in Fuel Cells: A Non- and Low- Platinum Approach* (ed. Shao, M.) 561–587 (Springer London, 2013). doi:10.1007/978-1-4471-4911-8_19
92. Stephens, I. E. L., Rossmeisl, J. & Chorkendorff, I. Toward sustainable fuel cells. *Science (80-.)*. **354**, 1378–1379 (2016).
93. Chen, C. *et al.* Highly crystalline multimetallic nanoframes with three-dimensional electrocatalytic surfaces. *Science (80-.)*. **343**, 1339–1343 (2014).
94. Stamenkovic, V. R. & Markovic, N. M. Nanosegregated cathode catalysts with ultra-low platinum loading. in *Annual Merit Review and Peer Evaluation Meeting* (2015).
95. Han, B. *et al.* Record activity and stability of dealloyed bimetallic catalysts for proton exchange membrane fuel cells. *Energy Environ. Sci.* **8**, 258–266 (2015).
96. Cui, C., Gan, L., Heggen, M., Rudi, S. & Strasser, P. Compositional segregation in shaped Pt alloy nanoparticles and their structural behaviour during electrocatalysis. *Nat. Mater.* **12**, 765–771 (2013).
97. Bu, L. *et al.* Biaxially strained PtPb/Pt core/shell nanoplate boosts oxygen reduction catalysis. *Science (80-.)*. **354**, 1410–1414 (2016).
98. Li, M. *et al.* Ultrafine jagged platinum nanowires enable ultrahigh mass activity for the oxygen reduction reaction. *Science (80-.)*. **354**, 1414–1419 (2016).
99. Mauger, S. A. *et al.* Fuel Cell Performance Implications of Membrane Electrode Assembly Fabrication with Platinum-Nickel Nanowire Catalysts. *J. Electrochem. Soc.* **165**, F238–F245 (2018).
100. Ly, A., Asset, T. & Atanassov, P. Integrating nanostructured Pt-based

- electrocatalysts in proton exchange membrane fuel cells. *J. Power Sources* **478**, 228516 (2020).
101. Oezaslan, M., Heggen, M. & Strasser, P. Size-Dependent morphology of dealloyed bimetallic catalysts: Linking the nano to the macro scale. *J. Am. Chem. Soc.* **134**, 514–524 (2012).
 102. Kongkanand, A. *et al.* Achieving High-Power PEM Fuel Cell Performance with an Ultralow-Pt-Content Core-Shell Catalyst. *ACS Catal.* **6**, 1578–1583 (2016).
 103. Dubau, L. *et al.* Tuning the Performance and the Stability of Porous Hollow PtNi/C Nanostructures for the Oxygen Reduction Reaction. *ACS Catal.* **5**, 5333–5341 (2015).
 104. Li, B. *et al.* High performance octahedral PtNi/C catalysts investigated from rotating disk electrode to membrane electrode assembly. *Nano Res.* **12**, 281–287 (2019).
 105. Dao, D. Van, Adilbish, G., Le, T. D., Lee, I. H. & Yu, Y. T. Triple phase boundary and power density enhancement in PEMFCs of a Pt/C electrode with double catalyst layers. *RSC Adv.* **9**, 15635–15641 (2019).
 106. O’Hayre, R., Barnett, D. M. & Prinz, F. B. The Triple Phase Boundary. *J. Electrochem. Soc.* **152**, A439 (2005).
 107. Karan, K. PEFC catalyst layer: Recent advances in materials, microstructural characterization, and modeling. *Curr. Opin. Electrochem.* **5**, 27–35 (2017).
 108. Lopez-Haro, M. *et al.* Three-dimensional analysis of Nafion layers in fuel cell electrodes. *Nat. Commun.* **5**, 1–6 (2014).
 109. Uchida, M., Aoyama, Y., Eda, N. & Ohta, A. Investigation of the Microstructure in the Catalyst Layer and Effects of Both Perfluorosulfonate Ionomer and PTFE- Loaded Carbon on the Catalyst Layer of Polymer Electrolyte Fuel Cells. *J. Electrochem. Soc.* **142**, 4143–4149 (1995).
 110. Ngo, T. T., Yu, T. L. & Lin, H. L. Nafion-based membrane electrode assemblies prepared from catalyst inks containing alcohol/water solvent mixtures. *J. Power Sources* **238**, 1–10 (2013).
 111. Uchida, M., Aoyama, Y., Eda, N. & Ohta, A. New Preparation Method for Polymer- Electrolyte Fuel Cells. *J. Electrochem. Soc.* **142**, 463–468 (1995).
 112. Kusoglu, A. & Weber, A. Z. New Insights into Perfluorinated Sulfonic-Acid Ionomers. *Chem. Rev.* **117**, 987–1104 (2017).
 113. Liu, J. & Zenyuk, I. V. Proton transport in ionomer-free regions of polymer electrolyte fuel cells and implications for oxygen reduction reaction. *Curr. Opin. Electrochem.* **12**, 202–208 (2018).

114. Jinnouchi, R., Kudo, K., Kitano, N. & Morimoto, Y. Molecular Dynamics Simulations on O₂ Permeation through Nafion Ionomer on Platinum Surface. *Electrochim. Acta* **188**, 767–776 (2016).
115. Kodama, K. *et al.* Effect of the Side-Chain Structure of Perfluoro-Sulfonic Acid Ionomers on the Oxygen Reduction Reaction on the Surface of Pt. *ACS Catal.* **8**, 694–700 (2018).
116. Yang, L. *et al.* Activity, Performance, and Durability for the Reduction of Oxygen in PEM Fuel Cells, of Fe/N/C Electrocatalysts Obtained from the Pyrolysis of Metal-Organic-Framework and Iron Porphyrin Precursors. *Electrochim. Acta* **159**, 184–197 (2015).
117. Harzer, G. S., Orfanidi, A., El-Sayed, H., Madkikar, P. & Gasteiger, H. A. Tailoring Catalyst Morphology towards High Performance for Low Pt Loaded PEMFC Cathodes. *J. Electrochem. Soc.* **165**, F770–F779 (2018).
118. Huang, J., Malek, A., Zhang, J. & Eikerling, M. H. Non-monotonic Surface Charging Behavior of Platinum: A Paradigm Change. *J. Phys. Chem. C* **120**, 13587–13595 (2016).
119. Seidel, Y. E. *et al.* Mesoscopic mass transport effects in electrocatalytic processes. *Faraday Discuss.* **140**, 9–10 (2008).
120. Sun, Y. *et al.* Activity-Selectivity Trends in the Electrochemical Production of Hydrogen Peroxide over Single-Site Metal-Nitrogen-Carbon Catalysts. *J. Am. Chem. Soc.* **141**, 12372–12381 (2019).
121. Choi, C. H. *et al.* Hydrogen peroxide synthesis via enhanced two-electron oxygen reduction pathway on carbon-coated pt surface. *J. Phys. Chem. C* **118**, 30063–30070 (2014).
122. Jaouen, F. O₂ reduction mechanism on non-noble metal catalysts for PEM fuel cells. Part II: A porous-electrode model to predict the quantity of H₂O₂ detected by rotating ring-disk-electrode. *J. Phys. Chem. C* **113**, 15433–15443 (2009).
123. Zhao, L. *et al.* Materials Engineering toward Durable Electrocatalysts for Proton Exchange Membrane Fuel Cells. *Adv. Energy Mater.* **12**, 1–27 (2022).
124. Ehelebe, K. *et al.* Benchmarking Fuel Cell Electrocatalysts Using Gas Diffusion Electrodes: Inter-lab Comparison and Best Practices. *ACS Energy Lett.* **7**, 816–826 (2022).
125. Zalis, C. M., Kramer, D. & Kucernak, A. R. Electrocatalytic performance of fuel cell reactions at low catalyst loading and high mass transport. *Phys. Chem. Chem. Phys.* **15**, 4329–4340 (2013).
126. Bragg, W. H. & Bragg, W. L. The reflection of X-rays by crystals. *Proc. R. Soc.*

- Lond. A* **88**, 428–438 (1913).
127. Engelhard, M. H., Droubay, T. C. & Du, Y. X-ray photoelectron spectroscopy applications. *Encycl. Spectrosc. Spectrom.* 716–724 (2016). doi:10.1016/B978-0-12-409547-2.12102-X
 128. Shard, A. G. Detection limits in XPS for more than 6000 binary systems using Al and Mg K α X-rays. *Surf. Interface Anal.* **46**, 175–185 (2014).
 129. Williams, D. & Carter, C. B. *Transmission Electron Microscopy, Vol. 1 - Basics*. (Plenum Press, 1996).
 130. Otten, M. A. X. T. High-Angle Annular Dark-Field Imaging on a TEM / STEM System. *J. Electron Microsc. Tech.* **17**, 221–230 (1991).
 131. Jenkins, R. & De Vries, J. L. *Practical X-Ray Spectrometry*. (Springer, 1969).
 132. Koningsberger, D. C. & Prins, R. *X-ray absorption : principles, applications, techniques of EXAFS, SEXAFS, and XANES*. (Wiley, 1988).
 133. CORNELIS, R. & NORDBERG, M. CHAPTER 2 - General Chemistry, Sampling, Analytical Methods, and Speciation**Partly based on Chapter 2: General chemistry of metals by V. Vouk and Chapter 3: Sampling and analytical methods by T. J. Kneip and L. Friberg in Friberg et al. (1986). in (eds. Nordberg, G. F., Fowler, B. A., Nordberg, M. & Friberg, L. T. B. T.-H. on the T. of M. (Third E.) 11–38 (Academic Press, 2007). doi:https://doi.org/10.1016/B978-012369413-3/50057-4
 134. Elmer, P. *The 30-minute Guide to ICP-MS*. Perkin Elmer, Shelton CT (2001). doi:10.1016/j.pnucene.2012.01.005
 135. Stevens, N. P. C., Rooney, M. B., Bond, a M. & Feldberg, S. W. A Comparison of Simulated and Experimental Voltammograms Obtained for the [Fe(CN)₆]^{3-/4-} Couple in the Absence of Added Supporting Electrolyte at a Rotating Ring Disk Electrode. **105**, (2001).
 136. Klassen, N. V., Marchington, D. & McGowan, H. C. E. H₂O₂ Determination by the I₃⁻ Method and by KMnO₄ Titration. *Anal. Chem.* **66**, 2921–2925 (1994).
 137. Skoog, D., Holler, F. & Crouch, S. *Principles of Instrumental Analysis*. (Thomson Brooks/Cole, 2007).
 138. Stöber, W. & Fink, A. Controlled Growth of Monodisperse Silica Spheres in the Micron Size Range. *J. Colloid Interface Sci. Sci.* **26**, 62–69 (1968).
 139. Hummers, W. S. & Offeman, R. E. Preparation of Graphitic Oxide. *J. Am. Chem. Soc.* **80**, 1339 (1958).
 140. Xi, J. *et al.* Confined-interface-directed synthesis of Palladium single-atom

- catalysts on graphene/amorphous carbon. *Appl. Catal. B Environ.* **225**, 291–297 (2018).
141. Lee, J. S., You, K. H. & Park, C. B. Highly photoactive, low bandgap TiO₂ nanoparticles wrapped by graphene. *Adv. Mater.* **24**, 1084–1088 (2012).
 142. Smith, R. K., Lewis, P. A. & Weiss, P. S. Patterning self-assembled monolayers. *Prog. Surf. Sci.* **75**, 1–68 (2004).
 143. Mostofi Sarkari, N., Doğan, Ö., Bat, E., Mohseni, M. & Ebrahimi, M. Assessing effects of (3-aminopropyl)trimethoxysilane self-assembled layers on surface characteristics of organosilane-grafted moisture-crosslinked polyethylene substrate: A comparative study between chemical vapor deposition and plasma-facilitated in situ. *Appl. Surf. Sci.* **497**, 143751 (2019).
 144. Lee, H., Dellatore, S. M., Miller, W. M. & Messersmith, P. B. Mussel-Inspired Surface Chemistry for Multifunctional Coatings. *Science (80-.)*. **318**, 426–431 (2007).
 145. Lange, C. W. & Pierpont, C. G. Nickel complexes containing catecholate, benzoquinone and semiquinone radical ligands. *Inorganica Chim. Acta* **263**, 219–224 (1997).
 146. Ledesma, E. B., Marsh, N. D., Sandrowitz, A. K. & Wornat, M. J. An experimental study on the thermal decomposition of catechol. *Proc. Combust. Inst.* **29**, 2299–2306 (2002).
 147. Medha, I. *et al.* (3-Aminopropyl)triethoxysilane and iron rice straw biochar composites for the sorption of Cr (VI) and Zn (II) using the extract of heavy metals contaminated soil. *Sci. Total Environ.* **771**, 144764 (2021).
 148. Jung, E. *et al.* Atomic-level tuning of Co–N–C catalyst for high-performance electrochemical H₂O₂ production. *Nat. Mater.* **19**, 436–442 (2020).
 149. Gasteiger, H. A., Kocha, S. S., Sompalli, B. & Wagner, F. T. Activity benchmarks and requirements for Pt, Pt-alloy, and non-Pt oxygen reduction catalysts for PEMFCs. *Appl. Catal. B Environ.* **56**, 9–35 (2005).
 150. Lin, X., Zalitis, C. M., Sharman, J. & Kucernak, A. Electrocatalyst Performance at the Gas/Electrolyte Interface under High-Mass-Transport Conditions: Optimization of the ‘floating Electrode’ Method. *ACS Appl. Mater. Interfaces* **12**, 47467–47481 (2020).
 151. Zhang, G. & Kucernak, A. Gas Accessible Membrane Electrode (GAME): A Versatile Platform for Elucidating Electrocatalytic Processes Using Real-Time and in Situ Hyphenated Electrochemical Techniques. *ACS Catal.* **10**, 9684–9693 (2020).
 152. Martens, S. *et al.* A comparison of rotating disc electrode, floating electrode

- technique and membrane electrode assembly measurements for catalyst testing. *J. Power Sources* **392**, 274–284 (2018).
153. Jackson, C., Lin, X., Levecque, P. B. J. & Kucernak, A. R. J. Toward Understanding the Utilization of Oxygen Reduction Electrocatalysts under High Mass Transport Conditions and High Overpotentials. *ACS Catal.* **12**, 200–211 (2022).
 154. Gómez-Marín, A. M., Schouten, K. J. P., Koper, M. T. M. & Feliu, J. M. Interaction of hydrogen peroxide with a Pt(111) electrode. *Electrochem. commun.* **22**, 153–156 (2012).
 155. Gómez-Marín, A. M., Boronat, A. & Feliu, J. M. Electrocatalytic oxidation and reduction of H₂O₂ on Au single crystals. *Russ. J. Electrochem.* **53**, 1029–1041 (2017).
 156. Vidal-Iglesias, F. J., Solla-Gullón, J., Herrero, E. & Feliu, J. M. Au Electrocatalysis for Oxygen Reduction. in *Electrocatalysis in Fuel Cells: A Non- and Low- Platinum Approach* (ed. Shao, M.) 483–512 (Springer London, 2013). doi:10.1007/978-1-4471-4911-8_16
 157. Servi, A. T. *et al.* The effects of iCVD film thickness and conformality on the permeability and wetting of MD membranes. *J. Memb. Sci.* **523**, 470–479 (2017).
 158. Wang, Y. L. *et al.* In Situ Deposition of Pd during Oxygen Reduction Yields Highly Selective and Active Electrocatalysts for Direct H₂O₂ Production. *ACS Catal.* **9**, 8453–8463 (2019).
 159. Haraldsted, J.-P. B. *et al.* Trace anodic migration of iridium and titanium ions and subsequent cathodic selectivity degradation in acid electrolysis systems. *Mater. Today Energy* **14**, (2019).
 160. Čolić, V., Yang, S., Révay, Z., Stephens, I. E. L. & Chorkendorff, I. Carbon catalysts for electrochemical hydrogen peroxide production in acidic media. *Electrochim. Acta* **272**, 192–202 (2018).
 161. Perez, J. F. *et al.* The pressurized-jet aerator : a new aeration system for high-performing H₂O₂ electrolyzers. *Electrochem. commun.* **89**, 19–22 (2018).
 162. Ma, S. *et al.* Ionic Exchange: Ionic Exchange of Metal–Organic Frameworks for Constructing Unsaturated Copper Single- Atom Catalysts for Boosting Oxygen Reduction Reaction (Small 23/2020). *Small* **16**, 2070129 (2020).
 163. Wang, X. *et al.* Regulation of Coordination Number over Single Co Sites: Triggering the Efficient Electroreduction of CO₂. *Angew. Chemie - Int. Ed.* **57**, 1944–1948 (2018).
 164. De Jong, K. P. *Synthesis of Solid Catalysts*. (Wiley-VCH Verlag GmbH, 2009).

165. Cejka, J., Corma, A. & Jones, S. *Catalyst Preparation, Science, and Engineering*. (CRC Press, Taylor and Francis Group, 2006).
166. Mujahid Alam, M., Mubarak, A. T., Assiri, M. A., Merajuddin Ahmed, S. & Fouda, A. M. A facile and efficient synthesis of 1,8-dioxodecahydroacridines derivatives catalyzed by cobalt-alanine metal complex under aqueous ethanol media. *BMC Chem.* **13**, 1–10 (2019).
167. Wang, D., Dong, N., Niu, Y. & Hui, S. A Review of Urea Pyrolysis to Produce NH₃ Used for NO_x Removal. *J. Chem.* **2019**, (2019).
168. Lau, V. W. hei & Lotsch, B. V. A Tour-Guide through Carbon Nitride-Land: Structure- and Dimensionality-Dependent Properties for Photo(Electro)Chemical Energy Conversion and Storage. *Adv. Energy Mater.* **12**, (2022).
169. Zhong, H., Estudillo-Wong, L. A., Gao, Y., Feng, Y. & Alonso-Vante, N. Cobalt-Based Multicomponent Oxygen Reduction Reaction Electrocatalysts Generated by Melamine Thermal Pyrolysis with High Performance in an Alkaline Hydrogen/Oxygen Microfuel Cell. *ACS Appl. Mater. Interfaces* **12**, 21605–21615 (2020).
170. Yang, H. Bin *et al.* Atomically dispersed Ni(i) as the active site for electrochemical CO₂ reduction. *Nat. Energy* **3**, 140–147 (2018).
171. Sahu, N. K., Prakash, A. & Bahadur, D. Role of different platinum precursors on the formation and reaction mechanism of FePt nanoparticles and their electrocatalytic performance towards methanol oxidation. *Dalt. Trans.* **43**, 4892–4900 (2014).
172. Volshtein, L. M. & Volodina, I. O. Cis-isomer intracomplex salt bivalent platinum with alpha-alanine. in *Presented by academecian A.A. Grinbuberg on November 21, 1959* (1959).
173. Nelson, D. D. The preparation of the coordination compounds of platinum (II) and arginine, histidine, lysine, and serine. (University of the Pacific, 1964).
174. Tian, S. *et al.* Catalytic Amination of Polylactic Acid to Alanine. *J. Am. Chem. Soc.* **143**, 16358–16363 (2021).
175. Fawzy, A. A Comparative Kinetic Study of Silver(I)-Catalyzed Oxidations of Alanine and Valine by Platinum (IV) in Perchloric and Sulfuric Acids Solutions. *Am. J. Phys. Chem.* **5**, 65 (2016).
176. Wei, H. *et al.* Ultralow-temperature photochemical synthesis of atomically dispersed Pt catalysts for the hydrogen evolution reaction. *Chem. Sci.* **10**, 2830–2836 (2019).
177. Primbs, M. *et al.* Establishing reactivity descriptors for platinum group metal

(PGM)-free Fe-N-C catalysts for PEM fuel cells. *Energy Environ. Sci.* **13**, 2480–2500 (2020).

Appendices

Appendix A

Chapter 4

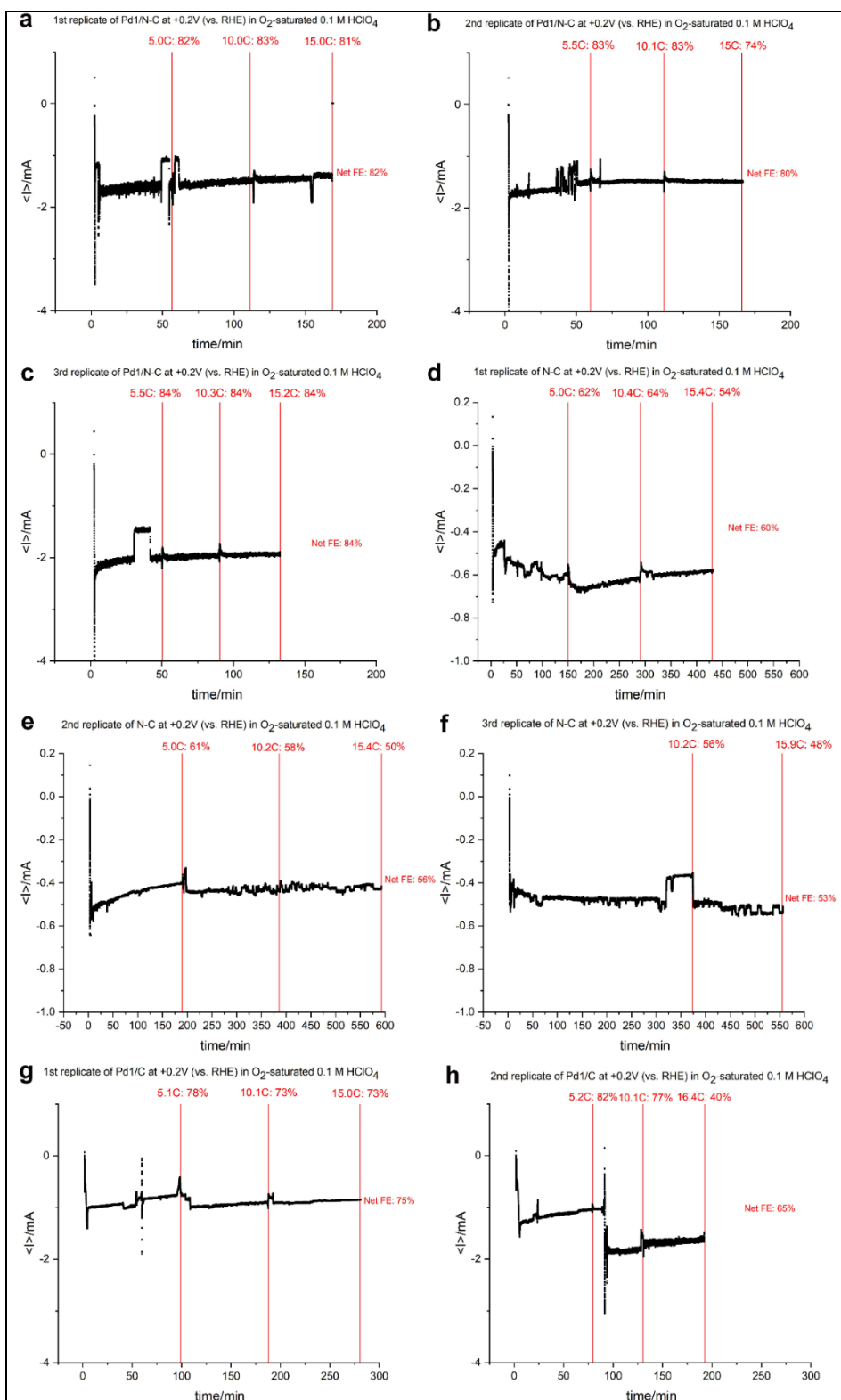
Figure A.1: GDE CA experiments from *Highly Active, selective, and stable Pd single-atom catalyst anchored on N-doped hollow carbon sphere for electrochemical H₂O₂ synthesis under acidic conditions*.²⁸

Chapter 5

Figure A.2: CA experiments from *Gas Accessible Membrane Electrode (GAME): A Versatile Platform for Elucidating Electrocatalytic Processes Using Real-Time and in Situ Hyphenated Electrochemical Techniques*.¹⁵¹

Figure A.3-6: CV and CA experiments showing the difficulties of controlling the activity from an abundantly available Au surface.

Figure A.7: In-situ electrodeposition of Pd²⁺ species during ORR operations, data adapted from Wang et al.¹⁵⁸



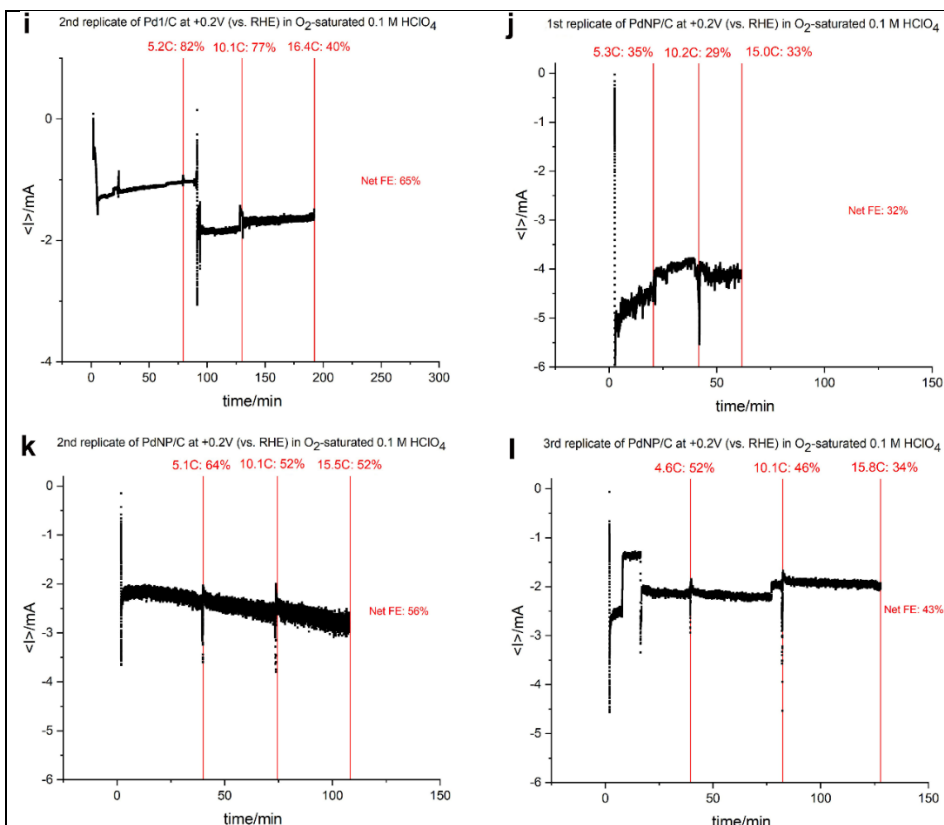


Figure A.1: Chronoamperometry (CA) of the experiments in three-compartment set-ups. (a-c) replicated test of Pd1/N-C SAC, (e-g) replicated test of N-C catalyst, (h-k) replicated test of Pd1/C SAC and (j-l) replicated test of PdNP/C catalyst. Experiments were performed at +0.2V (vs. RHE) in O₂-saturated 0.1 M HClO₄ and were concluded after an accumulated charge of at least 15 C. H₂O₂ was quantified four times in each experiment (0C, 5C, 10C, 15C) to determine the faradaic efficiency towards H₂O₂ of certain intervals of accumulated charge throughout the experiment (0-5C, 5-10C, 10-15C) and the net total faradaic efficiency (0-15C). H₂O₂ was quantified by permanganate titration using a 0.02 M KMnO₄ titrant. CA's were performed by Sungeun Yang, and the graphical figures were made by Jens-Peter Haraldsted. From ⁷⁸

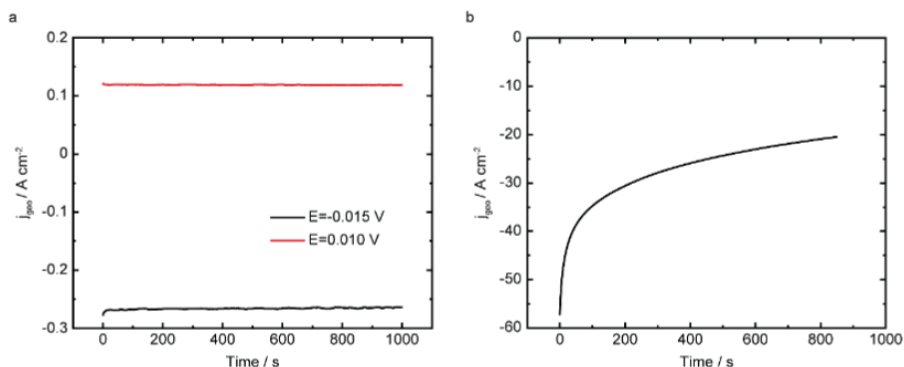


Figure A.2: CA experiments of (a) HER (black, at $-0.015 \text{ V}_{\text{VRHE}}$) and HOR (red, at $0.010 \text{ V}_{\text{VRHE}}$) recorded on an Au/PCTE electrode with a loading of $3.18 \mu\text{g}_{\text{Pt}} \cdot \text{cm}^{-2}$ in 4 M HClO_4 and (b) ORR at $+0.6 \text{ V}_{\text{VRHE}}$ in 1 M HClO_4 . This gas accessible membrane electrode is structurally similar to the floating electrodes and operates on essentially the same principles. From ¹⁵¹

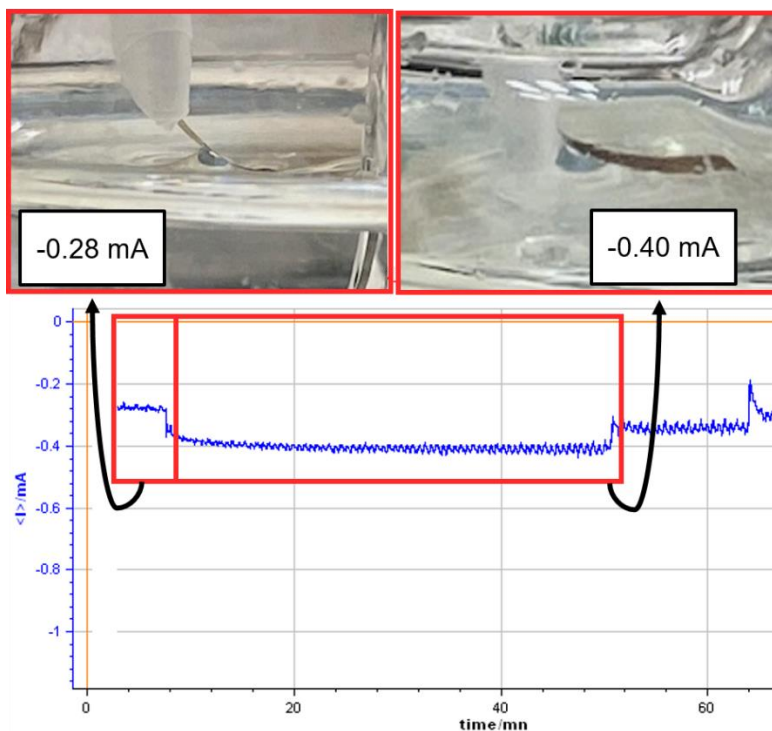


Figure A.3: AuFET experiment (blank) showing how roughly 70% of the Au's geometric surface area in contact with the electrolyte (left) results in roughly 70% of the current: roughly -0.28 mA . Increasing the contact of the Au's geometric surface area to roughly 100% yields the proportional amount of current expected: roughly -0.40 mA . CA was conducted at $+0.2 \text{ V}_{\text{VRHE}}$ in 1 M HClO_4 at room temperature.



Figure A.4: AuFET experiment where a drop accumulates above the electrolyte contact, resulting in increased currents over time due to increased contact of Au to the electrolyte. CA was conducted at $+0.2 V_{\text{VRHE}}$ with O_2 -headspace in 1 M HClO_4 at room temperature.

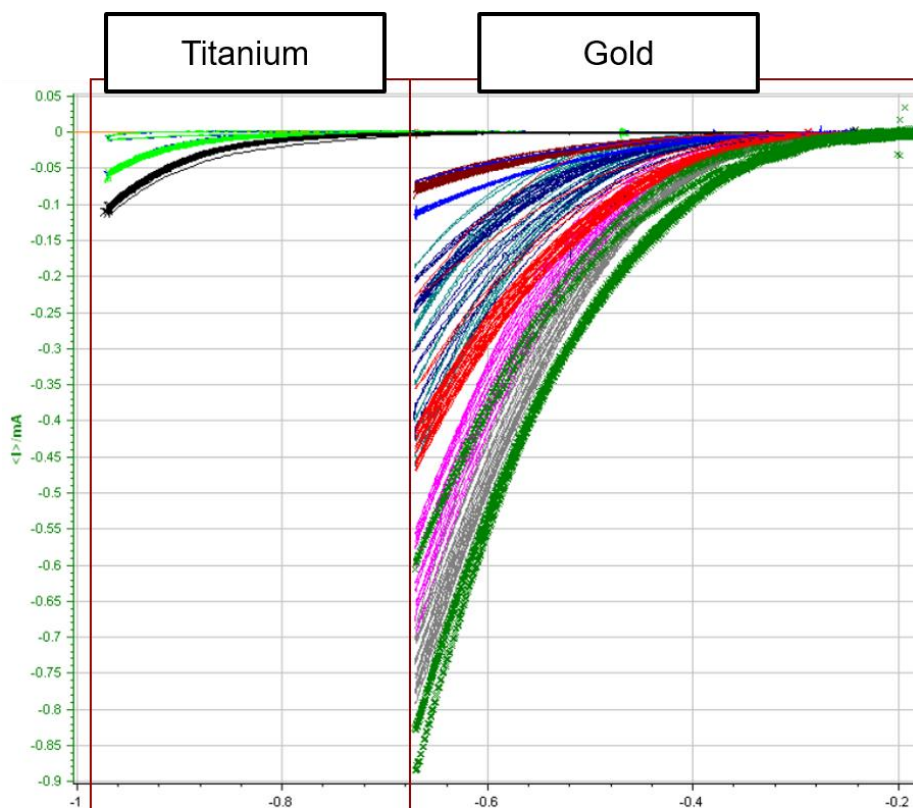


Figure A.5: CV's ($\text{mA}_{\text{measured}}$ against $V_{\text{vHg/HgSO}_4}$) of FET experiments loaded with Vulcan carbon support, where Au-coated FE's are more active than Ti-coated FE's. Au-coated floating electrodes were not only more active, but also have variable currents despite attempting to account for gold area in contact with electrolyte. CV's conducted with a $20 \text{ mV} \cdot \text{s}^{-1}$ scan speed and V is against an Hg/HgSO₄ reference electrode ($V_{\text{vHg/HgSO}_4}$). Conditions with an O₂-headspace in 1 M HClO₄ at room temperature.

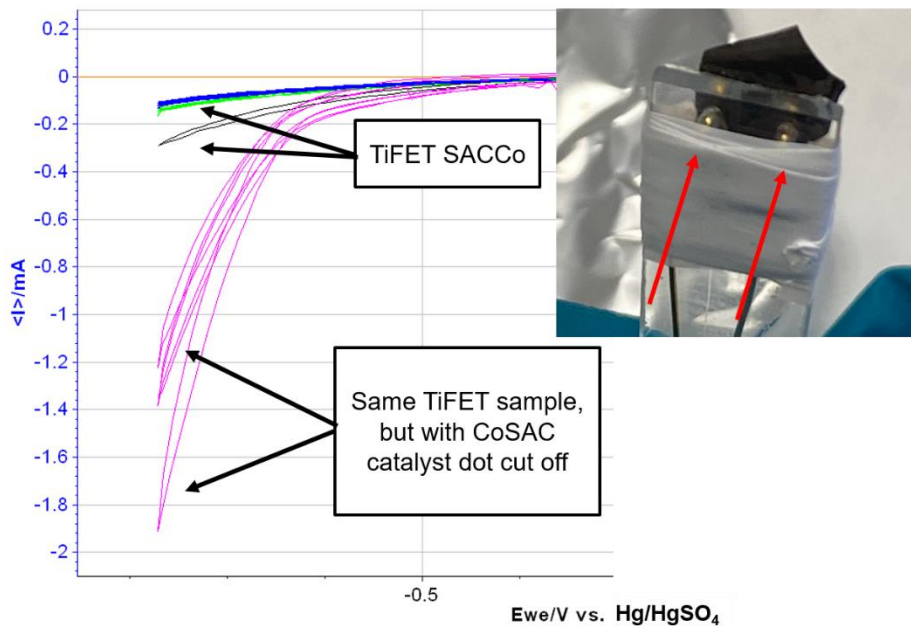


Figure A.6: CV's ($\text{mA}_{\text{measured}}$ against $V_{\text{vHg/HgSO}_4}$) of FET experiments loaded with CoSAC, where Ti-coated FE's activity is suspected to be contaminated by the Au-wires used as a current collector in direct contact with the FE. Sanity check of the TiFE with the catalyst spot removed and the with the electrolyte levels slightly higher to accommodate a shorter FE, results in clear electrochemical activity that could only come from the Au. CV's conducted with a $20 \text{ mV} \cdot \text{s}^{-1}$ scan speed and V is against an Hg/HgSO₄ reference electrode ($V_{\text{vHg/HgSO}_4}$). Conditions with an O₂-headspace in 1 M HClO₄ at room temperature.

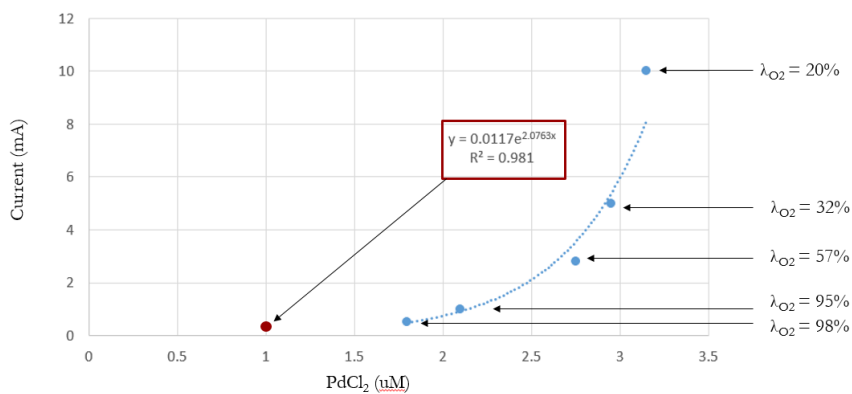


Figure A.7: In-situ electrodeposition of Pd²⁺ species (at +0.45 V_{VRHE}) in O₂-saturated electrolyte using varying concentrations of PdCl₂. λ_{O₂} values are from RRDE post-electrodeposition. Data points (light blue) are adapted from Wang et al.¹⁵⁸ Dark red data point is the value adapted for the Pd1/N-C catalyst (yielding a surprisingly low λ_{Faradaic} value of 33%).

Appendix B

Chapter 6

Figure B.1: Summary of allyl-Pd₂ wet-impregnated onto a C₃N₄ support. HAADF-TEM images performed by Frederik Ryberg Madsen.

Figure B.2: Scaling relations of M-N/C catalysts by Gao et al.⁷⁷

Figure B.3: Chemical synthesis of cobalt alanine by Mujahid Alam et al.¹⁶⁶

Figure B.4-6: RRDE CV experiments.

Figure B.7: TGA of Pt-based precursors by Sahu et al.¹⁷¹

Figure B.8-13: RRDE CV experiments.

Figure B.14: Effect of CoSAC catalyst loading on RRDE CV experiments by Gao et al.⁷⁷

Figure B.15-29: XPS analysis.

Figure B.30-32: XRD analysis.

Figure B.33-34: RRDE CA experiments.

Figure B.35: RRDE CA experiment of CoSAC by Gao et al.⁷⁷

Figure B.36: TiFET CA experiment of PdSAC.

Figure B.37: RDE+TiFET+MEA CV experiments of CoSAC and IrSAC.

Figure B.38: Inset of Figure 6.12 (a, b).

Figure B.39-47: HAADF-TEM images of IrSAC and CoSAC with accompanying EDS analysis (performed by Sofie Colding-Jørgensen).

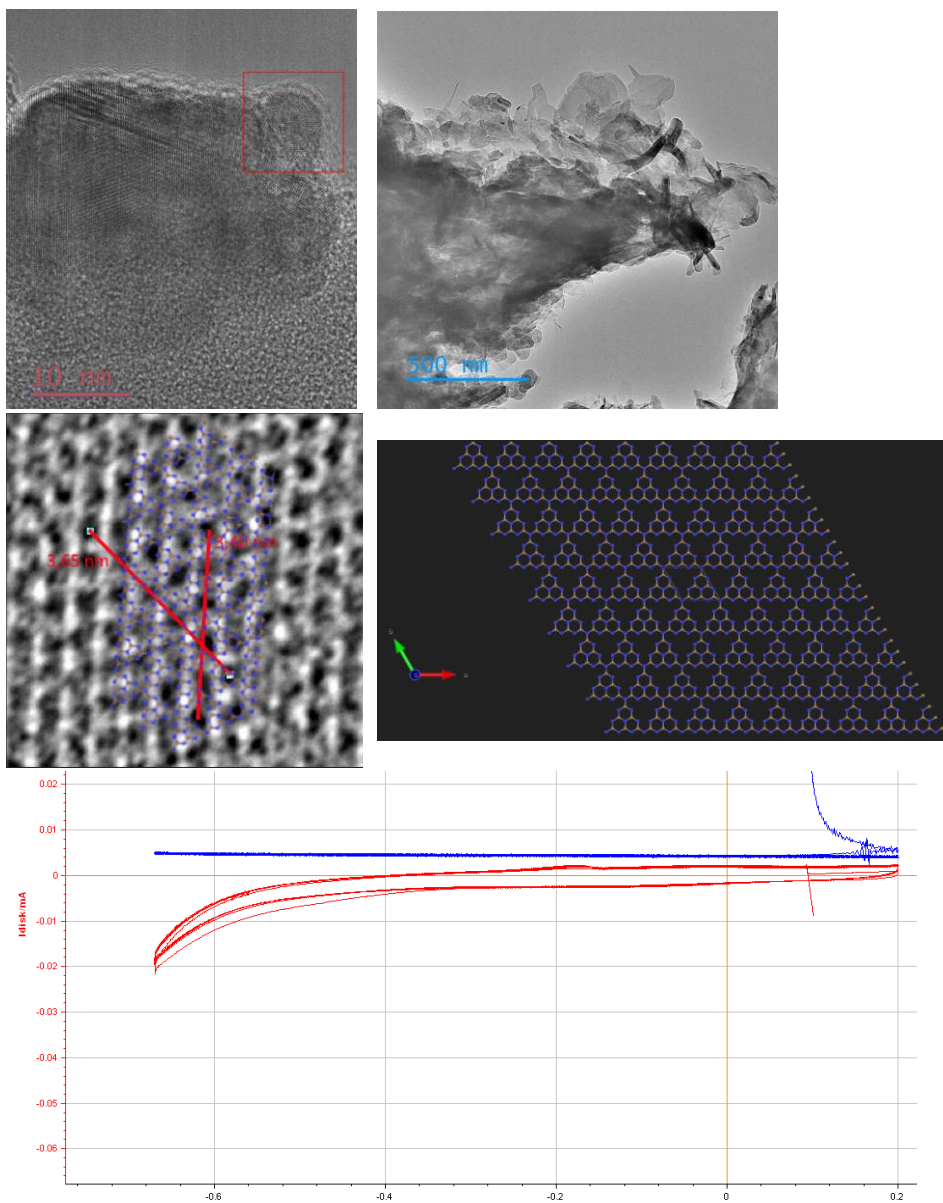


Figure B.1: RRDE experiment shows that Pd₂ precursor impregnated onto C₃N₄ support is completely inactive. 15 μg catalyst (C₃N₄+Pd₂) drop-casted onto 0.2 cm². TEM characterization was performed by Frederik Ryberg Madsen as part of his Master's thesis project.

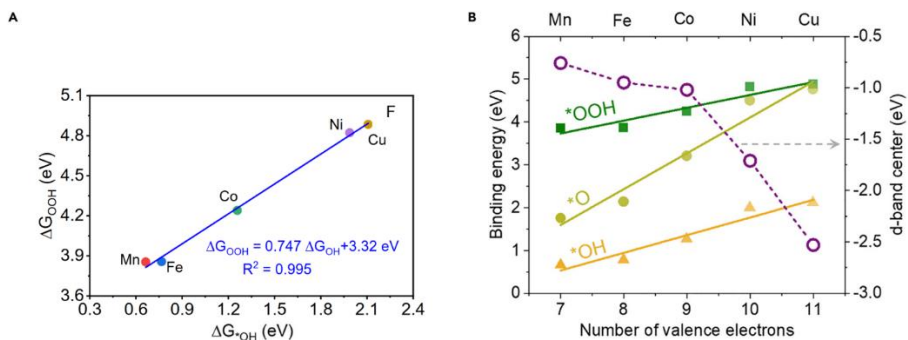


Figure B.2: (a) Scaling relationship between the adsorption energy of $*OH$ and $*OOH$. (b) Binding energy of $*OOH$, $*O$, and $*OH$ on M-SAC (M = Mn, Fe, Co, Ni, and Cu) and d-band center (open circle) of M atom in M-SAC (M = Mn, Fe, Co, Ni, and Cu).⁷⁷

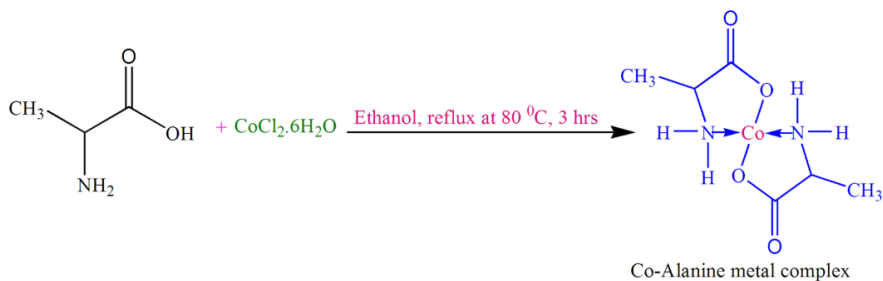


Figure B.3: Synthesis of Cobalt Alanine. Cobalt Alanine is a catalyst for the polymerization of functionalized benzene precursors.¹⁶⁶

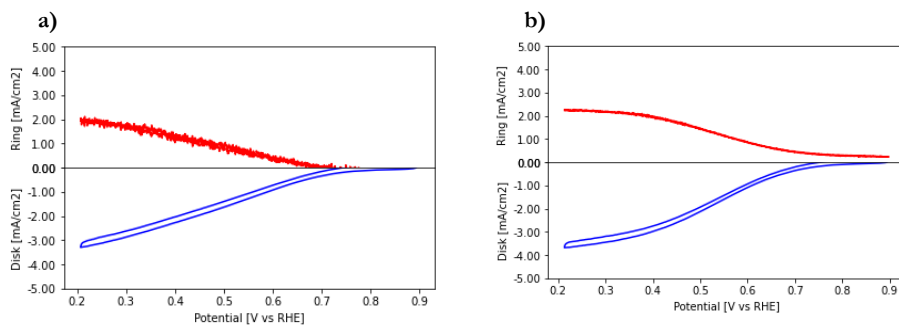


Figure B.4: RRDE measurements of (a) CoAcac(2.2), (b) CoAcac(3) samples for $2e^-$ ORR in acidic conditions. Catalyst loadings are $75 \mu\text{g}\cdot\text{cm}^{-2}$. Measurements in O_2 -saturated 0.1 M HClO_4 with a scan speed of $20 \text{ mV}\cdot\text{s}^{-1}$ and a rotating rate of 1600 rpm at room temperature.

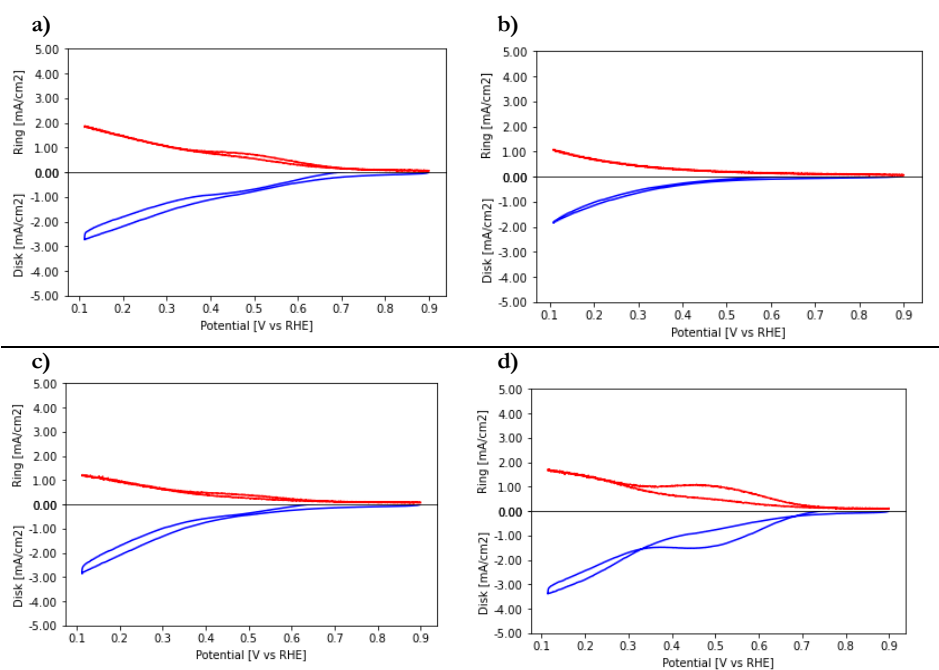


Figure B.5: RRDE measurements of (a) IrSAC(4), (b) IrSAC(4.2), (c) IrSAC(5), (d) IrSAC(6) samples for $2e^-$ ORR in acidic conditions. Catalyst loadings are $75 \mu\text{g}\cdot\text{cm}^{-2}$. Measurements in O_2 -saturated 0.1 M HClO_4 with a scan speed of $20 \text{ mV}\cdot\text{s}^{-1}$ and a rotating rate of 1600 rpm at room temperature.

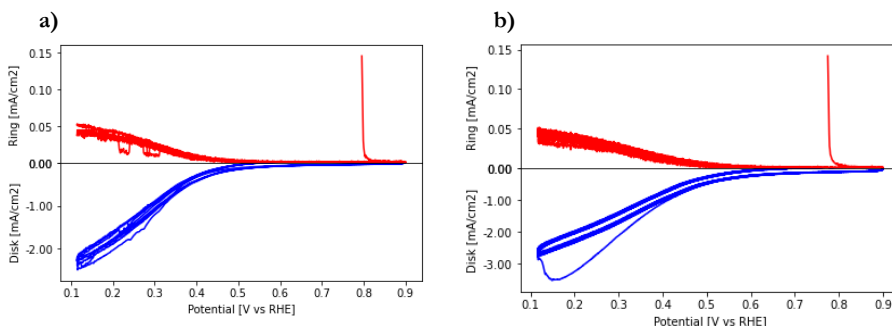


Figure B.6: RRDE measurements of (a) PtAcac1 (skip acid wash and reanneal steps) versus (b) PtAcac1.2 (reannealed) samples for $2e^-$ ORR in acidic conditions. Catalyst loadings are $75 \mu\text{g}^*\text{cm}^{-2}$. Measurements in O_2 -saturated 0.1 M HClO_4 with a scan speed of $20 \text{ mV}^*\text{s}^{-1}$ and a rotating rate of 1600 rpm at room temperature.

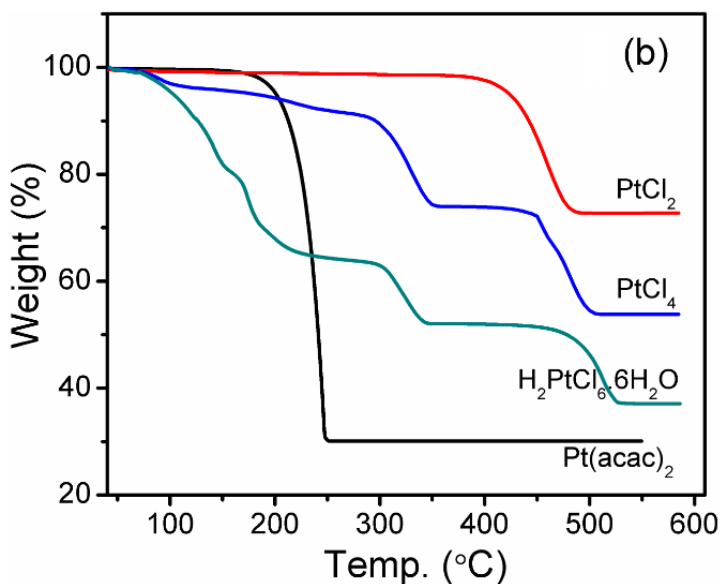


Figure B.7: Sahu et al.'s thermal gravimetric analysis, where they measured the mass loss of various Pt precursors (PtAcac , PtCl_2 , PtCl_4 , and H_2PtCl_6) as they are heated up to 600°C ($10^\circ\text{C}^*\text{min}^{-1}$) in an inert N_2 atmosphere.¹⁷¹

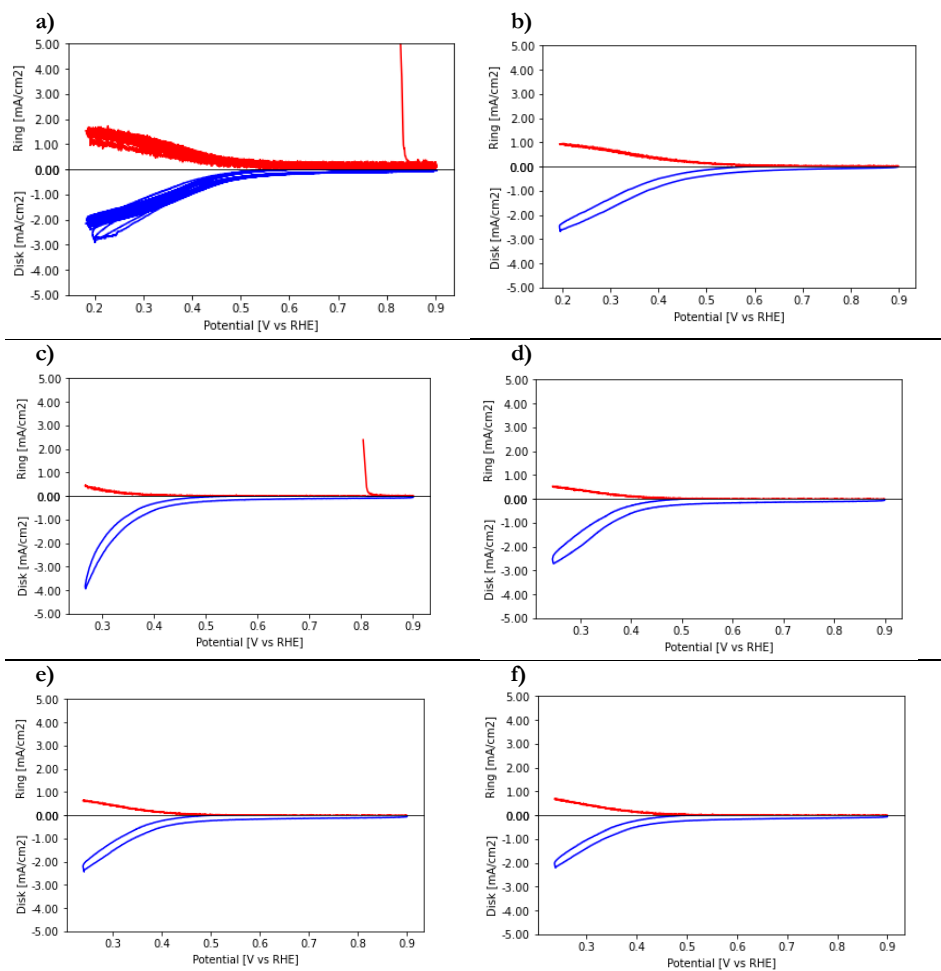


Figure B.8: RRDE measurements of (a) PtCl_2 , (b) PtAn_2 , and (c-d-e-f) PtCl_6 (cycles 1-5-10-15) samples for $2e^-$ ORR in acidic conditions. Catalyst loadings are $75 \mu\text{g}\cdot\text{cm}^{-2}$. Measurements in O_2 -saturated 0.1 M HClO_4 with a scan speed of $20 \text{ mV}\cdot\text{s}^{-1}$ and a rotating rate of 1600 rpm at room temperature.

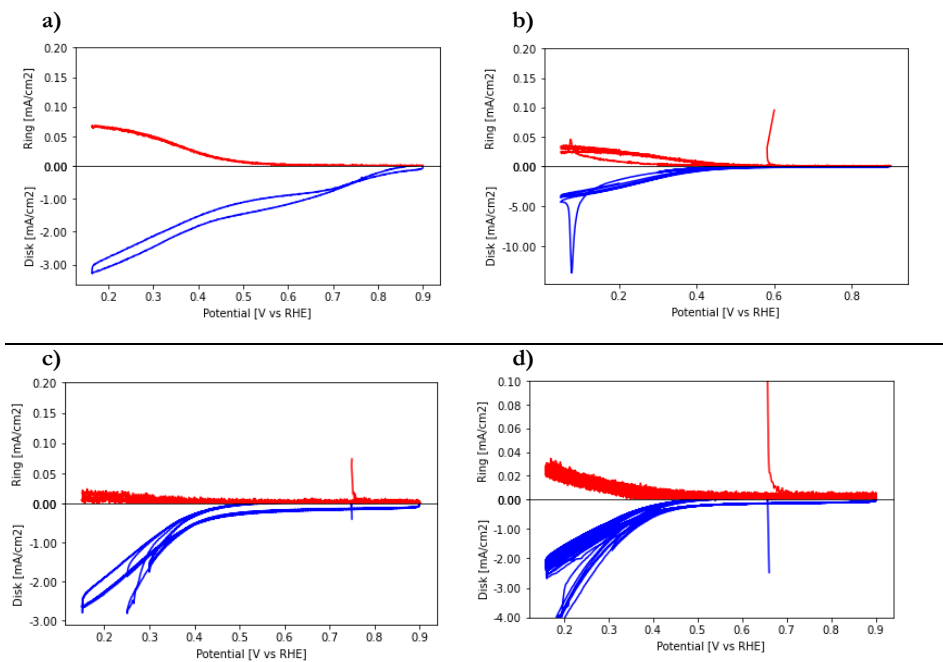


Figure B.9: RRDE measurements of (a) PtSAC PtCl₄(1), (b) PtSAC PtCl₄(2.1), (c) PtSAC PtCl₄(2.2) and (d) PtSAC PtCl₄(5) samples for 2e⁻ ORR in acidic conditions. Catalyst loadings are 75 μg*cm⁻². Measurements in O₂-saturated 0.1 M HClO₄ with a scan speed of 20 mV*s⁻¹ and a rotating rate of 1600 rpm at room temperature.

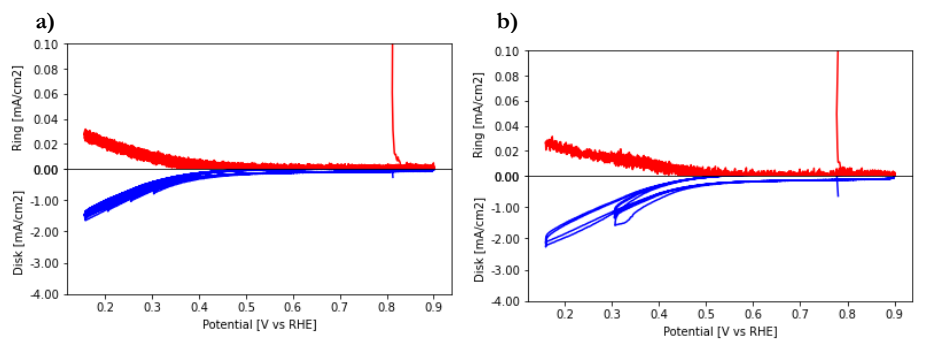


Figure B.10: RRDE measurements of (a) PtSAC PtCl₄(4.1) and (b) PtSAC PtCl₄(4.2) samples for 2e⁻ ORR in acidic conditions. Catalyst loadings are 75 μg*cm⁻². Measurements in O₂-saturated 0.1 M HClO₄ with a scan speed of 20 mV*s⁻¹ and a rotating rate of 1600 rpm at room temperature.

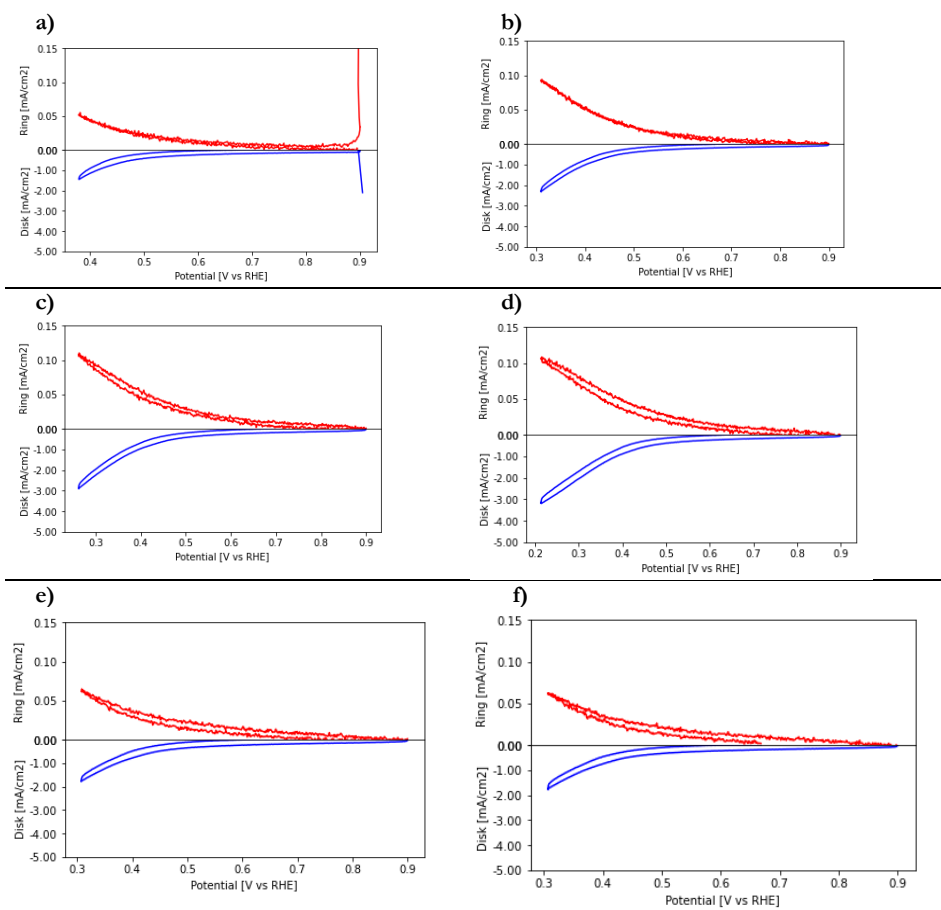


Figure B.11: RRDE measurements of PtCl₄(6) samples (a-b-c-d-e-f, cycles 1-5-10-15-25-30 respectively) for 2e⁻ ORR in acidic conditions. Catalyst loadings are 75 μg*cm⁻². Measurements in O₂-saturated 0.1 M HClO₄ with a scan speed of 20 mV*s⁻¹ and a rotating rate of 1600 rpm at room temperature.

Appendices

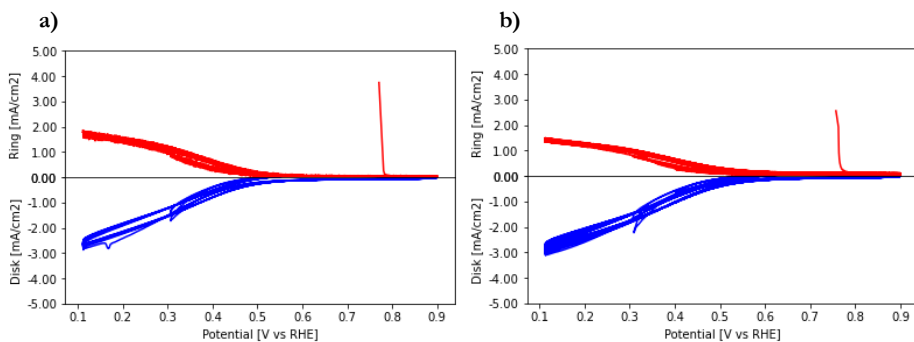


Figure B.12: RRDE measurements of (a) PdAcac(2), (b) PdAcac(3) samples for 2e⁻ ORR in acidic conditions. Catalyst loadings are 75 μg*cm⁻². Measurements in O₂-saturated 0.1 M HClO₄ with a scan speed of 20 mv*s⁻¹ and a rotating rate of 1600 rpm at room temperature.

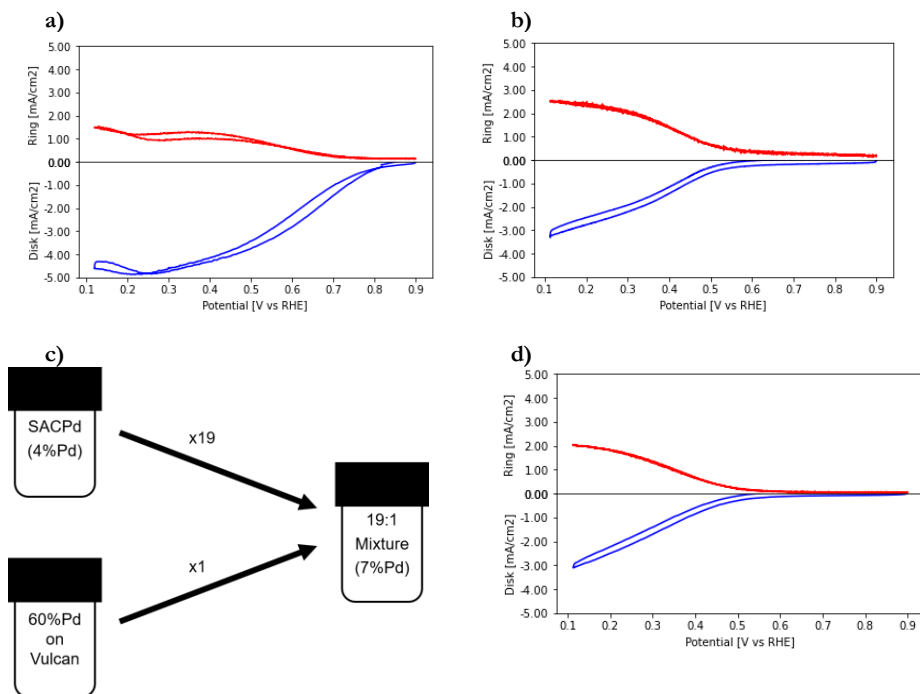


Figure B.13: RRDE measurements of (b+d) PdAcac(1), (a) PdAcac(1) mixed with 60%Pd (19:1) as shown in the schematic (c) samples for 2e⁻ ORR in acidic conditions. Catalyst loadings are 75 μg*cm⁻². Measurements in O₂-saturated 0.1 M HClO₄ with a scan speed of 20 mv*s⁻¹ and a rotating rate of 1600 rpm at room temperature.

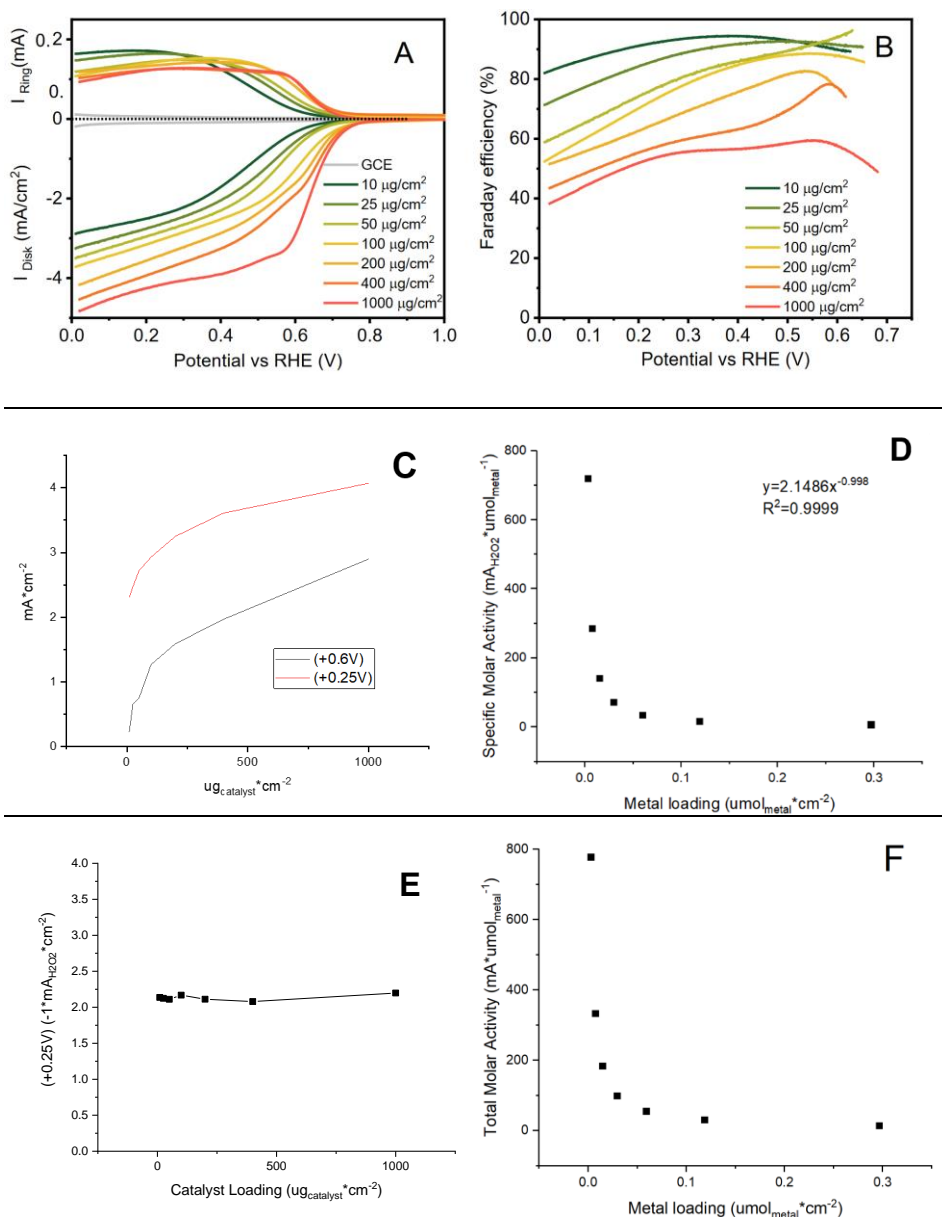


Figure B.14: Gao et al.'s Co-NC catalyst where higher catalyst loadings yields worse RRDE performance, both mass activity and selectivity (a and b respectively).⁷⁷ Total measured activity as a function of mass shows diminishing returns in higher catalyst loadings (c), where increased catalysts loadings doesn't actually increase the specific activity at all: catalyst loadings across 3 orders of magnitude stay at around $\sim 2.0 \text{ mA}_{\text{H}_2\text{O}_2}\cdot\text{cm}^{-2}$ (e). By converting this data into molar metal loadings ($\mu\text{mol}_{\text{metal}}^{-1}$), we see a bias for higher total activities (f) and higher specific activities (d) with lower metal molar loadings (at $+0.25\text{V}_{\text{RHE}}$ and assuming their 1.75 wt. % Co). (a+b) from ⁷⁷ while d-f are adapted from (a+b).

C1s (wt. %)	N1s (wt. %)	Co2p (wt. %)
85	12	3.1
85	11	3.9

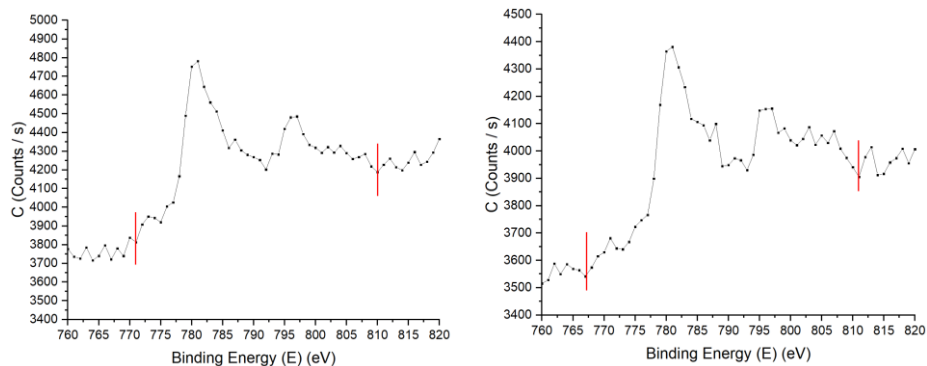


Figure B.15: XPS scans of CoAcac1, with elemental composition (wt.%) and the Co2p peaks presented.

C1s (wt. %)	N1s (wt. %)	Co2p (wt. %)
84	13	3.3
82	15	3.0

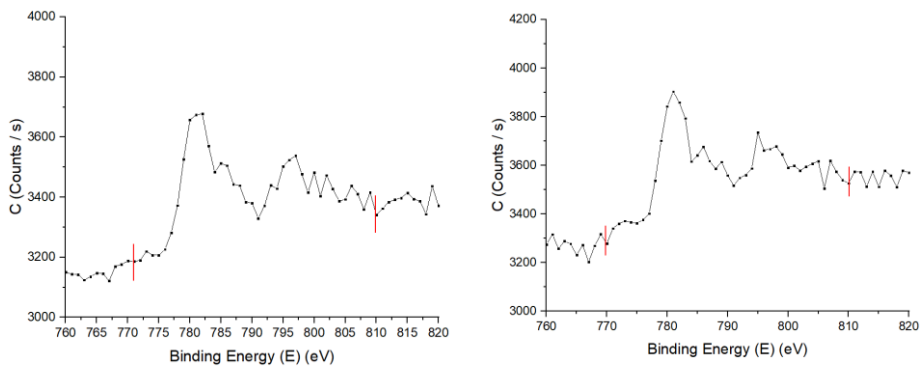


Figure B.16: XPS survey scans of CoAcac2, with elemental composition (wt.%) and the Co2p peaks presented.

C1s (wt. %)	N1s (wt. %)	Co2p (wt. %)
84	14	1.7

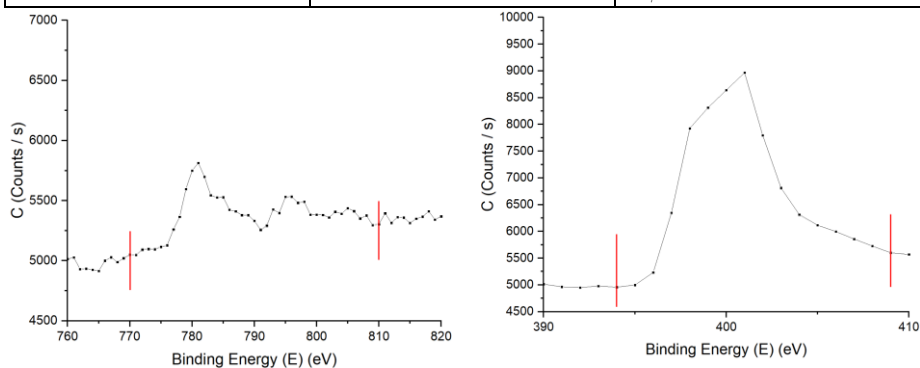


Figure B.17: XPS survey scan of CoAcac2.2 with elemental composition (wt.%) and the Co2p peak (left) and N1s peak (right) presented.

C1s (wt. %)	N1s (wt. %)	Co2p (wt. %)
87	15	2.7

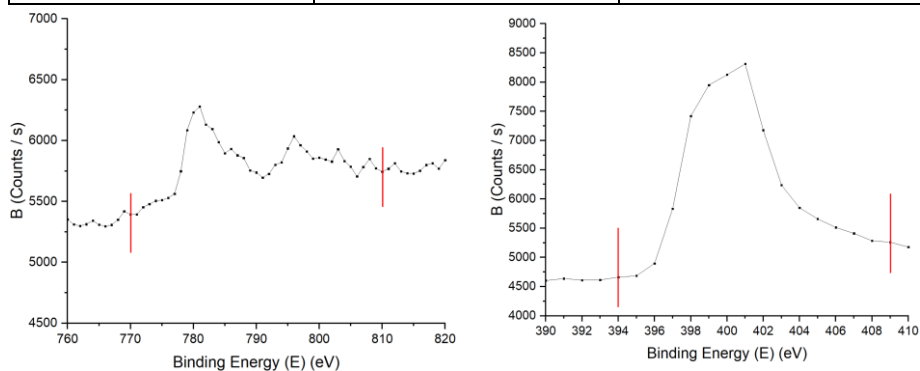


Figure B.18: XPS survey scan of CoAcac3 with elemental composition (wt.%) and the Co2p peak (left) and N1s peak (right) presented.

C1s (wt. %)	N1s (wt. %)	Ir4f (wt. %)	Pt4f (wt. %)
78	18	0.9	2.8
82	15	0.9	2.8

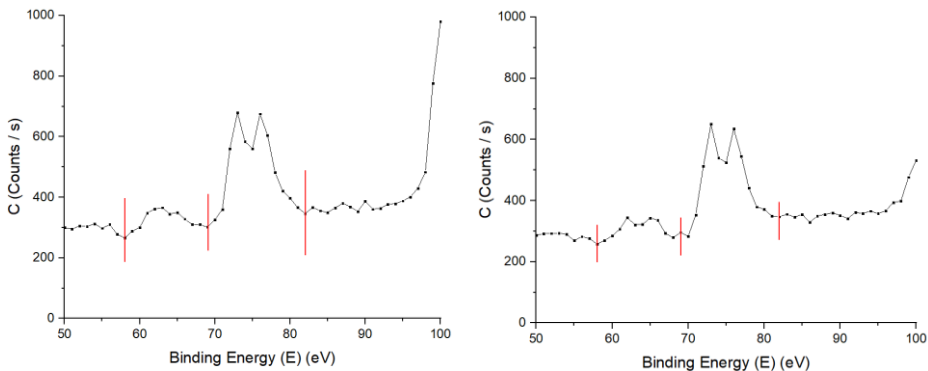


Figure B.19: XPS survey scans of IrAcac1, with elemental composition (wt.%) and the Pt4f and Ir4f peaks presented.

C1s (wt. %)	N1s (wt. %)	Ir4f (wt. %)
76	22	2.5
75	22	2.8

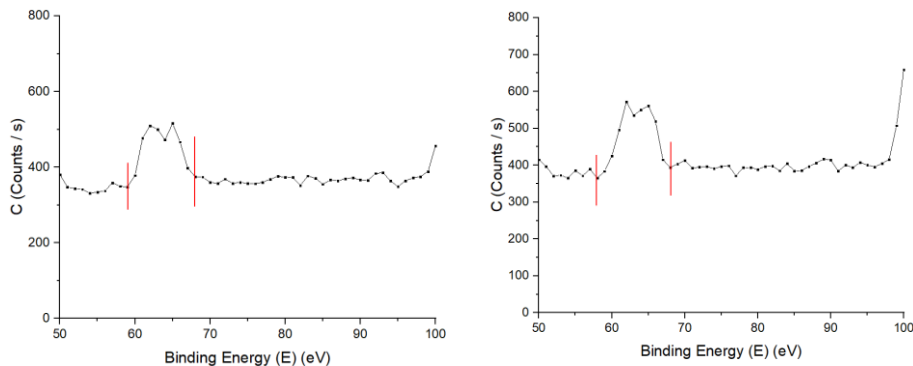


Figure B.20: XPS survey scans of IrAcac1.2, with elemental composition (wt.%) and the Ir4f peaks presented.

C1s (wt. %)	N1s (wt. %)	Ir4f (wt. %)
81	19	0.5
81	19	0.6

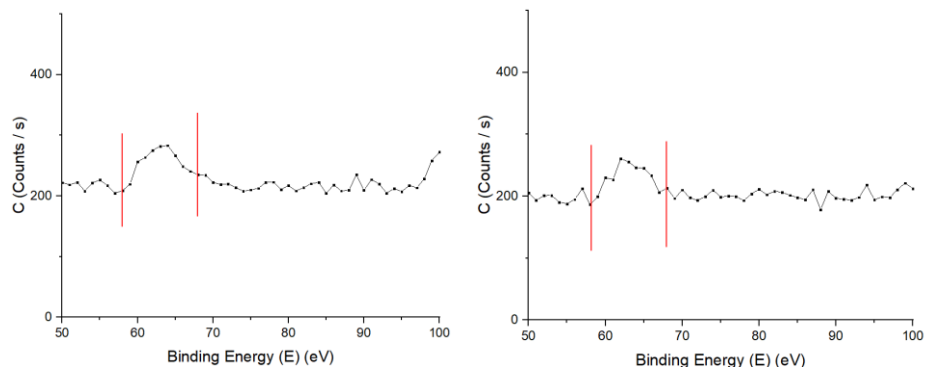


Figure B.21: XPS scans of IrAcac3, with elemental composition (wt.%) and the Ir4f peaks presented.

C1s (wt. %)	N1s (wt. %)	Ir4f (wt. %)
82	17	0.2

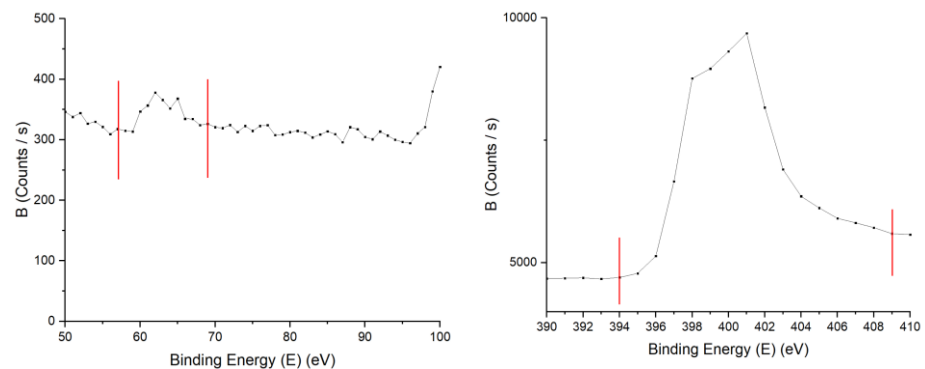


Figure B.22: XPS survey scan of IrAcac4 with elemental composition (wt.%) and the Ir4f peak (left) and N1s peak (right) presented.

C1s (wt. %)	N1s (wt. %)	Ir4f (wt. %)
83	16	0.2

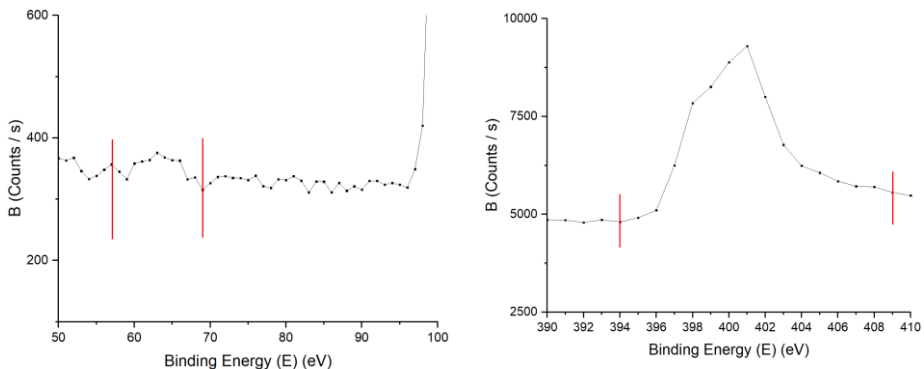


Figure B.23: XPS survey scan of IrAcac4.2 with elemental composition (wt.%) and the Ir4f peak (left) and N1s peak (right) presented.

C1s (wt. %)	N1s (wt. %)	Ir4f (wt. %)
83	16	0.7

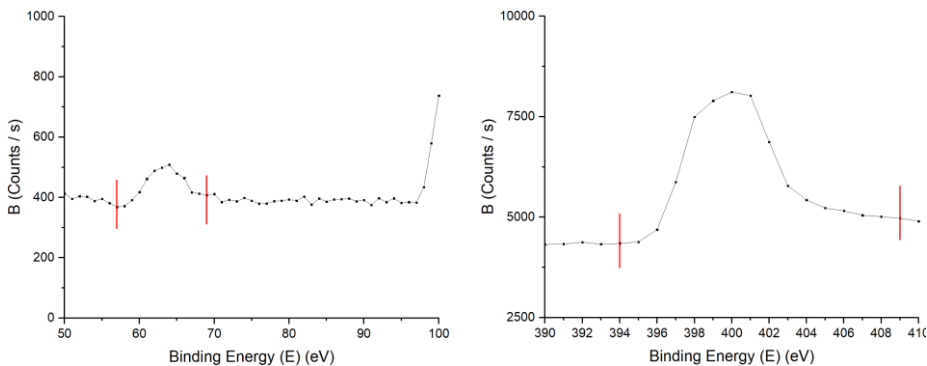


Figure B.24: XPS survey scan of IrAcac6 with elemental composition (wt.%) and the Ir4f peak (left) and N1s peak (right) presented.

C1s (wt. %)	N1s (wt. %)	Pt4f (wt. %)
69	16	15.3
67	17	15.5

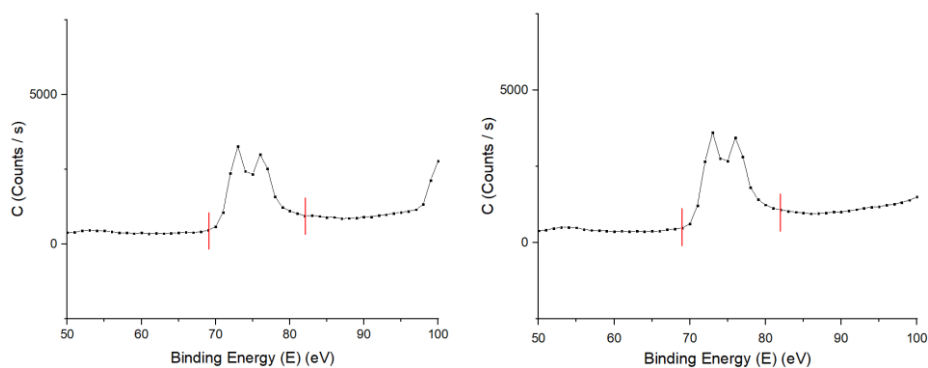


Figure B.25: XPS scans of PtCl₄(1), with elemental composition (wt.%) and the Pt4f peaks presented.

C1s (wt. %)	N1s (wt. %)	Pt4f (wt. %)
65	19	14.4
67	18	14.5

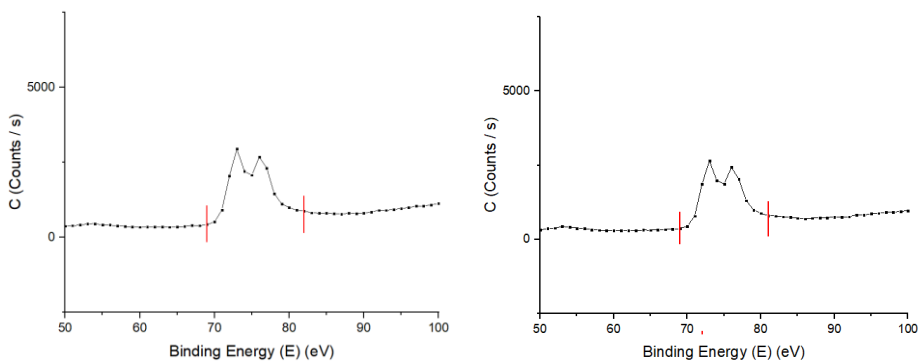


Figure B.26: XPS scans of PtCl₄(2), with elemental composition (wt.%) and the Pt4f peaks presented.

C1s (wt. %)	N1s (wt. %)	Pt4f (wt. %)
74	17	8.9

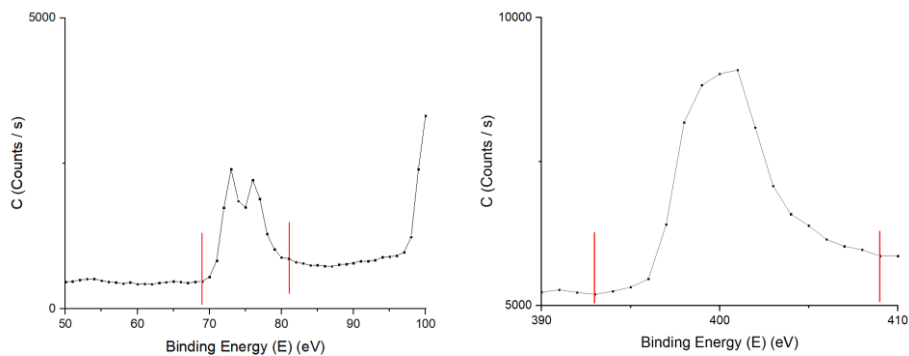


Figure B.27: XPS survey scan of zPt₂ with elemental composition (wt.%) and the Pt4f peak (left) and N1s peak (right) presented.

C1s (wt. %)	N1s (wt. %)	Pd3d (wt. %)
80	16	4.1
80	15	4.3

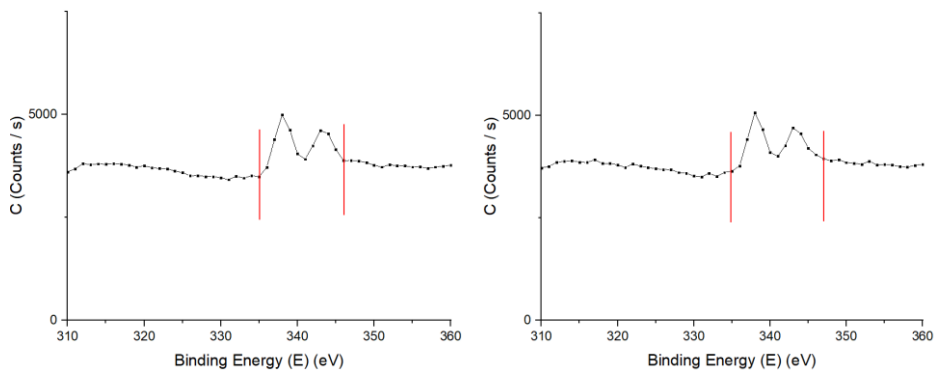


Figure B.28: XPS scans of PdAcac(1), with elemental composition (wt.%) and the Pd3d peaks presented (left, right).

C1s (wt. %)	N1s (wt. %)	Pd3d (wt. %)
77	20	3.7
77	19	3.6

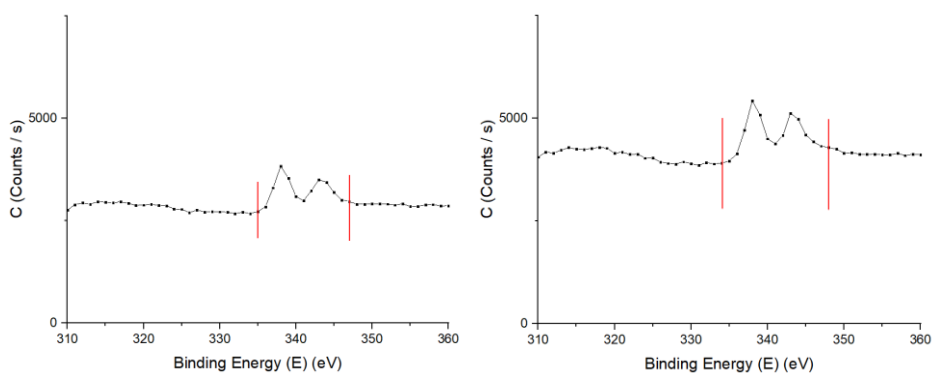


Figure B.29: XPS scans of PdAcac(2), with elemental composition (wt.%) and the Pd3d peaks presented.

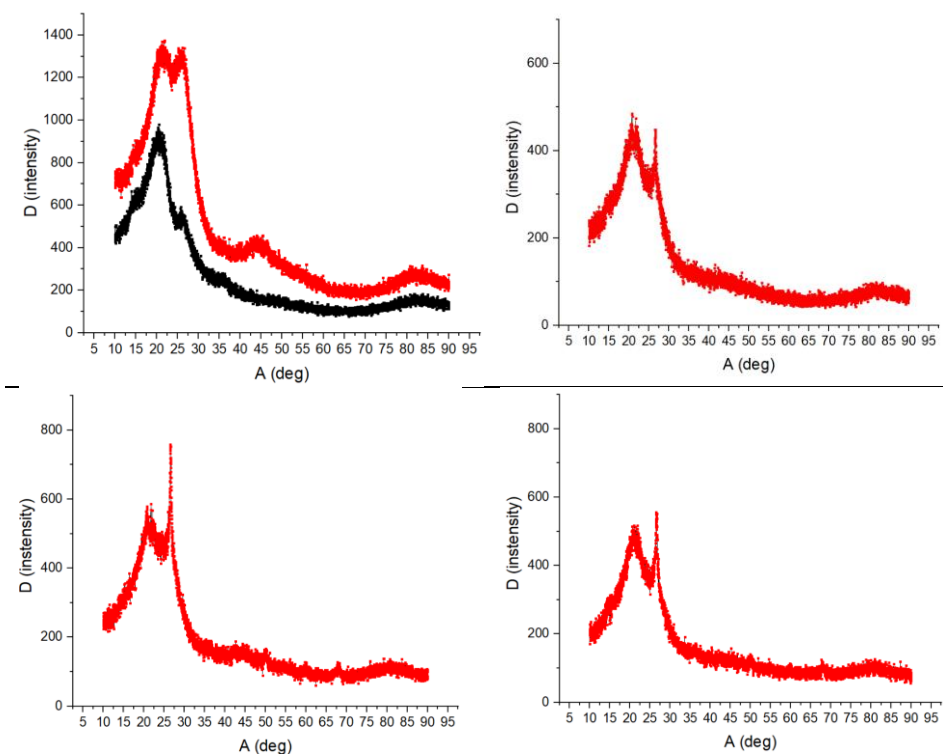


Figure B.30: XRD scans of (black) background and (red) sample: IrAcac(3) (top left), IrAcac(4) (top right), IrAcac(5) (bottom left), IrAcac(6) (bottom right)

Appendices

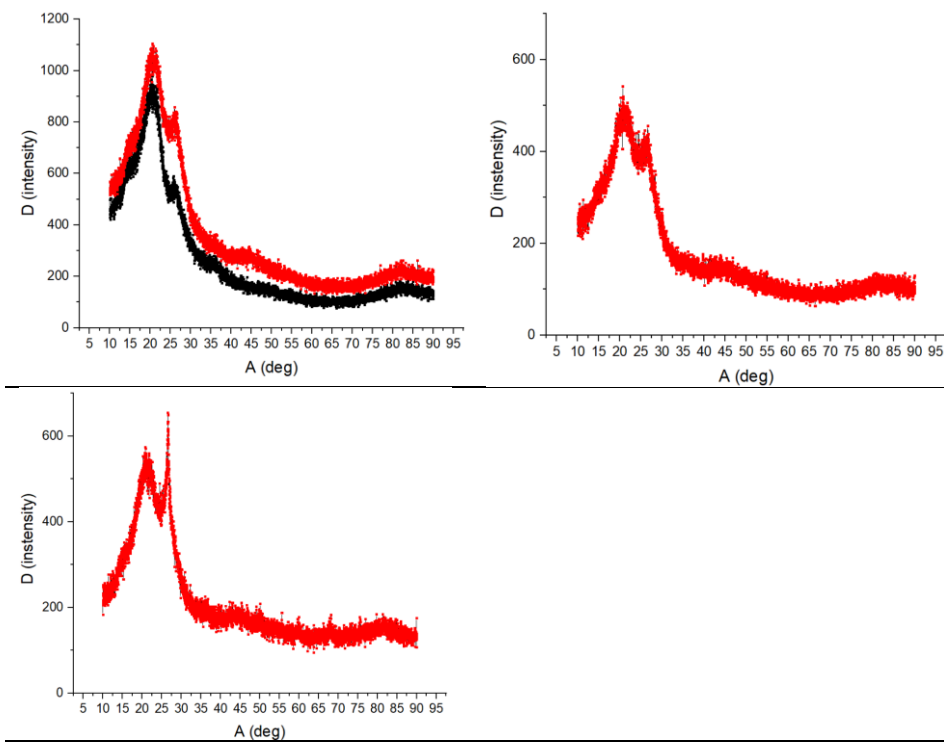


Figure B.31: XRD scans of (black) background and (red) sample: CoAcac(1) (top left), CoAcac(2.2) (top right), and CoAcac(3).

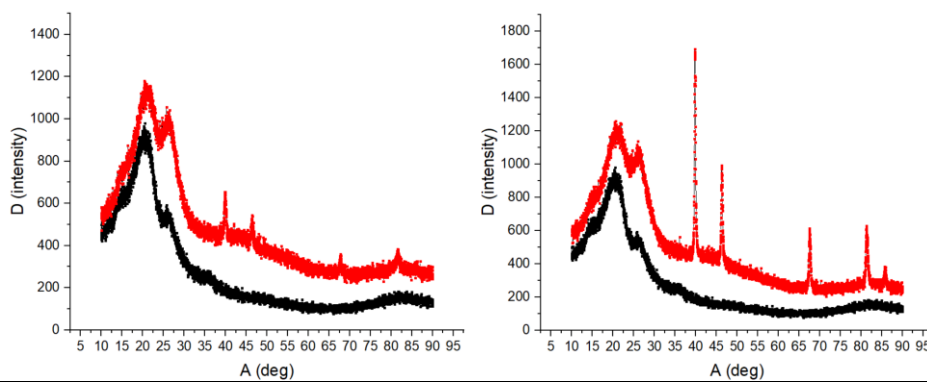


Figure B.32: XRD scans of (black) background and (red) sample: PtCl₄(1) (left) and PtCl₆(1) (right)

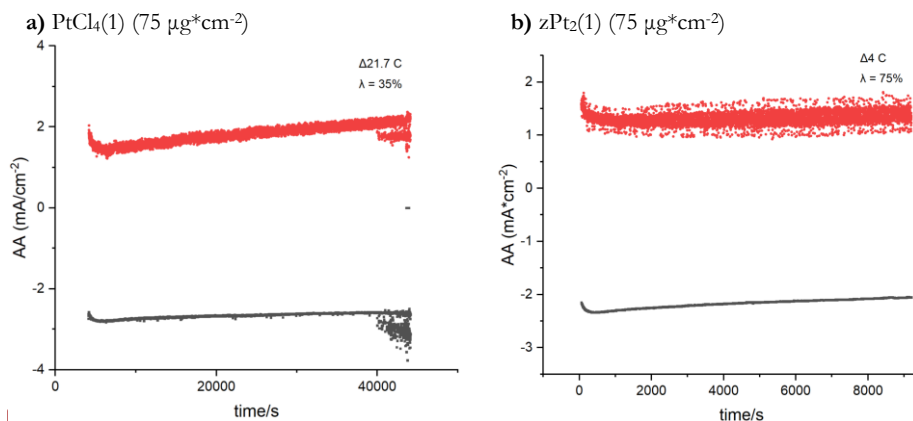


Figure B.33: RRDE CA experiments (+0.2V_{VRHE}) of (a) PtCl₄(1) (75 μg*cm⁻²) and (b) zPt₂(1) (75 μg*cm⁻²). Measurements in O₂-saturated 0.1 M HClO₄ and a rotating rate of 1600 rpm at room temperature. A combination of the total oxidation charge (C) from the Pt-ring and the quantification of the remaining H₂O₂ concentration via KMnO₄ titration was used to determine the faradaic efficiency (λ_{Faradaic}).

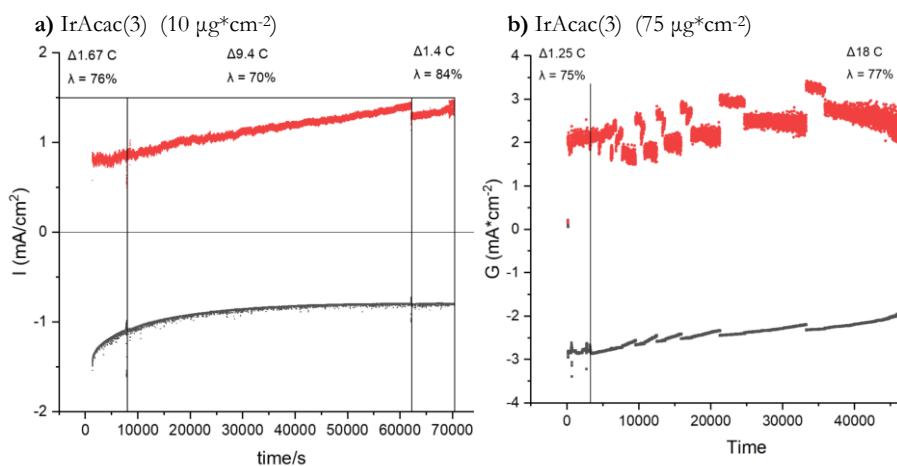


Figure B.34: RRDE CA experiments (+0.2V_{VRHE}) of (a) IrAcac(3) (10 μg*cm⁻²) and (b) IrAcac(3) (75 μg*cm⁻²). Measurements in O₂-saturated 0.1 M HClO₄ and a rotating rate of 1600 rpm at room temperature. A combination of the total oxidation charge (C) from the Pt-ring and the quantification of the remaining H₂O₂ concentration via KMnO₄ titration was used to determine the faradaic efficiency (λ_{Faradaic}).

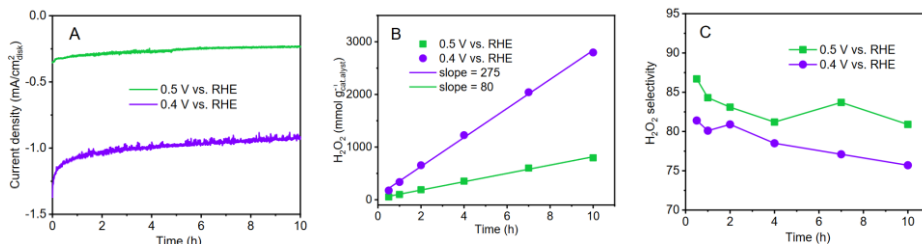


Figure B.35: Half-cell experiment for fixed potential chronoamperometry: (a) current density along with time at potentials of 0.5 and 0.4 V_{VRHE} , (b) average formation rate of H_2O_2 : 80 and 275 H_2O_2 ($mmol \cdot g^{-1}_{catalyst} \cdot h^{-1}$) at potentials of 0.5 and 0.4 V_{VRHE} , and (c) selectivity of H_2O_2 along with time. From ⁷⁷

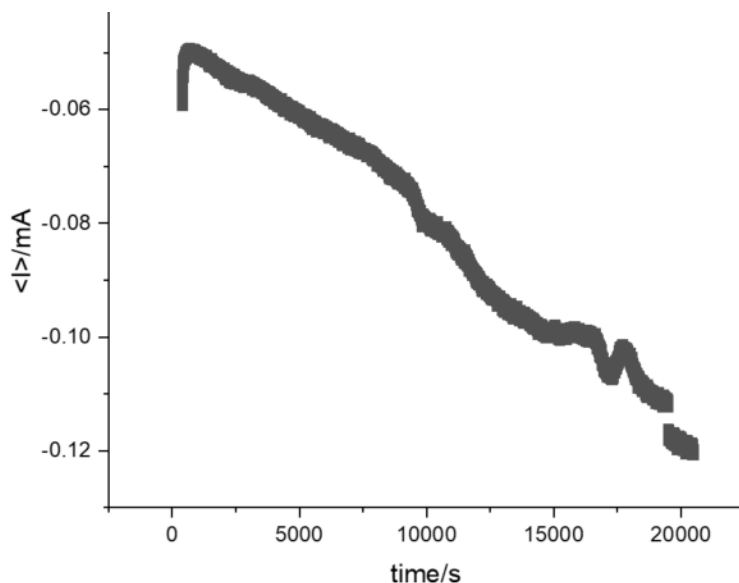


Figure B.36: CA TiFET experiment (catalyst loadings = $\sim 10 \mu g \cdot cm^{-2}$, $0.00 V_{VRHE}$ ($\pm 0.05 V$)) of PdSAC sample. Measurements in 1.0 M $HClO_4$ electrolyte at room temperature. TiFET experiments loaded with PdSAC sample failed to maintain a consistent current during CA operations, likely due to metal cation electrodeposition/agglomeration.

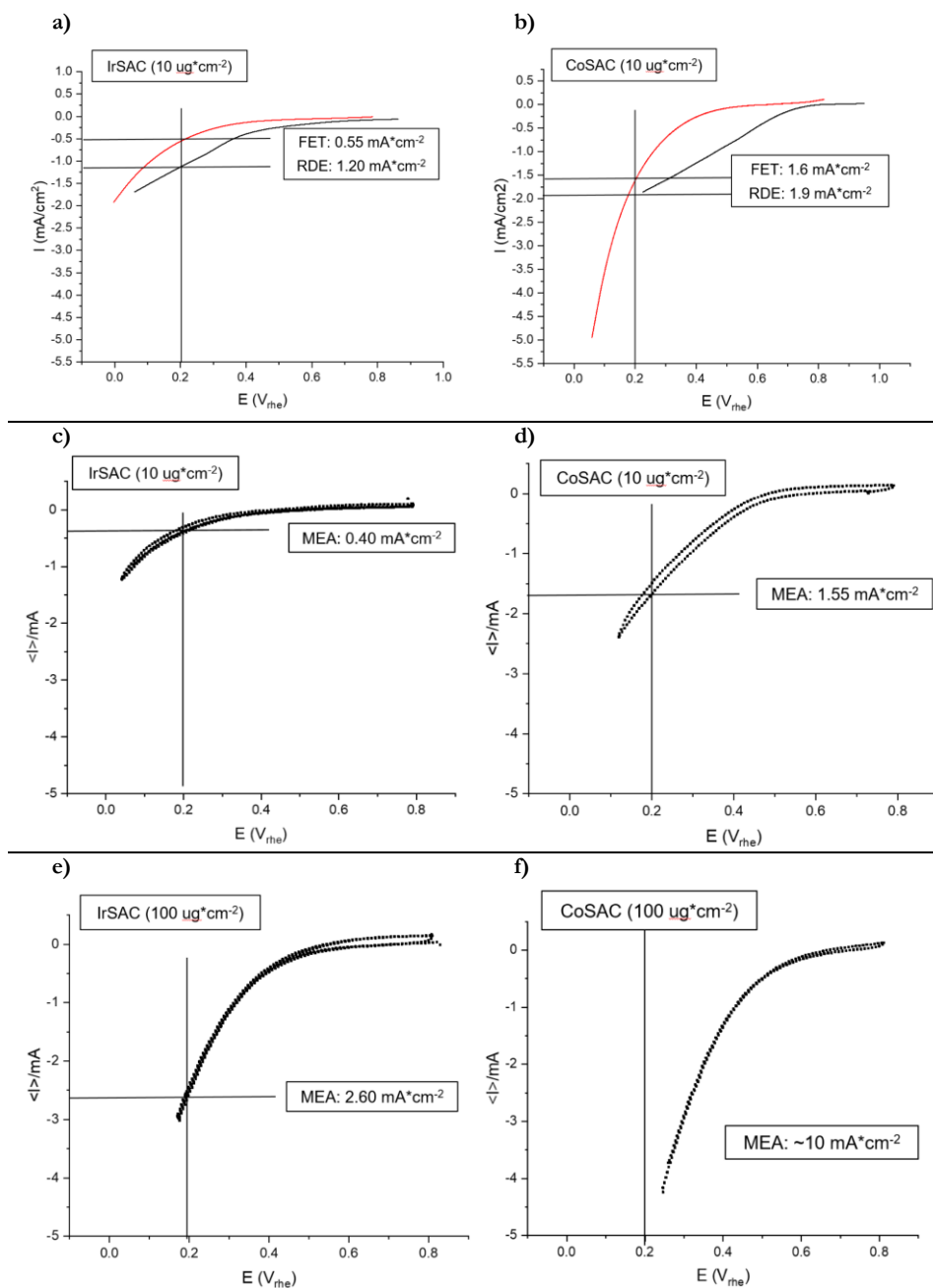


Figure B.37: CV cathodic sweeps of IrSAC (a, c, e) and CoSAC (b, d, f) in various setups (RDE, FET, MEA) and various absolute catalyst loadings. Measurements in O_2 -saturated 0.1 M HClO_4 (1.0 M HClO_4 for FET) with a scan speed of $20 \text{ mV}/\text{s}$ at room temperature. A rotating rate of 1600 rpm was used for the RDE measurements.

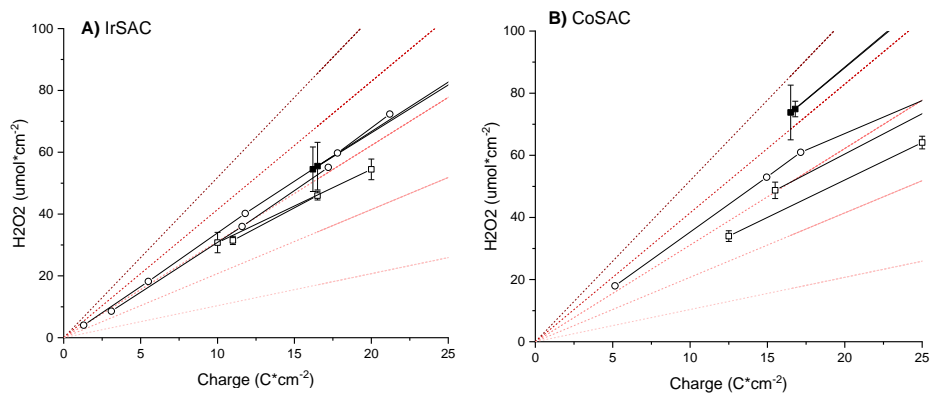


Figure B.38: ‘zoomed in’ (0-25 $\text{C}\cdot\text{cm}^{-2}$) on Figure 6.12 (a, b) with H_2O_2 yield over charge accumulated up to 50 $\text{C}\cdot\text{cm}^{-2}$ (■ = FET, □ = RDE, ○ = MEA). All experiments were conducted within the range of -0.05 to $+0.05$ V_{the} , with approximate catalyst loadings of $10 \mu\text{g}\cdot\text{cm}^{-2}$. FET experiments were conducted in 1M HClO_4 with an O_2 -saturated headspace. RDE and MEA experiments were conducted in O_2 -saturated 0.1M HClO_4 .

Element	Mass Fraction (wt. %)	Mass Error (%)	Fit Error (%)
C	85.50	1.57	0.13
N	8.15	1.64	1.25
O	3.63	0.73	0.07
Co	2.72	0.37	1.48

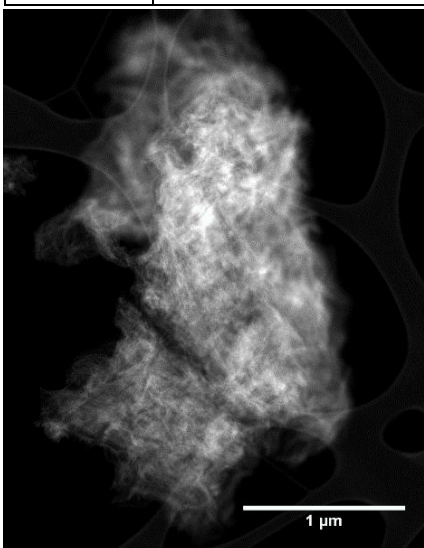


Figure B.39: EDS and HAADF-STEM analysis of CoSAC (CoAcac2). Analysis performed by Sofie Colding-Jørgensen.

Element	Mass Fraction (wt. %)	Mass Error (%)	Fit Error (%)
C	87.75	1.36	0.35
N	6.54	1.31	0.57
O	2.94	0.59	1.02
Si	0.19	0.04	1.33
Co	2.59	0.35	0.52

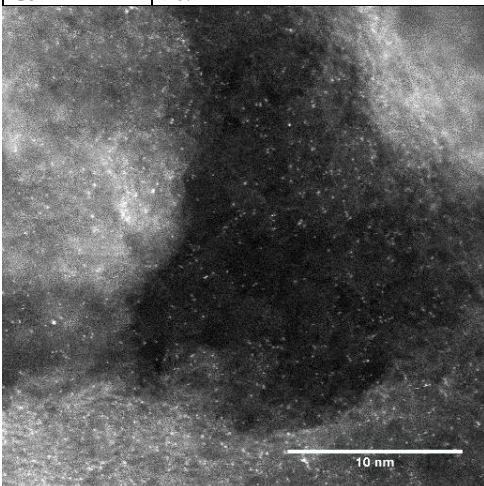


Figure B.40: EDS and HAADF-STEM analysis of CoSAC (CoAcac2). Analysis performed by Sofie Colding-Jørgensen.

Element	Mass Fraction (wt. %)	Mass Error (%)	Fit Error (%)
C	85.25	1.56	0.13
N	8.12	1.63	1.25
O	3.62	0.73	0.07
Si	0.29	0.06	0.88
Co	2.71	0.37	1.48

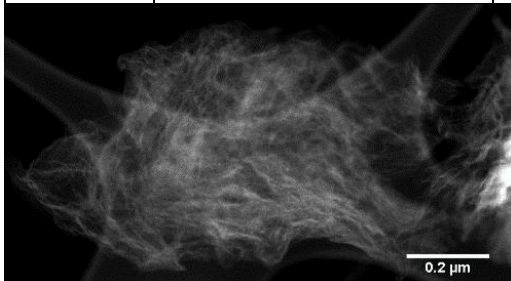


Figure B.41: EDS and HAADF-STEM analysis of CoSAC (CoAcac2). Analysis performed by Sofie Colding-Jørgensen.

Element	Mass Fraction (wt. %)	Mass Error (%)	Fit Error (%)
C	88.70	1.83	0.99
N	7.66	1.54	0.91
O	1.18	0.24	2.39
Si	0.22	0.05	9.26
Co	2.24	0.30	1.51

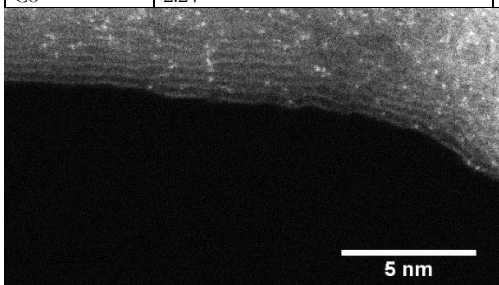


Figure B.42: EDS and HAADF-STEM analysis of CoSAC (CoAcac2). Analysis performed by Sofie Colding-Jørgensen.

Element	Mass Fraction (wt. %)	Mass Error (%)	Fit Error (%)
C	86.15	2.25	0.66
N	12.24	2.47	0.80
O	1.14	0.23	0.30
Ir	0.47	0.05	2.24

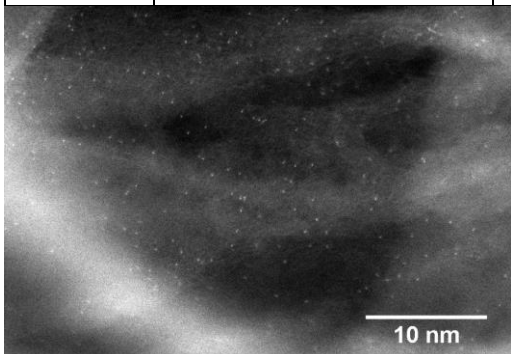


Figure B.43: EDS and HAADF-STEM analysis of IrSAC (IrAcac3). Analysis performed by Sofie Colding-Jørgensen.

Element	Mass Fraction (wt. %)	Mass Error (%)	Fit Error (%)
C	82.41	2.23	0.33
N	12.68	2.56	0.91
O	4.13	0.83	1.30
Ir	0.79	0.10	5.55

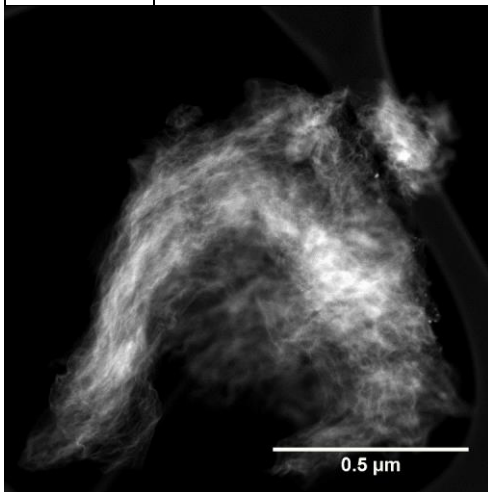


Figure B.44: EDS and HAADF-STEM analysis of IrSAC (IrAcac₃). Analysis performed by Sofie Colding-Jørgensen.

Element	Mass Fraction (wt. %)	Mass Error (%)	Fit Error (%)
C	60.76	2.17	0.41
N	10.64	2.17	1.38
O	3.79	0.77	2.32
Ag	23.60	2.84	1.27
Ir	1.21	0.23	15.87

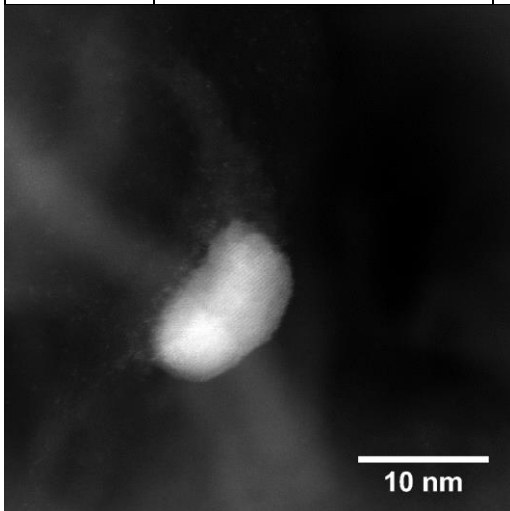


Figure B.45: EDS and HAADF-STEM analysis of IrSAC (IrAcac₃). Analysis performed by Sofie Colding-Jørgensen.

Element	Mass Fraction (wt. %)	Mass Error (%)	Fit Error (%)
C	85.15	2.24	1.00
N	10.90	2.20	0.05
O	3.29	0.66	0.37
Si	0.23	0.05	2.60
Ir	0.43	0.05	2.33

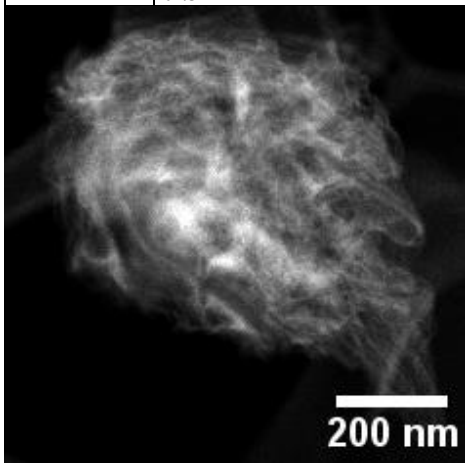


Figure B.46: EDS and HAADF-STEM analysis of IrSAC (IrAcac3). Analysis performed by Sofie Colding-Jørgensen.

Element	Mass Fraction (wt. %)	Mass Error (%)	Fit Error (%)
C	87.99	1.91	0.66
N	9.84	1.98	1.02
O	0.71	0.15	5.43
Si	0.15	0.05	24.64
Ag	0.17	0.06	33.20
Ir	0.81	0.14	13.66
Pt	0.33	0.12	35.33

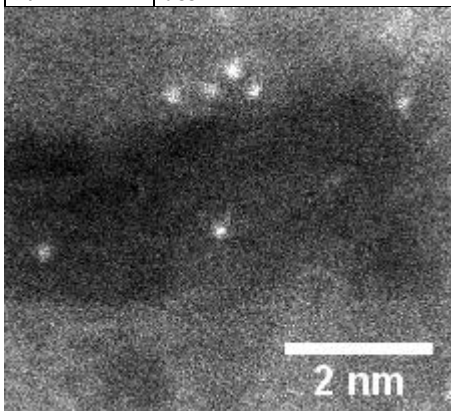


Figure B.47: EDS and HAADF-STEM analysis of IrSAC (IrAcac3). Analysis performed by Sofie Colding-Jørgensen.

Table B.1: ICP-MS analysis of IrSAC (IrAcac3) and CoSAC (CoAcac2) catalyst inks.

Sample	Co (wt. %)	Ag (wt. %)	Ir (wt. %)	Au (wt. %)
IrSAC3	0.03	0.02	0.16	0.0 (N.D.)
CoSAC2	1.52 (± 0.08)	0.03	0.0 (N.D.)	0.0 (N.D.)

Appendices

Appendix C

Paper I

The acidic electrolysis of H_2O_2 in high-mass transport conditions on stable Ir and Co single-atom catalysts.

Jens-Peter B. Haraldsted, Sofie Colding-Jørgensen, Thomas Smitshuysen, Christian Damsgaard, Ib Chorkendorff, Jakob Kibsgaard

In preparation

Appendices

Appendix D

Paper II

Highly Active, selective, and stable Pd single-atom catalyst anchored on N-doped hollow carbon sphere for electrochemical H₂O₂ synthesis under acidic conditions.

Jiangbo Xi, Sungeun Yang, Luca Silvioli, Sufeng Cao, Pei Liu, Qiongyang Chen, Yanyan Zhao, Hongyu Sun, Johannes Novak Hansen, Jens-Peter B. Haraldsted, Jakob Kibsgaard, Jan Rossmeisl, Sara Bals, Shuai Wang, Ib Chorkendorff



Highly active, selective, and stable Pd single-atom catalyst anchored on N-doped hollow carbon sphere for electrochemical H₂O₂ synthesis under acidic conditions



Jiangbo Xi ^{a,i,1}, Sungeun Yang ^{b,j,1}, Luca Silvioli ^{c,d,1}, Sufeng Cao ^{e,1}, Pei Liu ^f, Qiongyang Chen ^f, Yanyan Zhao ^g, Hongyu Sun ^h, Johannes Novak Hansen ^b, Jens-Peter B. Haraldsted ^b, Jakob Kibsgaard ^b, Jan Rossmeisl ^c, Sara Bals ^f, Shuai Wang ^{a,*}, Ib Chorkendorff ^{b,*}

^a Key Laboratory of Material Chemistry for Energy Conversion and Storage, Ministry of Education, School of Chemistry and Chemical Engineering, Huazhong University of Science and Technology, Wuhan 430074, PR China

^b Department of Physics, Technical University of Denmark, DK-2800 Kongens Lyngby, Denmark

^c Nano-Science Center, Department of Chemistry, University of Copenhagen, Copenhagen Ø DK-2100, Denmark

^d Seaborg Technologies ApS, Titangade 11, Copenhagen DK-2200, Denmark

^e Department of Chemical and Biological Engineering, Tufts University, Medford, MA 02155, United States

^f Electron Microscopy for Materials Science, University of Antwerp, Groenenborgerlaan 171, 2020 Antwerp, Belgium

^g Department of Chemistry, Merkert Chemistry Center, Boston College, Chestnut Hill, MA 02467, United States

^h Department of Micro- and Nanotechnology, Technical University of Denmark, DK-2800 Kongens Lyngby, Denmark

ⁱ School of Chemistry and Environmental Engineering, Key Laboratory of Green Chemical Engineering Process of Ministry of Education, Wuhan Institute of Technology, Wuhan 430205, China

^j Center for Energy Materials Research, Korea Institute of Science and Technology (KIST), Hwarangno 14-gil 5, Seongbuk-gu, Seoul 02792, South Korea

ARTICLE INFO

Article history:

Received 31 August 2020

Revised 29 October 2020

Accepted 13 November 2020

Available online 26 November 2020

Keywords:

Single-atom catalyst

Nitrogen doped carbon

Hydrogen peroxide

Electrochemical synthesis

Density functional theory

ABSTRACT

Single-atom catalysts (SACs) have recently attracted broad scientific interests due to their unique structural feature, the single-atom dispersion. Optimized electronic structure as well as high stability are required for single-atom catalysts to enable efficient electrochemical production of H₂O₂. Herein, we report a facile synthesis method that stabilizes atomic Pd species on the reduced graphene oxide/N-doped carbon hollow carbon nanospheres (Pd1/N-C). Pd1/N-C exhibited remarkable electrochemical H₂O₂ production rate with high faradaic efficiency, reaching 80%. The single-atom structure and its high H₂O₂ production rate were maintained even after 10,000 cycle stability test. The existence of single-atom Pd as well as its coordination with N species is responsible for its high activity, selectivity, and stability. The N coordination number and substrate doping around Pd atoms are found to be critical for an optimized adsorption energy of intermediate *OOH, resulting in efficient electrochemical H₂O₂ production.

© 2020 Elsevier Inc. All rights reserved.

1. Introduction

Hydrogen peroxide, H₂O₂, is an environmentally friendly oxidant with annual production over 5 million tons and its wide usage covers bleaching, chemicals synthesis, and waste water treatment [1,3,4]. Current production of H₂O₂ is limited by the anthraquinone process which is a viable batch process that requires a centralized plant [4]. Centralized production requires additional costs for distillation, transportation, and dilution at the point of use [1].

Thermal catalysis for H₂O₂ synthesis has potential for the decentralized production with high yields in batch reactors, but developments in flow reactors remain a challenge in this technology's applicability [2,5–12]. Electrochemical synthesis of H₂O₂ by the oxygen reduction reaction in acidic conditions holds promise for decentralized, on-site production, where the electrochemical device requires only water, air, and electricity [1,13–16]. Designing a selective and active cathode catalyst with high stability in acidic conditions is critical for realizing electrochemical H₂O₂ production [17]. Single atom catalysts (SACs), particularly single metal atoms stabilized in a porphyrin-like support, are promising as selective, active, and stable catalysts for various electrochemical reactions including the oxygen reduction reaction (ORR) resulting in the scalable electrochemical production of H₂O₂ [15,18–21].

* Corresponding authors.

E-mail addresses: chmsamuel@hust.edu.cn (S. Wang), ibchork@fysik.dtu.dk (I. Chorkendorff).

¹ These authors contributed equally.

Acidic conditions have an advantage over alkaline conditions for H₂O₂ production. In alkaline conditions, H₂O₂ can be easily produced by using a glassy carbon electrode, but the product HO₂⁻ is unstable, thus its applicability is limited to processes where the H₂O₂ must be used immediately. In contrast, acidic conditions stabilize H₂O₂, and allow the use of durable proton-exchange membranes resulting in the production of pure aqueous H₂O₂ solution, which has broader applications. The overall reactions of oxygen reduction and their thermodynamic equilibrium potentials versus reversible hydrogen electrode (RHE) in acidic conditions are as follows:



The oxygen reduction reaction can either produce H₂O₂ via 2-electron (2e) pathway (1) or H₂O via 4-electron (4e) pathway (2). Efficient catalyst for electrochemical H₂O₂ production should produce H₂O₂ via the 2e pathway with high selectivity at a high rate. Adsorption energies of reaction intermediates are often good descriptors to rationalize given catalytic reaction. The only intermediate in the 2e pathway is *OOH, and the 4e pathway has additional intermediates *OH and *O. There are two principles determining catalytic performance for electrochemical H₂O₂ production. The first principle is *electronic effect*. Adsorption energy of the intermediate *OOH is tuned by the electronic structure of catalyst, and it should neither be too strong nor too weak, as stated in the Sabatier principle. A weak affinity for the reaction intermediates is preferred to inhibit O-O bond dissociation, limiting the 4e pathway that yields H₂O production. The second principle is *geometric effect*. On a metal surface, the most stable adsorption site for *OOH and *OH is on-top, while *O prefer to sit in a hollow site. On single site catalysts, isolated atoms cannot provide a hollow adsorption site, therefore *O is forced to bind on-top site, weakening its adsorption energy as compared to the other reaction intermediates. The selective destabilization of *O as compared to *OOH is the reason why single site catalysts are frequently studied for the 2e pathway [1,16,22].

Single-atom catalysts (SAC) have the potential to provide optimal active site structures for state-of-the-art electrochemical H₂O₂ production in acidic conditions [1,13–15]. Siahrostami *et al.* (2013) provided a rational background for designing new catalysts for electrochemical H₂O₂ production by alloying a strong oxygen adsorbing element, Pt, with a weaker oxygen adsorbing element, Hg. Alloying these two elements resulted in the isolation of a single active Pt atom surrounded by less active Hg atoms, providing an optimized electronic structure, electronic effect, and geometric effect [22]. Following this idea, Verdager-Casadevall *et al.* (2014) examined a set of Metal-Hg surfaces and Pd-Hg was found to be the best catalyst providing the highest activity up to this date [16]. A similar strategy was applied for Pd-Au alloy [23,24], cobalt-porphyrin (Co-N₄) like structures [13,15,25,26], and more recently sulfide type catalysts, Pt₁-CuS_x [27] and CoS₂ [28], have been proposed where S atoms serving as weak *OOH adsorbing element. Atomically dispersed active sites satisfy the geometric requirements; and maximized utilization of noble metal atoms may dramatically reduce the materials cost. Previous work reported that Pt single-atoms on TiN [29], TiC [30], S doped carbon [31] provided high selectivity for 2e pathway with appreciable activity. Tuning the electronic structure of single-atom catalysts (SAC) can lead to even higher activity through an optimized electronic effect.

The anchoring site plays a crucial role in improving the activity, stability and selectivity of the SAC via a direct coordination effect between atomic metal and support [30,32,33]. The metal-coordination not only alters the electronic effect, but also, very importantly, determines the stability of the atomic structure. The interaction between support and metal atom can be strengthened by modifying support materials and introducing coordination sites for atomic metal [34–36]. Recent findings also showed that selectivity can be tuned through electronic effect and/or heteroatoms (e.g., N, O, S) electron donation between metal and heteroatom containing supports [37–39]. In line with this, a suitable support material that provides anchoring sites and coordination environment for single atoms are important to achieve satisfactory catalytic performance.

In this work, we propose a strategy to overcome the stability issue and improve the activity and the selectivity of SACs by introducing suitable coordination sites for Pd single-atoms. Pd atoms are anchored by doped N species on a hollow carbon nanosphere via dative coordination. We have previously synthesized hollow carbon nanospheres by taking a graphene oxide (GO) shell and coated it with amorphous carbon. These nanospheres anchored Pd single-atom sites and exhibited high stability towards 4-nitrophenol reduction reaction [40]. In this work we introduced N sites into the carbon support to further modify the coordination environment for Pd single-atom. Here we present the preparation of Pd single-atoms anchored on N-doped hollow carbon nanospheres (Pd1/N-C) and its enhanced electrochemical performance for the oxygen reduction reaction. The mass activity of Pd1/N-C was comparable to the best performing catalysts with 78.9 ± 2.5% faradaic efficiency. Single-atom dispersion of Pd1/N-C was maintained even after 10,000 cycle “on-off” test with little activity degradation showing its exceptional stability. The Pd single site surrounded by six coordinating pyridinic N atoms and moderate additional graphitic N doping was suggested as a possible explanation of the observed high activity by density functional theory (DFT) calculations.

2. Experimental section

2.1. The detailed fabrication process of Pd1/N-C SAC

2.1.1. Synthesis of GO wrapped SiO₂ (SiO₂@GO) spheres

SiO₂ spheres (100–200 nm) were synthesized as templates by the Stöber method [41]. GO was prepared according to a modified Hummers method [42]. In a typical synthesis, 0.2 g of SiO₂ spheres were firstly dispersed in 100 mL ethanol by sonication for 20 min. Next, 1 mL of 3-aminopropyltrimethoxysilane was added and refluxed for 5 h to obtain amine-functionalized SiO₂ nanospheres. After the products were centrifugated and re-dispersed in 100 mL DI water, 30 mL of 0.2 mg/mL GO aqueous solution was added and stirred vigorously for 1 h. During this process, the amino-functionalized SiO₂ nanospheres were tightly wrapped by a graphene oxide (GO) nanosheets through electrostatic reaction and hydrogen bonds between the amino group and the oxygen-containing groups on GO sheets (step 1 in Fig. S4) [43]. Finally, the products were collected by centrifugation, washed with water several times, and then dried at 60 °C overnight.

2.1.2. Synthesis of N-C

The surface of the SiO₂@GO nanospheres was further coated by polydopamine [44]. Typically, 200 mg of as-prepared SiO₂@GO spheres were dispersed in 100 mL of 2 mg mL⁻¹ dopamine Tris solution (pH 8.5, 10 mM Tris buffer) and allowed to react for 36 h under stirring at room temperature. The resultant SiO₂@GO@PDA was separated and collected, and subsequently washed

for 5 cycles and dried by freeze-drying. After that, the resulting powder was carbonized at 900 °C for 3 h under inert atmosphere. Finally, the as-prepared SiO₂@N-C spheres were then transformed into N-C hollow carbon nanospheres by etching the SiO₂ cores with HF solution (≈2%) for two times.

2.1.3. Synthesis of Pd1/N-C SAC

50 mg of N-C composites were dispersed in 50 mL DI water. Then, 0.5 mg of K₂PdCl₄ was added to the suspension and stirred for 2 h in an ice bath. During this process, Pd atoms were deposited on the confined interface of N-C support, leading to the formation of Pd1/N-C SAC. Afterwards, the reaction mixture was filtered and washed three times with pure water to remove the remaining reagents. Finally, the resulting solid Pd1/N-C catalysts were collected and dried by freeze-drying.

2.2. Electrochemical measurements details

All electrochemical measurements were conducted in a conventional three electrode electrochemical cell with a potentiostat or a bi-potentiostat (VMP2, Bio-Logic). A graphite rod (Grade 1, Ted Pella) was used as a counter electrode, and a mercury-mercurous sulphate reference electrode (SI Analytics) was used as the reference electrode. The electrolyte was 0.1 M HClO₄ prepared from 70% HClO₄ (Merck Suprapur) purged with either O₂ (5N5, AGA) or Ar (5N5, AGA). All measurements were performed at room temperature, 25 ± 1 °C. All potentials reported in this study are referred to the reversible hydrogen electrode (RHE) scale. The RHE was calibrated by performing hydrogen evolution and oxidation reactions in a H₂-purged electrolyte using a Pt wire. The catalyst ink was composed of 5 mg of catalyst dispersed in a solution containing 3.75 mL of ethanol (≥99.8%, Fluka Analytical), 1.25 mL of ultrapure water (18.2 MΩ cm, Millipore Synergy uV water purification system), and 15 μL of Nafion solution (5% in lower aliphatic alcohols, Sigma-Aldrich). The ink was ultrasonicated in an ultrasonic bath for at least 30 min before drop casting.

2.2.1. Rotating ring disk electrode measurements

Rotating ring disk electrode (ChangeDisk, Pine Research Inst.) with a glassy carbon disk electrode (Pine Research Inst.) and a platinum ring electrode was used for RRDE measurements. Glassy carbon electrode was polished before use with alumina slurry suspension (Buehler), first with 0.3 μm and then with 0.05 μm particle size. The electrode was cleaned between the two polishing steps by ultra-sonicating in ultrapure water and in isopropyl alcohol (EMSURE, Merck). After polishing with 0.05 μm silica powder, the electrode was cleaned by ultra-sonicating in ultrapure water and in isopropyl alcohol, three times repetitively. The ink was drop casted on to the glassy carbon electrode with a loading amount of 15 μg catalyst on to 5 mm diameter glassy carbon electrode. The ink was dried at room temperature. The Ohmic drop was measured by electrochemical impedance spectroscopy and compensated manually after the measurements. Before performing RRDE measurements, platinum ring electrode was activated by cycling between 0.05 V and 1.6 V for 100 cycles with a scan rate of 500 mV s⁻¹ in an Ar-saturated 0.1 M HClO₄. The ORR was conducted by performing cyclic voltammetry between -0.2 V to 0.7 V in an O₂-saturated 0.1 M HClO₄ solution with a scan rate of 50 mV/s and a rotating rate of 1600 rpm. First few cycles of ORR show low activity with small double layer capacitance region due to poor wetting of the electrode. After ~5 cycles of CVs catalyst coated glassy carbon electrode becomes completely wet and shows higher activity with larger double layer capacitance region. Blank CV was also measured in an Ar-saturated 0.1 M HClO₄ to subtract the double layer capacity region from ORR CVs. The potential of the Pt ring electrode was maintained at 1.4 V during the ORR measure-

ment to oxidize H₂O₂ produced. Accelerated durability tests were performed by cycling potential between 0.05 V and 0.7 V for 10,000 cycles with a scan rate of 500 mV s⁻¹ and a rotating rate of 400 rpm in an O₂-saturated 0.1 M HClO₄. The electrolyte was changed after the durability test to minimize the effect of H₂O₂ produced during the course of durability test on the forthcoming ORR measurement.

2.2.2. 3-compartment cell measurements

Gas diffusion electrode submerged in 0.1 M HClO₄ in three compartments set-up. The catalyst ink, described above, was drop-casted with a loading of 0.1 mg cm⁻² on a gas diffusion layer (H15, Freudenberg) substrate placed on a 60 °C hot plate on an area of approximately 2 cm². This gas diffusion electrode (GDE) was used as a working electrode for the H₂O₂ accumulation tests.

A conventional three-electrode electrochemical cell was used. Catalyst casted GDE was used as a working electrode, a graphite rod as a counter electrode, and a mercury-mercurous sulphate reference electrode as a reference electrode. The working electrode was separated from the counter electrode by Nafion 117 membrane. The Ohmic drop was measured by electrochemical impedance spectroscopy and compensated by 85% using automatic compensation (EC-Lab, BioLogic). Three electrode experiments with stagnant electrode were conducted at a potential of 0.2 V for up to 15 C of accumulated charge in an O₂-saturated 0.1 M HClO₄. Resulting hydrogen peroxide was quantified by permanganate titration method using 0.02 M KMnO₄ (Titripur, EMD Millipore).

2.3. Computational details

All ground state DFT calculations were performed at the GGA level with the Grid-based Projected Augmented Wave (GPAW) program [45,46] and the Atomic Simulation Environment (ASE) package [47]. We used finite difference mode with the BEEF-vdW exchange and correlation functional [48], sampling the Brillouin zone with a 2 × 2 × 1 Monkhorst-Pack *k*-point set and a grid spacing of *h* = 0.18 Å. All structures were relaxed to a force below 0.05 eV/Å. The unit cell for all structure is periodic in *x* and *y* directions, while we applied a vacuum of 8 Å to each side of the catalyst plane along the *z*-axis. To evaluate the Gibbs free energy contribution, the entropy and zero point energy corrections were added to the DFT energies [49]. For all the structures calculated, we added solvation corrections to take into account water induced stabilization of the reaction intermediates [50]. After publication, all structures with total energies will be available on Jan Rossmeisl's group homepage at the URL: <http://nano.ku.dk/english/research/theoretical-electrocatalysis/katladb/>.

3. Results and discussion

3.1. Preparation of catalysts

Pd1/N-C along with three control samples were prepared and tested for electrochemical H₂O₂ production. Synthesis of Pd1/N-C consists of four steps: (1) GO coating of SiO₂ nanospheres, SiO₂@GO; (2) dopamine polymerization and coating, SiO₂@GO@polydopamine (SiO₂@GO@PDA); (3) post carbonization and etching of SiO₂ template; (4) Pd deposition *via* the direct adsorption of Pd species (Fig. 1a and d) [40]. The additional three control samples were prepared to elucidate the effect of individual parameters: single-atom, N-dopant species, and carbon support. Pd nanoparticle deposited on reduced graphene oxide (RGO) (PdNP/C, Fig. 1c and d) was prepared as a control sample for the single-atom dispersion parameter. Pd single-atom on non-N-doped hollow amor-

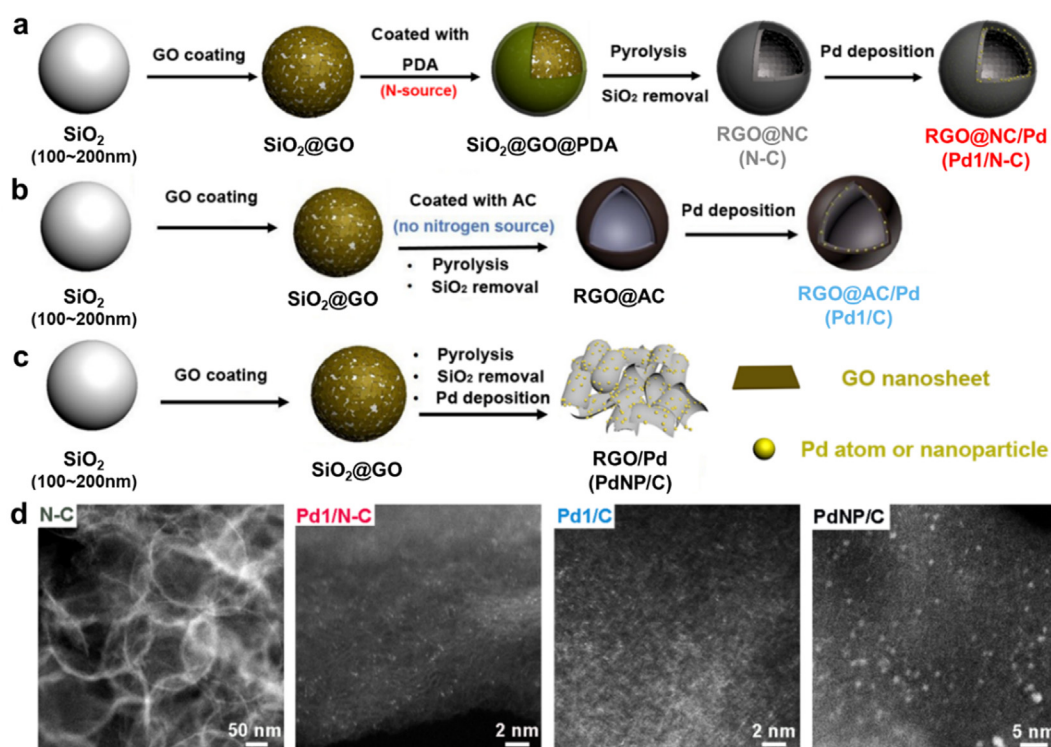


Fig. 1. Schematic illustration of the preparation steps and representative images. Schematic illustration of the preparation of (a) N-doped hollow carbon nanospheres without Pd (N-C) and Pd single-atom anchored at N-doped hollow carbon nanospheres (Pd1/N-C), (b) Pd single-atom at non-doped hollow AC nanospheres (Pd1/C), (c) Pd nanoparticles deposited on RGO (PdNP/C), and representative HAADF-STEM images of the catalysts.

phous carbon (AC) nanospheres (Pd1/C, Fig. 1b and d) was prepared as a control sample for the N-dopant species parameter. N-doped hollow carbon nanospheres without Pd (N-C, Fig. 1a and d) was prepared as a control sample for the carbon support parameter. Weight percent of Pd was controlled to 0.3 wt% except for N-C catalyst, and same catalyst amount was tested. Detailed description of the catalysts will be discussed later.

3.2. Electrochemical production of H_2O_2

Electrochemical H_2O_2 production using Pd1/N-C was first characterized with rotating ring-disk electrode (RRDE) measurements (Fig. 2). RRDE permits easy and fast determination of catalytic activity for oxygen reduction reaction as well as selectivity towards H_2O_2 . As seen in Fig. 2d, oxygen is reduced to either H_2O_2 or H_2O at the surface of the disk electrode with the catalyst of interest. Radial convection introduces the H_2O_2 product to the ring electrode where H_2O_2 is oxidized back to O_2 . Catalytic activity and selectivity for H_2O_2 production is determined by measuring and comparing the reductive current of the disk electrode and the oxidative current of the ring electrode. In this article, we refer to selectivity in terms of faradaic efficiency, i.e., the ratio between electrons used for H_2O_2 production and the total current used in the oxygen reduction reaction

Pd1/N-C SAC (Fig. 1a) was compared with the state-of-the-art catalyst surfaces measured by RRDE in the form of Tafel plots in Fig. 2a and b. [1,13,15,16,22–29,31,51] Peak faradaic efficiencies of each catalyst is plotted in Fig. 2c. Fig. 2a presents Tafel plots showing specific activity of different catalyst surfaces using polycrystalline surfaces (pc); the plot compares intrinsic activities of catalyst surfaces. To accurately benchmark the intrinsic activity of Pd1/N-C with polycrystalline surfaces, we have controlled the density of active atoms on the electrode to $2.15 \text{ nmol}_{Pd} \text{ cm}_{geo}^{-2}$, which is in the range of low index surfaces of precious metals such

as Pt, Pd, Au, and Ag ($2.00\text{--}2.53 \text{ nmol}_{PM} \text{ cm}_{geo}^{-2}$). Intrinsic activity of Pd1/N-C per site is slightly higher than Ag(pc) and Ag-Hg(pc) and lower than Pt-Hg(pc) and Pd-Hg(pc). The merit of SAC is its high utilization, that is high mass activity. The mass activity is compared in Fig. 2b. The mass activity of Pd1/N-C is comparable to the best reported catalysts, Pd-Hg/C and various Co-N/C catalysts. Since Pd is heavier atom, higher atomic mass, than Co, we replotted Fig. 2b into activity per mole for more precise comparison in Fig. S1. In this new plot, Pd1/N-C is more active than Co-N/C (2) and Co-N/C (3) catalysts in most of the potential range. Use of mercury, Hg, might draw concerns from end-users, making Pd1/N-C and Co-N/C catalysts the best candidates for electrochemical H_2O_2 production in terms of activity.

The Pd1/N-C catalyst sample (Fig. 1a) and three additional control samples were compared in a RRDE set-up (Fig. 3). Pd1/N-C showed the highest faradaic efficiency of $78.9 \pm 2.5\%$ as well as highest H_2O_2 production rate, shown by the highest ring current. The three control samples were prepared to elucidate the effects of individual parameters of the Pd1/N-C catalyst. The N-doped hollow carbon nanospheres without Pd single-atom (N-C, Fig. 1a), showed the lowest activity, suggesting insignificant effects from the support. The Pd-nanoparticles catalyst (PdNP/C) was prepared (Fig. 1c) to test the effects of the single atom parameter. PdNP/C had a lower faradaic efficiency towards H_2O_2 . As expected and in contrast to single atom sites, a nanoparticle structure with continuous active sites facilitates the 4e pathway to H_2O due to the presence of hollow sites. A single atom Pd catalyst without N-doping (Pd1/C) was prepared (Fig. 1b) to test the effects of the N-dopant. Pd1/C had less activity as well as less selectivity towards H_2O_2 in comparison to Pd1/N-C. This suggests that the N-dopant coordinates with the Pd single-atom to increase the activity and selectivity. In addition, Pd1/C had a selectivity comparable to the PdNP/C, challenging the effect of the single atom site parameter, in RRDE set-up.

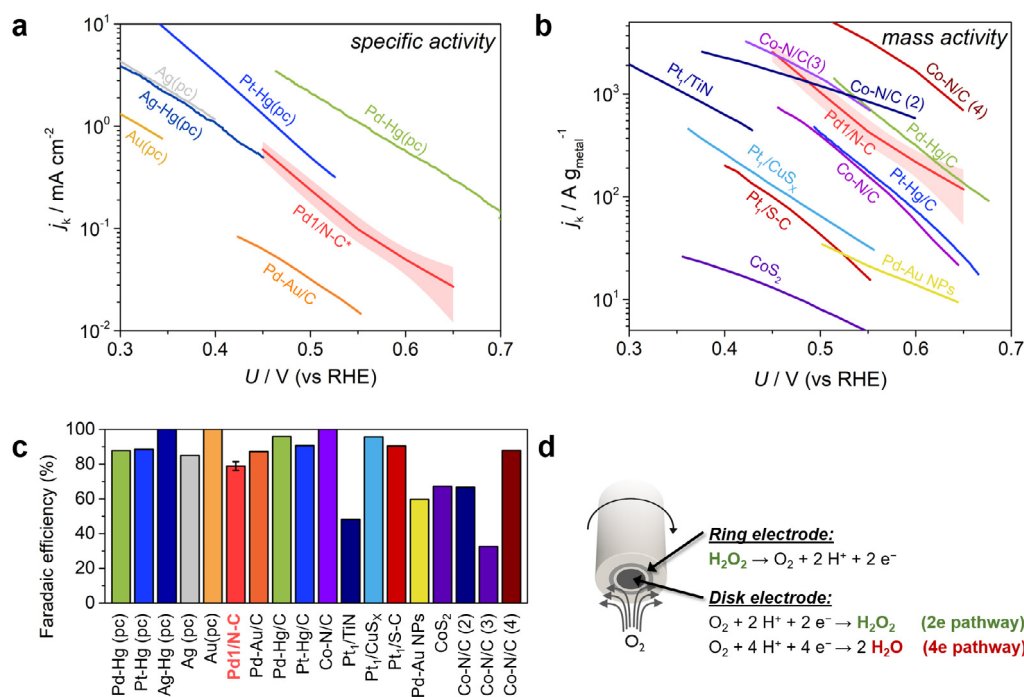


Fig. 2. Comparison of state-of-the-art catalysts and present work for electrochemical production of H_2O_2 using RRDE measurements. Tafel plots of mass-transport corrected kinetic current densities for electrochemical H_2O_2 production in acidic media based on RRDE measurements for (a) specific activity, and (b) mass activity. Red line and pale red bands of Pd1/N-C indicate mean and standard deviation of three independent measurements. (c) Peak faradaic efficiency towards H_2O_2 . (d) Schematic of RRDE measurement. Data adapted from Ref. [22] for Pt–Hg(pc, polycrystalline) and Pt–Hg/C; Ref. [16] for Pd–Hg(pc) and Pd–Hg/C; Ref. [1] for Ag(pc), and Ag–Hg(pc); Ref. [23] for Pd–Au NPs; Ref. [51], for Au(pc); Ref. [24] for Pd–Au/C; Ref. [26] for Co–N/C; Ref. [29] for Pt₁/TiN; Ref. [31] for Pt₁/S–C; Ref. [27] for Pt₁/CuS_x; Ref. [28] for CoS₂; Ref. [13] for Co–N/C (2); Ref. [15] for Co–N/C (3); Ref. [25] for Co–N/C (4). Data noted with asterisk, *, have been normalized with the geometric surface area of the working electrode.

The most critical issue in SACs is its low stability and obtaining stable SACs is a key challenge for the development of SACs [40,52–54]. The operating potential of electrochemical production

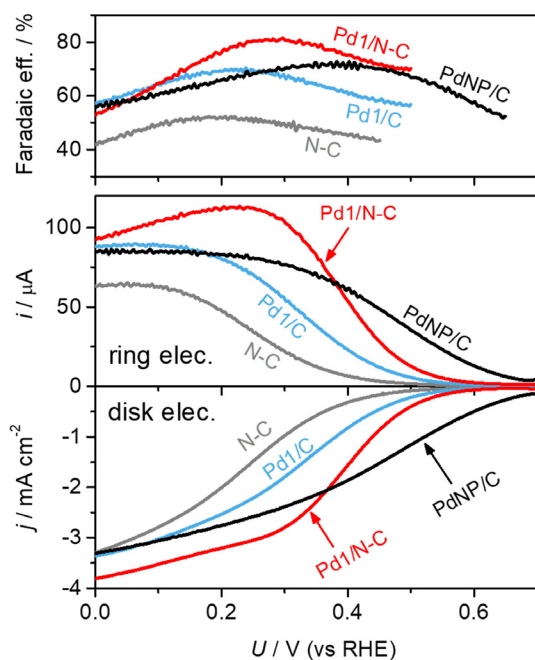


Fig. 3. Comparison of Pd1/N-C with control samples, electrochemical production of H_2O_2 using RRDE measurements. Oxygen reduction reaction on different catalysts using rotating ring-disk electrode. From bottom to top: current density plot from the disk electrode showing total oxygen reduction current, current from oxidation of H_2O_2 at the ring electrode, and Faradaic efficiency towards H_2O_2 production. Measurements in O_2 -saturated 0.1 M HClO_4 with a rotating rate of 1600 rpm at room temperature.

of H_2O_2 is below 1.0 V vs RHE, where electrochemical oxidation of carbon support is not significant. However, H_2O_2 is highly oxidizing chemical and known to oxidize carbon supports chemically even below 1.0 V vs RHE [55,56]. The durability of the prepared catalysts was assessed by adopting “on-off” accelerated durability test. The potential was cycled between 0.05 V and 0.7 V for 10,000 cycles and H_2O_2 was accumulated in the electrolyte solution over time. The potential range represents “off-condition” at 0.7 V where no H_2O_2 is being produced, and “on-condition” at 0.05 V where H_2O_2 is being produced with limiting current density for all four catalysts. Oxygen reduction reaction RRDE measurements were performed before and after the “on-off” cycling and compared in Fig. 4a. When the production rate of H_2O_2 were compared, Pd1/N-C was far better than other 3 samples after 10,000 cycles “on-off” test. The H_2O_2 production current, depicted by the ring current curve, was only slightly shifted negatively for Pd1/N-C, while the peak current and selectivity remained almost the same before and after the stability test. This suggests that although 2e pathway deactivated to a certain extent, 4e pathway also deactivated to a similar or to a greater extent after 10,000 cycles “on-off” test. We note that if the selectivity is maintained, the decrease in the activity can be easily compensated by slightly increasing the applied voltage. H_2O_2 production currents decreased for other three samples after the stability tests. This accentuates the improved stability of Pd1/N-C compared to other samples. All four samples showed similar extent of activity degradation for oxygen reduction reaction, shown in disk currents. Potentials where current density reaches -1.5 mA cm^{-2} , half-wave potential for 2e pathway, were compared before and after the stability tests. Potential difference was 0.05 V (0.40–0.35 V) for Pd1/N-C, which was similar or better than 0.06 V (0.33–0.27 V) for Pd1/C, 0.05 V (0.26–0.21 V) for N-C, and 0.1 V (0.45–0.35 V) for PdNP/C. Interestingly, PdNP/C showed the poorest stability. Even after 10,000 cycle “on-off” test, Pd1/N-C showed no obvious sign of aggregation observed by HAADF-

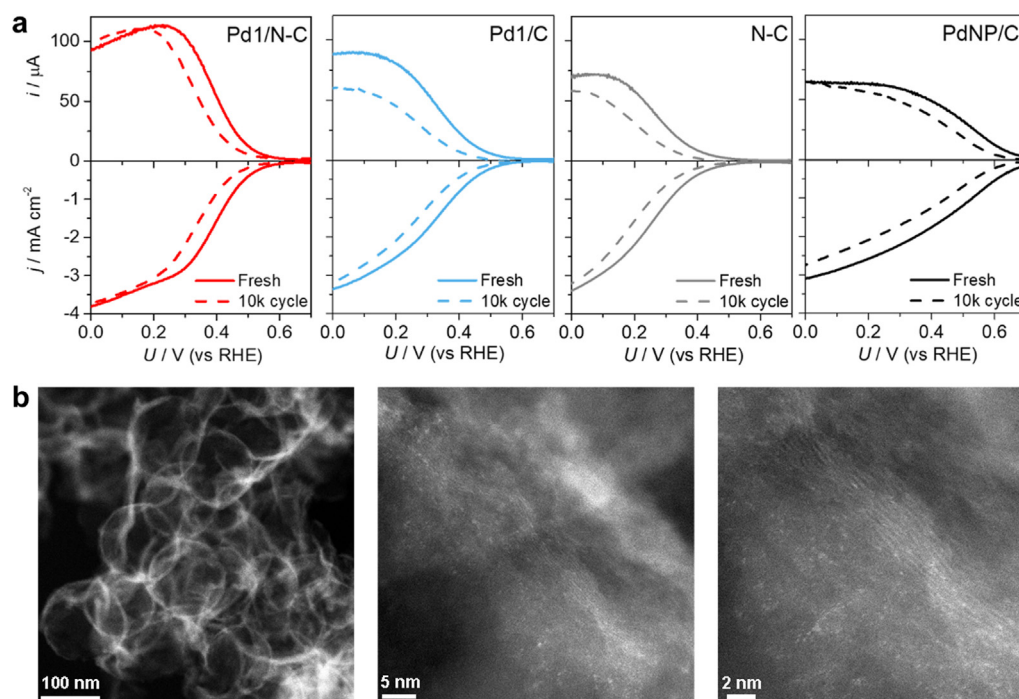


Fig. 4. Electrochemical durability assessment by 10,000 cycle “on-off” test. (a) Oxygen reduction reaction on different catalysts using a rotating ring-disk electrode before and after 10,000 cycle “on-off” durability test. Measurements in O_2 -saturated 0.1 M $HClO_4$ with a rotating rate of 1600 rpm at room temperature. “On-off” durability test was performed by potential cycling between 0.05 V and 0.7 V with a scan rate of 500 mV s^{-1} in O_2 -saturated 0.1 M $HClO_4$ with a rotating rate of 400 rpm at room temperature. (b) Aberration-corrected HAADF-STEM image of Pd1/N-C SAC and enlarged HAADF-STEM image after 10,000 cycle “on-off” test.

STEM, Fig. 4b). No nanometer sized metal cluster was observed at lower magnification and only the single-atoms and few sub-nanometer Pd clusters were observed at higher magnification. Preservation of atomically dispersed Pd single-atoms was key to retain high selectivity after the stability test.

While RRDE measurements are a convenient and widely practiced tool to benchmark electrochemical production of H_2O_2 , they have limitations in determining the selectivity of catalysts. As we have discussed in our earlier perspective article, RRDE measurements only provide an upper-bound selectivity [1]. A thin catalyst layer on the disk electrode coupled with forced convection by rotating the electrode shortens the residence time of produced H_2O_2 . As a result, further reduction of H_2O_2 to H_2O is poorly represented in RRDE measurements in comparison to more realistic scalable set-ups. For this reason, some catalysts that showed high selectivity in RRDE measurements fail to perform in more realistic set-ups with higher local concentrations of H_2O_2 and slower mass transport [1]. It is therefore imperative to test H_2O_2 production catalysts in more realistic conditions. We have adopted a three-compartment set-up where a catalyst-deposited gas diffusion electrode (GDE) is submerged into the O_2 -purged electrolyte and the working electrode potential is held at 0.2 V vs RHE (Fig. 5a and Fig. S2). During testing, there was no forced convection other than the bubbling of O_2 gas and over 100 ppm of H_2O_2 accumulated in the electrolyte, where the H_2O_2 was quantified by permanganate titration using a 0.02 M $KMnO_4$ titrant. At concentrations over 100 ppm without forced convection, further reduction of H_2O_2 to H_2O is no longer negligible. In these conditions, the Pd1/N-C catalyst again had the highest partial current density for H_2O_2 (Fig. 5c) and maintained faradaic efficiencies of over 80% across experiments with an accumulated total charge of 15 C (Fig. 5b). Again, the N-doped hollow carbon nanospheres without Pd single-atom (N-C), showed the lowest activity. PdNP/C catalyst had an improved overall oxygen reduction activity but with lower selectivity towards H_2O_2 , than both N-C and Pd1/C, which is different

from the RRDE results. Pd1/C had less activity as well as less selectivity towards H_2O_2 in comparison to Pd1/N-C. This is the same as the RRDE results and reconfirms that the N-dopant coordinates with the Pd single-atom to increase the activity and selectivity. We conclude that coordinating Pd single-atoms to N-doped carbon is successful strategy for preparing an efficient catalyst for the selective electrochemical production H_2O_2 in realistic applied set-ups. It should also be noted that the selectivity of Pd1/C was higher than PdNP/C, confirming the effects of the single atom site parameter. These observations reinforce our arguments for benchmarking H_2O_2 production using a more realistic scalable set-up in addition to RRDE measurements. The performance of the Pd1/N-C catalyst in a scalable set-up stresses the impact of this catalyst.

3.3. Characterization of Pd1/N-C SAC and control samples.

A templating method was employed in the synthesis of the N-C nanospheres as shown in Fig. 1a. Fig. S3 and Fig. S4, show hollow nanosphere structure. Hollow structured spherules with the shell thicknesses of ~ 10 nm, can be used as support of nano-reactor in heterogeneous catalysis. The morphology of Pd1/N-C SACs and PdNP/C composites were initially characterized by scanning electron microscopy (SEM) and aberration-corrected high-angle annular dark-field scanning transmission electron microscopy (HAADF-STEM). As can be seen from the SEM images, the Pd1/N-C atomic catalysts demonstrate spherical structure (Supplementary Fig. S3), while PdNP/C composite exhibited a randomly-stacked sheet-like morphology (Supplementary Fig. S5), indicating that the outer PDA-derived carbon coating facilitates the resulting hollow carbon nanosphere structure. Tomography results (Fig. S6, S7, Supplementary Movie 1 and Movie 2) further indicate a hollow nanosphere structure. However, the contrast of the initial RGO coating and the subsequent N-doped amorphous carbon coating is indistinguishable. It can be speculated that there is a double carbon shell present from the connection of two tangent spheres

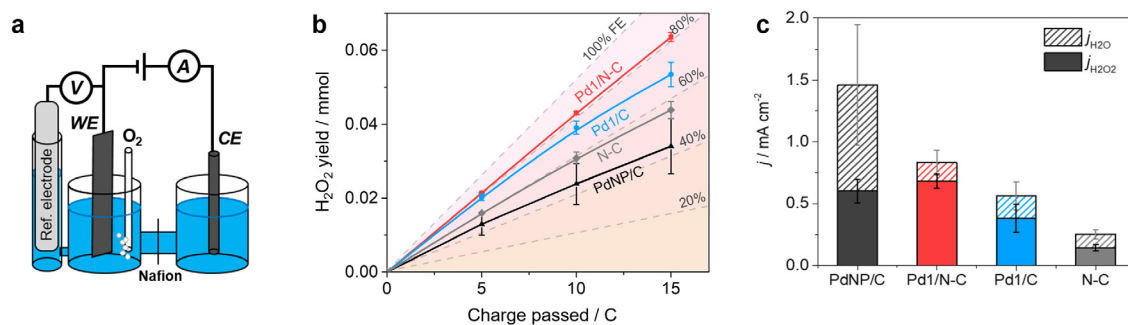


Fig. 5. Electrochemical production of H₂O₂ using three compartments set-up with stagnant electrolyte. (a) Schematic of three compartment set-up. (b) H₂O₂ yield over charge accumulated up to 15 C. Potential of working electrode was held at 0.2 V vs RHE in 0.1 M HClO₄. Dashed lines indicate corresponding lines for given faradaic efficiencies. (c) Partial current densities of measurements in (b).

(Fig. S6a) and the orthoslice showing a partially peeled off RGO layer (Fig. S7c).

In addition, Raman spectroscopy was used to study the structural defects of the N-C and RGO supports. The higher I_D/I_G value of N-C can be attributed to the higher N-doping content, which creates more defects than that for RGO supports (Supplementary Fig. S8). Supplementary Fig. S9a and S9c exhibits the N₂ adsorption/desorption isotherms of N-C and RGO support materials. The respective specific surface areas (SSA) for N-C and RGO supports are 635.7 m² g⁻¹ and 460.9 m² g⁻¹, which are calculated by Brunauer-Emmett-Teller (BET) method. As can be seen from pore size distribution, N-C shows a characteristic microporous property, which mainly originates from numerous micropores with a maximum peak at ca. 1.9 nm (Supplementary Fig. S9b and d). Notably, the micropore ratio of N-C was slightly higher than that of RGO support.

The detailed morphology of Pd1/N-C was characterized by electron tomography and aberration-corrected HAADF-STEM. Fig. 6 shows HAADF-STEM images of Pd1/N-C with different magnification. Notably, no Pd nanoparticle or cluster was observed in the low magnification images of the Pd1/N-C SAC. At higher magnification, Fig. 6 shows that the bright dots (Pd) were well dispersed with an average size of 3–4 Å, which matches the van der Waals diameter of a single Pd atom [57]. In comparison, many Pd clusters were observed in HAADF-STEM images for the PdNP/C (0.4–3 nm, 0.312 wt%) composite (Supplementary Fig. S10). According to the energy dispersive X-ray spectroscopy (EDS) analysis (Fig. S11), C, O, and N were uniformly distributed over the entire spherical architecture of Pd1/N-C (Fig. S11b), confirming the successful N doping of N-C. However, Pd signal is too weak to be identified due to the low content of Pd species.

To elucidate coordination environment and chemical state of the Pd single-atom of Pd1/N-C, X-ray absorption near edge structure (XANES) and extended X-ray absorption fine structure (EXAFS) were conducted. As can be seen from Fig. 7a, the chemical valence of Pd in Pd1/N-C SAC was positive, which can be determined by its higher white line intensity and higher edge energy compared to Pd foil from XANES spectra. In the EXAFS spectra (Fig. 7b), electron-rich N atoms (with lone-pairs) was found to be coordinated with Pd, further confirming that Pd species existed as isolated atoms and anchored by N doped carbon support. The coordination configurations for the Pd-N_x moieties in Pd1/N-C SAC were then investigated by quantitative least-squares EXAFS curve-fitting analysis. Findings demonstrate that the number of coordinating N atoms of Pd is around six and the mean N-Pd bond length was 2.13 Å. To further validate 6 coordination number (CN) of Pd-N, another common CN of Pd-N, 4, has also been investigated by EXAFS fitting, with the CN set as 4. The 0.047 R factor from this fitting is not acceptable for EXAFS fitting, which rules out the pos-

sibility of 4 CN of Pd-N (Supplementary Table 1). These N atoms act as anchoring sites and could adjust electron density of Pd via coordination, which may lead to an improved catalytic performance [58,59].

X-ray photoelectron spectroscopy (XPS) was employed to investigate the surface composition and oxidation states of the Pd1/N-C SAC. The survey scan (Fig. S12) and Pd 3d scan (Fig. 7d) reveal the existence of C, O, N (ca. 3.8 at.%), and Pd, which is consistent with the element composition of Pd1/N-C. The high-resolution XPS spectrum for N 1s could be deconvoluted into four peaks centered at the binding energy of 398.5, 400.1, 401.3 and 403.0 eV, which were assigned to pyridinic-N, pyrrolic-N, graphitic-N and pyridinic oxide, respectively (Fig. 7c), while Pd was entirely oxidic, Pd²⁺ (Fig. 7d) [60]. The dominant N species in Pd1/N-C was graphitic-N (54.2%), pyridinic-N (21.0%) and pyrrolic-N (20.7%), which could serve as anchoring sites for Pd single-atoms and lead to the formation of heterojunction between incorporated N atoms and Pd species [59]. The doped N atoms might donate electron density to Pd²⁺, and enhance binding strength with the Pd species, resulting in an enhanced stability.

3.4. DFT modeling

To rationalize the observed activity of Pd SAC towards the 2e pathway, we investigated the nature of the Pd active site by means of DFT. The computational details are found in the Supplementary Information. In our previous works, we calculated the activity of 10 different metal atoms coordinated with four pyridinic N (4 N) [1,61]. The results predicted very low activity for Pd/N-C in such coordination site, due to severe limitations of weak binding of the oxygen intermediates [1]. Co/N-C showed instead the highest computed activity for 2e ORR, being the closest to the top of 2e volcano [1]. In this report, we investigate the origin of Pd site activity in relation to our previous understanding, creating a set of model catalysts using inputs from material characterization of Pd1/N-C. Through the ORR associative pathway mechanism [63], we calculated the limiting potential for the ORR on each structure and presented it in a volcano plot relationship (Fig. 8a) [64]. Specifically, we incorporated the EXAFS fitting result modeling structures with a six-fold coordination geometry of pyridinic N atoms (6 N). As XPS result indicated a significant amount of graphitic N in the N-C substrate, we also studied the effect of graphitic N doping around the coordination site. We modelled various N-doped 6 N structures (Fig. 8b) where the total amount of N (coordinating + doping) was varied from ~12% [(6 + 1)N-a,b,c] to ~16% [(6 + 3)N] atomic concentration. To evaluate the N-doping effect on our previously published structural motif, we also reported four-fold pyridinic coordinated catalysts (4 N), varying the overall atomic concentra-

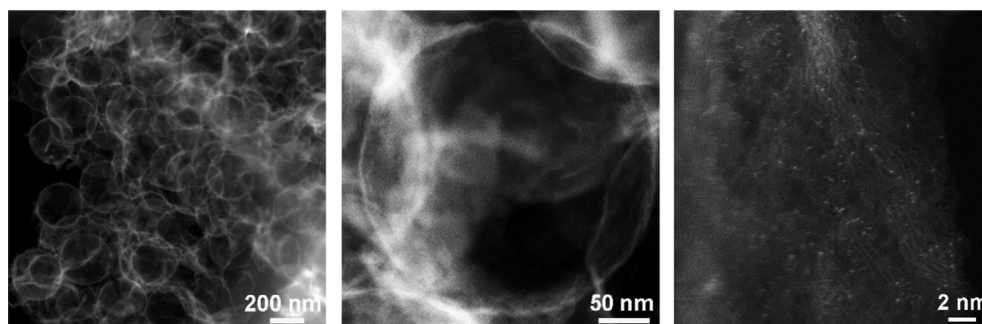


Fig. 6. Atomic structure characterizations of Pd1/N-C SAC by HAADF-STEM. Aberration-corrected HAADF-STEM images of Pd1/N-C SAC; images revealing hollow structure of N-C hollow carbon nanospheres, and high density of Pd atoms (bright dots) deposited on N-C.

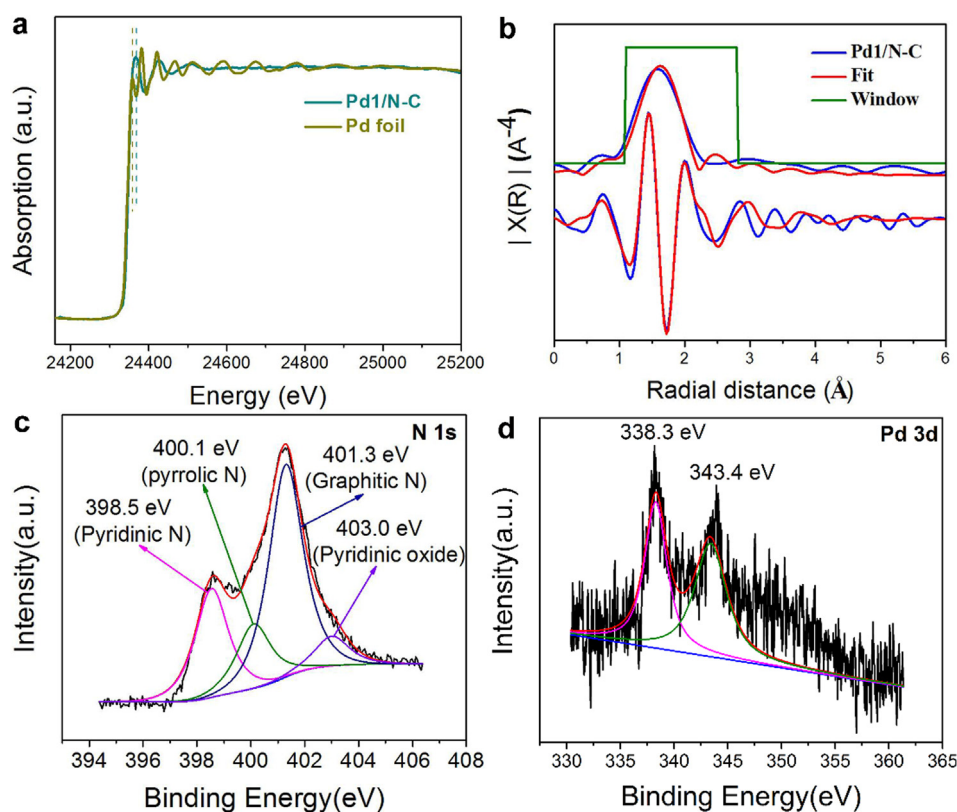


Fig. 7. (a) Characterizations of Pd1/N-C SAC by X-ray absorption spectroscopy and X-ray photoelectron spectroscopy (XPS). (a) Pd K X-ray absorption near edge structure (XANES) spectra of Pd1/N-C SAC and Pd foil; (b) EXAFS functions and the fittings of Pd1/N-C SAC. XPS spectra of the Pd1/N-C SAC; (c) N 1s, (d) Pd 3d.

tion of N from 5% to 12%. All the model structures are reported in Fig. 8b for visual clarity.

In Fig. 8a, the 2e and 4e pathway volcano lines are shown in green and black, respectively. The structures computed limiting potential are presented with dots following the same color coding. The green background in the plot indicates the area where the computed selectivity to peroxide for single site catalysts is 100%, from purely thermodynamic perspective and taking into account the specific geometric effect on single sites (*O destabilization relative to H_2O_2 reversible potential), faded at the boundary to account for the inherent uncertainty in ground state DFT predictions. A detailed explanation of this selectivity area can be found in the [Supplementary Information](#).

We recently proved the 4 N model structure to be an accurate approximation to study catalytic trends in single site transition metal catalysts [13,62], demonstrating the positive structural

effects of single site catalysis for 2e ORR altogether. However, in the present study a discrepancy between the 4 N model and the observed catalytic performance for Pd SAC emerges. Within the 4 N coordination, Pd was predicted to be a very weak binder for *OOH – a selective but inactive catalyst. Notably, when the coordination number is switched from 4 N to 6 N (always within pyridinic coordination, see 6 N in Fig. 8b), we observed an increase in computed activity, due to a stronger interaction between the active site and the reaction intermediates. The stronger interaction originates from the wider graphene vacancy, which host a six-fold N coordination geometry. With the Pd center at greater distance from the N ligands, we predicted a decreasing inductive electronic effect as compared to 4 N, even though two more N ligands are coordinating the metal atom. The addition of graphitic N in the graphene sheet further reduces the electron donation from the coordinating N, enhancing the binding strength of the Pd metal center.

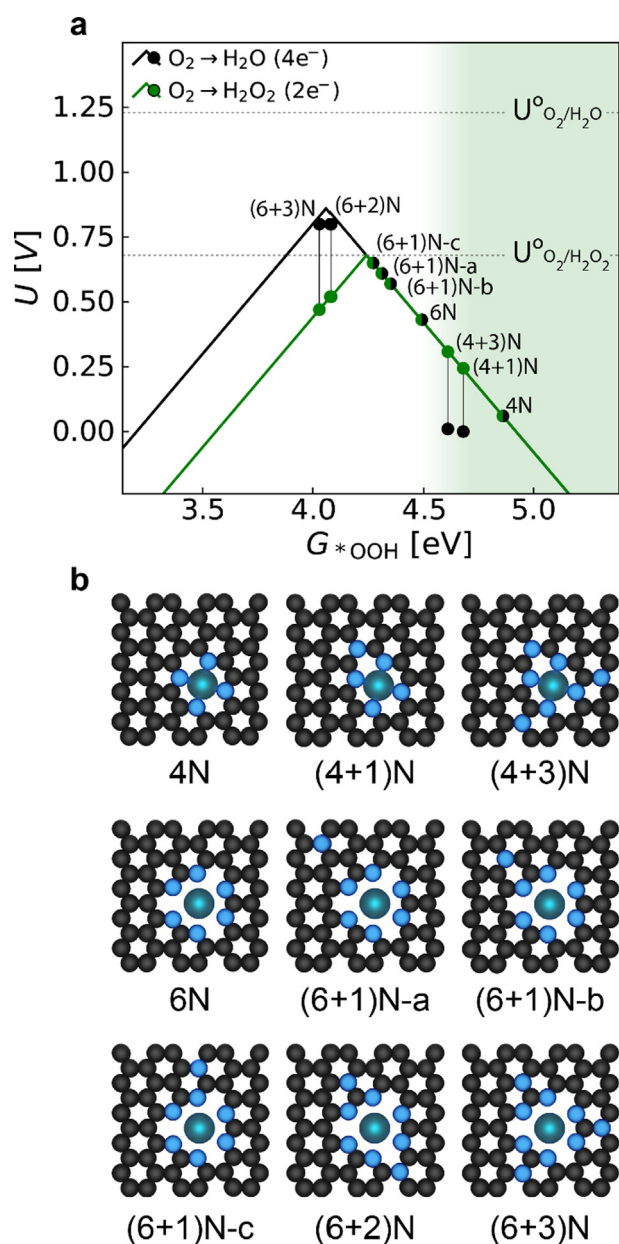


Fig. 8. DFT modeling results. (a) Computational Sabatier volcano plot. The calculated onset potential is plotted as function of the descriptor G^*_{OOH} ($^*_{\text{OOH}}$ formation free energy). Each structure has an onset potential for 2e (green dots) and 4e (black dots), connected by a black vertical line for readability. If these potentials coincide, the dot is half-green, half-black. The green area represents the theoretical 100% H_2O_2 selectivity threshold. (b) Unit cell rendering for the Pd-SAC structures modelled. Black, teal and light blue spheres represent C, Pd and N atoms, respectively.

For its electron withdrawing nature, graphitic N engages part of the electronic density that pyridinic N uses for the dative coordination with the Pd atom. Fig. S13 shows the progressive loss of electron density around Pd upon increasing amount of doped graphitic N. Beyond 16% overall N atomic concentration (structure (6 + 3)N, Fig. 8b), we found the coordination site is unable to stabilize the metal center. Pd migrates at the defect edge, coordinating only to two N, yielding structures severely limited by ORR intermediates strong retention (Fig. S14). The binding strength of Pd is increased by the doping of graphitic N and, regardless of the exact position, one graphitic N at the surroundings of the coordinating center [(6 + 1)N-a,b,c] determines increased computed activity. In fact,

structures (6 + 1)N-a, b or c approach the ideal G^*_{OOH} to reach the top of the 2e volcano, where rate of 2e ORR is highest. Further N-doping with 2 and 3 graphitic N yields model catalysts even more active, which lie at the top of the 4e volcano. Their computed rate deviate from experimental observations, as Pd SAC shows high selectivity to H_2O_2 . In fact, for these two catalysts the 2e rate is significantly lower than the 4e rate, as evidenced by the y-axis gap between black and green dots in Fig. 8a. Notably, also the N-doping on the 4 N structure determines increased affinity of Pd for the ORR intermediates. Despite being activated, (4 + 1)N and (4 + 3)N model catalysts possess a lower 4e activity than the reference Pd 4 N catalyst, as the 4e pathway rate limiting step becomes the reduction $^*_{\text{OOH}} \rightarrow ^*_{\text{O}}$. However, the 2e rate is defined only by the thermodynamics of a single intermediate, $^*_{\text{OOH}}$. Hence, we observe an onset potential gap in favor of the 2e reaction for (4 + 1)N and (4 + 3)N, i.e. a higher reaction rate for the peroxide formation than for the full reduction.

By comparing experimental results with DFT calculations, we suggest that the high activity of Pd1/N-C stems from 6 N coordinating environment, possibly sustained by additional graphitic N-doping around the coordinating site. The optimal doping in the immediate surroundings of the metal center is predicted between one and two graphitic N, which still secures good stability to the Pd site. Table S2 reports the sites reduction potential referenced to fcc bulk Pd, showing higher thermodynamic stability toward oxidative leaching for the sites proposed as active and selective, compared to the standard reduction potential of palladium. Table S2 further shows that an excessive N doping results in lower reduction potential thus lower Pd atom retention in the coordination site. As we have presented above, the intrinsic activity of Pd1/N-C still does not match the highly selective Pd-Hg(pc) catalyst, although we show how site coordination and moderate doping potentially enable catalytic activities close to thermodynamic limit for peroxide production. This thermodynamic model is useful to qualitatively determine the features of a real catalytic surface, however, it does not necessarily represent accurately the synthesized catalyst, which is likely a mixture of differently coordinated Pd active sites. Also other kinetic limitations could play a major role. Nonetheless, we indicate how the control on N content in the substrate could be a key to enable creation of highly active sites, achieving even higher activity for electrochemical H_2O_2 production using Pd SAC.

4. Conclusion

Pd single-atoms on N-doped hollow carbon nanosphere, Pd1/N-C, exhibited excellent catalytic performance for electrochemical H_2O_2 production owing to its optimized electronic and geometric structure. Presence of single-atom active sites and coordination effect of Pd single-atom with N-species are main reasons for high activity and selectivity. Pd1/N-C also showed improved stability of Pd1/N-C after 10,000 cycle “on-off” test. DFT calculations suggests that 6 N coordinating environment with additional doping of graphitic N can explain the high catalytic activity. The method for benchmarking electrochemical H_2O_2 synthesis requires more attention. Comparison of measurements from RRDE and three compartment set-up exhibited the effect of mass transport and H_2O_2 concentration on the catalysis. For example, PdNP/C could have been considered as a promising candidate when RRDE measurement is considered, but in a more realistic set-up PdNP/C failed to produce H_2O_2 with reasonable selectivity. SACs have unique potential in heterogeneous catalysis field as shown in the case of Pd1/N-C for H_2O_2 synthesis. The proposed synthesis strategy could be adopted to other SAC systems if the active atom has coordination strength with N species. Carbon substrate doping could be fur-

ther investigated, also with other well-known dopant species (O, B, S, etc.). Controlling the coordinating sphere of active atoms via controlled synthesis of coordination sites, as well as control over site proximity dopants could be a key for successful development of other single-atom catalysts of this kind.

Author contributions

J. B. X. performed the synthesis, most of the structural characterizations. S. Y., J. N. H., J. –P. B. H., J. K., and I. C. designed and performed the electrochemical tests. S. F. C. and Y. Y. Z. performed the XAFS measurement and analyzed the EXAFS and XANES data. H. Y. S and P. L. conducted the HAADF-STEM characterization. L. S. and J. R. designed and performed the computational modeling. P. L., Q. Y. C, and S. B. conducted the 3D tomography characterization. The paper was co-written by J. B. X., S. Y., L. S., S. F. C. and P. L. The research was supervised by S. W. and I. C. All authors discussed the results and commented on the manuscript. J. B. X., S. Y., L. S. and S. F. C. contributed equally.

Declaration of Competing Interest

The authors declare that they have no known competing financial interests or personal relationships that could have appeared to influence the work reported in this paper.

Acknowledgements

This research was financially supported by the National Natural Science Foundation of China (No. 51772110), Natural Science Foundation of Hubei Province (No. 2019CFB539), Danmarks Innovationsfond within the ProActive project (5160-00003B), Villum Foundation V-SUSTAIN grant 9455 to the Villum Center for the Science of Sustainable Fuels and Chemicals, the Carlsberg Foundation grant CF18-0435, the Institutional Research Program (2E30220) of the Korea Institute of Science and Technology (KIST), Shenzhen Science and Technology Plan under Grant (JCYJ20170818160751460) and the Open Project of Key Laboratory of Green Chemical Engineering Process of Ministry of Education (No. GCP20200205). The authors would like to acknowledge the Analytical and Testing Center of Huazhong University of Science and Technology and the Wuhan National Laboratory for Optoelectronics for SEM, TEM, Raman and XPS measurements.

Appendix A. Supplementary material

Supplementary data to this article can be found online at <https://doi.org/10.1016/j.jcat.2020.11.020>.

References

- [1] S. Yang, A. Verdager-Casadevall, L. Arnarson, L. Silvioli, V. Colic, R. Frydendal, J. Rossmeisl, I. Chorkendorff, I.E. Stephens, *ACS Catal.* 8 (2018) 4064–4081.
- [2] S.J. Freakley, Q. He, J.H. Harthy, L. Lu, D.A. Crole, D.J. Morgan, E.N. Ntainjua, J.K. Edwards, A.F. Caraley, A.Y. Borrissevich, C.J. Kiely, G.J. Hutchings, *Science* 351 (2016) 965–968.
- [3] R. Ciriminna, L. Albanese, F. Meneguzzo, M. Pagliaro, *ChemSusChem* 9 (2016) 3374–3381.
- [4] J.M. Campos-Martin, G. Blanco-Brieva, J.L. Fierro, *Angew. Chem. Int. Ed.* 45 (2006) 6962–6984.
- [5] J.K. Edwards, B.E. Solsona, P. Landon, A.F. Carley, A. Herzing, C.J. Keily, G.J. Hutchings, *J. Catal.* 236 (2005) 69–79.
- [6] R.J. Lewis, K. Ueura, Y. Fukuta, S.J. Freakley, L.Q. Kuang, R. Wang, Q. He, J.K. Edwards, D.J. Morgan, Y. Yamamoto, G.J. Hutchings, *ChemCatChem* 11 (2019) 1673–1680.
- [7] J.K. Edwards, S.J. Freakley, R.J. Lewis, J.C. Pritchard, G.J. Hutchings, *Catal. Today* 248 (2015) 3–9.
- [8] S.L. Wang, K.G. Gao, W. Li, J.L. Zhang, *Appl. Catal. A- Gen.* 531 (2017) 89–95.
- [9] E. Ghedini, F. Menegazzo, M. Signoreto, M. Manzoli, F. Pinna, G. Strukul, *J. Catal.* 273 (2010) 266–273.

- [10] F. Menegazzo, M. Manzoli, M. Signoreto, F. Pinna, G. Strukul, *Catal. Today* 248 (2015) 18–27.
- [11] A. Pashkova, L. Greiner, U. Krtschil, C. Hofmann, R. Zapf, *Appl. Catal. A- Gen.* 464 (2013) 281–287.
- [12] T. Ishihara, R. Nakashima, Y. Ooishi, H. Hagiwara, M. Matsuka, S. Ida, *Catal. Today* 248 (2015) 35–39.
- [13] Y.Y. Sun, L. Silvioli, N.R. Sahaie, W. Ju, J.K. Li, A. Zitolo, S. Li, A. Bagger, L. Arnarson, X.L. Wang, T. Moeller, D. Bernsmeier, J. Rossmeisl, F. Jaouen, P. Strasser, *J. Am. Chem. Soc.* 141 (2019) 12372–12381.
- [14] X.Y. Guo, S.R. Lin, J.X. Gu, S.L. Zhang, Z.F. Chen, S.P. Huang, *ACS Catal.* 9 (2019) 11042–11054.
- [15] E. Jung, H. Shin, B.H. Lee, V. Efremov, S. Lee, H. Seok Lee, J. Kim, W.H. Antink, S. Park, K.S. Lee, S.P. Cho, J.S. Yoo, Y.E. Sung, T. Hyeon, *Nat. Mater.* 19 (2020) 436–442.
- [16] A. Verdager-Casadevall, D. Deiana, M. Karamad, S. Siahrostami, P. Malacrida, T.W. Hansen, J. Rossmeisl, I. Chorkendorff, I.E. Stephens, *Nano Lett.* 14 (2014) 1603–1608.
- [17] C.H. Choi, H.K. Lim, M.W. Chung, G. Chon, N.R. Sahaie, A. Altin, M.T. Sougrati, L. Stievano, H.S. Oh, E.S. Park, F. Luo, P. Strasser, G. Dražić, K.J.J. Mayrhofer, H. Kim, F. Jaouen, *Energy Environ. Sci.* 11 (2018) 3176–3182.
- [18] H.B. Yang, S.F. Hung, S. Liu, K.D. Yuan, S. Miao, L.P. Zhang, X. Huang, H.Y. Wang, W.Z. Cai, R. Chen, J.J. Gao, X.F. Yang, W. Chen, Y.Q. Huang, H.M. Chen, C.M. Li, T. Zhang, B. Liu, *Nat. Energy* 3 (2018) 140–147.
- [19] J.Z. Li, M.J. Chen, D.A. Cullen, S. Hwang, M.Y. Wang, B.Y. Li, K.X. Liu, S. Karakalos, M. Lucero, H.G. Zhang, C. Lei, H. Xu, G.E. Sterbinsky, Z.X. Feng, D. Su, K.L. More, G.F. Wang, Z.B. Wang, G. Wu, *Nat. Catal.* 1 (2018) 935–945.
- [20] A. Zitolo, V. Goellner, V. Armel, M.T. Sougrati, T. Mineva, L. Stievano, E. Fonda, F. Jaouen, *Nat. Mater.* 14 (2015) 937–942.
- [21] H.L. Fei, J.C. Dong, Y.X. Feng, C.S. Allen, C.Z. Wan, B. Voloskiy, M.F. Li, Z.P. Zhao, Y.L. Wang, H.T. Sun, P.F. An, W.X. Chen, Z.Y. Guo, C. Lee, D.L. Chen, I. Shakir, M.J. Liu, T.D. Hu, Y.D. Li, A.I. Kirkland, X.F. Duan, Y. Huang, *Nat. Catal.* 1 (2018) 63–72.
- [22] S. Siahrostami, A. Verdager-Casadevall, M. Karamad, D. Deiana, P. Malacrida, B. Wickman, M. Escudero-Escribano, E.A. Paoli, R. Frydendal, T.W. Hansen, I. Chorkendorff, I.E.L. Stephens, J. Rossmeisl, *Nat. Mater.* 12 (2013) 1137–1143.
- [23] E. Pizzutilo, O. Kasian, C.H. Choi, S. Cherevko, G.J. Hutchings, K.J.J. Mayrhofer, S. J. Freakley, *Chem. Phys. Lett.* 683 (2017) 436–442.
- [24] J.S. Jirkovsky, I. Panas, E. Ahlberg, M. Halasa, S. Romani, D.J. Schiffrin, *J. Am. Chem. Soc.* 133 (2011) 19432–19441.
- [25] J.J. Gao, H.B. Yang, X. Huang, S.F. Hung, W.C. Cai, C.M. Jia, S. Miao, H.M. Chen, X. F. Yang, Y.Q. Huang, T. Zhang, B. Liu, *Chem* 6 (2020) 1–17.
- [26] I. Yamanaka, R. Ichihashi, T. Iwasaki, N. Nishimura, T. Murayama, W. Ueda, S. Takenaka, *Electrochim. Acta* 108 (2013) 321–329.
- [27] R.A. Shen, W.X. Chen, Q. Peng, S.Q. Lu, L.R. Zheng, X. Cao, Y. Wang, W. Zhu, J.T. Zhang, Z.B. Huang, C. Chen, D.S. Wang, Y.D. Li, *Chem.* 5 (2019) 2099–2110.
- [28] H.Y. Sheng, E.D. Hermes, X.H. Yang, D.W. Ying, A.N. Janes, W.J. Li, J.R. Schmidt, S. Jin, *ACS Catal.* 9 (2019) 8433–8442.
- [29] S. Yang, J. Kim, Y.J. Tak, A. Soon, H. Lee, *Angew. Chem. Int. Ed.* 55 (2016) 2058–2062.
- [30] S. Yang, Y.J. Tak, J. Kim, A. Soon, H. Lee, *ACS Catal.* 7 (2017) 1301–1307.
- [31] C.H. Choi, M. Kim, H.C. Kwon, S.J. Cho, S. Yun, H.T. Kim, K.J. Mayrhofer, H. Kim, M. Choi, *Nat. Commun.* 7 (2016) 10922.
- [32] S. Mitchell, E. Vorobyeva, J. Pérez-Ramírez, *Angew. Chem. Int. Ed.* 57 (2018) 15316–15329.
- [33] S.W. Li, J.J. Liu, Z. Yin, P.J. Ren, L.L. Lin, Y. Gong, C. Yang, X.S. Zheng, R.C. Cao, S.Y. Yao, Y.C. Deng, X. Liu, L. Gu, W. Zhou, J.F. Zhu, X.D. Wen, B.J. Xu, D. Ma, *ACS Catal.* 10 (2020) 907–913.
- [34] R.H. Lin, D. Albani, E. Fako, S.K. Kaiser, O.V. Safonova, N. López, J. Pérez-Ramírez, *Angew. Chem.* 131 (2019) 514–519.
- [35] R. Jiang, L. Li, T. Sheng, G.F. Hu, Y.G. Chen, L.Y. Wang, *J. Am. Chem. Soc.* 140 (2018) 11594–11598.
- [36] P.Q. Yin, T. Yao, Y.E. Wu, L.R. Zheng, Y. Lin, W. Liu, H.X. Ju, J.F. Zhu, X. Hong, Z.X. Deng, G. Zhou, *Angew. Chem. Int. Ed.* 55 (2016) 10800–10805.
- [37] G.X. Chen, C.F. Xu, X.Q. Huang, J.Y. Ye, L. Gu, G. Li, Z.C. Tang, B.H. Wu, H.Y. Yang, Z.P. Zhao, Z.Y. Zhou, G. Fu, N.F. Zheng, *Nat. Mater.* 15 (2016) 564–569.
- [38] Y.J. Chen, S.F. Ji, Y.G. Wang, J.C. Dong, W.X. Chen, Z. Li, R.A. Shen, L.R. Zheng, Z.B. Zhuang, D.S. Wang, Y.D. Li, *Angew. Chem. Int. Ed.* 56 (2017) 6937–6941.
- [39] H.C. Tao, C. Choi, L.X. Ding, Z. Jiang, Z.S. Han, M.W. Jia, Q. Fan, Y.N. Gao, H.H. Wang, A.W. Robertson, S. Hong, Y. Jung, S.Z. Liu, Z.Y. Sun, *Chem.* 5 (2019) 204–214.
- [40] J.B. Xi, H.Y. Sun, D. Wang, Z.Y. Zhang, X.M. Duan, J.W. Xiao, F. Xiao, L.M. Liu, S. Wang, *Appl. Catal. B: Environ.* 225 (2018) 291–297.
- [41] W. Stöber, A. Fink, E. Bohn, *J. Colloid Interface Sci.* 26 (1968) 62–69.
- [42] W.S. Hummers Jr, R.E. Offeman, *J. Am. Chem. Soc.* 80 (1958) 1339.
- [43] J.S. Lee, K.H. You, C.B. Park, *Adv. Mater.* 24 (2012) 1084–1088.
- [44] H. Lee, S.M. Dellatore, W.M. Miller, P.B. Messersmith, *Science* 318 (2007) 426–430.
- [45] A.H. Larsen, J. Jørgen Mortensen, J. Blomqvist, I.E. Castelli, R. Christensen, M. Dułak, J. Friis, M.N. Groves, B. Hammer, C. Hargus, E.D. Hermes, P.C. Jennings, P. B. Jensen, J. Kermode, J.R. Kitchin, E.L. Kolsbjerg, J. Kubal, K. Kaasbjerg, S. Lysgaard, J.B. Maronsson, T. Maxson, T. Olsen, L. Pastewka, A. Peterson, C. Rostgaard, J. Schiøtz, O. Schütt, M. Strange, K.S. Thygesen, T. Vegge, L. Vilhelmsen, M. Walter, Z.H. Zeng, K.W. Jacobsen, *J. Phys. Condens. Matter* 29 (2017) 273002.
- [46] J.J. Mortensen, L.B. Hansen, K.W. Jacobsen, *Phys. Rev. B - Condens. Matter Mater.* 71 (2005) 1–11.

- [47] S.R. Bahn, K.W. Jacobsen, *Comput. Sci. Eng.* 4 (2002) 56–66.
- [48] J. Wellendorff, K.T. Lundgaard, A. Møgelhøj, V. Petzold, D.D. Landis, J.K. Nørskov, T. Bligaard, K.W. Jacobsen, *Phys. Rev. B - Condens. Matter Phys.* 85 (2012) 32–34.
- [49] J. Rossmeisl, Z.W. Qu, H. Zhu, G.J. Kroes, J.K. Nørskov, *J. Electroanal. Chem.* 607 (2007) 83–89.
- [50] F. Calle-Vallejo, J.I. Martínez, J. Rossmeisl, *Phys. Chem. Chem. Phys.* 13 (2011) 15639–15643.
- [51] J.S. Jirkovský, M. Halasa, D.J. Schiffrin, *Phys. Chem. Chem. Phys.* 12 (2010) 8042–8053.
- [52] J. Kim, C.W. Roh, S.K. Sahoo, S. Yang, J. Bae, J.W. Han, H. Lee, *Adv. Energy Mater.* 8 (2018) 1–8.
- [53] H.J. Qiu, Y. Ito, W.T. Cong, Y.W. Tan, P. Liu, A. Hirata, T. Fujita, Z. Tang, M.W. Chen, *Angew. Chem. Int. Ed.* 54 (2015) 14031–14035.
- [54] J. Jones, H.F. Xiong, A.T. DeLaRiva, E.J. Peterson, H. Pham, S.R. Challa, G.S. Qi, S. Oh, M.H. Wiebenga, X.I.P. Hernández, Y. Wang, A.K. Datye, *Science* 353 (2016) 150–154.
- [55] A.M. Chaparro, N. Mueller, C. Atienza, L. Daza, J. Electroanal. Chem. 591 (2006) 69–73.
- [56] S. Maass, F. Finsterwalder, G. Frank, R. Hartmann, C. Merten, *J. Power Sources* 176 (2008) 444–451.
- [57] G. Vilé, D. Albani, M. Nachtegaal, Z.P. Chen, D. Dontsova, M. Antonietti, N. López, J. Pérez-Ramírez, *Angew. Chem. Int. Ed.* 54 (2015) 11265–11269.
- [58] P.X. Liu, N.F. Zheng, *Natl. Sci. Rev.* 5 (2018) 1–3.
- [59] Y.J. Chen, S.F. Ji, C. Chen, Q. Peng, D.S. Wang, Y.D. Li, *Joule* 2 (2018) 1242–1264.
- [60] S.Q. Zhou, L. Shang, Y.X. Zhao, R. Shi, G.I.N. Waterhouse, Y.C. Huang, L.R. Zheng, T.R. Zhang, *Adv. Mater.* 31 (2019) 1900509.
- [61] P.F. Zhang, Y.T. Gong, H.R. Li, Z.R. Chen, Y. Wang, *Nat. Commun.* 4 (2013) 1593.
- [62] W. Ju, A. Bagger, G.P. Hao, A.S. Varela, I. Sinev, V. Bon, B.R. Cuenya, S. Kaskel, J. Rossmeisl, P. Strasser, *Nat. Commun.* 8 (2017) 944.
- [63] J.K. Nørskov, J. Rossmeisl, A. Logadottir, L. Lindqvist, J.R. Kitchin, T. Bligaard, H. Jónsson, *J. Phys. Chem. B* 108 (2004) 17886–17892.
- [64] V. Viswanathan, H.A. Hansen, J. Rossmeisl, J.K. Nørskov, *J. Phys. Chem. Lett.* 3 (2012) 2948–2951.